Title	Applications of Femtosecond Laser Ablation of Metals to Microprocessing
Author(s)	佐野, 智一
Citation	大阪大学, 2004, 博士論文
Version Type	VoR
URL	https://hdl.handle.net/11094/1888
rights	
Note	

Applications of Femtosecond Laser Ablation

of Metals to Microprocessing

金属のフェムト秒レーザーアブレーションの微細加工への応用

Tomokazu Sano

佐野　智一

Doctoral Dissertation

Applications of Femtosecond Laser Ablation

of Metals to Microprocessing

金属のフェムト秒レーザーアブレーションの微細加工への応用

Tomokazu Sano

佐野　智一

Osaka University

Graduate School of Engineering

大阪大学大学院　工学研究科

2003

Abstract

In this study, the femtosecond laser ablation of metals is applied to three kinds of microprocessing; laser direct writing of micro metal patterns in Chapter 2, fabrication of microspike arrays for the micro field emitter utilizing the optical diffraction through the contact mask opening in Chapter 3, and the quenching of the high pressure phase of iron using the femtosecond laser driven shock wave in Chapter 4. In Chapter 2, advantages of the femtosecond laser induced forward transfer of thin metal films are shown compared to the case for the excimer laser. In Chapter 3, the micro removal processing which can not be achieved without using the femtosecond laser is realized. In Chapter 4, a new method that the femtosecond laser is used as the shock wave driver is tried to quench the high pressure phase of iron, which is impossible using the conventional shock compression method. Contents described in this dissertation are summarized as follows.

In Chapter 2, laser induced forward transfers of thin metal films using a single pulse of the excimer laser (wavelength: 248 nm, pulse width: 30 ns) with the flat-top profile of the laser intensity (Excimer-LIFT) and the femtosecond laser (wavelength: 800 nm, pulse width: 120 fs) with the Gaussian profile (Fs-LIFT) are described. The purpose is to achieve the high-resolution deposition of micropatterns. The different point between the Excimer-LIFT and the Fs-LIFT processes is the absorption of the laser energy from the laser induced plume. For the Excimer-LIFT, the ablation occurs during the laser pulse and the laser induced plume is generated. The plume is heated by absorbing the latter part of the laser pulse. The scatter of microparticles expands as a result of the growth of the plume due to the evaporation of the deposited pattern. For the Fs-LIFT, on the other hand, the growth of the plume depends only on the fluence because the ablation occurs after the whole laser pulse and the laser energy is not absorbed by the plume. Therefore, the scatter of microparticles is prevented. Scatter of droplets depends on the melted area outside the laser irradiated region in the thin film for the Excimer-LIFT and the difference of the laser intensity in the laser beam for the Fs-LIFT. The Fs-LIFT is a powerful tool to achieve the high-resolution micropatterning of metals when the thin film does not contact with the acceptor substrate.

In Chapter 3, microspike arrays are fabricated by irradiating the femtosecond laser on the tungsten surface through the mask opening in air with the aim of fabricating the micro field emitter for the field emission display using only the femtosecond laser. Natural logarithm of the calculated intensity distributions diffracted at the edge of the mask opening is qualitatively

consistent with the experimental results of the shape and arrays of microspikes. The ability of the field emission of microspike arrays is evaluated. This method can be a powerful tool to fabricate the field emitter eco-friendlily.

In Chapter 4, the high pressure phase of iron is quenched using the shock wave driven by the femtosecond laser ablation of iron. Temperatures inside and behind the shock front as functions of the pressure and the volume are calculated using thermodynamic theory because the phase transition occurs inside the shock front. Correct values of the constant-volume specific heat C_{VH} and the Grüneisen parameter γ on the Hugoniot are required to calculate the temperatures inside and behind the shock front correctly. Therefore, these values are evaluated combining the Walsh-Christian equation with the Mie-Grüneisen equation. The reason for the quenching of the ε and γ phases may be due to the incomplete hcp – bcc and fcc – bcc transitions because the rise time of the shock release wave may be similar to that of the shock compression wave. Though the mechanism of the quenching is not clear, this mechanism can be applied to other materials. Therefore, high pressure phases which are impossible to quench using conventional methods can be realized using this method. This method can pioneer new scientific and industrial fields which produce new materials of high pressure phase.

Originalities and advantages of applications of the femtosecond laser ablation of metals to microprocessing, which have not been investigated actively, are described in this dissertation. The author hopes that this dissertation will be a trigger to diffuse the femtosecond laser ablation of metals into the industrial market and to stimulate scientific researchers of the related fields.

Acknowledgements

The author compiles his studies which have been performed since he was appointed Assistant Professor of Miyamoto laboratory, Department of Manufacturing Science, Graduate School of Engineering, Osaka University in 1999 into this dissertation.

The author wishes to thank Prof. Isamu Miyamoto of Department of Manufacturing Science, Graduate School of Engineering, Osaka University for his great guidance of this dissertation. The author is also deeply grateful to him for preparation of research environment. The author is deeply thankful to Prof. Kojiro F. Kobayashi of Department of Manufacturing Science, Graduate School of Engineering, Osaka University for his helpful discussions on rapid quenching of metals. The author wishes to thank Dean, Graduate School of Engineering, Osaka University, Prof. Yukichi Umakoshi of Department of Materials Science and Engineering, Graduate School of Engineering, Osaka University for his helpful discussions on phase transitions in metals. The author gives his thanks to Prof. Kazuo A. Tanaka of Institute of Laser Engineering, Osaka University and Department of Electronic, Information Systems and Energy Engineering, Graduate School of Engineering, Osaka University for his helpful discussions on the laser ablation of metals.

The author is deeply thankful to Prof. Ari Ide-Ektessabi of International Innovation Center, Kyoto University for his various advices since the author was a student. The author is also grateful to him for measurements using AFM, Synchrotron X-ray fluorescence measurement, and RBS analysis. The author wishes to thank Professor emeritus Yukio Sano of Kobe University of Mercantile Marine for his guidance of shock physics in solids.

The author wishes to thank Associate Professor Etuji Ohmura of Department of Manufacturing Science, Graduate School of Engineering, Osaka University for helpful discussions and advices. The author wishes to thank Associate Professor Yasuhito Gotoh of Department of Electronic Science and Engineering, Graduate School of Engineering, Kyoto University for helpful advices since the author was a student. The author is deeply grateful to Associate Professor Yoshinori Hirata of Department of Adaptive Machine Systems, Graduate School of Engineering, Osaka University for the measurement of the field emission current. The author is deeply thankful to Assistant Professor Hiroaki Mori of Department of Manufacturing

Electric Co., Ltd., at present under same roof and shared terrible troubles with them. The author is deeply grateful to them. The author wishes to thank alumni and members of Ektessabi lab. and Ide lab., Department of Precision Engineering, Graduate School of Engineering, Kyoto University.

Finally, the author would like to thank his parents, dear wife, Yasue 泰江, and son, Hiroaki 博亮, for their encouragement to accomplish the present work.

Table of Contents

Chapter 1

Introduction

Applications of the femtosecond laser ablation of metals to microprocessing are described in this dissertation. In this chapter, purposes of this dissertation are represented after principle of the intense femtosecond laser oscillation, femtosecond laser – metals interaction, femtosecond laser driven shock wave in metals, and femtosecond laser system used in this study are introduced.

1.1 Intense femtosecond laser

The laser with the pulse width below picoseconds order is called ultrashort pulsed laser or femtosecond laser. Ultrashort pulsed laser was developed in the middle of 1960s. The size of the system was large and the pulse stability was not good. The ultrashort pulsed laser, however, became small-size and highly stable after the development of the Kerr lens mode-locked laser using a Ti:Sapphire medium in 1991 [1]. Schematic of the Kerr lens mode-locked laser is shown in FIG. 1.1. A continuum pumping beam stimulates the Ti:Sapphire medium, and the laser with the range of the wavelength from infrared to ultraviolet is oscillated and amplified in the oscillator with four mirrors. A slit for mode-locking keeps the laser intensity constant. Scattered light goes back through prisms. Ultrashort pulse is oscillated cyclically through a half-mirror.

The table-top femtosecond pulse above TW was achieved by the development of the chirped pulse amplifier (CPA) [2,3]. Schematic illustration of the CPA is shown in FIG. 1.2. As a result of the irradiation of a low intensity femtosecond pulse into a pair of gratings, the pulse width is stretched (in other words, chirped). This stretched pulse is amplified in an amplifier. The amplified pulse is compressed as a result of the irradiation into another pair of gratings. The intense femtosecond laser pulse is generated as mentioned above.
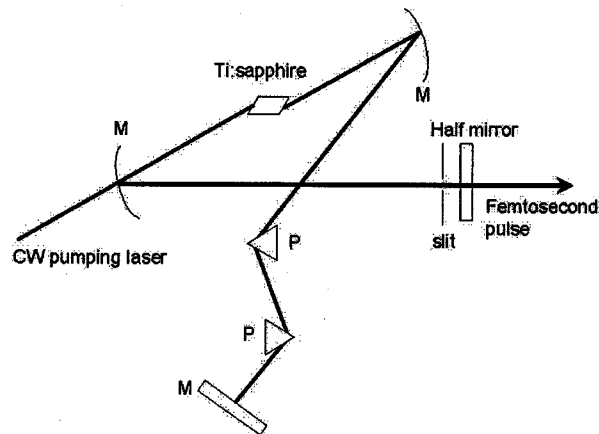
FIG. 1.1.   Schematic illustration of a Kerr lens mode locked laser oscillator.
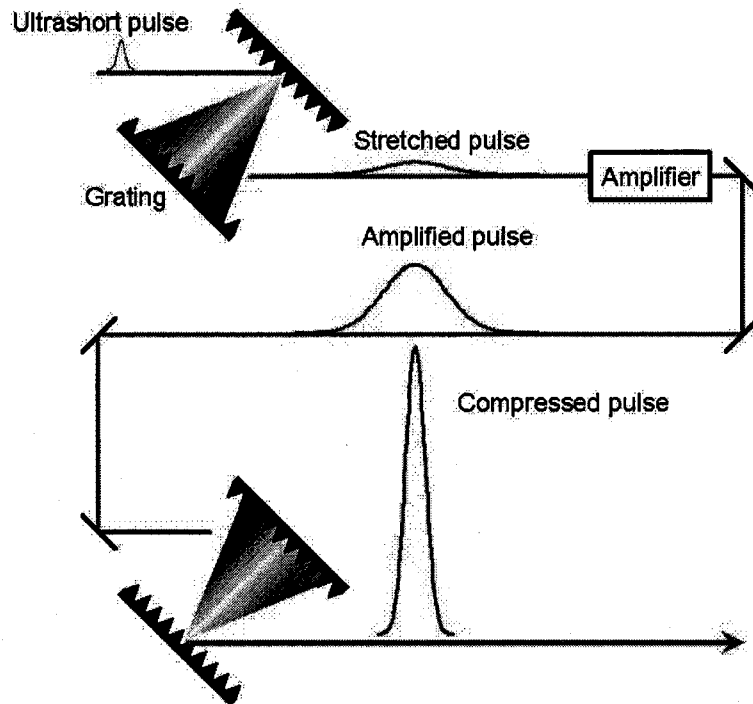
FIG. 1.2.   Schematic illustration of chirped-pulse amplification.

1.2   Femtosecond laser – metal interactions

New applications of the intense femtosecond laser have been opened in fields of industry, materials science, medicine, *etc.*, because the rapid development of the intense femtosecond laser in this decade. Femtosecond laser ablation is one of the important physical phenomena, and is applied to microprocessing, film deposition, new material production, and so on. Characters of the femtosecond laser ablation compared with the nanosecond laser ablation are: highly efficient energy deposition due to no absorption of laser energy into the laser generated plasma because the pulse is over before the expansion of the plasma, direct process from solid to gas or plasma via no solid – liquid process, and little secondary damage to solids due to thermal conduction. Therefore, the femtosecond laser has the advantage to the applications described above [4-15].

In this section, processes after the irradiation of the femtosecond laser on the metal surface, *viz.*, laser absorption, nonequilibrium relaxation between electrons and phonons, and ablation, are explained.

Nonequilibrium dynamics of the electron gas in metals irradiated by the femtosecond laser has been studied actively in these 20 years. Direct experimental studies on fundamental

3

processes such as the electron – electron scattering and the electron – phonon interaction have become possible due to the appearance of the femtosecond pulse [16-46]. Theoretical studies based on the data obtained from experimental studies have also been performed [47-52].

Electron – phonon nonequilibrium is important in the regime of picoseconds order. At first, free electrons in the metal absorb the laser energy as the lattice remains cold. The energy is delivered among free electrons by the electron – electron collisions in femtoseconds order, and thermalization of the electron gas occurs. Energy transfer between the electron and the lattice is dominated by the electron – phonon collision. The electron – phonon collision time τ_{ep} is as short as the electron – electron collision time τ_{ee} [42]. The time for energy transfer from hot electrons to the lattice is usually several tens of picoseconds and longer than the thermalization of the electron gas due to the difference of the mass between the electron and the phonon. This process was verified experimentally [17,19,20,24,36,53], and is described by the classical two temperature model [54-57].

The two temperature model assumes that the electron and the lattice subsystems are characterized by the temperatures T_e, T_l, respectively. Spatial and temporal evolutions of these temperatures are determined by the following equations:

$$C_e \frac{\partial T_e}{\partial t} = \frac{\partial}{\partial x} \kappa(T_e) \frac{\partial T_e}{\partial x} - G(T_e - T_l) + P(x,t),$$ (1.1)

$$C_l \frac{\partial T_l}{\partial t} = G(T_e - T_l),$$ (1.2)

where $C_e(T_e)$ is the temperature-dependent electron heat capacity per unit volume, C_l is the lattice heat capacity, $\kappa(T_e)$ is the electron thermal conductivity, $P(x,t)$ is the term of the laser heat source (absorbed power density), and G is the parameter characterizing the electron – phonon coupling, which is usually determined by fitting the analytical solutions of Eqs. (1.1) and (1.2) into the experimental data.

In the lower electron temperature regime ($T_e \ll T_F$), the electron heat capacity is approximated by linear temperature dependence, $C_e \approx C_e'T_e = \pi^2 (T_e/T_F) N_e k_B / 2$, ($N_e$ is the electron density, T_F is the Fermi temperature). Next, it is assumed that the electron heat propagation length during the laser pulse is larger than the skin depth. This assumption eliminates the $P(x,t)$ in the right term of Eq. (1.1), and the term of the heat source is considered the boundary condition,

$$\kappa \frac{\partial T_e}{\partial x} \bigg|_{x=0} = -I(t),$$ (1.3)

where $I(t) = AI_l(t)$ is the absorbed laser intensity (A is the surface absorptivity).

4

When the electron temperature is much higher than the lattice temperature, $T_F > T_e \gg T_l$, there are two regimes of the electron heat transfer. The one is the usual regime that the electron heat conductivity is determined by the electron – phonon collision. The numerical analysis in this regime was performed in Ref. [35]. The other is the unusual regime that the electron – electron collision is important. The solution of the thermal conduction equation for this case is obtained, and is consistent with the different temperature-dependence of the electron thermal conductivity, $\kappa \propto T_e^{\alpha}$, $\alpha < 1$. The numerical solution for $\alpha \geq 1$ (or $\alpha \geq 0$ if C_e is independent of the electron temperature) is well known and can be seen in Ref. [60].

When $\alpha = -1$, that is the electron relaxation is determined by the electron – electron collision, the heat propagation velocity is independent of the time. In addition, the value of this velocity decreases as $v_T \propto 1/F$ with increasing of the laser fluence F. This counterintuitive dynamics results in the increment of the efficiency of the energy deposition. Decay of the heat propagation velocity with the increment of the laser fluence is a reason for the success of the femtosecond laser processing of materials.

The efficiency of the ultrashort pulsed laser heating of metals is determined by the dynamics of the heat propagation during the time $t < \tau_{el} = C_e/G$, where τ_{el} is the characteristic time for the electron – lattice energy transfer. $\tau_{el} > 1$ ps is satisfied for principal metals. When the laser pulse width τ_p is sufficiently shorter than τ_{el}, the laser energy is firstly deposited into the electron subsystem. The lattice remains cold during the time $t \ll \tau_{el}$, and strong overheating of the electron occurs. The process which determines the energy transfer in this time scale is only the electron heat conduction.

For the electron temperature, the electron heat conductivity is given by $\kappa = C_e v_F^2 \tau/3$ [61,62], where v_F is the Fermi velocity, and τ is the electron relaxation time, which is determined by the electron – phonon and the electron – electron collisions, $1/\tau = 1/\tau_{ep} + 1/\tau_{ee}$. When the lattice temperature is higher than the Debye temperature $T_l \geq \Theta = \hbar\omega_D/k_B$, where ω_D is the Debye frequency (maximum phonon frequency), all vibrational modes of lattices are excited and the good approximation for the electron – phonon collision frequency is given by $1/\tau_{ep} \sim k_B T_l/\hbar$ [61,62]. The electron – electron collision frequency is estimated by $1/\tau_{ee} \sim (k_B T_e)^2/\hbar\varepsilon_F$, where ε_F is the Fermi energy [61,62].

In case of the equilibrium between the electron – lattice subsystems ($T_l = T_e < T_F$), the condition, $1/\tau_{ep} > 1/\tau_{ee}$, is satisfied, and the electron – electron collisions are negligible. When $T_e \gg T_l$, this case is correspondent to the strong overheating of the electron subsystem and

frequencies $1/\tau_{ee}$ and $1/\tau_{ep}$ are equal to the characteristic electron temperature $T_e = T_*$, where

$$T_* \sim \sqrt{\frac{\varepsilon_F T_l}{k_B}}.$$ (1.4)

For metals with the Fermi energy $\varepsilon_F \sim 5$ eV and $T_l \sim 300$ K, this temperature is the order of $T_* \sim 4 \times 10^3$ K. In this case two different regimes of the electron heat transport are confirmed.

If the electron temperature remains low, $T_e \leq T_*$, during the interaction with the laser pulse, the electron – phonon collision determines the heat transport. The electron relaxation time is given by $\tau \approx \tau_{ep} \propto 1/T_l$, and the heat conductivity is characterized by the temperature dependent $\kappa \propto T_e \tau_{ep} \propto T_e/T_l$. In this case the thermal diffusivity $\chi = \kappa/C_e$ is nearly constant, and the usual electron heat transport regime is realized [35]. The heat penetration depth is scales as $l_T = (2\chi t)^{1/2}$ and the heat front velocity decreases with the time as $v_T = (\chi/t)^{1/2}$. The surface electron temperature is expressed as follows [35]:

$$T_e = \left(\frac{4}{\pi \chi \tau_p}\right)^{1/4} \left(\frac{F}{C_e'}\right)^{1/2} \propto \frac{F^{1/2}}{\tau_p^{1/4}}.$$ (1.5)

The characteristic laser fluence F_* which is correspondent to $T_e = T_*$ is given by this equation. From Eqs. (1.4) and (1.5), equations;

$$F_* \cong \frac{C_e' T_l \varepsilon_F \sqrt{\chi \tau_p}}{k_B} \cong \sqrt{\frac{k_B T_l}{\hbar} \tau_p} F_m, \quad F_m = \frac{\pi}{9} \frac{m \varepsilon_F^2}{\hbar^2}.$$ (1.6)

are obtained. For metals with the Fermi energy $\varepsilon_F \sim 5$ eV and the pulse width $\tau_p \sim 100$ fs, $F_* \sim 4$ mJ/cm^2, $F_m \sim 2$ mJ/cm^2 are obtained. $T_l \sim 300$ K is assumed here. The value of F_* becomes a little bit higher due to the lattice heating during the laser pulse.

When $T_e \gg T^* \gg T_l$ is satisfied in the high fluence $F > F_*$, the electron relaxation time is determined by the electron – electron collisions, $\tau \approx \tau_{ee} \propto 1/T_e^2$, and the heat conductivity $\kappa \propto T_e \tau_{ee} \propto 1/T_e$ decreases with the increment of the electron temperature. For the degenerate electron gas and strongly nonequilibrium between electrons and lattices, these equations are valid. These situations are realized during the time $t \leq \tau_{el}$, and this is interesting. The heat diffusivity decreases with the increment of the electron temperature as $\chi \propto T_e^{-2}$.

By using the energy conservation law during and after the laser pulse,

$$C_e' T_e^2 l_T \sim I t \quad (t < \tau_p),$$ (1.7)

$$C_e' T_e^2 l_T \sim F \quad (t \geq \tau_p),$$ (1.8)

and the equation for the heat penetration depth;

6

$$l_T \sim \sqrt{\chi t} \sim v_F \sqrt{\tau_{ee} t} \cong \frac{v_F \sqrt{\hbar \varepsilon_F t}}{k_B T_e}, \qquad (1.9)$$

and a simple scaling law for the surface electron temperature,

$$T_e \sim \frac{I k_B \sqrt{t}}{C_e' v_F \sqrt{\hbar \varepsilon_F}} \sim T_F \frac{I \sqrt{t}}{N_e v_F \sqrt{\hbar \varepsilon_F}} \quad (t < \tau_p), \qquad (1.10)$$

$$T_e \sim \frac{F k_B}{C_e' v_F \sqrt{\hbar \varepsilon_F t}} \sim T_F \frac{F}{N_e v_F \sqrt{\hbar \varepsilon_F t}} \quad (t \geq \tau_p), \qquad (1.11)$$

and the heat penetration depth,

$$l_T \sim \frac{v_F^2 \hbar \varepsilon_F C_e'}{I k_B^2} \sim \frac{v_F^2 \hbar N_e}{I} \quad (t < \tau_p), \qquad (1.12)$$

$$l_T \sim \frac{v_F^2 \hbar \varepsilon_F C_e' t}{F k_B^2} \sim \frac{v_F^2 \hbar N_e}{F} t \quad (t \geq \tau_p), \qquad (1.13)$$

are obtained. The heat penetration depth is independent on the time (see Eq. (1.12)) and decreases with the increment of the laser intensity during the laser pulse with the constant intensity. In this case, most of the absorbed laser energy is deposited into the thin surface layer, and decreases with the increment of the laser intensity. This occurs due to the decay of the heat loss from the thin layer because the electron relaxation time and the heat diffusivity are the function of the electron temperature ($\propto T_e^{-2}$) which decreases rapidly. After the laser pulse an extremely peculiar regime of the heat transport appears (see Eq. (1.13)). The heat penetration depth becomes greater in proportion to the time, $l_T \propto t$, and the heat propagation velocity $v_T \sim v_F^2 \hbar N_e / F$ decreases with the increment of the laser fluence. This is a contrast to the counterintuitive prediction.

The radiative heat transport is important at the extremely high electron temperatures. For $T_e \leq T_F$, the situation that the radiative heat conductivity $\kappa_r = 16 \sigma T_e^3 l_r / 3$ (where $\sigma = \pi^2 k_B^4 / 60 \hbar^3 c^2$ is the Stefan-Boltzmann constant and l_r is the radiative mean free path) is sufficiently smaller than the electron heat conductivity κ_e is equivalent to $\alpha \hbar \omega_p \ll \Re$. $\alpha = 1/137$, ω_p is the plasma frequency, and $\Re = 13.6$ here. It is assumed here that l_r is the order of the skin depth, $l_r \sim c / \omega_p$, and $T_e = T_F$. It is obvious from these estimations that the radiative heat transport is negligible.

There are two forces which cause the transfer of momentum from the laser field in the laser-energy absorbed region and high energy electrons to ions [63-65]. One is due to the electric field caused by the charge separation, and the other is the ponderomotive force. The

charge separation occurs when the energy absorbed by electrons exceeds the Fermi energy. The Fermi energy is nearly equal to the sum of the bonding energy and the work function, so that electrons escape from the target [66-69]. Ions are pulled from the target by the electric field caused by the charge separation. At the same time, the ponderomotive force in the laser field in the skin depth pushes electrons into the inside of the target. Correspondingly, the ponderomotive force creates the mechanism for the ion acceleration to the target. Thus, the mechanism of the femtosecond laser ablation is quite different from that of the thermal ablation by long pulsed laser.

Fundamental mechanism of the ablation process is not yet understood precisely. Pressure wave formation [70-72], thermodynamic evolution of expanding materials [73,74], and identification of collective emission process [8,51,52,73,75-80] have to be understood to describe the process in the mesoscopic scale. Many mechanisms are thought to play a role in the ablation below the plasma formation threshold: optical dynamic spallation [70,79] (in organic materials), heterogeneous nucleations of gas bubble and phase explosion [52,73,75-77,79], spinodal decomposition [73,80], fragmentation [52], and vaporization [8]. The ablation mechanism were suggested as follows using molecular dynamic simulations based on these phenomena [51].

The main response for the absorption of the pulse energy is the expansion to release the storage of the important thermoelastic pressure induced by the heating of the constant volume of the target. The material is, however, relaxed by emitting the strong pressure wave, which play a important role in the ablation process [70,78,79,81,82].

Although the tensile component is formed at low fluences below the ablation threshold, it actually disappears with the increment of the fluence due to the thermo-softening of the surface material. Thus, the tensile wave intermediate effect such as the spallation is observed only at low fluences. The relaxation of the thermoelastic stress occurs at an early stage by the irradiation of two compressive pressure waves: One goes toward the free surface, and the other goes inside the bulk [71,72,79]. The wave irradiated at the free surface reflects and becomes the tensile stress (negative pressure). However, the tensile component is not formed completely before the reflected wave reaches the approximately skin depth under the surface [71]. Thus, the resulted acoustic wave has bipolar profile: the compressive stress and the following tensile stress.

At middle fluences, the phase explosion is the main mechanism of the ablation. This mechanism occurs in the region of the gradual expansion of the material, and may form the condition that the Newton's rings are formed.

At high fluences, the pressure profile has a single structure; the tensile component disappears completely. Thus, the reflection does not occur because the wave irradiated at the free surface is dissipated at the surface layer. This pressure intensity is proportional to the incident energy. The tensile stress is also formed. This is not induced by the elastic wave but by the development of the melting front. At an early stage, this stress propagates in the sound velocity, and becomes lower later. At high strain rates, the plume is formed by the mechanical fragmentation of the expanded materials. Complete evaporation of the surface layer is also observed. This mechanism can occurs at different places under the surface of the target at the same time. Thus, the formation of the pressure wave must be considered to predict the ablation rate.

1.3 Femtosecond laser driven shock wave in metals

The shock wave propagates in metals due to the shock loading on the metal surface when an intense femtosecond laser is irradiated on the surface as described in the previous section. In this section, the properties of the femtosecond laser driven shock wave are described.

For many years, the nanosecond laser driven shock wave has been studied to create and observe materials at extreme conditions of pressure, density, and temperature [83-117,128-135]. The critical different point between the femtosecond and the nanosecond laser ablations is the absorption of the laser energy into the laser induced plume during the laser pulse. For the nanosecond laser, the temporal shock wave profile is relatively long due to the pressure loading from the plume which absorbs the laser energy. The heating effect of the target emitted from the plume is not also negligible. While for the femtosecond laser, the femtosecond laser driven shock wave is characterized by only the femtosecond laser – metal interaction because the ablation occurs after the whole laser energy deposition.

The ultrasonic heat wave driven by the heat conduction propagates into the undisturbed target when the thin layer of the target is heated rapidly to 100 – 1000 eV. The heat wave slows down when the thickness of the heated material becomes larger. At the same time, the hydrodynamic expansion of the heated material into the vacuum starts. The shock front overtakes the heat front when the heat front approaches the sound velocity. This physical state is the classical problem of the hydrodynamic phenomena [118]. When the intense femtosecond laser is irradiated on the solid surface, the shock pressure of approximately 1 TPa is generated in the laser absorbed region because the lattice is heated far before the thermal expansion occurs. In this situation, finally the shock front goes ahead after the heat front propagates in the solid

through 100 – 200 nm, which depends on the laser intensity [119].

Evans *et al.* measured the shock velocity and the particle velocity using the frequency domain interferometer with the time resolution of subpicoseconds [120-123] when the femtosecond laser (800 nm, 120 fs, ~ 10^{14} W/cm^2) is irradiated on the surface of thin Al film (10 – 400 nm on fused silica substrate (2 mm)), and estimated the shock pressure of 100 – 300 GPa assuming that the shock is along the Hugoniot [124].

Gahagan *et al.* also measured rise times of the femtosecond laser driven shock wave using the frequency domain interferometer [125]. The shock wave was driven by the femtosecond laser (800 nm, 130 fs, 0.2 – 0.5 mJ) which is irradiated on deposited metal thin films (polycrystalline Al and Ni (250 – 2000 nm)) through the cover glass for microscope observation. The Gaussian profile of the laser profile of the incident beam is flattened because the nonlinear absorption of the laser driving the shock wave into the glass substrate functions as the optical limiter. Therefore, the planar shock wave is generated in the metal [126]. The dynamic behavior of the surface and the reflectivity of the laser from the thin metal film during the generation of the shock wave were measured at the same time using the frequency domain interferometer, and the shock rise time from 10 % to 90 % was estimated several picoseconds. Gahagan *et al.* also developed the ultrafast time resolution two dimensional interferometric microscope to evaluate properties of the laser driven shock wave [127].

Properties of the femtosecond laser driven shock wave have been investigated using the method with high spatial and temporal resolution in these days as described above. However, detail properties such as the mechanism of generation, the shock wave profile, and the dynamics of propagation are not investigated and not understood well.

1.4   Femtosecond laser system used in this study

In this study, Femtosecond Laser System produced by Spectra-Physics Inc. was used. The schematic is shown in FIG. 1.3. The femtosecond pulse (FIG. 1.3(b), 790 nm, < 130 fs, 82 MHz, 0.9 W) is oscillated by stimulating the Ti:Sapphire using the LD-pumped Nd:YVO$_4$ laser (FIG. 1.3(a), 532 nm, CW, 5 W). This seed pulse is stretched by a pair of gratings in the regenerative amplifier (FIG. 1.3(d)), amplified by the LD-pumped Nd:YLF laser (FIG. 1.3(c), 527 nm, 200 ns, 1 kHz, 10 W), compressed by a pair of gratings, and finally the intense femtosecond pulse with the wavelength of 800 nm, the pulse width of 120 fs, the maximum pulse energy of ~ 1 mJ, and maximum repetition rate of 1 kHz is obtained. This pulse width is measured using the single shot autocorrelator (FIG. 1.3(e)). The beam has the horizontal linear

polarization and the Gaussian intensity profile. The measured intensity profile of the raw beam and focused beams using focusing lens with focal length of 70, 150 300 mm are shown in FIG. 1.4. Measurements were performed in air with sufficiently low intensities to prevent the air breakdown. The measured $1/e$ beam diameter are (a) 5.4 x 4.3 mm² for the raw beam, (b) 12.5 x 14.5 μm² for the 70 mm focusing lens, (c) 21.4 x 24.3 μm² for the 150 mm focusing lens, and (d) 46.0 x 45.6 μm² for the 300 mm focusing lens.
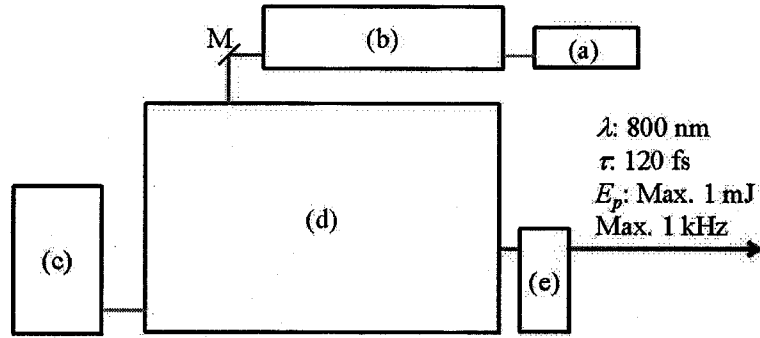
FIG. 1.3. Setup of femtosecond pulse laser system. (a) LD pumped Nd:YVO₄ laser (532 nm, CW, 5 W) for pumping femtosecond oscillator. (b) Ultra-short pulse laser system (790 nm, < 130 fs, 82 MHz, 0.9 W). (c) LD pumped Nd:YLF laser for pumping regenerative amplifier (527 nm, 200 ns, 1 kHz, 10 W). (d) Regenerative amplifier system (800 nm, 120 fs, 1 kHz, 1 W). (e) Single shot autocorrelator.
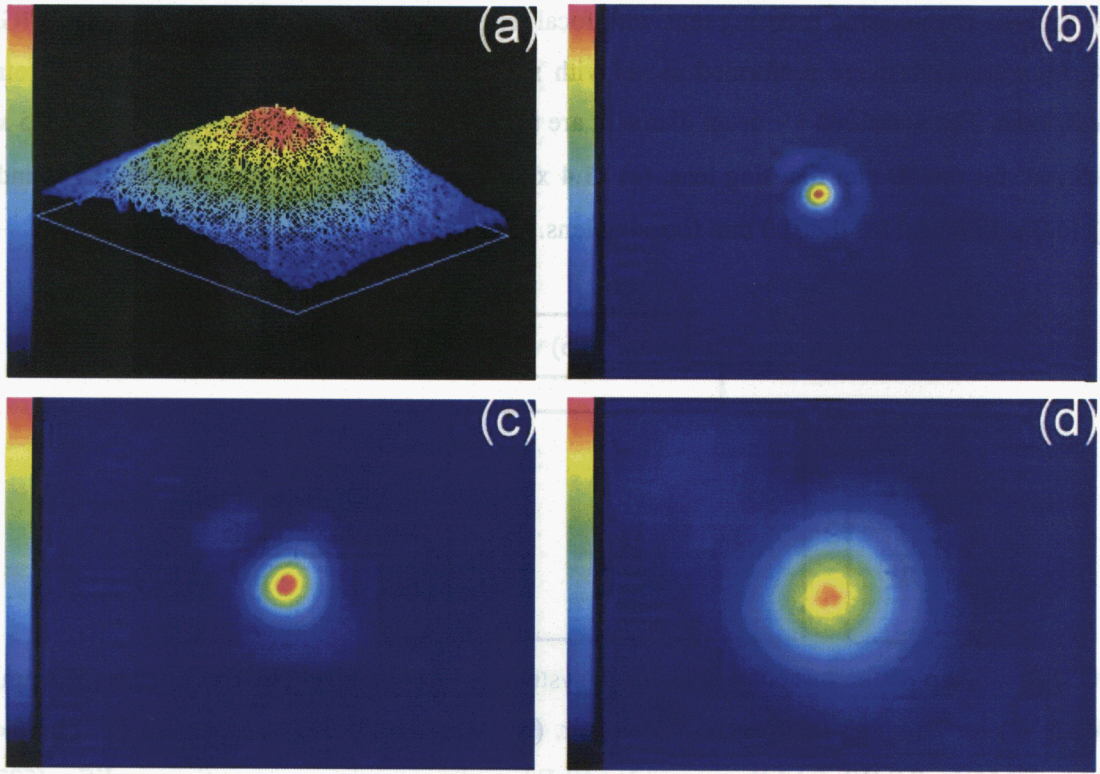
FIG. 1.4.   (a) Distribution of a raw beam. Beam size: 5.4 x 4.3 mm². (b) Distribution of focused beam using f = 70 mm lens. Beam size: 12.5 x 14.5 μm². (c) Distribution of focused beam using f = 150 mm lens. Beam size: 21.4 x 24.3 μm². (d) Distribution of focused beam using f = 300 mm lens. Beam size: 46.0 x 45.6 μm².

1.5   Purposes

Femtosecond laser is a powerful tool for microprocessing. Many applications of the femtosecond laser in the fields of industry, material sciences, medicine, and so on are proposed. The femtosecond laser, however, does not have many applications to metals. Micro removal processing and pulsed laser deposition are the main applications of the femtosecond laser to metals proposed. Original applications to metals are not proposed although advantages of the femtosecond laser ablation of metals are shown compared with the case of the longer pulsed laser.

Purposes of this dissertation are to represent originalities and advantages of the femtosecond laser ablation of metals and to pioneer new scientific and industrial fields. In this dissertation, the femtosecond laser ablation of metals is applied to three kinds of

microprocessing; laser direct writing of micro metal patterns in Chapter 2, fabrication of microspike arrays for the micro field emitter utilizing the optical diffraction through the contact mask opening in Chapter 3, and the quenching of the high pressure phase of iron using the femtosecond laser driven shock wave in Chapter 4. In Chapter 2, advantages of the femtosecond laser induced forward transfer of thin metal films are shown compared to the case for the excimer laser. In Chapter 3, the micro removal processing which can not be achieved without using the femtosecond laser is realized. In Chapter 4, a new method that the femtosecond laser is used as the shock wave driver is tried to quench the high pressure phase of iron, which is impossible using the conventional shock compression method. This dissertation consists of the independent three chapters above mentioned. Research flows of this dissertation and each chapter are shown in FIG. 1.5.Content of each chapter will be introduced briefly as follows.

In Chapter 1, the principle of the intense femtosecond laser oscillation, femtosecond laser – metal interaction, and femtosecond laser driven shock wave in metals, femtosecond laser system used in this study, and purposes of this dissertation are described.

In Chapter 2, Laser induced forward transfers (LIFT) of thin metal films using a single pulse of excimer laser (wavelength: 248 nm, pulse width: 30 ns) with the flat-top profile of the laser intensity (Excimer-LIFT) and the femtosecond laser (wavelength: 800 nm, pulse width: 120 fs) with the Gaussian profile (Fs-LIFT) are performed to achieve the high-resolution deposition of micropatterns. The Fs-LIFT is a powerful tool to achieve the high-resolution micropatterning of metals when the thin film does not contact with the acceptor substrate.

In Chapter 3, Microspike-arrays are fabricated by irradiating the femtosecond laser on the tungsten surface through the mask opening in air with the aim of fabricating the micro field emitter for the field emission display using only the femtosecond laser. Natural logarithm of the calculated intensity distributions diffracted at the edge of the mask opening is qualitatively consistent with the experimental results of the sharp shape and arrays of microspikes. The ability of the field emission of microspike-arrays is evaluated. This method can be a powerful tool to fabricate the field emitter.

In Chapter 4, the femtosecond laser driven shock quenching of the high pressure phase (ε phase) of iron is described. Thermal properties of iron under the shock compression state are calculated theoretically. Temperatures behind and inside the steady-plane shock wave fronts are calculated using the results obtained. The detail of the femtosecond laser driven shock quenching of the ε phase in iron is explained.

In Chapter 5, this dissertation is concluded.

Chapter 1. Introduction
- Intense femtosecond laser oscillation
- Femtosecond laser – metal interaction
- Femtosecond laser driven shock wave in metals
- Femtosecond laser used in this study
- Contents and Purpose

Advantage
Chapter 2. Laser induced forward transfer of thin metal films

Originality
Chapter 3. Femtosecond laser fabrication of microspike-arrays for micro field emitter on tungsten surface

New phenomenon
Chapter 4. Femtosecond laser quenching of the high-pressure phase of iron

Chapter 5. Conclusions

FIG. 1.5.   (a) Research flow of this dissertation.

2.1 Introduction   (laser direct writing, purposes)

2.2 Excimer-LIFT
2.3 Fs-LIFT
- Optimum condition for high-resolution patterning
- Photographing of the laser induced plume
- Photographing of the transferring material

- Process of the LIFT

2.4 Conclusions
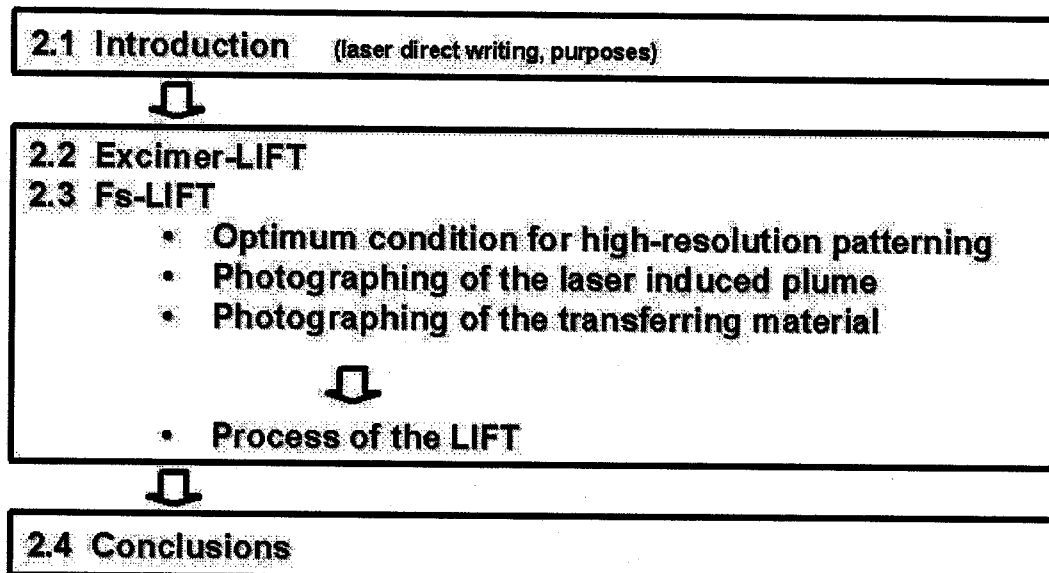
FIG. 1.5.   (b) Research flow of Chapter 2.

14

3.1 Introduction (LIPSS, FED, purposes)

⬇

3.2, 3.3 Fabrication of microspike-arrays

⬇

3.3 Theoretical calculations of diffracted intensity distribution

⬇

3.4 Measurement of the field emission current

⬇

3.6 Conclusions
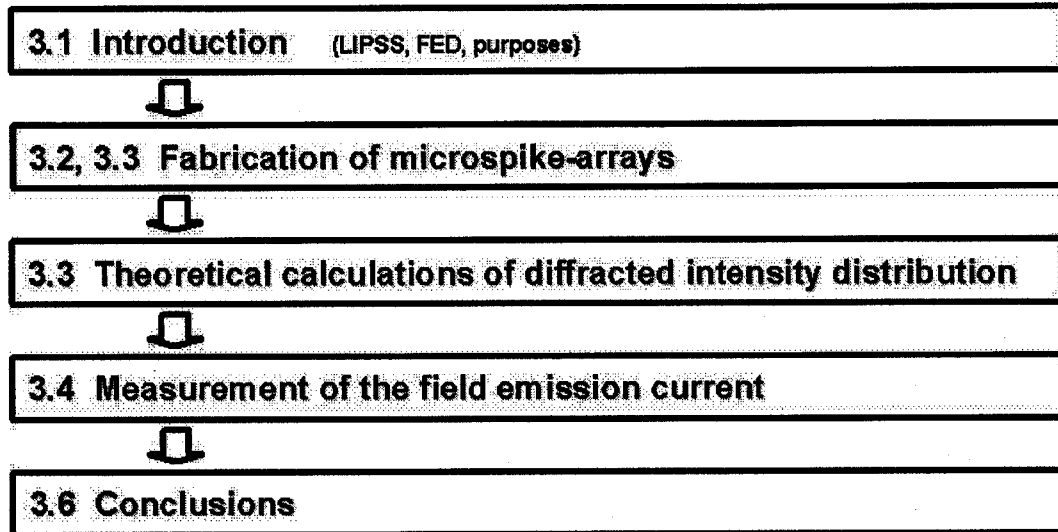
FIG. 1.5. (c) Research flow of Chapter 3.

4.1 Introduction
· Physical properties of iron
· Phase transition in iron
· Purpose

Experiments   Calculations

⬇   ⬇

4.2, 4.3 Experiments
· Femtosecond laser irradiation
· Analysis
   · EBSP
   · TEM
   · SR-XRD

4.4 Thermal properties of iron
· Estimates of C_{VH} and γ on the Hugoniot

⬇

4.5 Temperature calculations
· Temperature inside the shock front
· Temperature behind the shock front

4.6 Detail explanation
· Phase transition
· Quenching

⬇

4.7 Conclusions

FIG. 1.5. (d) Research flow of Chapter 4.

References in Chapter 1

[1]   D. E. Spence, P. N. Kean, and W. Sibbett, "60-fsec pulse generation from a self-mode-locked Ti:sapphire laser," Opt. Lett. 16, 42-44 (1991).

[2]   D. Stricland and G. Mourou, "Compression of amplified chirped optical pulses," Opt. Commun. 56, 219-221 (1985).

[3]   P. Maine, D. Strickland, P. Bado, M. Pessot, and G. Mourou, "Generation of ultrahigh peak power pulses by chirped pulse amplification," IEEE J. Quantum Electron. 24, 398-403 (1988).

[4]   M. Y. Shen, C. H. Crouch, J. E. Carey, R. Youkin, E. Mazur, M. Sheehy, and C. M. Friend, "Formation of regular arrays of silicon microspikes by femtosecond laser irradiation through a mask," Appl. Phys. Lett. 82, 1715-1717 (2003).

[5]   T.-H. Her, R. J. Finlay, C. Wu, S. Deliwala, and E. Mazur "Microstructuring of silicon with femtosecond laser pulses," Appl. Phys. Lett. 73, 1673-1675 (1998).

[6]   C. Momma, S. Nolte, B. N. Chichkov, F. v. Alvensleben, and A. Tünnermann, "Precise laser ablation with ultrashort pulses," Appl. Surf. Sci. 109-110, 15-19 (1997).

[7]   S. Nolte, C. Momma, H. Jacobs, A. Tünnermann, B. N. Chichkov, B. Wellegehausen, and H. Welling, "Ablation of metals by ultrashort laser pulses," J. Opt. Soc. Am. B 14, 2716-2722 (1997).

[8]   B. N. Chichkov, C. Momma, S. Nolte, F. v. Alvensleben, and A. Tünnermann "Femtosecond, picosecond and nanosecond laser ablation of solids," Appl. Phys. A 63, 109-115 (1996).

[9]   C. Momma, B. N. Chichkov, S. Nolte, F. v. Alvensleben, A. Tünnermann, H. Welling, and B. Wellegehausen, "Short-pulse laser ablation of solid targets," Opt. Commun. 129, 134-142 (1996).

[10] P. Simon and J. Ihlemann, "Ablation of submicron structures on metals and semiconductors by femtosecond UV-laser pulses," Appl. Surf. Sci. 109-110, 25-29 (1997).

[11] P. Simon and J. Ihlemann, "Machining of submicron structures on metals and semiconductors by ultrashort UV-laser pulses," Appl. Phys. A 63, 505-508 (1996).

[12] A. Luft, U. Franz, A. Emsermann, and J. Kaspar, "A study of thermal and mechanical effects on materials induced by pulsed laser drilling," Appl. Phys. A 63, 93-101 (1996).

[13] P. S. Banks, M. D. Feit, A. M. Rubenchik, B. C. Stuart, and M. D. Perry, "Materials effects in ultra-short pulse laser drilling of metal," Appl. Phys. A 69, S377-S380 (1999).

[14] A. M. Komashko, M. D. Feit, A. M. Rubenchik, M. D. Perry, and P. S. Banks, "Simulation of material removal efficiency with ultrashort laser pulses," Appl. Phys. A 69, S95-S98 (1999).

[15] A. M. Rubenchik, M. D. Feit, M. D. Perry, and J. T. Larsen, "Numerical simulation of ultra-short laser pulse energy deposition and bulk transport for material processing," Appl. Surf. Sci. 127-129, 193-198 (1998).

[16] G. L. Eesley, "Observation of nonequilibrium electron heating in Copper," Phys. Rev. Lett. 51, 2140-2143 (1983).

[17] G. L. Eesley, "Generation of nonequilibrium electron and lattice temperatures in copper by picosecond laser pulses," Phys. Rev. B 33, 2144-2151 (1986).

[18] G. L. Eesley, J. Heremans, M. S. Meyer, G. L. Doll, and S. H. Liou, "Relaxation time of the order parameter in a high-temperature superconductor," Phys. Rev. Lett. 65, 3445-3448 (1990).

[19] J. G. Fujimoto, J. M. Liu, E. P. Ippen, and N. Bloembergen, "Femtosecond laser interaction with metallic tungsten and nonequilibrium electron and lattice temperatures," Phys. Rev. Lett. 53, 1837-1840 (1984).

[20] R. W. Schoenlein, W. Z. Lin, J. G. Fujimoto, and G. L. Eesley, "Femtosecond studies of nonequilibrium electronic processes in metals," Phys. Rev. Lett. 58, 1680-1683 (1987).

[21] S. D. Brorson, J. G. Fujimoto, and E. P. Ippen, "Femtosecond electronic heat-transport dynamics in thin gold films," Phys. Rev. Lett. 59, 1962-1965 (1987).

[22] C.-K Sun, F. Vallée, L. H. Acioli, E. P. Ippen, and J. G. Fujimoto, "Femtosecond investigation of electron thermalization in gold," Phys. Rev. B 48, 12365-12368 (1993).

[23] C.-K Sun, F. Vallée, L. H. Acioli, E. P. Ippen, and J. G. Fujimoto, "Femtosecond-tunable measurement of electron thermalization in gold," Phys. Rev. B 50, 15337-15348 (1994).

[24] H. E. Elsayed-Ali, T. B. Norris, M. A. Pessot, and G. A. Mourou, "Time-resolved observation of electron-phonon relaxation in copper," Phys. Rev. Lett. 58, 1212-1215 (1987).

[25] H. E. Elsayed-Ali, T. Juhasz, G. O. Smith, and W. E. Bron, "Femtosecond thermoreflectivity and thermotransmissivity of polycrystalline and single-crystalline gold films," Phys. Rev. B 43, 4488-4491 (1991).

[26] C. A. Schmuttenmaer, M. Aeschlimann, H. E. Elsayed-Ali, R. J. D. Miller, D. A. Mantell, J. Cao, and Y. Gao, "Time-resolved two-photon photoemission from Cu(100): Energy dependence of electron relaxation," Phys. Rev. B 50, 8957-8960 (1994).

[27] W. S. Fann, R. Storz, H. W. K. Tom, and J. Bokor, "Direct measurement of

nonequilibrium electron-energy distributions in subpicosecond laser-heated gold films,"
Phys. Rev. Lett. 68, 2834-2837 (1992).

[28] W. S. Fann, R. Storz, and H. W. K. Tom, "Electron thermalization in gold," Phys. Rev. B 46, 13592-13595 (1992).

[29] R. H. M. Groeneveld, R. Sprik, and A. Lagendijk, "Ultrafast relaxation of electrons probed by surface plasmons at a thin silver film." Phys. Rev. Lett. 64, 784-787 (1990).

[30] R. H. M. Groeneveld, R. Sprik, and A. Lagendijk, "Effect of a nonthermal electron distribution on the electron-phonon energy relaxation process in noble metals," Phys. Rev. B 45, 5079-5082 (1992).

[31] R. H. M. Groeneveld, R. Sprik, and A. Lagendijk, "Femtosecond spectroscopy of electron-electron and electron-phonon energy relaxation in Ag and Au," Phys. Rev. B 51, 11433-11455 (1995).

[32] N. Del Fatti, R. Bouffanais, F. Vallée, and C. Flytzanis, "Nonequilibrium electron interactions in metal films," Phys. Rev. Lett. 81, 922-925 (1998).

[33] N. Del Fatti, C. Voisin, M. Achermann, S. Tzortzakis, D. Christofilos, and F. Vallée, "Nonequilibrium electron dynamics in noble metals," Phys. Rev. B 61, 16956-16966 (2000).

[34] H. M. Milchberg, R. R. Freeman, S. C. Davey, and R. M. More "Resistivity of a simple metal from room temperature to 106 K," Phys. Rev. Lett. 61, 2364-2367 (1988).

[35] P. B. Corkum, F. Brunel, N. K. Sherman, and T. Srinivasan-Rao, "Thermal response of metals to ultrashort-pulse laser excitation," Phys. Rev. Lett. 61, 2886-2889 (1988).

[36] S. D. Brorson, A. Kazeroonian, J. S. Moodera, D. W. Face, T. K. Cheng, E. P. Ippen, M. S. Dresselhaus, and G. Dresselhaus "Femtosecond room-temperature measurement of the electron-phonon coupling constant λ in metallic superconductors," Phys. Rev. Lett. 64, 2172-2175 (1990).

[37] M. Mihailide, Q. Xing, K. M Yoo, and R. R. Alfano, "Electron-phonon relaxation dynamics of niobium metal as a function of temperature," Phys. Rev. B 49, 3207-3212 (1994).

[38] O. B. Wright, "Ultrafast nonequilibrium stress generation in gold and silver," Phys. Rev. B 49, 9985-9988 (1994).

[39] X. Y. Wang, D. M. Riffe, Y.-S. Lee, and M. C. Downer, "Time-resolved electron-temperature measurement in a highly excited gold target using femtosecond thermionic emission," Phys. Rev. B 50, 8016-8019 (1994).

[40] T. Hertel, E. Knoesel, M. Wolf, and G. Ertl, "Ultrafast electron dynamics at Cu(111):

18

Response of an electron gas to optical excitation," Phys. Rev. Lett. 76, 535-538 (1996).

[41] M. Aeschlimann, M. Bauer, S. Pawlik, W. Weber, R. Burgermeister, D. Oberli, and H. C. Siegmann, "Ultrafast spin-dependent electron dynamics in fcc Co," Phys. Rev. Lett. 79, 5158-5161 (1997).

[42] D. Bejan and G. Raseev, "Nonequilibrium electron distribution in metals," Phys. Rev. B 55, 4250-4256 (1997).

[43] V. E. Gusev and O. B. Wright, "Ultrafast nonequilibrium dynamics of electrons in metals," Phys. Rev. B 57, 2878-2888 (1998).

[44] A. V. Lugovskoy and I. Bray, "Ultrafast electron dynamics in metals under laser irradiation," Phys. Rev. B 60, 3279-3288 (1999).

[45] M. Bonn, D. N. Denzler, S. Funk, M. Wolf, S.-S. Wellershoff, and J. Hohlfeld, "Ultrafast electron dynamics at metal surfaces: Competition between electron-phonon coupling and hot-electron transport," Phys. Rev. B 61, 1101-1105 (2000).

[46] S.-S. Wellershoff, J. Hohlfeld, J. Güdde, and E. Matthias, "The role of electron-phonon coupling in femtosecond laser damage of metals," Appl. Phys. A 69, S99-S107 (1999).

[47] A. P. Kanavin, I. V. Smetanin, V. A. Isakov, Yu. V. Afanasiev, B. N. Chichkov, B. Wellegehausen, S. Nolte, C. Momma, and A. Tünnermann, "Heat transport in metals irradiated by ultrashort laser pulses," Phys. Rev. B 57, 14698-14703 (1998).

[48] B. Rethfeld, A. Kaiser, M. Vicanek, and G. Simon, "Ultrafast dynamics of nonequilibrium electrons in metals under femtosecond laser irradiation," Phys. Rev. B 65, 214303 (2002).

[49] B. Rethfeld, K. Sokolowski-Tinten, and D. von der Linde, "Ultrafast thermal melting of laser-excited solids by homogeneous nucleation," Phys. Rev. B 65, 92103 (2002).

[50] B. Rethfeld, A. Kaiser, M. Vicanek, and G. Simon, "Femtosecond laser-induced heating of electron gas in aluminium," Appl. Phys. A 69, S109-S112 (1999).

[51] D. Perez and L. J. Lewis, "Molecular-dynamics study of ablation of solids under femtosecond laser pulses," Phys. Rev. B 67, 184102 (2003).

[52] D. Perez, and L. J. Lewis, "Ablation of solids under femtosecond laser pulses," Phys. Rev. Lett. 89, 255504 (2002).

[53] M. B. Agranat, S. I. Anisimov, S. I. Ashitkov, B. I. Makshantsev, and I. B. Ovchinnikova, Sov. Phys. Solid State 29, 1875 (1987).

[54] S. I. Anisimov, A. M. Bonch-Bruevich, M. A. El'yashevich, Y. A. Imas, N. A. Pavlenko, and G. S. Romanov, Sov. Phys. Tech. Phys. 11, 945 (1967).

[55] S. I. Anisimov, B. L. Kapeliovich, and T. L. Perel'man, "Electron emission from metal surfaces exposed to ultrashort laser pulses," Sov. Phys. JETP 39, 375-377 (1975).

[56] M. I. Kaganov, I. M. Lifshitz, and L. V. Tanatarov, "Relaxation between electrons and crystalline lattice," Sov. Phys. JETP 4, 173-178 (1957).

[57] P. B. Allen, "Theory of thermal relaxation of electrons in metals," Phys. Rev. Lett. 59, 1460-1463 (1987).

[58] A. A. Abrikosov, *Fundamentals of the Theory of Metals* (North-Holland, Amsterdam, 1988).

[59] N. W. Ashcroft and N. D. Mermin, *Solid State Physics* (Holt, Reinhard and Winston, New York, 1976).

[60] Ya. B. Zeldovich and Yu. P. Raizer, *Physics of Shock Waves and High-Temperature Hydrodynamic Phenomena* (Dover, New York, 2002).

[61] A. A. Abrikosov, *Fundamentals of the Theory of Metals* (North-Holland, Amsterdam, 1988).

[62] N. W. Ashcroft and N. D. Mermin, *Solid State Physics* (Holt, Reinhoard and Winston, New York, 1976).

[63] E. G. Gamaly, A. V. Rode, B. Luther-Davies, and V. T. Tikhonchuk, "Ablation of solids by femtosecond lasers: Ablation mechanism and ablation thresholds for metals and dielectrics," Phys. Plasmas 9, 949-957 (2002).

[64] P. P. Pronko, S. K. Dutta, D. Du, and R. K Singh, "Thermophysical effects in laser processing of materials with picosecond and femtosecond pulses," J. Appl. Phys. 78, 6233-6240 (1995).

[65] H. M. Milchberg and R. R. Freeman, "Studies of hot dense plasmas produced by an intense subpicosecond laser," Phys. Fluids B 2, 1395-1399 (1990).

[66] S. S. Mao, X. Mao, R. Greif, and R. E. Russo, "Influence of preformed shock wave on the development of picosecond laser ablation plasma," J. Appl. Phys. 89, 4096-4098 (2001).

[67] S. S. Mao, X. Mao, R. Greif, and R. E. Russo, "Initiation of an early-stage plasma during picosecond laser ablation of solids," Appl. Phys. Lett. 77, 2464-2466 (2000).

[68] S. S. Mao, X. Mao, R. Greif, and R. E. Russo, "Simulation of a picosecond laser ablation plasma," Appl. Phys. Lett. 76, 3370-3372 (2000).

[69] S. S. Mao, X. Mao, R. Greif, and R. E. Russo, "Dynamics of an air breakdown plasma on a solid surface during picosecond laser ablation," Appl. Phys. Lett. 76, 31-33 (2000).

[70] I. Itzkan, D. Albagli, M. Dark, L. Perelman, C. von Rosenberg, and M. Fields, Proc. Natl. Acad. Sci. U.S.A. 92, 1960 (1995).

[71] J. C. Bushnell and D. J. McCloskey, "Thermoelastic stress production in solids," J. Appl. Phys. 39, 5541 (1968).

[72] J. I. Etcheverry and M. Mesaros, "Molecular dynamics simulation of the production of acoustic waves by pulsed laser irradiation," Phys. Rev. B 60, 9430-9434 (1999).

[73] K. Sokolowski-Tinten, J. Bialkowski, A. Cavalleri, D. von der Linde, A. Oparin, J. Meyer-ter-Vehn, S. I. Anisimov, "Transient states of matter during short pulse laser ablation," Phys. Rev. Lett. 81, 224-227 (1998).

[74] V. Zhakhovskii, K. Nishiara, S. Anisimov, and N. Ingamov, "Molecular-dynamics simulation of rarefaction waves in media that can undergo phase transitions," JETP Lett. 71, 167-172 (2001).

[75] R. Kelly and A. Miotello, "Comments on explosive mechanisms of laser sputtering," Appl. Surf. Sci. 96-98, 205-215 (1996).

[76] A. Miotello and R. Kelly, "Critical assessment of thermal models for laser sputtering at high fluences," Appl. Phys. Lett. 67, 3535-3537 (1995).

[77] A. Miotello and R. Kelly, "Laser-induced phase explosion: new physical problems when a condensed phase approaches the thermodynamic critical temperature," Appl. Phys. A 69, S67-S73 (1999).

[78] G. Paltaud and H. Schmidt-Kloiber, "Microcavity dynamics during laser-induced spallation of liquids and gels," Appl. Phys. A 62, 303-311 (1996).

[79] L. V. Zhigilei and B. J. Garrison, "Microscopic mechanisms of laser ablation of organic solids in the thermal and stress confinement irradiation regimes," J. Appl. Phys. 88, 1281-1298 (2000).

[80] F. Vidal, T. Johnston, S. Laville, O. Bathélemy, M. Chaker, B. L. Drogoff, J. Margot, and M. Sabsabi, "Critical-point phase separation in laser ablation of conductors," Phys. Rev. Lett. 86, 2573-2576 (2001).

[81] A. Oraevsky, S. Jacques, and F. Tittel, "Mechanism of laser ablation for aqueous media irradiated under confined-stress conditions," J. Appl. Phys. 78, 1281-1290 (1995).

[82] C. Schafer, H. M. Urbassek, and L. V. Zhigilei, "Metal ablation by picosecond laser pulses: A hybrid simulation," Phys. Rev. B 66, 115404 (2002).

[83] L. R. Veeser and J. C. Solem, "Studies of laser-driven shock waves in aluminum," Phys. Rev. Lett. 40, 1391-1394 (1978).

[84] R. J. Trainor, J. W. Shaner, J. M. Auerbach, and N. C. Holmes, "Ultrahigh-pressure laser-driven shock-wave experiments in aluminum," Phys. Rev. Lett. 42, 1154-1157 (1979).

[85] L. R. Veeser, J. C. Solem, and A. J. Lieber, "Impedance-match experiments using laser-driven shock waves," Appl. Phys. Lett. 35, 761-763 (1979).

[86] F. Cottet and J. P. Romain, "Formation and decay of laser-generated shock wave," Phys. Rev. A 25, 576-579 (1982).

[87] R. Fabbro, E. Fabre, F. Amiranoff, C. Garban-Labaune, J. Virmont, M. Weinfeld, and C. E. Max, "Laser-wavelength dependence of mass-ablation rate and heat-flux inhibition in laser produced plasmas," Phys. Rev. A 26, 2289-2292 (1982).

[88] F. Cottet, J. P. Romain, R. Fabbro, and B. Faral, "Measurements of laser shock pressure and estimate of energy lost at 1.05-um wavelength," J. Appl. Phys. 55, 4125-4127 (1984).

[89] F. Cottet, J. P. Romain, R. Fabbro, and B. Faral, "Ultrahigh-pressure laser-driven shock-wave experiments at 0.26 um wavelength," Phys. Rev. Lett. 52, 1884-1886 (1984).

[90] J. P. Romain, M. Hallouin, M. Gerland, F. Cottet, and L. Marty, "$\alpha \rightarrow \varepsilon$ phase transition in iron induced by laser generated shock waves," in *Shock Waves in Condensed Matter 1987*, edited by S.C. Schmidt and N.C. Holmes (Elsevier Science Publishers B.V., Amsterdam, 1988), p. 787-790.

[91] F. Cottet, L. Marty, M. Hallouin, J. P. Romain, J. Virmont, R. Fabbro, and B. Faral, "Two-dimensional study of shock breakout at the rear face of laser-irradiated metallic targets," J. Appl. Phys. 64, 4474-4477 (1988).

[92] F. Cottet and M. Boustie, "Spallation studies in aluminum targets using shock waves induced by laser irradiation at various pulse durations," J. Appl. Phys. 66, 4067-4073 (1989).

[93] R. Fabbro, J. Fournier, P. Ballard, D. Devaux, and J. Virmont "Physical study of laser-produced plasma in confined geometry," J. Appl. Phys. 68, 775-784 (1990).

[94] D. Devaux, R. Fabbro, L. Tollier, and E. Bartnicki, "Generation of shock waves by laser-induced plasma in confined geometry," J. Appl. Phys. 74, 2268-2273 (1993).

[95] S. Couturier, T. de Rességuier, M. Hallouin, J. P. Romain, and F. Bauer, "Shock profile induced by short laser pulses," J. Appl. Phys. 79, 9338-9342 (1996).

[96] L. Tollier, R. Fabbro, and E. Bartnicki, "Study of the laser-driven spallation process by the velocity interferometer system for any reflector interferometry technique. I. Laser-shock characterization," J. Appl. Phys. 83, 1224-1230 (1998).

[97] T. de Rességuier and M. Hallouin, "Stress relaxation and precursor decay in laser shock-loaded iron," J. Appl. Phys. 84, 1932-1938 (1998).

[98] T. de Rességuier and M. Hallouin, "Interaction of two laser shocks inside iron samples," J. Appl. Phys. 90, 4377-4384 (2001).

[99] Th. Löwer, R. Sigel, K. Eidmann, I. B. Földes, S. Hüller, J. Massen, G.D. Tsakiris, S. Witkowski, W. Preuss, H. Nishimura, H. Shiraga, Y. Kato, S. Nakai, and T. Endo,

"Uniform multimegabar shock waves in solids driven by laser-generated thermal radiation," Phys. Rev. Lett. 72, 3186-3189 (1994).

[100] A. Benuzzi, Th. Löwer, M. Koenig, B. Faral, D. Batani, D. Beretta, C. Danson, and D. Pepler, "Indirect and direct laser driven shock waves and applications to copper equation of state measurements in the 10-40 Mbar pressure range," Phys. Rev. E 54, 2162-2165 (1996).

[101] M. Basko, Th. Löwer, V. N. Kondrashov, A. Kendl, R. Sigel, and J. Meyer-ter-Vehn, "Optical probing of laser-induced indirectly driven shock waves in aluminum," Phys. Rev. E 56, 1019-1031 (1997).

[102] A. H. Clauer and J. H. Holbrook, "Effects of laser induced shock waves," in *Shock waves and high-strain-rate phenomena in metals*, edited by M. A. Meyers and L. E. Murr (Plenum Press, 1981), p. 675.

[103] R. M. More, "Laser-driven shockwave experiments at extreme high pressures," in *Laser interaction and related plasma phenomena*, edited by H. J. Schwarz, H. Hora, M. J. Lubin, and B. Yaakobi (Plenum Press, 1981), p. 253.

[104] R. J. Trainor, N .C. Holmes, R. A. Anderson, E. M. Campbell, W. C. Mead, R. J. Olness, R. E. Turner, and F. Ze, "Shock wave pressure enhancement using short wavelength (0.35 um) laser irradiation," Appl. Phys. Lett. 43, 542-544 (1983).

[105] D. Salzmann, S. Eliezer, A. D. Krumbein, and L. Gitter, "Laser-driven shock-wave propagation in pure and layered targets," Phys. Rev. A 28, 1738-1751 (1983).

[106] S. Eliezer, I. Gilath, and T. Bar-Noy, "Laser-induced spall in metals: Experiment and simulation," J. Appl. Phys. 67, 715-724 (1990).

[107] M. Koenig, B. Faral, J. M. Boudenne, D. Batani, A. Benuzzi, S. Bossi, C. Rémond, J. P. Perrine, M. Temporal, and S. Atzeni, "Relative consistency of equations of state by laser driven shock waves," Phys. Rev. Lett. 74, 2260-2263 (1995).

[108] E. Moshe, E. Dekel, Z. Henis, and S. Eliezer, "Development of an optically recording velocity interferometer system for laser induced shock waves measurements," Appl. Phys. Lett. 69, 1379-1381 (1996).

[109] N. C. Woolsey and J. S. Wark, "Modeling of time resolved x-ray diffraction from laser-shocked crystal," J. Appl. Phys. 81, 3023-3037 (1997).

[110] I. V. Erofeev, V. V. Silberschmidt, A. A. Kalin, V. A. Moiseev, and I. V. Solomatin, "Evolution of a laser-generated shock wave in iron and its interaction with martensitic transformation and twinning," Shock Waves 8, 177-181 (1998).

[111] A. Benuzzi-Mounaix, M. Koenig, J. M. Boudenne, T. A. Hall, "Chirped pulse reflectivity

and frequency domain interferometry in laser driven shock experiments," Phys. Rev. E 60, 2488-2491 (1999).

[112] T. R. Boehly, J. A. Delettrez, J. P. Knauer, D. D. Meyerhofer, B. Yaakobi, R. P. J. Town, and D. Hoarty, "Effect of shock heating on the stability of laser-driven targets," Phys. Rev. Lett. 87, 145003 (2001).

[113] T. R. Boehly, T. J. B. Collins, O. Gotchev, T. J. Kessler, J. P. Knauer, T. C. Sangster, and D. D. Meyerhofer, "Observations of modulated shock waves in solid targets driven by spatially modulated laser beams," J. Appl. Phys. 92, 1212-1215 (2002).

[114] A. Benuzzi-Mounaix, M. Koenig, G. Huser, B. Faral, D. Batani, E. Henry, M. Tomasini, B. Marchet, T. A. Hall, M. Boustie, Th. De Rességuier, M. Hallouin, F. Guyot, D. Andrault, and Th. Charpin, "Absolute equation of state measurements of iron using laser driven shocks," Phys. Plasmas 9, 2466-2469 (2002).

[115] C. Oros, "Investigations involving shock waves generation and shock pressure measurement in direct ablation regime and confined ablation regime," Shock Waves 11, 393-397 (2002).

[116] M. A. Meyers, F. Gregori, B. K. Kad, M. S. Schneider, D. H. Kalantar, B. A. Remington, G. Ravichandran, T. Bohely, and J. S. Wark, "Laser-induced shock compression of monocrystalline copper: characterization and analysis," Acta Mater. 51, 1211-1228 (2003).

[117] D. H. Kalantar, J. Belak, E. Bringa, K. Budil, M. Caturla, J. Colvin, M. Kumar, K. T. Lorenz, R. E. Rudd, J, Stölken, A. M. Allen, K. Rosolankova, J. S. Wark, M. A. Meyers, and M. Schneider, "High-pressure, high-strain-rate lattice response of shocked materials," Phys. Plasmas 10, 1659-1576 (2003).

[118] R. Pakula and R. Sigel, "Self-similar expansion of dense matter due to heat transfer by nonlinear conduction," Phys. Fluids 28, 232-244 (1985).

[119] A. Ng, A. Forsman, and P. Celliers, "Heat front propagation in femtosecond-laser-heated solids," Phys. Rev. E 51, 5208-5211 (1995).

[120] E. Tokunaga, A. Terasaki, T. Kobayashi, "Frequency-domain interferometer for femtosecond time-resolved phase spectroscopy," Opt. Lett. 17, 1131-1133 (1992).

[121] E. Tokunaga, A. Terasaki, T. Kobayashi, "Induced phase modulation of chirped continuum pulses studied with a femtosecond frequency-domain interferometer," Opt. Lett. 18, 370-372 (1993).

[122] J. P. Geindre, P. Audebert, A. Rousse, F. Falliès, J. C. Gauthier, A. Mysyrowicz, A. D. Santos, G. Hamoniaux, and A. Antonetti, "Frequency-domain interferometer for

measuring the phase and amplitude of a femtosecond pulse probing a laser-produced plasma," Opt. Lett. 19, 1997-1999 (1994).

[123] E. Tokunaga, A. Terasaki, and T. Kobayashi, "Femtosecond phase spectroscopy by use of frequency-domain interference," J. Opt. Soc. Am. B 12, 753-771 (1995).

[124] R. Evans, A. D. Badger, F. Falliès, M. Mahdieh, T. A. Hall, P. Audebert, J.-P. Geindre, J.-C. Gautheier, A. Mysyrowicz, G. Grillon, and A. Antonetti, "Time- and space-resolved optical probing of femtosecond-laser-driven shock waves in aluminum," Phys. Rev. Lett. 77, 3359-3362 (1996).

[125] K. T. Gahagan, D. S. Moore, D. J. Funk, R. L. Rabie, S. J. Buelow, and J. W. Nicholson, "Measurement of shock wave rise times in metal thin films," Phys. Rev. Lett. 85, 3205-3208 (2000).

[126] D. S. Moore, K. T. Gahagan, J. H. Reho, D. J. Funk, S. J. Buelow, and R. L. Rabie, "Ultrafast nonlinear optical method for generation of planar shocks," Appl. Phys. Lett. 78, 40-42 (2001).

[127] K. T. Gahagan, D. S. Moore, D. J. Funk, J. H. Reho, and R. L. Rabie, "Ultrafast interferometric microscopy for laser-driven shock wave characterization," J. Appl. Phys. 92, 3679-3682 (2002).

[128] H. Azechi, S. Oda, K. Tanaka, T. Norimatsu, T. Sasaki, T. Yamanaka, and C. Yamanaka, "Laser-driven shock wave inside a glass microbaloon target," Appl. Phys. Lett. 32, 216-218 (1978).

[129] R. Kodama, K. A. Tanaka, M. Nakai, K. Nishihara, T. Norimatsu, T. Yamanaka, and S. Nakai, "Time-resolved measurements of laser-induced shock waves in deuterated polystyrene porous targets by x-ray backlighting," Phys. Fluids B 3, 735-744 (1991).

[130] T. Endo, K. Shigemori, H. Azechi, A. Nishiguchi, K. Mima, M. Sato, M. Nakai, S. Nakaji, N. Miyanaga, S. Matsuoka, A. Ando, K. A. Tanaka, and S. Nakai, "Dynamic behavior of rippled shock waves and subsequently induced areal-density-perturbation growth in laser-irradiated foils," Phys. Rev. Lett. 74, 3608-3611 (1995).

[131] X. Z. Li, M. Nakano, Y. Yamauchi, K. Kishida, and K. A. Tanaka, "Microcracks, spall and fracture in glass: A study using short pulsed laser shock waves," J. Appl. Phys. 83, 3583-3594 (1998).

[132] K. A. Tanaka, M. Hara, N. Ozaki, Y. Sasatani, K. Kondo, M. Nakano, K. Nishihara, H. Takenaka, M. Yoshida, and K. Mima, "Multi-layered flyer accelerated by laser induced shock waves," Phys. Plasmas 7, 676-680 (2000).

[133] N. Ozaki, Y. Sasatani, K. Kishida, M. Nakano, M. Miyanaga, K. Nagai, K. Nishihara, T.

Norimatsu, K. A. Tanaka, Y. Fujimoto, K. Wakabahashi, S. Hattori, T. Tange, K. Kondo, M. Yoshida, N. Kozu, M. Ishiguchi, and H. Takenaka, "Planar shock wave generated by uniform irradiation from two overlapped partially coherent laser beams," J. Appl. Phys. 89, 2571-2575 (2001).

[134] N. Ozaki, K. A. Tanaka, Y. Sasatani, K. Fujita, K. Takamatsu, M. Nakano, M. Yoshida, K. Okada, E. Takahashi, Y. Owadano, H. Takenana, and K. Kondo, "Hugoniot measurements for polyimide with laser and explosives," Phys. Plasmas 10, 2475-2479 (2003).

[135] K. Takamatsu, N. Ozaki, K. A. Tanaka, T. Ono, K. Nagai, M. Nakai, T. Watari, A. Sunahara, M. Nakano, T. Kataoka, H. Takenaka, M. Yoshida, K. Kondo, and T. Yamanaka, "Equation-of-state measurements of polyimide at pressures up to 5.8 GPa using low-density foam with laser-driven shock waves," Phys. Rev. E 67, 56406 (2003).

Chapter 2

Laser induced forward transfer of thin metal films

Laser induced forward transfers (LIFT) of thin metal films using a single pulse of excimer laser (wavelength: 248 nm, pulse width: 30 ns) with the flat-top profile of the laser intensity (Excimer-LIFT) and the femtosecond laser (wavelength: 800 nm, pulse width: 120 fs) with the Gaussian profile (Fs-LIFT) are performed to achieve the high-resolution deposition of micropatterns. The different point between the Excimer-LIFT and the Fs-LIFT processes is the absorption of the laser energy from the laser induced plume. For the Excimer-LIFT, the ablation occurs during the laser pulse and the laser induced plume is generated. The plume is heated by absorbing the latter part of the laser pulse. The scatter of microparticles expands as a result of the growth of the plume due to the evaporation of the deposited pattern. For the Fs-LIFT, on the other hand, the growth of the plume depends only on the fluence because the ablation occurs after the whole laser pulse and the laser energy is not absorbed by the plume. Therefore, the scatter of microparticles is prevented. Scatter of droplets depends on the melted area outside the laser irradiated region in the thin film for the Excimer-LIFT and the difference of the laser intensity in the laser beam for the Fs-LIFT. The Fs-LIFT is a powerful tool to achieve the high-resolution micropatterning of metals when the thin film does not contact with the acceptor substrate.

2.1 Introduction

2.1.1 Laser direct writing

Laser direct writing technologies such as the ink jet have been developed to fabricate the structure directly on the substrate [1]. It takes shorter times to fabricate structures compared to other methods such as the lithography. The mechanical force of the piezo-device or the pressure of the bubble generated by heating is used as a driving force to transfer the ink to a point on the substrate. In this section, the method that uses the laser ablation as a driving force is described bellow.

2.1.1.1 Laser induced forward transfer

Laser Induced Forward Transfer (LIFT) is one of the laser direct writing methods. LIFT process consists of three main steps. First, the thin film pre-coated on the transparent substrate is ablated by a laser beam, which is irradiated through the substrate and deposits the pulse energy onto the film-substrate interface. Second, the removed material is transferred to the acceptor substrate which is placed in close proximity to the film. Third, transferred material is landed and deposited onto the acceptor substrate. Schematic of the LIFT is shown in FIG. 2.1. The main advantages of the LIFT are; it is the eco-friendly and clean process because it is the dry process without using organic solvent, and it can be performed in air and at room temperature. The disadvantage is that thin film deposition on the transparent substrate is needed before the LIFT.

The LIFT technique has been studied actively since the first report by Bohandy et al. [2] due to its high ability to be applied to micro electronic/photonic devices. Various kinds of materials such as metals (Al [3], Au [5], Cu [2,5,6], Cr [5-12], Pd [13], Pt [12], Sn [7], Ti [7,8], V [7], W [14,15,16,17]), semiconductors (Ge [7]), multi layers (Ge/Se [18]), high T_C compound (YBaCuO, BiSrCaCuO [19]), metal oxides (In_2O_3 [5,12,20,21]), diamond nanoparticle [22], Rhodamine 610 [23], and PMMA [24] were deposited using different kinds of lasers such as Excimer lasers and Nd:YAG laser. Microdevices such as microwire, microresistor, and electrode for TFT are suggested to be produced using the LIFT technique [25]. Zergioti *et al.* manufactured the patterns for hologram and gratings [5]. Applications to the corrections of the quartz crystal and the mask repair are also expected.
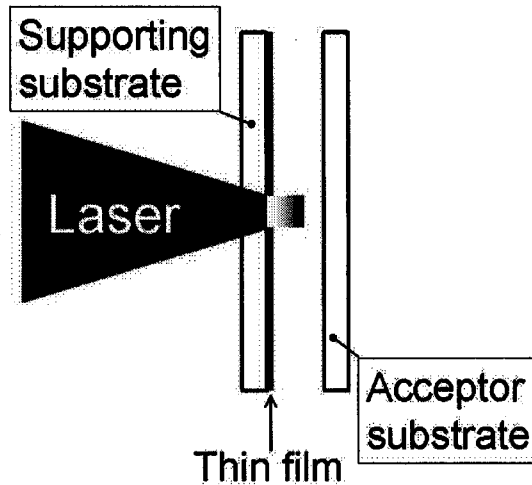
FIG. 2.1.   Schematic illustration of LIFT.

Mechanisms of LIFT as well as applications have also been reported. Adrian *et al.* [26] and Baseman *et al.* [27,28] calculated the temperature distribution in the thin film during laser heating using calculus of finite difference and finite element method, respectively, and suggested that a thin film was heated by laser beam till the pressure at the interface between the film and the substrate reaches a value enough to remove and propel the film from the substrate. Fogarassy investigated the LIFT mechanism of YBaCuO and BiSrCaCuO high T_C thin film irradiated by a single pulse ArF excimer laser (193 nm, 20 ns) [19]. Time-resolved change of temperature rise on the laser irradiated surface was calculated by thermo-hydrodynamic calculation. The calculated results and experimental results analyzed by using RBS showed that film removal was attained just above the temperature threshold of surface melting of these two compounds. The deposited structure showed good smooth and good adherence with the acceptor substrate at the threshold of complete removal. Meanwhile, when overheated, the surface of the deposited structure was roughened due to overheating and, as a result, the material showed poor adherence. Schltze *et al* investigated the phase front dynamics in a thin film using Harrach's analytical solutions [29] and the blow-off process of a thin film irradiated by Nd:YAG laser (1064 nm, 120 ns) with Gaussian profile and Nd:glass laser (1064 nm, 40 ns) with flat-top [3,4]. Two blow-off mechanism was proposed; the first is in case of low laser intensities and/or thin film. The film is completely melted and blown off by the evaporated pressure generated at the interface between the film and the support substrate. The other case is high laser intensities and/or thick film. The film was explosively blown off due to high evaporated pressure at the interface as a result of the overheat of liquid phase or burst of solid phase.

Kántor *et al.* performed LIFT systematically using long pulsed (100 – 1000 μs) lasers comparing the results of LIFT using short pulsed lasers [15-17]. Thin metal film is removed completely without damaging the surface of the supporting substrate just above the ablation threshold (several tens of mJ/cm^2) using ns pulsed lasers. However, the deposited structure shows poor adherence with the acceptor substrate. Debris formation and heat damage occurs due to complete ablation of the film using high fluence (typically above 1 J/cm^2) laser pulse [6,7]. On the other hand, a micrometer sized pattern of tungsten with well adherence with the acceptor substrate was achieved using long pulsed laser as a result of transfer of tungsten in solid phase. Time-resolved transmittance and reflectance measurements and temperature distribution calculation in the film showed that ablation starts at a well defined temperature independent of pulse width and pulse shape in case of LIFT using long pulsed laser. In this case there are no distinct boundary between removal, transfer and deposition in space and time.

2.1.1.2 Matrix-assisted pulsed laser evaporation direct write

The process of the Matrix-assisted pulsed laser evaporation direct write (MAPLE DW) is similar to that of the LIFT. The different point is the use of ribbons instead of thin films [30,31]. The ribbon consists of the nanoparticle of the transferring material dispersed in the polymeric matrix. The thickness of the ribbon is about 5 μm. The process of the MAPLE DW consists of three steps; the matrix is vaporized or cracked and the ribbon is removed due to the laser irradiation (removal process), nanoparticles in the ribbon are transferred to the acceptor substrate (transfer process), and nanoparticles are deposited onto the acceptor substrate (deposition process).

The different advantage of the MAPLE DW from the LIFT is that organic matters are able to be transferred because the matters are not highly heated. The disadvantage is the mix of the matrix in the deposited matters.

Many kinds of materials, such as metals (Ag [30,32]), ceramics ($BaTiO_3$ (BTO) [30,33,34,35], $SrTiO_3$ (STO) [29], $Y_3Fe_5O_{12}$ (YIG) [30,34], SiO_2 [35], TiO_2 [35]), organic matters (poly(epichlorohydrin) [33,36], epoxy resin [37], fluoroalcolpolysiloxane [36]), graphite ([34,36]), phosphors (Y_2O_3:Eu, Zn_2SiO_4:Mn [34]), enzyme (Horseradish peroxidase (HRP) [38]), cell (Chinese hamster overies (CHO) [38]), and bacteria (Chinese hamster overies (CHO) [38]), have been transferred using the MAPLE DW technique because the temperature rise of the nanoparticles are prevented. Wire [30,31], resistor [37], condenser [30,33,34], coil [30], chemical sensors [36-38], and pixels of CRT display [40] are also fabricated using the MAPLE DW technique.

High speed photographing of the ribbon was performed during the laser irradiation to investigate the process of the MAPLE DW [41,42]. The ribbon was removed about 500 ns after the laser irradiation and the removed area expanded till 1 μs after the irradiation. The transferring velocity of the ribbon was about 200 km/s. Molecular dynamics simulation of the MAPLE DW was also performed [43].

2.1.1.3 Laser ablation transfer

Laser Ablation Transfer (LAT) is the way to transfer the colors and is similar to the LIFT [44,45]. The different point from the LIFT is that the film consists of two layers. Al film is deposited first on the supporting substrate and after that colors are coated on the Al film. Al film is ablated due to the laser irradiation. Colors are removed due to the evaporated pressure of the Al and transferred to the acceptor substrate. Al film is used to add the propulsion to colors. This method is used in the field of the print. Color images of high resolution are fabricated in short time using this method.

2.1.1.4 Laser explosive microfabrication

Laser Explosive Microfabrication (LEM) is the generic of the method of microprocessing using the laser induced explosive ablation. Typical one is the laser micro explosive joining [46]. In this method, two layers are deposited on the supporting substrate similar to the LAT. Thin film adhered to the supporting substrate is ablated due to the laser irradiation, and as a result it is joined with another film.

2.1.2 Purposes

Purposes of this chapter are, first, to perform the micro patterning of metals with high resolution using the LIFT process and, second, to elucidate the mechanism of the LIFT. In this study two kinds of lasers are used; the one is the femtosecond laser (wavelength: 800 nm, pulse width: 120 fs, spatial distribution of the intensity: Gaussian) and the other is the excimer laser (wavelength: 248 nm, pulse width: 30 ns, spatial distribution of the intensity: top-flat). Optimum condition to achieve the high-resolution deposition is investigated varying the experimental conditions systematically. Observations of the LIFT process are also performed. Based on these experimental results, mechanism of each LIFT is elucidated. Finally, these LIFTs are compared.

2.2 Excimer laser induced forward transfer of thin metal films

2.2.1 Introduction

In this section, Excimer Laser Induced Forward Transfer (Excimer-LIFT) of thin metal films is described. Influences of experimental parameters on the deposited patterns are investigated systematically when a single pulse of KrF excimer laser (wavelength: 248 nm, pulse width: 30 ns) is irradiated on three kinds of thin metal films (Ni, Cu, and Au). Dynamics of the thin film during the laser pulse, the laser induced plume, and the transferring materials are observed. The mechanism of the Excimer-LIFT is shown based on the experimental results. Microwires are fabricated using the Excimer-LIFT process and the resistance of the wire is measured.

2.2.2 Experiments

2.2.2.1 Excimer laser

KrF excimer laser (Lambda Physik, COMPEX110, wavelength: 248 nm, pulse width: 30 ns) is used in this study. The beam shape is 8 mm x 25 mm with flat-top profile.

2.2.2.2 Sample preparations

Three kinds of metals (Ni, Cu, and Au) were deposited on quartz substrates of 2 mm thickness using ion sputtering method. The thicknesses of the thin films are listed in TABLE 2.1. The films were irradiated by a single pulse of KrF excimer laser using a mask projection method. The removed material was deposited on the Si wafer as an acceptor substrate.

TABLE 2.1.   Thin metal films used in this study.

Material	Thickness (nm)
Ni	180
	500
	670
	780
Cu	160
	750
Au	140
	400

2.2.2.3 Time-resolved measurements of the He-Ne laser intensity reflected from metal films

The intensity of a He-Ne laser beam (wavelength 633 nm) reflected from the front and rear side of the thin film, respectively, were measured using photodiodes to investigate the film behavior during the laser pulse. The experimental setup is shown in FIG. 2.2. The wavelength of He-Ne laser was only detected using band-pass filter. Both a part of the incident of excimer laser and reflected He-Ne laser were detected by the photodiode simultaneously.
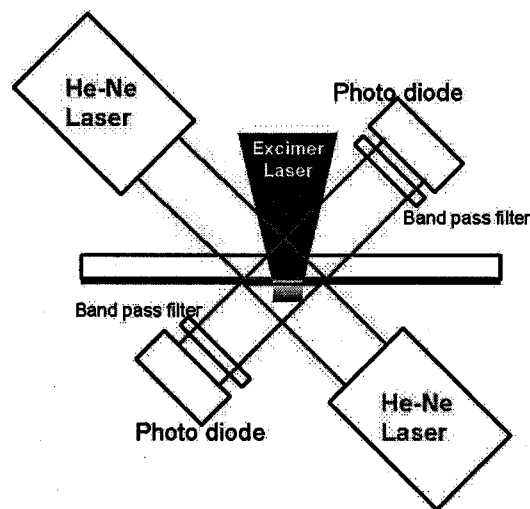
FIG. 2.2. Schematic illustration of the measurement of the intensity of the He-Ne probe lasers reflected from the surface of the film and the interface between the film and the support substrate.

2.2.2.4 Photographing of the laser induced plume

The dynamics of the laser induced plume and the shadowgraph of the transferring material were photographed using an image intensified CCD camera (Hamamatsu Photonics K.K., C2925-01). Experimental setup is shown in FIG. 2.3. A He-Ne laser (wavelength 633 nm) was used for illumination in photographing the shadowgraph. Photos were taken at different delay times after laser irradiation, controlling the timing of both the excimer laser pulse and the gate opening of the CCD camera by using a pulse generator. PIN photodiode (Hamamatsu Photonics K.K., S1722-02) was used to detect the pulse of the excimer laser. The circuit diagram for the detection of the excimer laser pulse is shown ins FIG. 2.4.
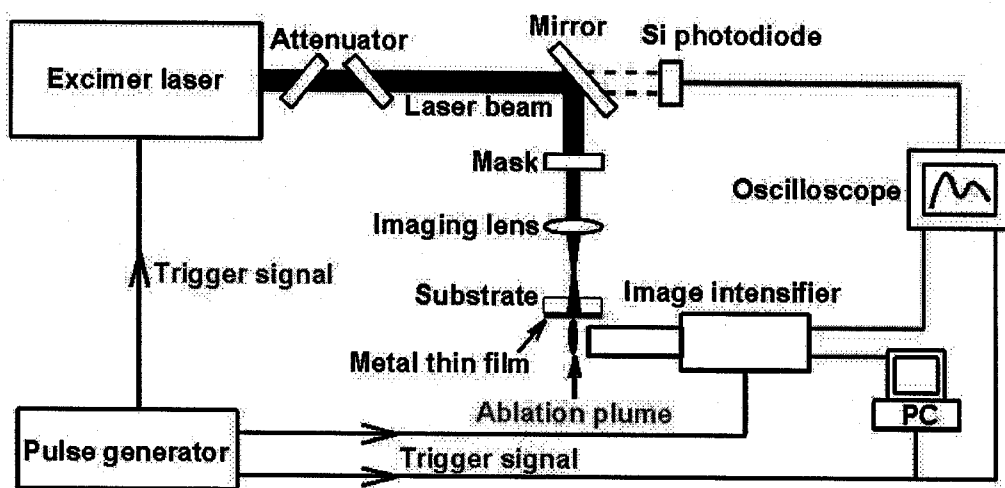
FIG. 2.3. Experimental setup for photographing images of the laser induced plume.
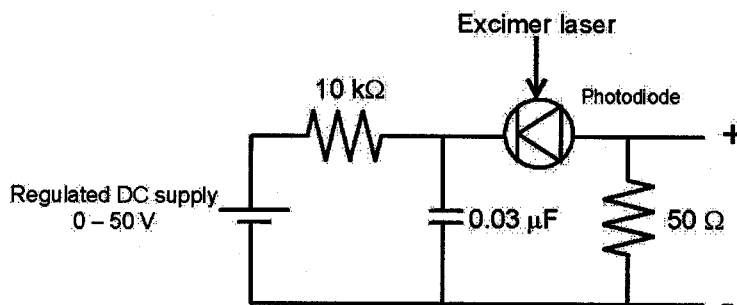
FIG. 2.4. Circuit for detecting the laser beam.

2.2.3 Characterization of deposited patterns

2.2.3.1 Influence of the film-substrate distance

In this section, the influence of the distance between the film and the acceptor substrate on the deposited pattern is described. Typical image of the deposited pattern is shown in FIG. 2.5. The white line in the figure indicates the outline of the laser irradiated region.
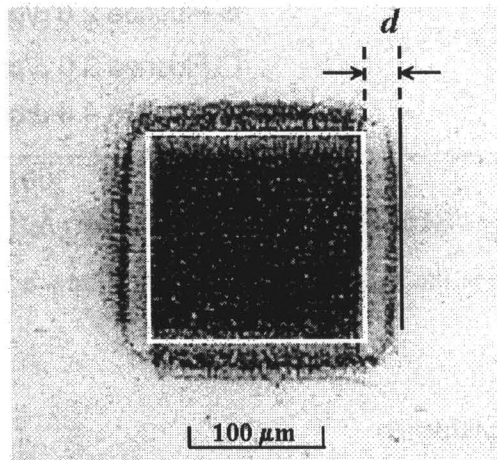
FIG. 2.5. Optical microscope image of a deposited pattern. Thin Ni film (180 nm) was irradiated by a single pulse of KrF excimer laser (1.5 J/cm^2). The film – acceptor substrate distance was 20 μm.

Some materials spread outward perpendicular to the edge of the dense central part of the structure which agrees with the laser irradiated region. This spread length d is shown in FIG. 2.6 as a function of the film-acceptor substrate distance L. Our recent studies revealed that the length d increases linearly with the distance L over several hundreds micrometer because the transferring material is not influenced by the external force [47-50]. The length d increases, however, nonlinearly for $L = 100$ μm. Gas around the plume flows below it when the hot plume becomes cool because the density of the hot plume is low [51]. This non-linearity means that the transferring material is influenced by the external force originated from the flowing gas in this region.
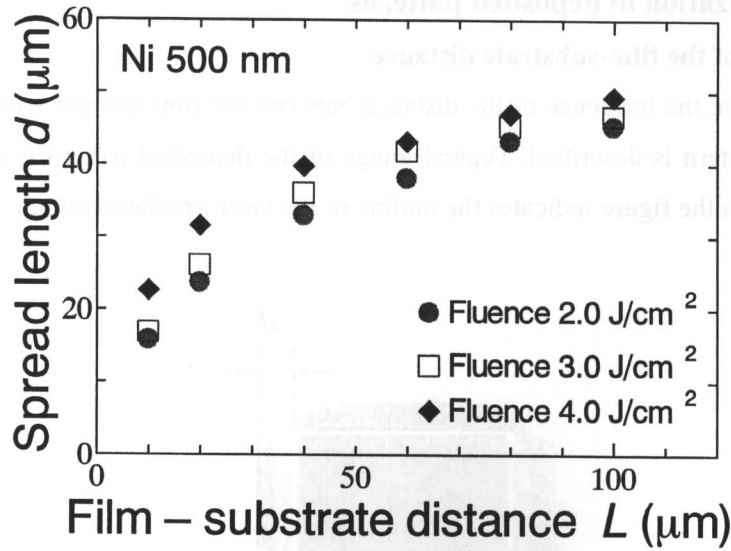
FIG. 2.6. Relationship between the spread length d and the film – acceptor substrate distance L.

2.2.3.2 Influence of the laser fluence

The appearance of deposited patterns at optimum, lower and higher fluences are shown in FIG 2.7. The appearance and size accuracy become worse both at lower and higher fluences. This tendency was true for the other film thicknesses. Optimum fluence depends on mainly the film thickness when the film shows good adherence with the supporting substrate. The value becomes larger as the thickness become thicker. It is found that the incomplete removal of the thin film from the supporting substrate causes the spread at lower fluences.
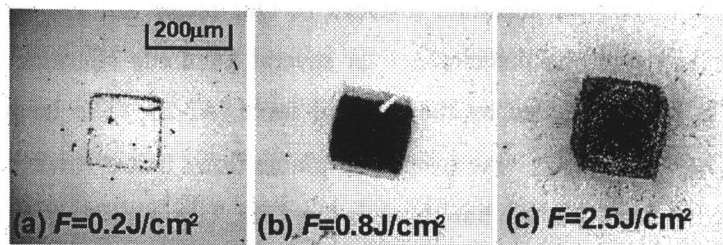
FIG. 2.7. Optical microscope images of deposited patterns. Thin Ni film (180 nm) was irradiated by a single pulse of KrF excimer laser with the film – acceptor substrate distance of 10 μm and with fluences: (a) below optimum (0.2 J/cm²), (b) at optimum (0.8 J/cm²), and (c) above optimum (2.5 J/cm²).

36

2.2.3.3 Scatter of microparticles

The problem in fabricating micro structures is the resolution of the deposited structure. Factors which influence the resolution are mainly as follows:

I. Droplets around the pattern

II. Droplets which are generated in performing at lower or higher fluences

III. particles around the pattern

FIGURE 2.8 shows the deposited patterns and the corresponding removal area of the thin film. White line in the figure indicates the outline of the laser irradiated region. The size of the pattern is similar to the laser irradiated region. Droplets are deposited around it. On the other hand, the removal region of the thin film is larger than the laser irradiated region. Therefore, the region around the laser irradiated region of the thin film is removed and deposited around the dense pattern as droplets. The spread length of the droplets is suppressed by getting small the film – acceptor substrate distance.

For the higher fluence, droplets caused by the effect of the laser pulse after deposition spread as shown in FIG. 2.9. For the lower fluence, on the other hand, droplets spread due to the incomplete removal of the thin film from the supporting substrate. These droplets are inhibited at optimum fluence. The optimum fluence depends on the film thickness, physical properties of the film, and the adhesion of the film to the supporting substrate.
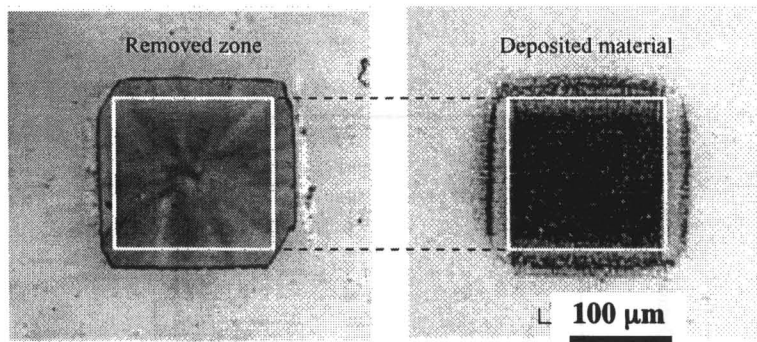
FIG. 2.8. Relationship between deposited material and removed zone. Film: Ni (180 nm), Laser fluence $F = 1.5$ J/cm^2, Film – acceptor substrate distance $L = 20$ μm.
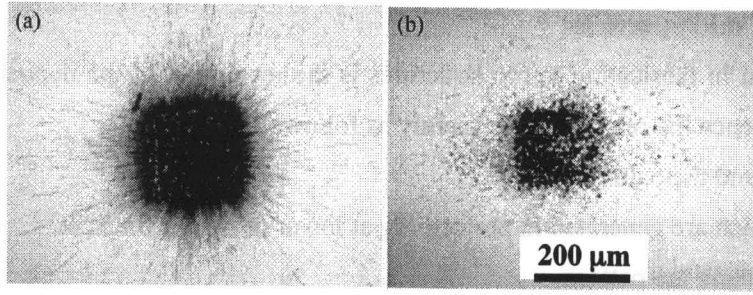
FIG. 2.9. Optical microscope images of deposited patterns at (a) excess and (b) deficient fluence. Film: Ni (500 nm), (a) $F = 4.0$ J/cm^2, $L = 10$ μm, (b) $F = 1.6$ J/cm^2, $L = 300$ μm.
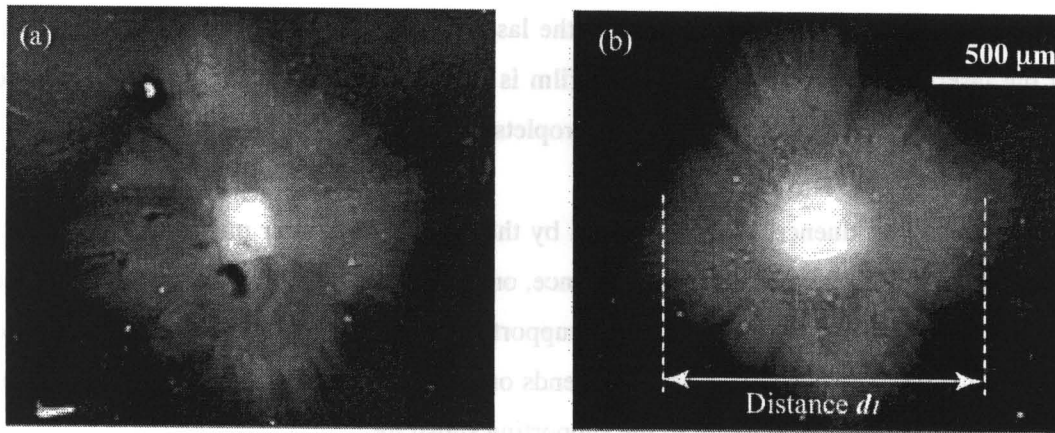
FIG. 2.10. SEM images of deposited patterns. Film: Ni (180 nm), $L = 10$ μm, (a) $F = 1.5$ J/cm^2, (b) $F = 0.8$ J/cm^2.
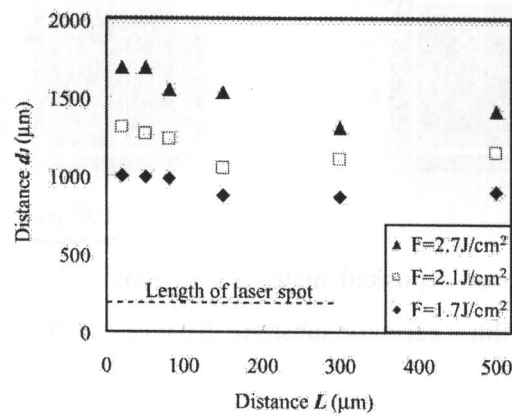
FIG. 2.11. Relationship between distance L and d_1. Film: Ni (180 nm).

Now, the problem of the deposition of particles on the acceptor substrate is considered. Typical SEM images of deposited patterns are shown in FIG. 2.10. Particles extend around the

dense deposited pattern.

The extended distance of particles is defined as d_1 as shown in FIG. 2.10(b). d_1 is plotted as a function of L in FIG. 2.11. Dotted line in the figure indicates the length of the edge of the laser spot. d_1 increases with the decrement of L while the spread length of droplets decreases.

Particles are considered to be included in the laser induced plume [47,52]. Particles are deposited when the plume extends along the acceptor substrate plane and cools down. Therefore, particles are not deposited if the plume does not extend along the substrate. Thus, I performed the LIFT at $L = 0$, which means that the film is contacted with the substrate. SEM image of the deposited pattern obtained at $L = 0$ is shown in FIG. 2.12(a). This image shows no extend of particles, that is to say that high resolution deposition is achieved.

For high fluence at L = 0, however, particles extend around the dense deposited pattern as shown in FIG. 2.12(b). Optical images of removal area of thin films are shown in FIG. 2.12(c) and (d) for the optimum and higher fluences, respectively. Removed size is larger than the laser spot size for higher fluence as shown in FIG. 2.12(d) while it is similar with the laser spot size for the optimum fluence as shown in FIG. 2.12(c). Therefore, it is suggested that removal mechanisms are different from the inside and outside of the laser irradiated region. For higher fluence, the plume thrusts the film and particles extend.
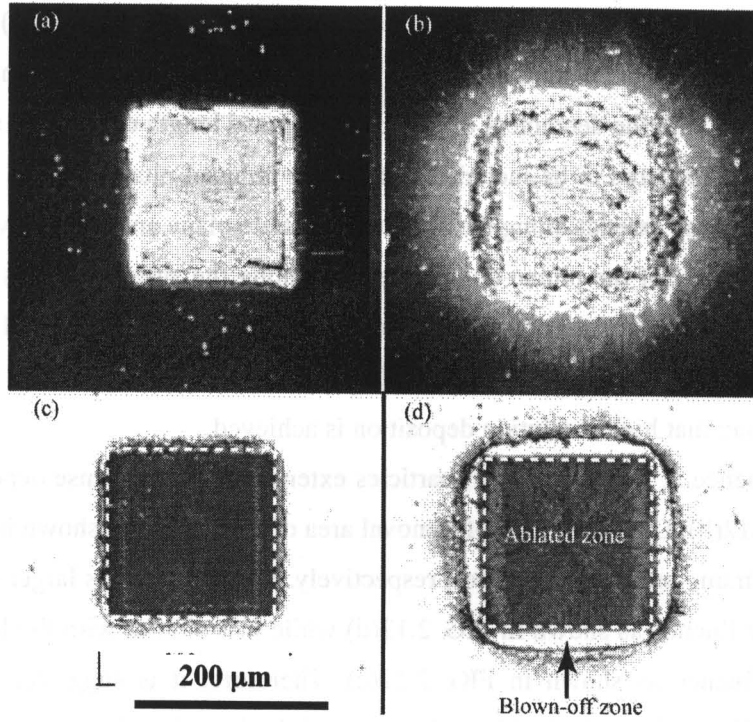
FIG. 2.12.   (a), (b) SEM images of deposited patterns, and (c), (d) optical microscope images of removed zones. Film: Ni (230 nm), L = 0 μm. (a), (c) F = 1.7 J/cm^2, and (b), (d) F = 2.7 J/cm^2.
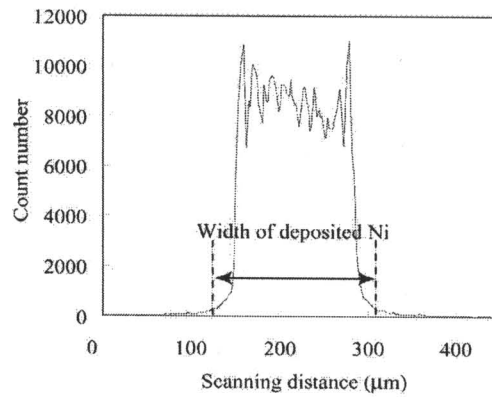
FIG. 2.13.   Result of x-ray fluorescence spectrometry for a deposited pattern. Film: Ni (230 nm), L = 0 μm, F = 1.7 J/cm^2.

X-ray fluorescence analysis was performed in order to confirm the existence of particles around the dense deposited pattern with high accuracy. Measurement was performed at BL-4A, Photon Factory, High Energy Accelerator Research Organization (KEK). Detected result of

40

NiKα for the sample which is shown in FIG2.12(a) is shown in FIG. 2.13. Little signals of NiKα are detected outside the deposited pattern. It is found that contact of the film with the substrate is useful method to achieve the high resolution.

2.2.3.4 Influence of the laser spot size

In this section, the influence of the laser spot size on the resolution of the deposited pattern is described. SEM images of deposited patterns are shown in FIG. 2.14 when LIFT is performed at $L = 0$ and the lateral length of the laser spot size is varied from $10 - 86$ μm and the longitudinal length is constant. Particles are not observed at each condition. SEM images of deposited patterns are shown in FIG. 2.15 when LIFT is performed at $L = 0$ and the laser fluence is varied and the laser spot size is constant. For higher fluence, extends of particles are observed.

Extended length of droplets is plotted in FIG. 2.16 as a function of the lateral length of the laser spot. Extended length of droplets is defined as shown in FIG. 2.17. The extended length decreases with the decrement of the lateral length of the laser spot. Thin film outside the laser spot is considered to be peeled from the supporting substrate. The reason of the decrement of the extended length with the decrement of the lateral length of the laser spot is suggested as follows.

Schematic illustration of the removal process of the thin film is shown in FIG. 2.18. The force F of the thin film in the laser irradiated region is expressed by

$$F = lwP, \qquad (2.1)$$

where P is the pressure of the plume, l is the longitudinal length and w is the lateral length of the laser spot. Thin film outside the laser irradiated region is peeled by the force F. F decreases linearly in proportion to w as expressed in Eq. (2.1). The peeled area outside the laser irradiated region decreases as a result of the decrement of F. Nonlinearity of the extended length of droplets as shown in FIG. 2.16 seems due to the plume.
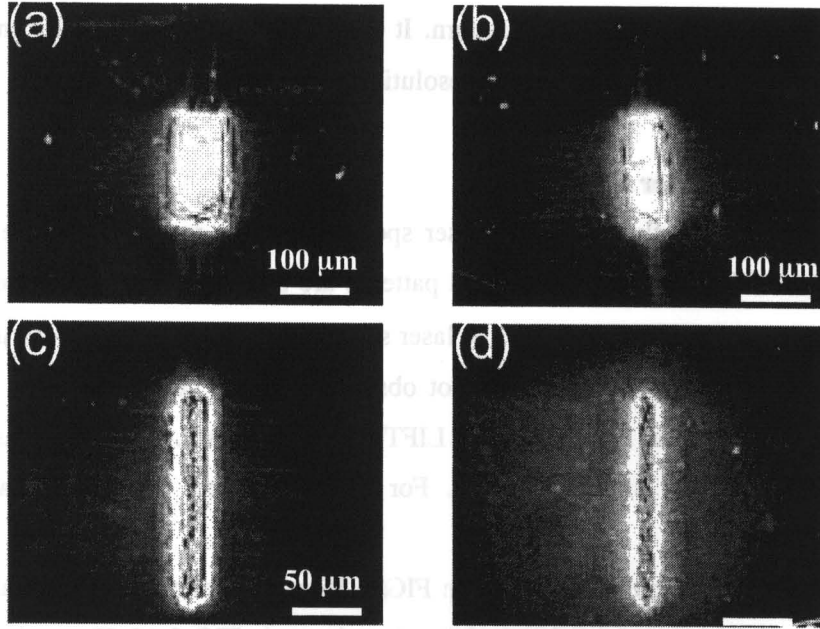
FIG. 2.14. SEM images of deposited patterns fabricated at various widths of laser spot. Ni (230 nm), F = 1.7 J/cm^2, L = 0 µm, Width of laser spot W = (a) 86, (b) 53, (c) 24, and (d) 10 µm, respectively.
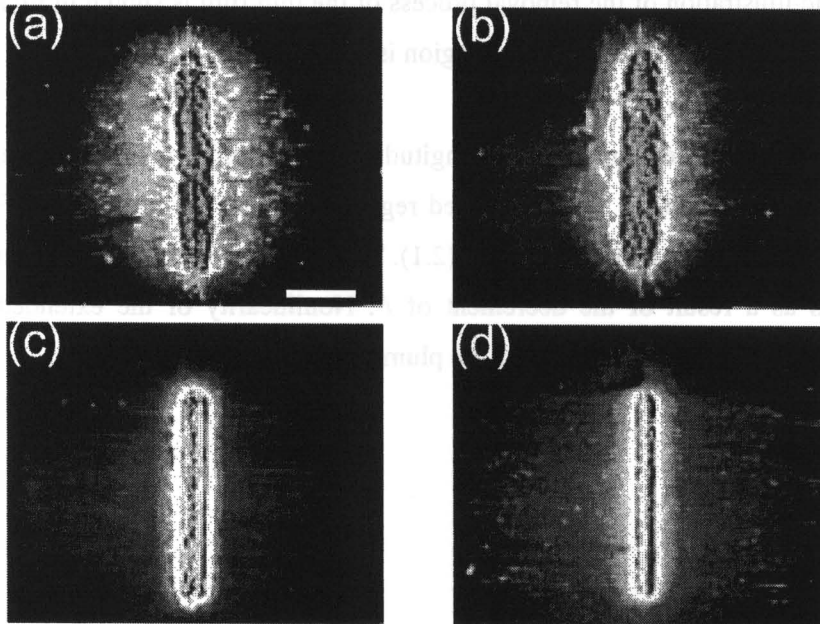
FIG. 2.15. SEM images of deposited patterns fabricated at various fluences. Ni (230 nm), L = 0 µm, W = 24 µm, F = (a) 2.7, (b) 2.1, (c) 1.7, and (d) 1.2 J/cm^2, respectively.
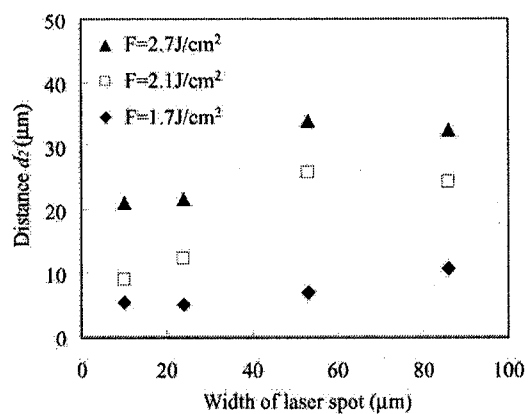
FIG. 2.16. Relationship between width of laser spot and distance d2. Ni (230 nm), L = 0 μm.
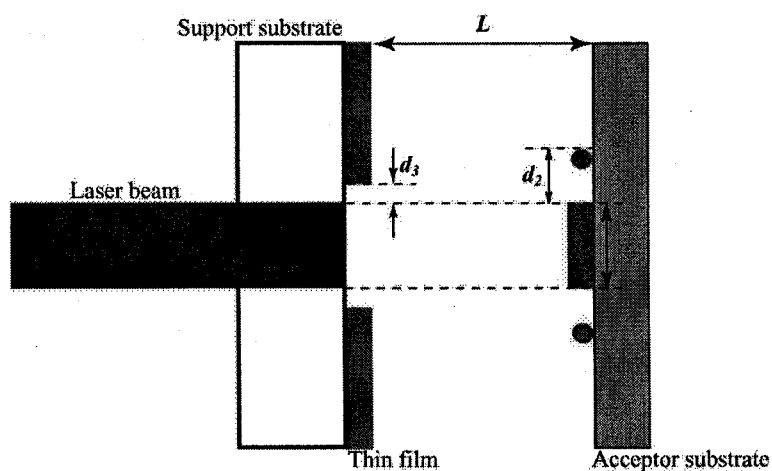
FIG. 2.17. Schematic illustration of the removed zone of the thin film and the deposited pattern.
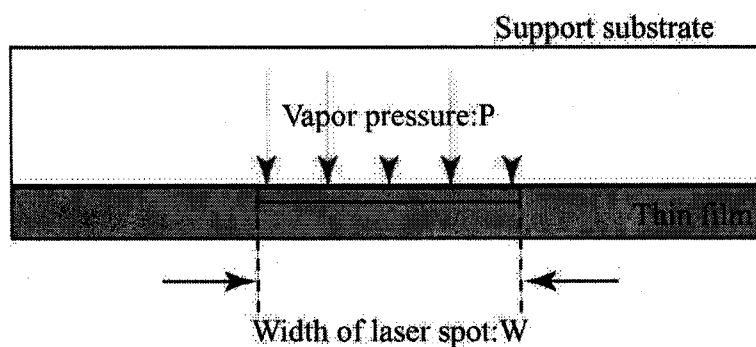
FIG. 2.18. Schematic illustration of the removal process of Excimer-LIFT.

43

2.2.3.5 Surface morphology

Surface morphology of deposited pattern fabricated at $L = 0$ is investigated using AFM. AFM images of deposited patterns are shown in FIG. 2.19 and 2.20. FIGURE 2.19 shows the edge of the pattern. Any droplets and particles are not observed outside the pattern. The edge of the pattern is about four times higher than the inside of the pattern. FIGURE 2.20 shows the AFM image of the central part of the pattern. The surface is flat rather than the edge part and is porous. These results mean that surface morphologies of the central and edge part are different.
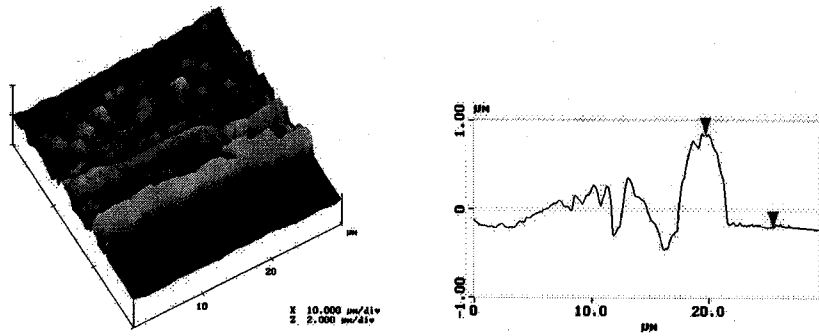
FIG. 2.19. AFM images at the edge of the deposited pattern. Left: 3D profile, right: cross sectional image. Ni (230 nm), $F = 1.7$ J/cm^2, $L = 0$ μm.
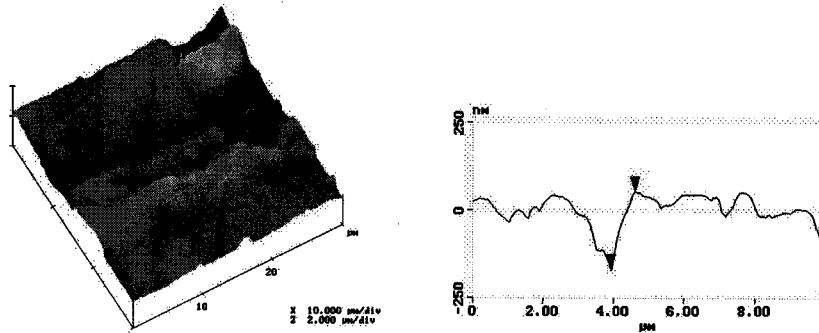
FIG. 2.20. AFM images at the center of the deposited pattern. Left: 3D profile, right: cross sectional image. Ni (230 nm), $F = 1.7$ J/cm^2, $L = 0$ μm.

2.2.4 Dynamics of thin metal films during the laser irradiation

Changes in the intensity of He-Ne laser reflected from the front and rear side of thin film, respectively, were measured to investigate the film behavior during incident excimer laser pulse at optimum and higher fluences. The measured reflected intensity from rear side, that is the film - supporting substrate interface, is shown in FIG. 2.21(a). In both cases, the change begins before the peak of the incident laser pulse, and the intensity drops and then keeps constant. It is found that the change of the rear side starts and finishes during laser pulse and that there is no big difference between optimum and higher fluence. FIGURE 2.21(b) shows the reflected intensity from the front side of the film. In this case also there is no quite difference of the onset of the change, and the change finishes during incident laser pulse in both cases. These results mean that film removal finishes during the duration of the incident laser pulse.
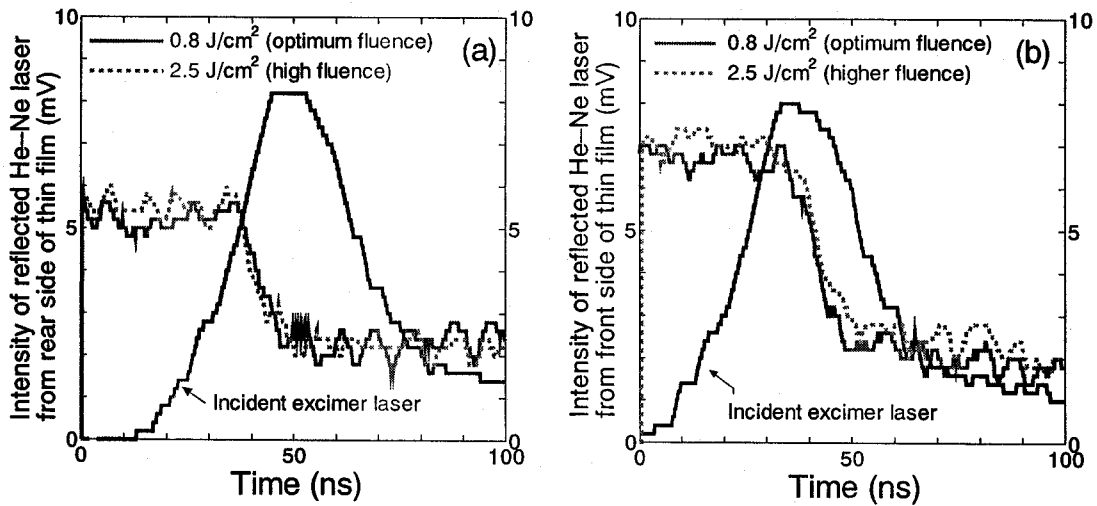
FIG. 2.21. Time evolution of the intensity of He-Ne laser reflected from (a) the film – support substrate interface and (b) the film surface of Ni (180 nm) at optimum and higher fluences of a single pulse of a KrF excimer laser.

2.2.5 Dynamics of the laser induced plume

The behavior of the ablated material was observed using an image intensified CCD camera. FIGURE 2.22 shows the plume images and the velocity of the leading edge of the plume at early stage of plume expansion is approximately 400 m/s and 200 m/s at higher and optimum fluences, respectively. The velocity increases with increase of fluence. And at higher fluence some parts flies away outside, however, there is no lateral extent at optimum fluence.

Plume images and shadowgraphs of transferring material at optimum and higher

fluences are shown in FIG. 2.23. Comparing the position of the plume with transferring material at the same delay time, it is found that the transferring material precedes the plume.

FIGURE 2.23 (b) and (c) show that the velocity of the transferring materials at higher fluence is larger than that at optimum fluence. The velocity depends on the pressure induced by laser irradiation at the film-supporting substrate interface as showed in FIG. 2.22. During laser pulse the behavior of thin film does not strongly depend on the fluence. This means the quantity of deposited energy onto the film become larger as the fluence become higher. The energy evaporates the film material and then the higher pressure at the interface causes higher velocity of the plume. As a result, higher fluence causes higher velocity of transferring material. The shock generated by the collision of the materials with the acceptor substrate become larger with increase of the velocity. This shock pushes the deposited structure outward on the acceptor substrate. As a result, the spread length become larger with increase of fluence. Not only fine appearance but high size accuracy can be obtained at optimum fluence.

The images of the plume with and without the acceptor substrate are shown in FIG. 2.24. The ablated material extends in laser irradiated direction without the substrate, while the plume spread outward with the substrate. This result means the plume influences the transferring material in case the acceptor substrate is close to the film.
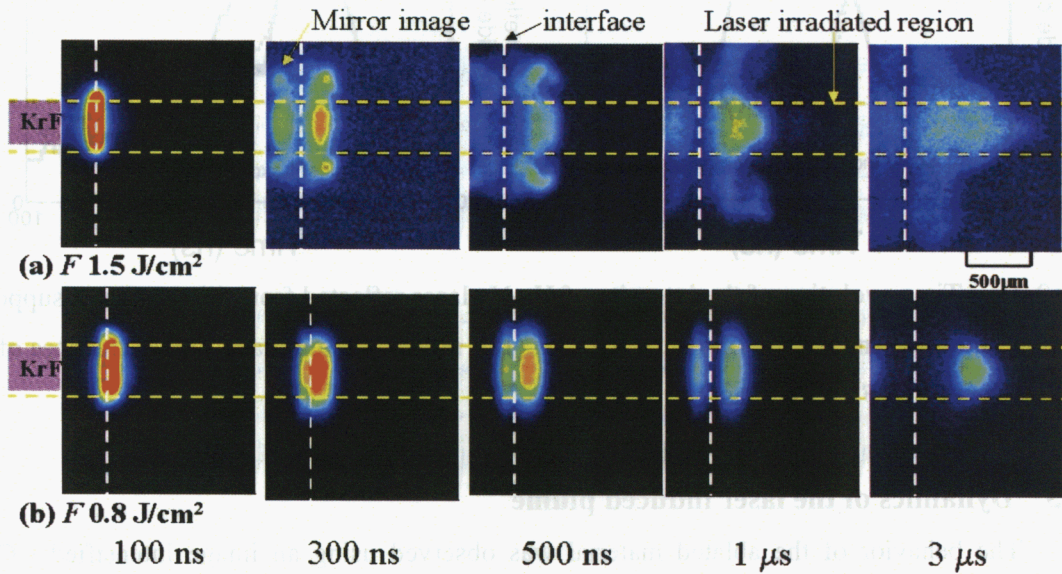
FIG. 2.22. Plume images of Au (400 nm) photographed using an image intensified CCD camera at different delay times. (a) high fluence, and (b) optimum fluence. Gate time: 50 ns.
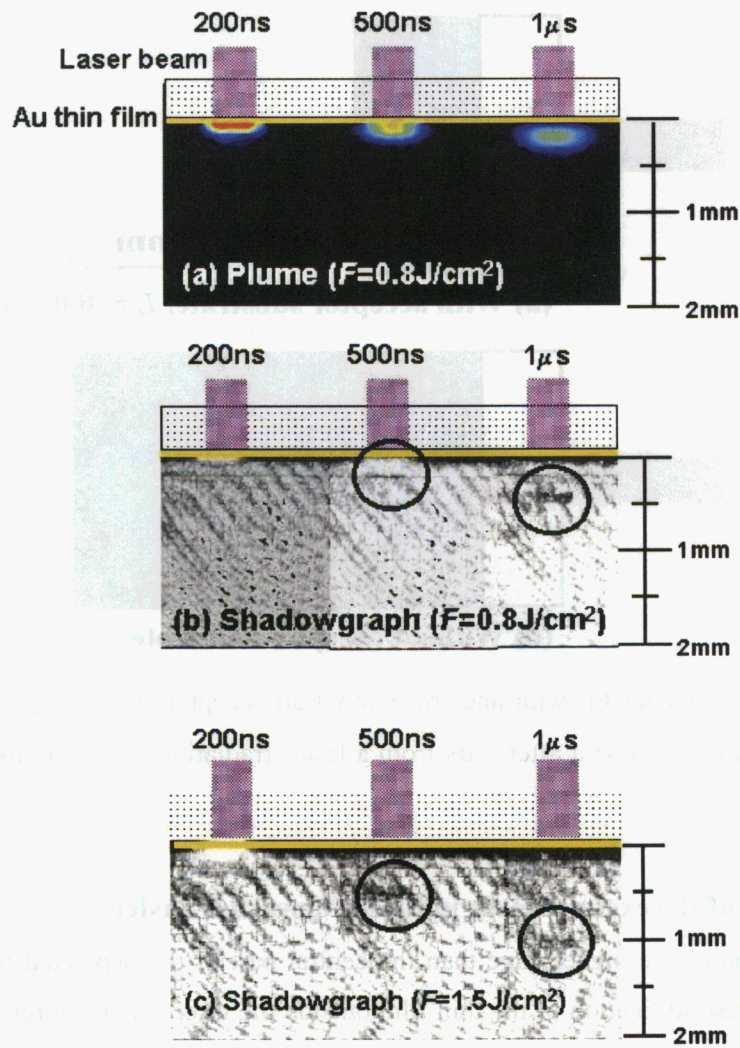
FIG. 2.23.   Position of the (a) plumes and shadowgraphs of transferring materials of Au (400 nm) at (b) optimum (0.8 J/cm^2) and (c) higher (1.5 J/cm^2) fluences.

(a) With acceptor substrate: $L = 300\ \mu m$

(b) Without acceptor substrate
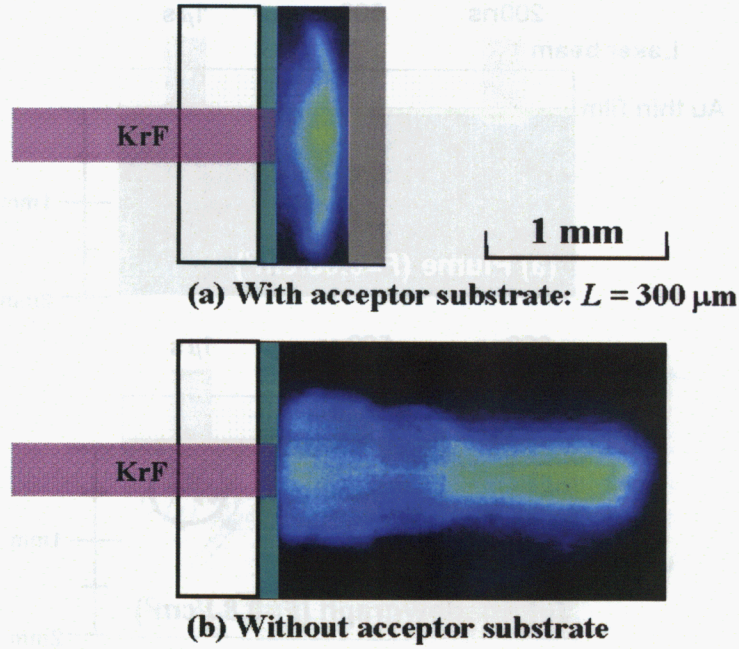
FIG. 2.24. Plume images (a) with and (b) without an acceptor substrate photographed using image intensified CCD camera after 3 μs from a laser irradiation. Ni (500 nm), $F = 2.0$ J/cm^2, gate time: 50 ns.

2.2.6 Process of the excimer laser induced forward transfer

The reason of the higher edge than the central part of the deposited pattern seems the melting and the resolidification of the thin film outside the laser irradiated region at $L = 0$. The extended length of the deposited pattern d_2 and the corresponding length of the removal region of the film d_3 are shown in FIG. 2.25 when the lateral length of the laser spot is varied. d_3 is larger than d_2 at each condition. Because the volume of the peeled thin film outside the laser irradiated region after deposition on the acceptor substrate, the height of the material increases due to the decrement of the lateral length on the substrate.

Based on the above-mentioned results, the excimer-LIFT process is described as shown in FIG. 2.26. FIGURE 2.26 (a) shows the state just after the laser irradiation. Thin film is melted, and evaporated, and the laser induced plume is generated followed by the laser pulse. FIGURE 2.26 (b) shows the removal process of the film. Pressure of the plume is exerted along the laser irradiation direction on the laser irradiated region. Thin film outside the laser irradiated region is influenced by the forces from the thin film inside the laser irradiated region and the surrounding film because the thin film is peeled. The directions of forces are perpendicular and lateral to the film plane from the thin film inside the laser irradiated region and the surrounding film,

48

respectively. Resultant force of these forces is exerted on the thin film outside the laser irradiated region. FIGURE 2.26 (c) shows the transfer process. Thin film inside and outside the laser irradiated region is transformed along the laser irradiation direction and at a constant angle, respectively. Therefore, the extended length of droplets increases with the increment of the distance between the film and the acceptor substrate.
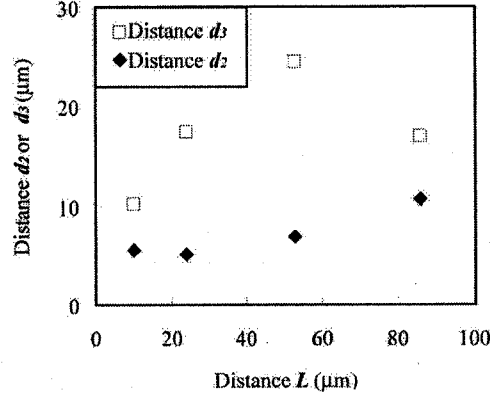
FIG. 2.25. Relationship between distance L and distance d_2 and d_3. Ni (230 nm), F = 1.7 J/cm^2, L = 0 μm.

2.2.7 Fabrication of micro wires

Micro Ni wires (10 mm x 200 μm) are fabricated using LIFT process as shown in FIG. 2.27(a). Deposition is performed twice at the same point. Resistances of wires are measured. Ratio of experimental resistance to theoretical resistance is shown in FIG. 2.28. Experimental resistance R of Ni wires is estimated using the following equation,

$$R = \rho \frac{L}{S} = \rho \frac{L}{Wd}.$$ (2.2)

where is ρ the resistivity (6.9x10^{-8} Ωm), L is the length, S is the cross section, W is the width, and d is the thickness of wires. Resistance of bulk Ni wire is calculated 5.1 Ω. As shown in FIG. 2.28, resistances of micro Ni wires fabricated using LIFT process is 5 – 15 times larger than the that of bulk. The values is similar to that fabricated using other direct writing method such as LCVD. The resistance might be reduced by annealing wires.

49
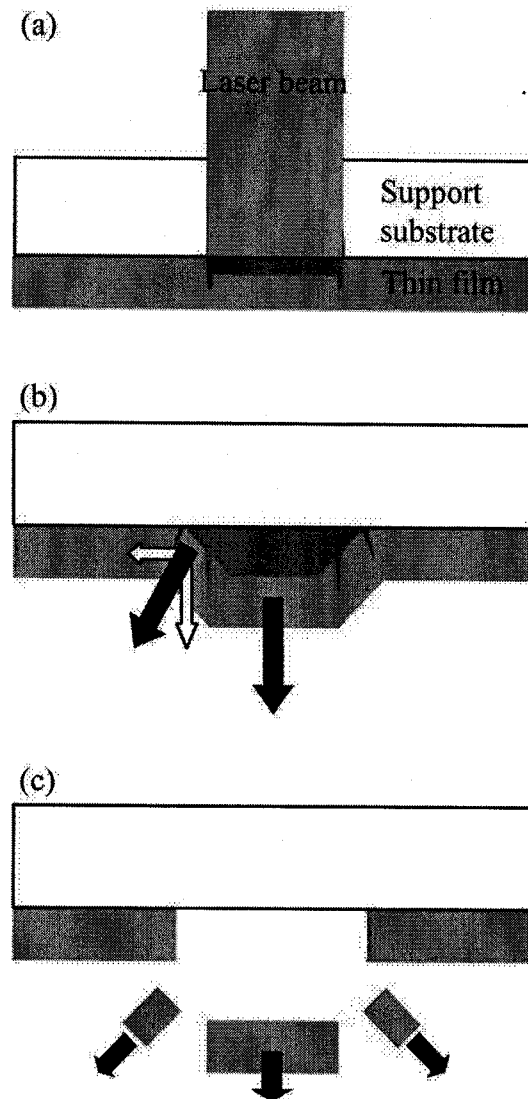
FIG. 2.26. Schematic illustration of removal process of thin film deposited on the supporting substrate under optimized deposition condition in the laser rear patterning.
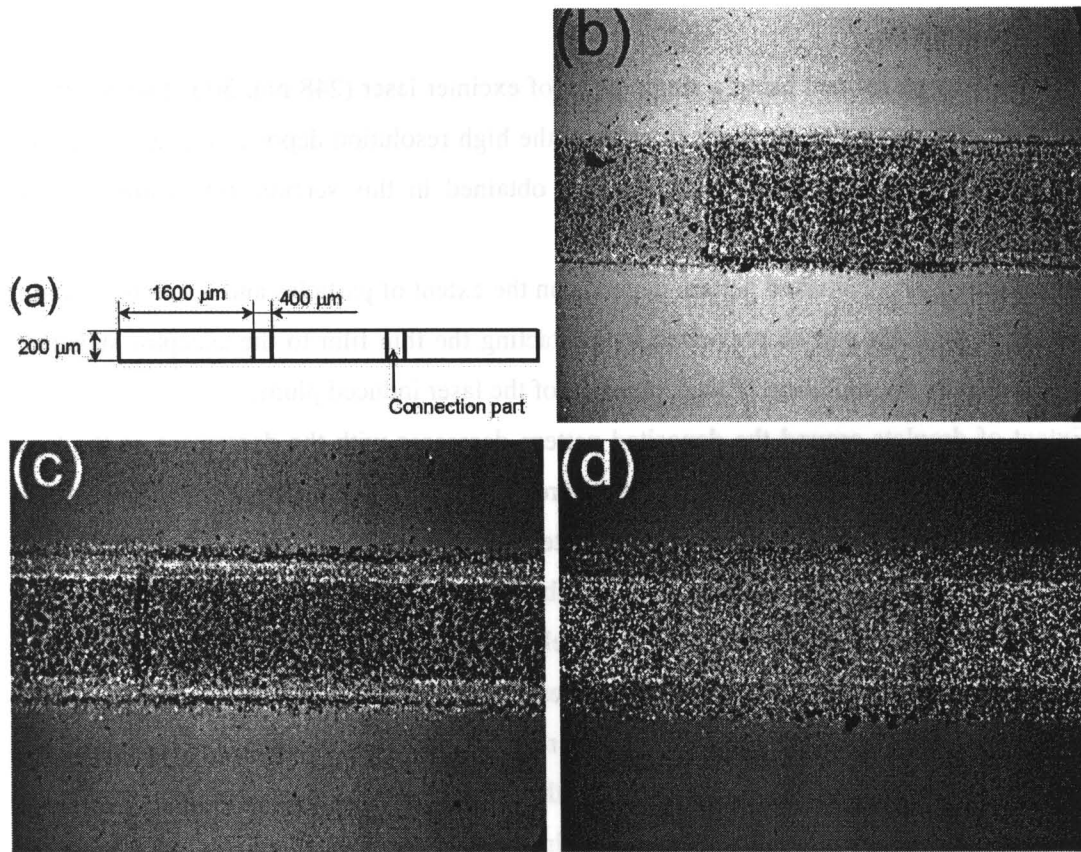
FIG. 2.27. Schematic illustration of micro Ni wires using LIFT process. Ni thin film (670 nm) was used. (b) $F = 1.5$ J/cm^2, $L = 10$ μm, (c) $F = 1.5$ J/cm^2, $L = 100$ μm, and (d) $F = 1.1$ J/cm^2, $L = 100$ μm.
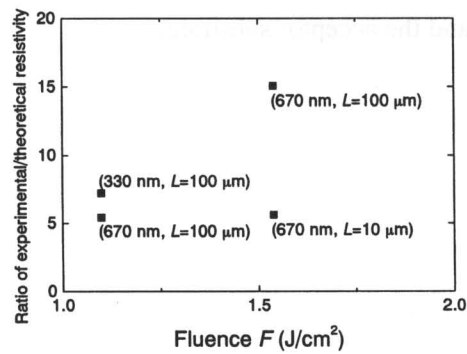
FIG. 2.28. Ratio of experimental resistance to theoretical resistance.

2.2.8 Conclusions

LIFT was performed using a single pulse of excimer laser (248 nm, 30 ns) with flat top profile of the laser intensity. Methods to achieve the high resolution deposition and mechanism of the Excimer-LIFT were considered. Results obtained in this section are summarized as follows;

1. Resolution of the deposited pattern depends on the extent of particles and droplets around it. Extent of particles can be prevented by contacting the thin film to the acceptor substrate. This is due to the inhibition of the expansion of the laser induced plume.

2. Extent of droplets around the deposited pattern decreases with the decrement of the laser spot size. This is due to the reduction of the area of the peeled thin film.

3. Extent of droplets around the deposited pattern also decreases with the decrement of the distance between the film and the acceptor substrate.

4. After the laser irradiation, the thin film is melted and evaporated. The laser induced plume is generated followed by the laser pulse. Pressure of the plume is exerted along the laser irradiation direction on the laser irradiated region. Thin film outside the laser irradiated region is influenced by the forces from the thin film inside the laser irradiated region and the surrounding film because the thin film is peeled. The directions of forces are perpendicular and lateral to the film plane from the thin film inside the laser irradiated region and the surrounding film, respectively. Resultant force of these forces is exerted on the thin film outside the laser irradiated region. Thin film inside and outside the laser irradiated region is transformed along the laser irradiation direction and at a constant angle, respectively. Therefore, the extended length of droplets increases with the increment of the distance between the film and the acceptor substrate.

2.3 Femtosecond laser induced forward transfer of thin metal films

2.3.1 Introduction

Ultrashort pulsed laser induced forward transfer of Cr [5,9,10-12], Pt [12], In_2O_3 [5,12,20,21] was previously investigated only by Zergioti *et al*. They used distributed-feedback dye-laser-based fs excimer laser system (wavelength: 248nm, pulse width: 500fs) and fabricated deposited patterns of sub-micron. These patterns were applied to diffractive structure, computer-generated holographic pattern [5,10-12], computer-generated multilevel structure [5], and microprinted grating [21]. Plume dynamics was also investigate [9].

Although fabrication of micropatterns and investigation of plume dynamics were performed, mechanism of Fs-LIFT is not understood. In this section, femtosecond laser induced forward transfer (Fs-LIFT) of thin Ni film is performed. Influences of laser irradiation conditions on the deposited pattern are systematically investigated. Laser induced plume is also observed. Based on these experimental results, mechanism of the Fs-LIFT is considered.

2.3.2 Experiments

2.3.2.1 Femtosecond laser

In this study, a femtosecond laser system (Spectra-Physics) described in Sec. 1.4 was used. Experimental setup is shown in FIG. 2.29. The beam diameter was magnified twice using a beam expander, and the central part of the magnified beam was cut by an aperture.
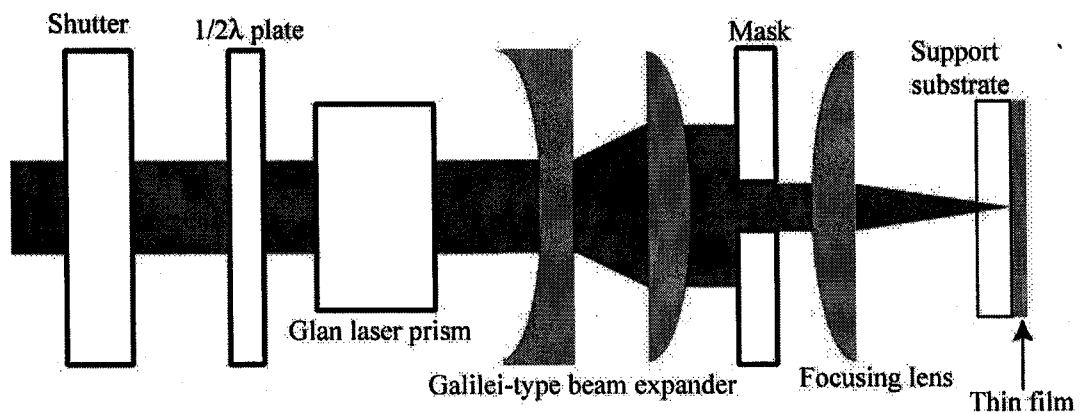
FIG. 2.29. Schematic illustration of the optics for fs-LIFT.

2.3.2.2 Sample preparations

Thin Ni film (thickness: 120 nm) on a quartz substrate was prepared by using an ion sputtering method. Si wafer was used as an acceptor substrate.

2.3.3 Characterization of deposited patterns
2.3.3.1 Influence of the film-substrate distance

Influences of the film-substrate distance are investigated. Deposited patterns obtained are shown in FIGs. 2.30 and 2.31. A circle in the figure indicates the laser spot size. The diameter of the aperture used is 5 mm. The appearance of a deposited pattern for $L = 0$ is quite different from that for $L \neq 0$.

The diameter of the deposited patter increases with the increment of the fluence for $L = 0$. This result is different from the case of the Excimer-LIFT. Droplets scatters around the deposited pattern for $L \neq 0$. The scattered length of droplets is independent on the laser fluence for the Fs-LIFT while it increases with the increment of the fluence for the Excimer-LIFT.

The appearance obtained using the Fs-LIFT process is quite different from the Excimer-LIFT. For the Excimer-LIFT, droplets around the deposited pattern come from the thin film around the laser irradiated region. For the Fs-LIFT, the diameter of the deposited pattern is smaller than the laser spot size for $L \neq 0$. This means droplets around the pattern come from the thin film inside the laser irradiated region.

Removed area of a thin film for the diameter of the aperture of 5 mm is shown in FIG. 2.32. Circles in the figure indicate the laser spot. The diameter of the removed area increases with the increment of the fluence. This result is agreement of the case of the deposited pattern shown in FIGs. 2.30 and 2.31.

Removed area of a thin film for the diameter of the aperture of 1 mm is shown in FIG. 2.33. Melted and resolidified-like region is observed around the removed area. The diameters of the deposited pattern, removed area for L = 0, that for the rear ablation, and that for the front ablation are shown in FIG. 2.34 as a function of the fluence. Each diameter increases with the increment of the fluence. The diameter of the removed area for the rear ablation is 4 – 7 times larger than that for the front ablation. This difference is caused by the existence of the plume. The diameter of the removed area for L = 0 is 3 – 7 μm larger than that for the rear ablation. This is due to the existence of the acceptor substrate.

	$F = 2.8 \ \mathrm{J/cm^2}$	$F = 1.5 \ \mathrm{J/cm^2}$
$L = 0 \ \mu\mathrm{m}$	(a) 50 μm	(e)
$L = 10 \ \mu\mathrm{m}$	(b)	(f)
$L = 50 \ \mu\mathrm{m}$	(c)	(g)
$L = 100 \ \mu\mathrm{m}$	(d)	(h)
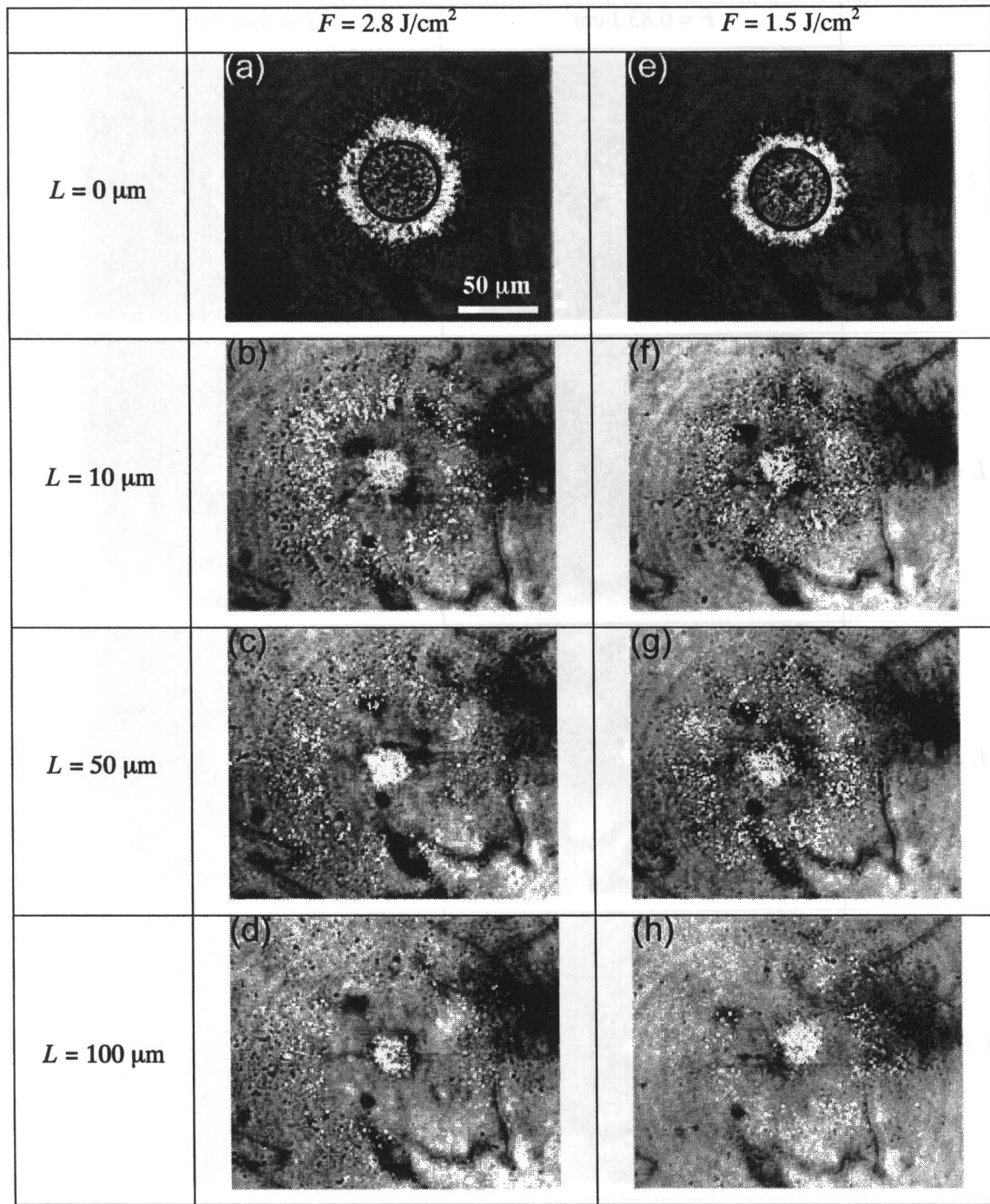
FIG. 2.30.   Optical microscope images of deposited patterns. Ni (120 nm), $F = 2.8$, 1.5 J/cm^2, L = 0, 10, 50, 100 μm, Mask diameter: 5 mm.

55

	$F = 0.83 \text{ J/cm}^2$	$F = 0.41 \text{ J/cm}^2$
$L = 0 \ \mu m$	(a) 50 μm	(e)
$L = 10 \ \mu m$	(b)	(f)
$L = 50 \ \mu m$	(c)	(g)
$L = 100 \ \mu m$	(d)	(h)

FIG. 2.31.   Optical microscope images of deposited patterns. Ni (120 nm), $F = 0.83$, 0.41 J/cm^2, $L = 0, 10, 50, 100 \ \mu m$, Mask diameter: 5 mm.

	$F = 2.8$ J/cm^2	$F = 1.5$ J/cm^2	$F = 0.41$ J/cm^2
$L = 0$ μm	(a)	(f)	(k) 50 μm
$L = 10$ μm	(b)	(g)	(l)
$L = 50$ μm	(c)	(h)	(m)
$L = 100$ μm	(d)	(i)	(n)
No acceptor substrate	(e)	(j)	(o)
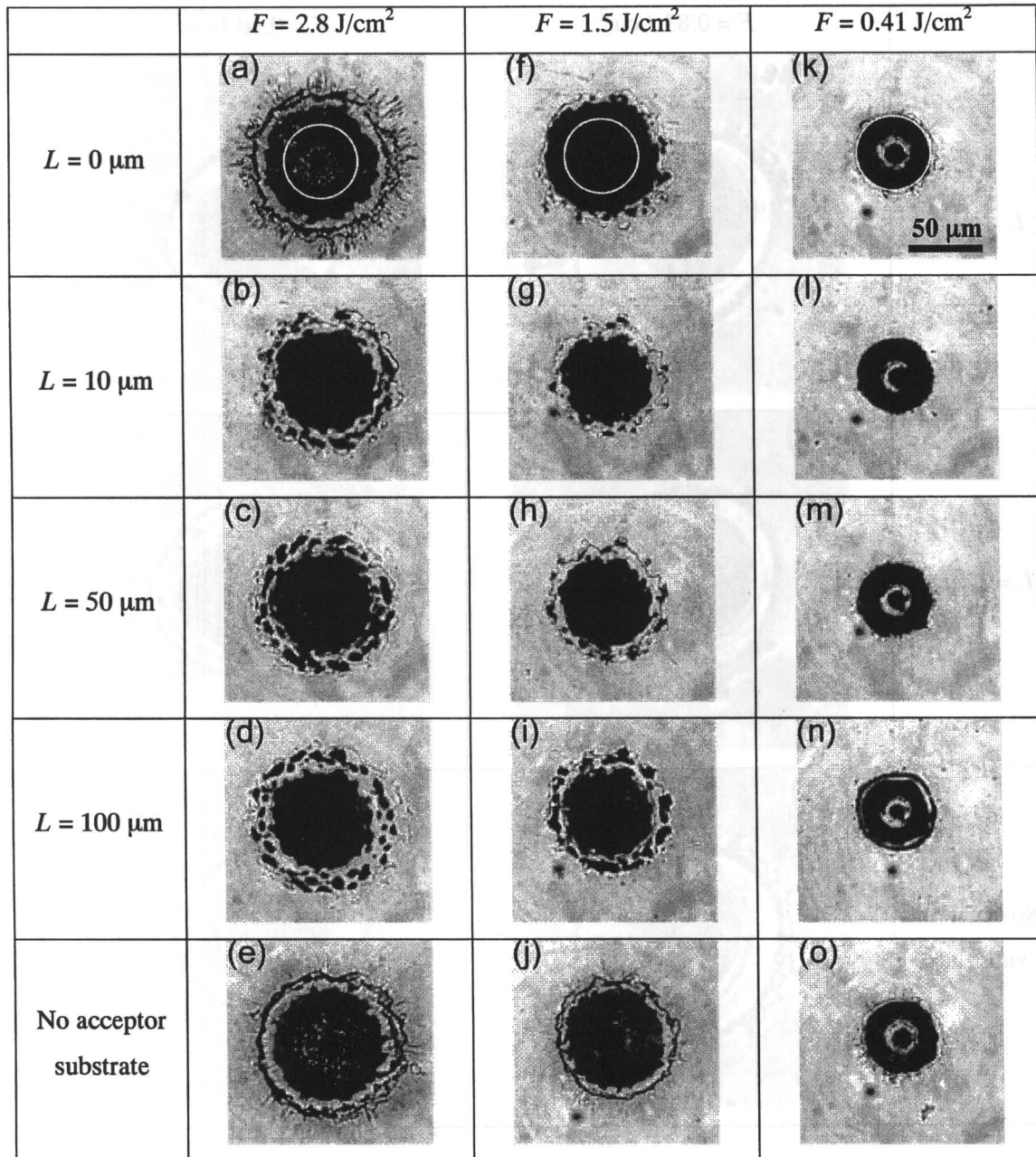
FIG. 2.32.   Optical microscope images of removal zone of thin films after fs-LIFT process. Ni (120 nm), $F = 2.8$, 1.5, 0.41 J/cm^2, $L = 0$, 10, 50, 100, 8 μm, Mask diameter: 5 mm.
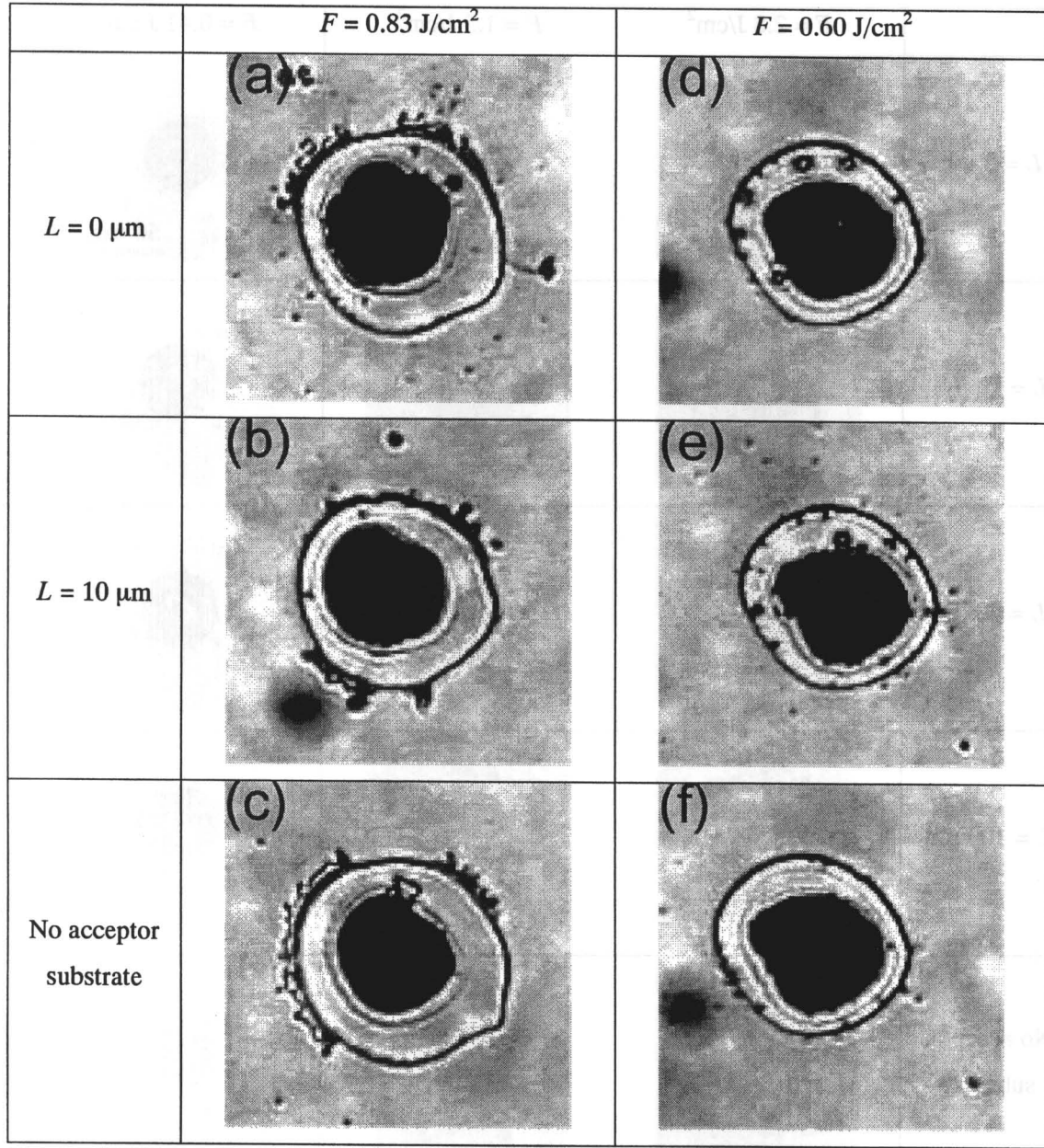
	$F = 0.83 \text{ J/cm}^2$	$F = 0.60 \text{ J/cm}^2$
$L = 0 \ \mu\text{m}$	(a)	(d)
$L = 10 \ \mu\text{m}$	(b)	(e)
No acceptor substrate	(c)	(f)

FIG. 2.30.   Optical microscope images of removal zone of thin films after fs-LIFT process. Ni (120 nm), $F = 0.83, 0.60 \text{ J/cm}^2$, $L = 0, 10, 8 \ \mu\text{m}$, Mask diameter: 1 mm.
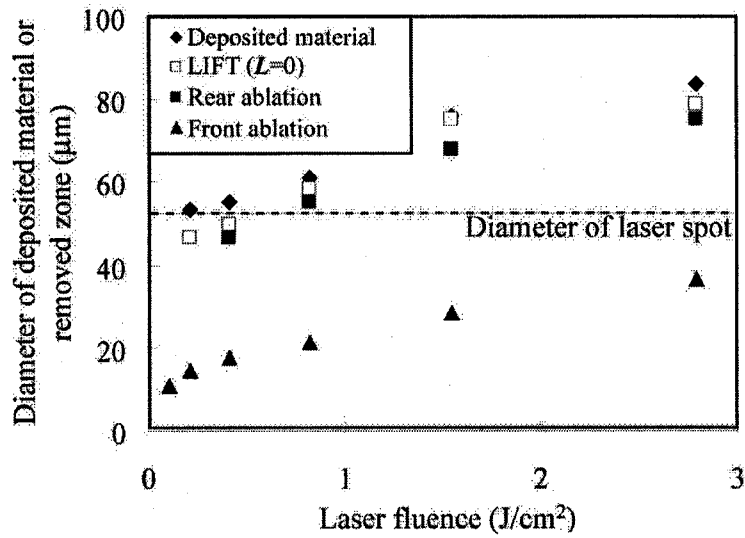
FIG. 2.34. Relationship between laser fluence and the diameter of the deposited patterns and removed zone. Ni (120 nm), Mask diameter: 5 mm.

2.3.3.2 Influence of the spatial distribution of the laser fluence

The difference of the appearance of deposited patterns obtained using the aperture diameter of 1 mm and 5 mm are compared in order to investigate the influence of the spatial distribution of the fluence. Optical microscopic images of deposited patterns are shown in FIG. 2.35. For the aperture diameter of 1 mm, the scatter of droplets is inhibited for $L \neq 0$. This phenomenon is not observed for the Excimer-LIFT. The main factor of this difference seems the difference of the laser intensity between the central part and the outside of the laser spot. The difference of the fluence in the same plane of the thin film causes the difference of the pressure originated from the ablation. This difference of the pressure causes the scatter of droplets.

	$F = 0.60 \text{ J/cm}^2$	$F = 0.41 \text{ J/cm}^2$
$L = 0 \ \mu\text{m}$	(a) 50 μm	(c)
$L = 10 \ \mu\text{m}$	(b)	(d)
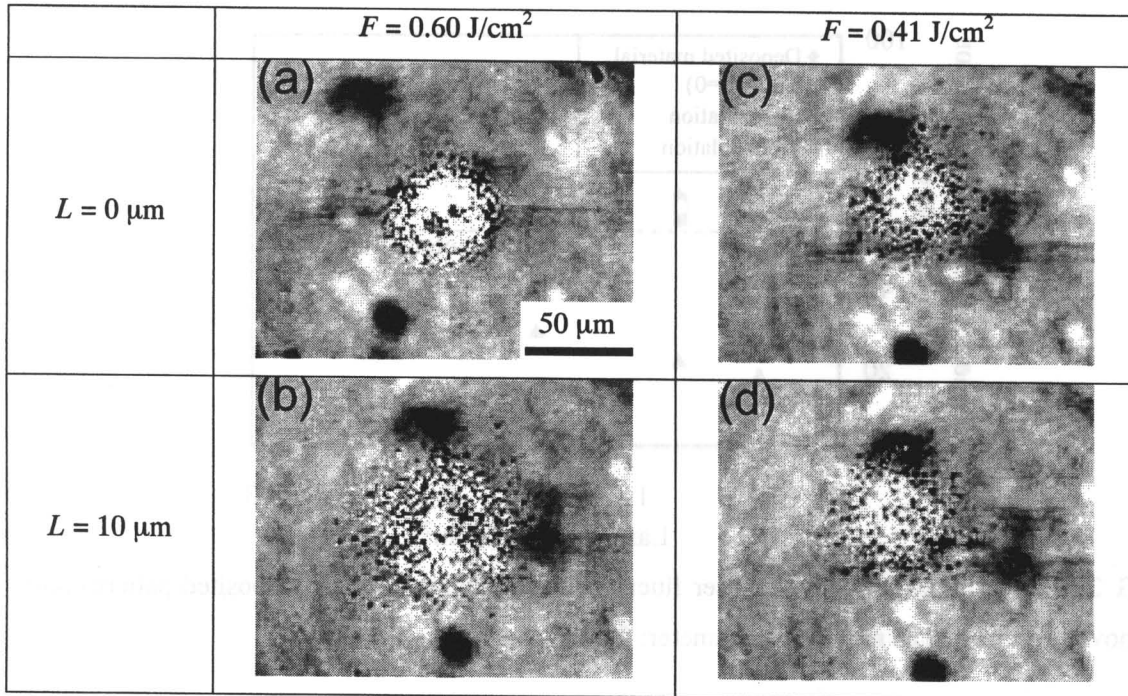
FIG. 2.35. Optical microscope images of deposited patterns. Ni (120 nm), $F = 0.60, 0.41 \text{ J/cm}^2$, $L = 0, 10 \ \mu\text{m}$, Mask diameter: 1 mm.

2.3.3.3 Scatter of microparticles

SEM images of deposited patterns are shown in FIGs. 2.36 and 2.37. Microparticles are observed for $L = 0$. This means the blowoff of the plume even for $L = 0$. However, the diameter of the scattered area of microparticles is smaller than that for the Excimer-LIFT at the same fluence for $L \neq 0$.

	$F = 1.5$ J/cm^2	$F = 0.41$ J/cm^2
L = 0 µm	(a) 200 µm	(e)
L = 10 µm	(b)	(f)
L = 50 µm	(c)	(g)
L = 100 µm	(d)	(h)
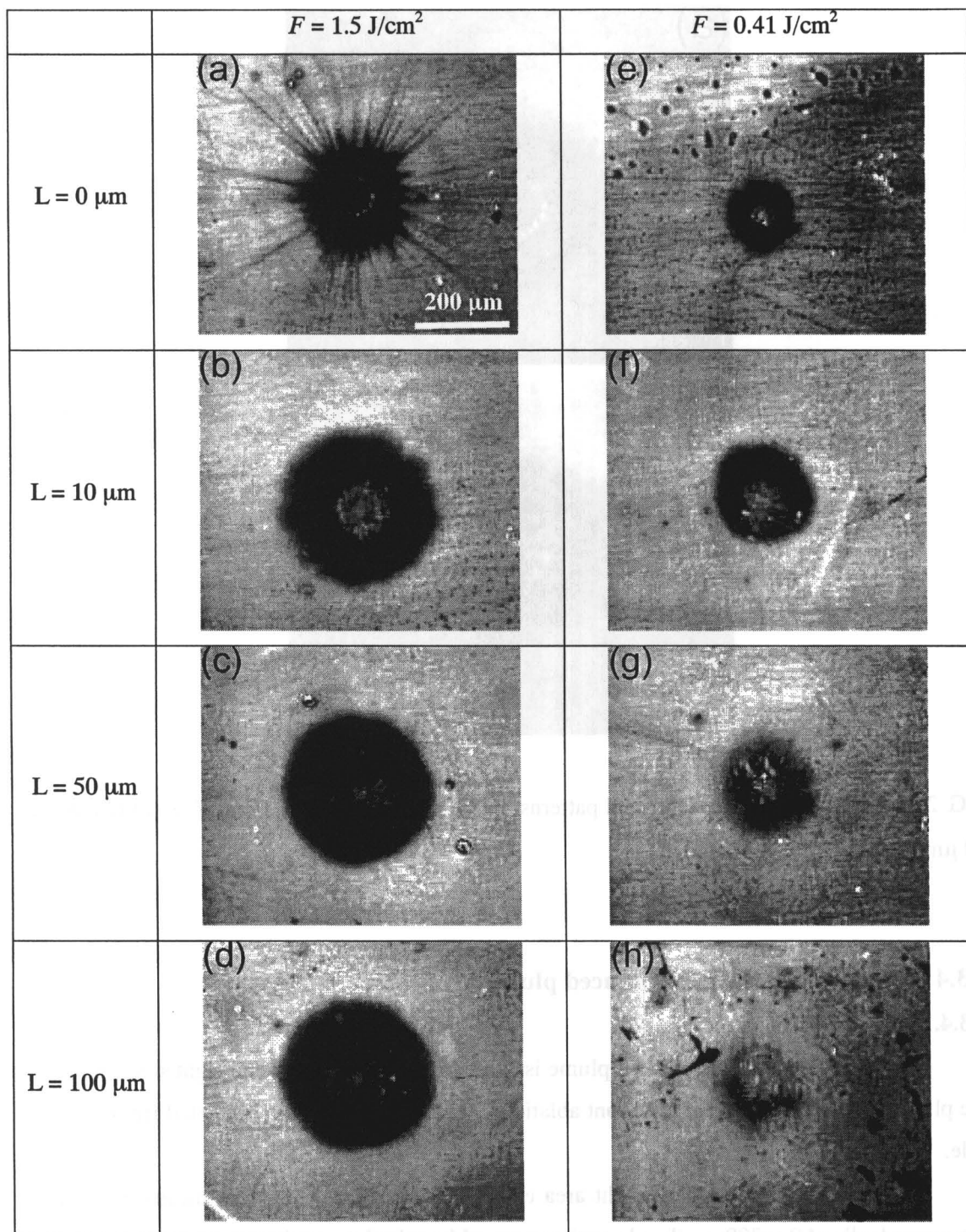
FIG. 2.36.   SEM images of deposited patterns. Ni (120 nm), $F = 1.5$, 0.41 J/cm$_2$, $L = 0$, 10, 50, 100 µm, Mask diameter: 5 mm.
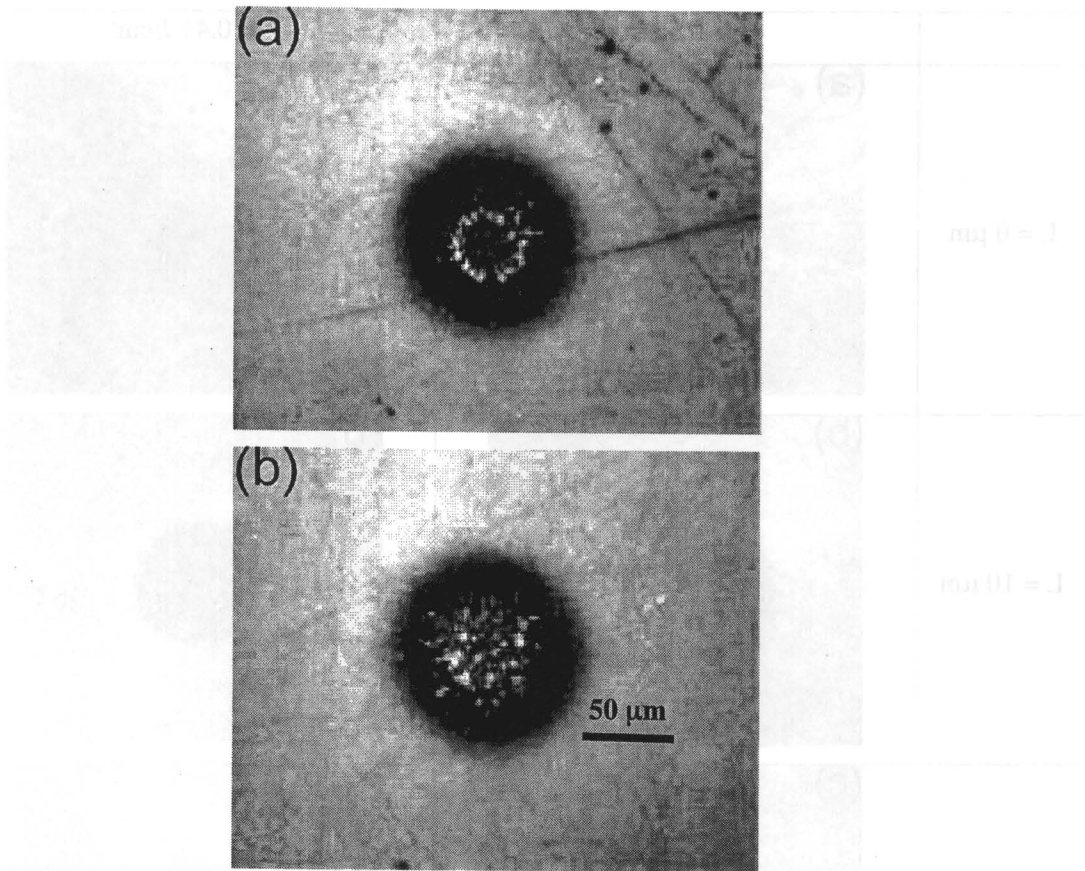
FIG. 2.37.   SEM images of deposited patterns. Ni (120 nm), F = 0.41 J/cm$_2$, L = (a) 0 and (b) 10 μm, Mask diameter: 1 mm.

2.3.4   Dynamics of the laser induced plume

2.3.4.1   Evolution of the plume

Evolution of the laser induced plume is shown in FIG. 2.38. Left and right sides indicate the plumes induced by the rear and front ablations, respectively. Laser is irradiated from the left side.

For the rear ablation, the bright area expands as the time goes. This means the plume grows gradually. After 300 ns, the plume is separated into the front and the back parts. The back part is brighter than the front part. For the front ablation, the plume decays gradually. The bright area for the rear ablation is smaller than that for the front ablation. Because the plume for the rear ablation is confined in the interface between the film and the supporting substrate, the plume can not be diffused immediately after the ablation. This causes the small bright area.

Delay time	Rear ablation	Front ablation
50 ns	(a)	(f)
100 ns	(b)	(g)
200 ns	(c)	(h)
300 ns	(d)	(i)
500 ns	(e)	(j)
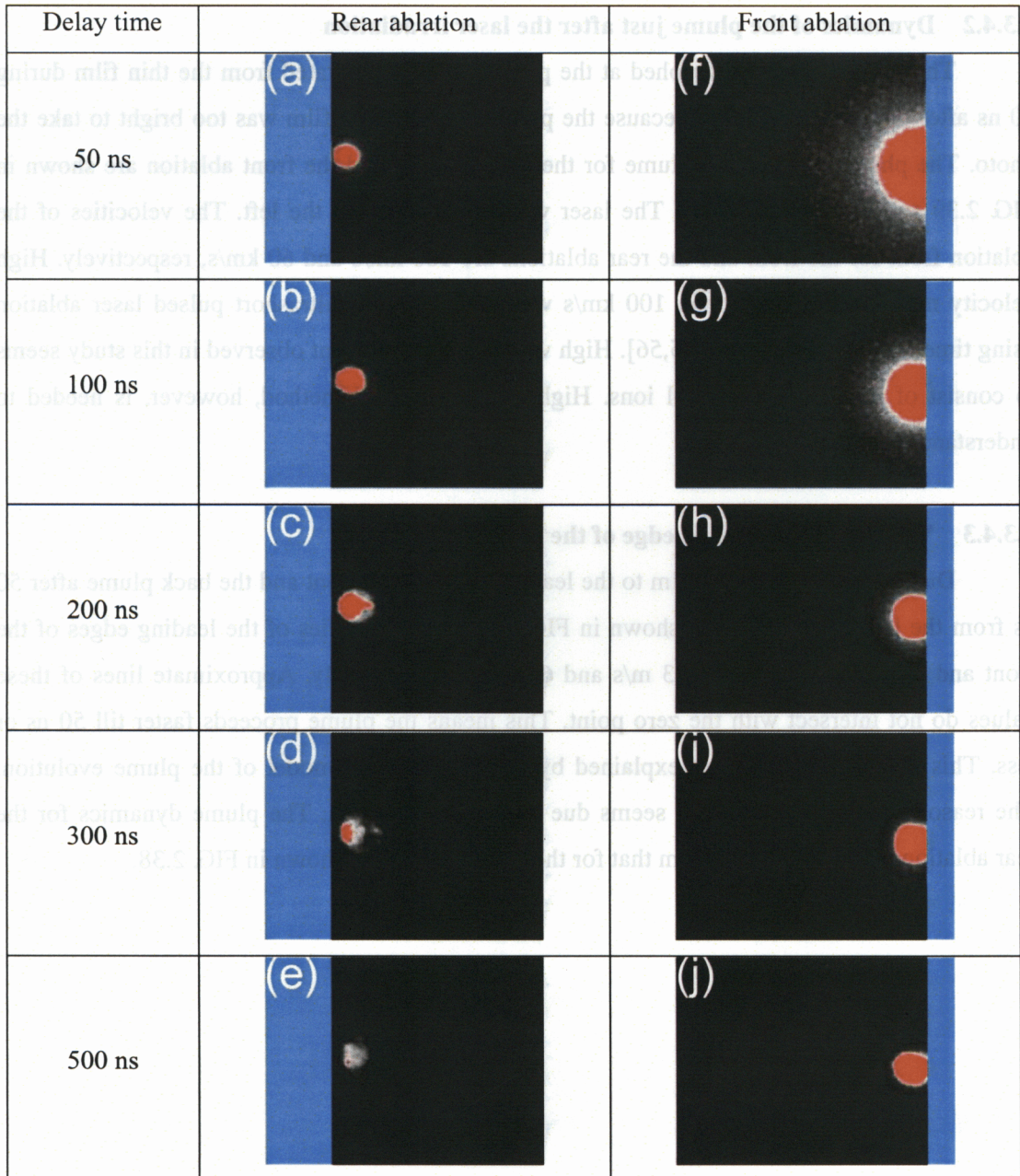
FIG. 2.38.   Plume dynamics of rear and front ablation of Ni (120 nm) films photographed using image intensified CCD camera. No mask, gate time: 50 ns, delay time: 50, 100, 200, 300, 500 ns. Rear ablation: $F = 3.5$ J/cm^2, Front ablation: $F = 5.5$ J/cm^2.

2.3.4.2 Dynamics of the plume just after the laser irradiation

The plume was photographed at the place which is separated from the thin film during 50 ns after the laser irradiation because the plume near the thin film was too bright to take the photo. The photographs of the plume for the rear ablation and the front ablation are shown in FIG. 2.39 and 2.40, respectively. The laser was irradiated from the left. The velocities of the ablation front for the front and the rear ablations are 160 km/s and 60 km/s, respectively. High velocity metal ion of more than 100 km/s was detected after ultrashort pulsed laser ablation using time-of-flight technique [55,56]. High velocity ablation front observed in this study seems to consist of high velocity metal ions. Higher time resolved method, however, is needed to understand this in more detail.

2.3.4.3 Velocity of the leading edge of the plume

Distances from the thin film to the leading edge of the front and the back plume after 50 ns from the laser irradiation are shown in FIG. 2.41. The velocities of the leading edges of the front and the back plume are 693 m/s and 68.3 m/s, respectively. Approximate lines of these values do not intersect with the zero point. This means the plume proceeds faster till 50 ns or less. This phenomenon can not explained by the conventional model of the plume evolution. The reason for this phenomenon seems due to the rear ablation. The plume dynamics for the rear ablation is quite different from that for the front ablation as shown in FIG. 2.38.

Distance from surface of thin film

0mm   1mm   2mm   3mm   4mm   5mm

Fluence=3.5J/cm^2

Fluence=1.8J/cm^2
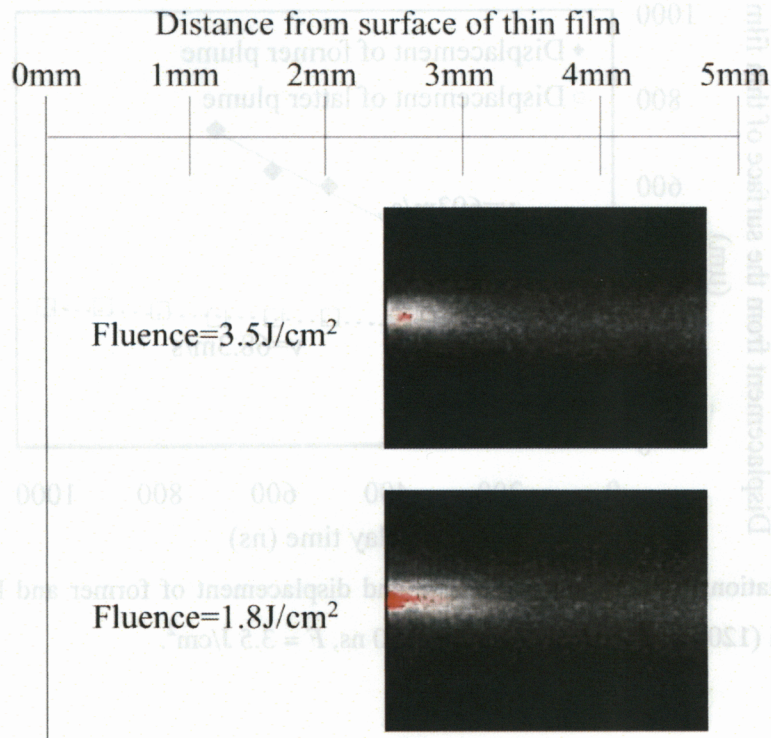
FIG. 2.39. Plume dynamics of rear ablation photographed using image intensified CCD camera. Ni (120 nm), gate time: 50 ns, delay time: 0 ns.

Distance from surface of thin film

8mm   7mm   6mm   5mm   4mm   3mm   2mm   1mm   0mm

Fluence=5.5J/cm^2
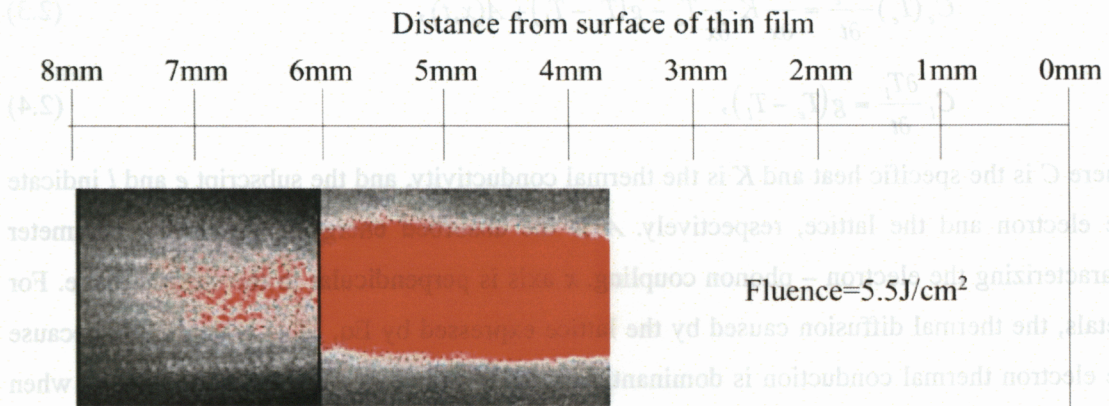
FIG. 2.40. Plume dynamics of front ablation photographed using image intensified CCD camera. Ni (120 nm), gate time: 50 ns, delay time: 0 ns.

65
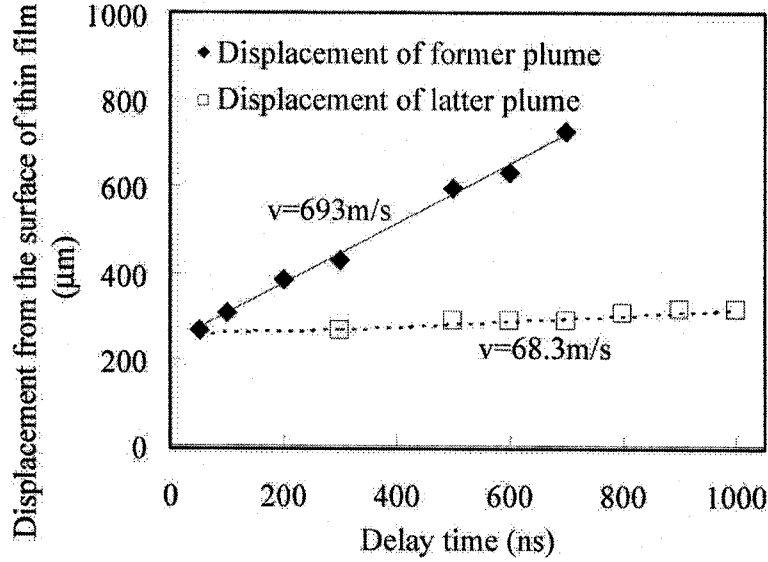
FIG. 2.41. Relationship between delay time and displacement of former and latter plume in rear ablation. Ni (120 nm), no mask, gate time: 50 ns, $F = 3.5$ J/cm^2.

2.3.5 Process of the femtosecond laser induced forward transfer

Two temperature model for the electron temperature T_e and lattice temperature T_l in a metal after the femtosecond laser irradiation is expressed by

$$C_e(T_e)\frac{\partial T_e}{\partial t} = \frac{\partial}{\partial x}K\frac{\partial}{\partial x}T_e - g(T_e - T_l) + A(x,t),$$ (2.3)

$$C_l\frac{\partial T_l}{\partial t} = g(T_e - T_l),$$ (2.4)

where C is the specific heat and K is the thermal conductivity, and the subscript e and l indicate the electron and the lattice, respectively. A is the absorbed energy and g is the parameter characterizing the electron – phonon coupling. x axis is perpendicular to the surface plane. For metals, the thermal diffusion caused by the lattice expressed by Eq. (2.4) is negligible because the electron thermal conduction is dominant. Eqs. (2.3) and (2.4) are coupled as follows when the electron – phonon coupling disappears;

$$C\frac{\partial T}{\partial t} = K\frac{\partial^2 T}{\partial x^2} + A(x,t).$$ (2.5)

Temperature increment ΔT in a metal when the laser with the fluence of F_{abs} is irradiated on the metal surface is obtained by resolving the Eq. (2.5) using the Dirac delta function as follows;

66

$$\Delta T = T - T_0 = \frac{F_{abs}}{C\sqrt{\pi Dt}} \exp\left(\frac{-z^2}{4Dt}\right),$$ (2.6)

where D is the thermal diffusivity. The absorbed laser energy is diffused in a region of the thermal diffusion length of $L = \sqrt{D\tau}$, where τ is the laser pulse width. For the femtosecond laser ablation of thin metal film, the threshold fluence depends on the relationship between the film thickness d and the electron diffusion length L_c. L_c is expressed by Eq. (2.7).

$$L_c = \sqrt{\frac{2K_{e,0}}{A_e T_l} \tau_R} = \left(\frac{128}{\pi}\right)^{\frac{1}{8}} \left(\frac{K_{e,0}^2 C_l}{A_e T_m g^2}\right)^{\frac{1}{4}},$$ (2.7)

where A_e is the specific heat constant, τ_R is the relaxation time between the electron and the lattice, and T_m is the melting temperature. For $d < L_c$, the threshold fluence for the melting and the evaporation is proportional to d. For $d > L_c$, the threshold fluence is independent of d. $L_c = $ 31 nm for Ni is obtained by substituting values listed in Table 2.2 into Eq. (2.7).

TABLE 2.2. Physical properties of Ni.

g (W/m^{3}K)	3.6×10^{17}
A_e (J/m^{3}K^2)	1065
$K_{e,0}$ (W/Km)	91
C_l (J/m^{3}K)	4.1×10^6
T_m (K)	1728

Film thickness of Ni used in this study was 120 nm. The laser energy is absorbed in the region from the surface to 31 nm deep. The opposite side of the film remains solid state when the heated side begins to ablate. Therefore, the plume is confined in the interface between the solid-film and the supporting substrate. Thus, the temperature gradient in the metal film for the femtosecond laser seems larger than that for the excimer laser.

Based on the above-mentioned results, the process of the Fs-LIFT is proposed as shown in FIG. 2.42. FIGUREs 2.42 (a) and (c) show the case for the larger difference of the laser intensity between the central and the edge parts of the laser beam and FIGUREs 2.42 (b) and (d) show the case for the smaller one. The larger difference of the laser intensity in the laser beam causes the wider scattered area of droplets.
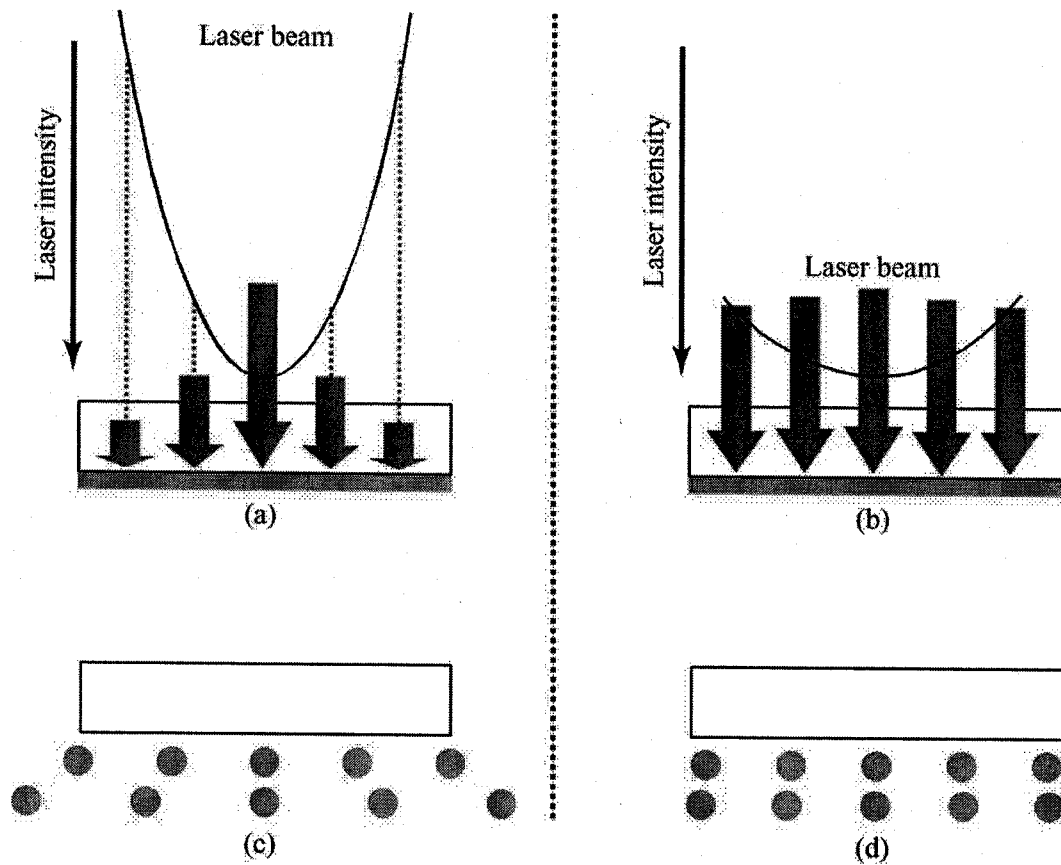
FIG. 2.42.   Illustration of removal process of thin film in fs-LIFT process. (a), (c) Irradiation of the whole Gaussian laser beam, and (b), (d) Irradiation of the center part of Gaussian laser beam. (a), (c) Laser irradiation, (b), (d) Removal of thin film.

2.3.6 Conclusions

LIFT of thin Ni film was performed using a femtosecond laser (wavelength: 800 nm, pulse width: 120 fs) with the Gaussian profile of the laser intensity. Influences of laser irradiation conditions on the deposited pattern were systematically investigated. Laser induced plume was also observed. Based on these experimental results, methods to achieve the high resolution deposition and mechanism of the Fs-LIFT were considered. Results obtained in this section are summarized as follows;

1. High-resolution deposition of patterns using the Fs-LIFT method is achieved when the difference of the laser intensity between the central and the edge parts of the laser beam is small.

2. For the Fs-LIFT, scatter of microparticles is inhibited because the plume is generated after the whole laser pulse.

3. The laser energy is absorbed in the region from the surface to 31 nm deep. Film thickness of Ni used in this study was 120 nm. The opposite side of the film remains solid state when the heated side begins to ablate. Therefore, the plume is confined in the interface between the solid-film and the supporting substrate. Thus, the temperature gradient in the metal film for the femtosecond laser seems larger than that for the excimer laser. The larger difference of the laser intensity in the laser beam causes the wider scattered area of droplets.

2.4 Conclusions

In this chapter, laser induced forward transfers of thin metal films using a single pulse of excimer laser (wavelength: 248 nm, pulse width: 30 ns) with the flat-top profile of the laser intensity (Excimer-LIFT) and femtosecond laser (wavelength: 800 nm, pulse width: 120 fs) with the Gaussian profile (Fs-LIFT) were described. The purpose was to achieve the high-resolution deposition of micropatterns. Results obtained in this study are summarized as follows;

1. For Excimer-LIFT, high-resolution deposition of micropattern is achieved when the thin film contacts with the acceptor substrate to prevent the scatter of droplets and the laser spot size is small to inhibit the scatter of microparticles. For Fs-LIFT, it is achieved when the fluence is low to prevent the scatter of droplets and the difference of the laser intensity in the laser beam is small to inhibit the scatter of microparticles.

2. The different point between the Excimer-LIFT and the Fs-LIFT processes is the absorption of the laser energy from the laser induced plume. For the Excimer-LIFT, the ablation occurs during the laser pulse and the laser induced plume is generated. The plume is heated by absorbing the latter part of the laser pulse. The scatter of microparticles expands as a result of the growth of the plume due to the evaporation of the deposited pattern. For the Fs-LIFT, on the other hand, the growth of the plume depends only on the fluence because the ablation occurs after the whole laser pulse and the laser energy is not absorbed by the plume. Therefore, the scatter of microparticles is prevented.

3. Scatter of droplets depends on the melted area outside the laser irradiated region in the thin film for the Excimer-LIFT and the difference of the laser intensity in the laser beam for the Fs-LIFT.

4. The Fs-LIFT is a powerful tool to achieve the high-resolution micropatterning of metals when the thin film does not contact with the acceptor substrate.

References in Chapter 2

[1]   A. Piqué and D. B. Chrisey, *Direct-write technologies for rapid prototyping applications*, (Academic Press, San Diego, 2002).

[2]   J. Bohandy, B. F. Kim, and F. J. Adrian, J. Appl. Phys. 60, 1538 (1986).

[3]   V. Schltze and M. Wagner, Appl. Phys. A 53, 241 (1991).

[4]   V. Schltze and M. Wagner, Appl. Surf. Sci. 52, 303 (1991).

[5]   I. Zergioti, S. Mailis, N. A. Vainos, P. Papakonstantinou, C. Kalpouzos, C. P. Grigoropoulos, and C. Fotakis, Appl. Phys. A 66, 579 (1998).

[6]   I. Zergiote, S. Mailis, N. A. Vainos, C. Fotakis, S. Chen, and C. P. Grigoropoulos, Appl. Surf. Sci. 127-129, 601 (1998).

[7]   P. Mogyorósi, T. Szörényi, K. Bali, Zs. Tóth, and I. Hevese, Appl. Surf. Sci. 36, 157 (1989).

[8]   Z. Kántor, Z. Tóth, T. Szörényi, Appl. Phys. A 54, 170 (1992).

[9]   D.G. Papazoglou, A. Karaiskou, I. Zergioti, and C. Fotakis, Appl. Phys. Lett. 81, 1594-1596 (2002).

[10]   I. Zergioti, S. Mailis, N. A. Vainos, C. Fotakis, S. Chen, and C. P. Grigoropoulos, Appl. Surf. Sci. 127-129, 601-605 (1998).

[11]   I. Zergioti, S. Mailis, N. A. Vainos, A. Ikiades, C.P. Grigoropoulos, and C. Fotakis, Appl. Surf. Sci. 138-139, 82-86 (1999).

[12]   P. Papakonstantinou, N. A. Vainos, and C. Fotakis, Appl. Surf. Sci. 151, 159-170 (1999).

[13]   H. Esrom, J. Y. Zhang, U. Kogelschatz, and A. J. Pedraza, Appl. Surf. Sci. 86, 202 (1995).

[14]   Z. Tóth, T. Szörényi, and A. L. Tóth, Appl. Surf. Sci. 69, 317 (1993).

[15]   Z. Kántor, Z. Tóth, T. Szörényi, and A. L. Tóth, Appl. Phys. Lett. 64, 3506 (1994).

[16]   Z. Kántor, and T. Szörényi, J. Appl. Phys. 78, 2775 (1995).

[17]   Z. Kántor, Z. Tóth, and T. Szörényi, Appl. Surf. Sci. 86, 196-201 (1995).

[18]   T. Szörényi and Z. Tóth, Appl. Phys. A 52, 273 (1991).

[19]   E. Fogarassy and C. Fuchs, J. Appl. Phys. 66, 457-459 (1989).

[20]   I. Zergioti, D. G. Papazoglou, A. Karaiskou, N. A. Vainos, and C. Fotakis, Appl. Surf. Sci. 197-198, 868-872 (2002).

[21]   G. Koundourakis, C. Rockstuhl, D. Papazoglou, A. Klini, I. Zergioti, N. A. Vainos, and C. Fotakis, Appl. Phys. Lett. 78, 868-870 (2001).

[22]   S. M. Pimenov, G. A. Shafeev, A. A. Smolin, V. I. Konov, and B. K. Vodolaga, Appl. Surf. Sci. 86, 208-212 (1995).

[23] Y. Nakata, T. Okada, and M. Maeda, Jpn. J. Appl. Phys. 41, L839-L841 (2002).

[24] T. Mito, T. Tsujita, H. Masuhara, N. Hayashi, and K. Suzuki, Jpn. J. Appl. Phys. 40, L805-L806 (2001).

[25] T. Sameshima, Appl. Surf. Sci. 96-98, 352-358 (1996).

[26] F. J. Adrian, J. Bohandy, B. F. Kim, A. N. Jette, and P. Thompson, J. Vac. Sci. Technol. B 5, 1490 (1987).

[27] R. J. Baseman and N. M. Frogerg, Appl. Phys. Lett. 55, 1841 (1989).

[28] R. J. Baseman, N. M. Froberg, J. C. Andreshak, and Z. Schlesinger, Appl. Phys. Lett. 56, 1412 (1990).

[29] R. J. Harrach, J. Appl. Phys. 48, 2370 (1977).

[30] A. Piqué, D. B. Chrisey, R. C. Y. Auyeung, J. Fitz-Gerald, H. D. Wu, R. A. McGill, S. Lakeou, P. K. Wu, V. Nguyen, and M. Duignan, Appl. Phys. A 69, S279-S284 (1999).

[31] D. B. Chrisey, Science 289, 879-881 (2000).

[32] D. B. Chrisey, A. Piqué, R. Modi, H. D. Wu, R. C. Y. Auyeung, H. D. Young, Appl. Surf. Sci. 168, 345-352 (2000).

[33] D. B. Chrisey, A. Piqué, J. Fitz-Gerald, R. C. Y. Auyeung, R. A. McGill, H. D. Wu, and M. Duignan, Appl. Surf. Sci. 154-155, 593-600 (2000).

[34] A. Piqué, D. B. Chrisey, J. M. Fitz-Gerald, and R. A. McGill, R. C. Y. Auyeung, H. D. Wu, S. Lakeou, V. Nguyen. R. Chung, and M. Duignan, J. Mater. Res. 15, 1872-1875 (2000).

[35] D. Young, H. D. Wu, R. C. Y. Auyeung, R. Modi, J. Fitz-Gerald, A. Piqué, D. B. Chrisey, P. Atanassova, and T. Kodas, J. Mater. Res. 16, 1720-1725 (2001).

[36] A. Piqué, R. C. Y. Auyeung, J. L. Stepnowski, D. W. Weir, C. B. Arnold, R. A. McGill, and D. B. Chrisey, Surf. Coat. Technol. 163-164, 293-299 (2003).

[37] A. Piqué, R. C. Y. Auyeung, J. L. Stepnowski, D. W. Weir, C. B. Arnold, R. A. McGill, and D. B. Chrisey, J. Mater. Res. 16, 3214-3233 (2001).

[38] P. K. Wu, B. R. Ringeisen, J. Callahan, M. Brooks, D. M. Bubb, H. D. Wu, A. Piqué, B. Spargo, R. A. McGill, and D. B. Chrisey, Thin Solid Films 398-399, 607-614 (2001).

[39] B. R. Ringeisen, D. B. Chrisey, A. Piqué, H. D. Young, R. Modi, M. Bucaro, J. Jones-Meehan, and B. J. Spargo, Biomaterials 23, 161-166 (2002).

[40] J. M. Fitz-Gerald, A. Piqué, D. B. Chrisey, P. D. Rack, M. Zeleznik, R. C. Y. Auyeung, and S. Lakeou, Appl. Phys. Lett. 76, 1386-1388 (2000).

[41] D. Young, R. C. Y. Auyeung, A. Piqué, D. B. Chrisey, and D. D. Dlott, Appl. Phys. Lett. 78, 3169-3171 (2001).

[42] D. Young, R. C. Y. Auyeung, A. Piqué, D. B. Chrisey, and D. D. Dlott, Appl. Surf. Sci.

197-198, 181-187 (2002).

[43] T. E. Itina, L. V. Zhigilei, and B. J. Garrison, Nucl. Instrum. Meth. B 180, 238-244 (2001).

[44] I. Y. S. Lee, W. A. Tolbert, D. D. Dlott, M. M. Doxtander, D. M. Foley, D. R. Arnold, E. W. Ellis, J. Imaging Sci. Techn. 36, 180-187 (1992).

[45] W. A. Tolbert, I. Y. S. Lee, M. M. Doxtader, E. W. Ellis, and D. D. Dlott, J. Imaging Sci. Techn. 37, 411-421 (1993).

[46] D. E. Alexander, G. S. Was, and F. J. Mayer, J. Mater. Sci. 23, 2182-2186 (1988).

[47] T. Sano, T. Nakayama, H. Yamada, and I. Miyamoto, Appl. Surf. Sci. 186, 221-226 (2002).

[48] T. Sano, I. Miyamoto, H. Hayashi, and H. Ochi, Proc. SPIE 3933, 356-364 (2000),

[49] T. Sano and I. Miyamoto, Proc. SPIE 4088, 401-404 (2000).

[50] T. Sano, H. Yamada, T. Nakayama, and I. Miyamoto, Proc. SPIE 4426, 70-73 (2001).

[51] P. L. G. Ventzek, R. M. Gilgenbach, J. A. Sell, and D. M. Heffelfinger, J. Appl. Phys. 68, 965 (1990).

[52] H. Yamada, T. Sano, T. Nakayama, and I. Miyamoto, Appl. Surf. Sci. 197-198, 411-415 (2002).

[53] E. Matthias, M. Reichling, J. Siegel, O. W. Kading, S. Petzoldt, H. Skurk, P. Bizenberger, and E. Neske, Appl. Phys. A 58, 129-136 (1994).

[54] Z. Tóth, B. Hopp, Z. Kántor, F. Ignacz, T. Szörényi, and Z, Bor, Appl. Phys. A 60, 431-436 (1995).

[55] R. Stoian, H. Varel, A. Rosenfeld, D. Ashkenasi, R. Kelly, and E. E. B. Campbell, Appl. Surf. Sci. 165, 44-55 (2000).

[56] S. Amoruso, X. Wang, C. Altucci, C. de Lisio, M. Armenante, R. Bruzzese, N. Spinelli, and R. Velotta, Appl. Surf. Sci. 186, 358-363 (2002).

[57] E. G. Gamaly, Phys. Fluids B 5, 944-949 (1993).

[58] E. D. Palik, in *Handbook of optical constants of solids*, (Academic Press, Orland, 1985).

[59] O. Agyeman, Jpn. J. Appl. Phys. 41, 666-669 (2002).

[60] F. J. Mayer and G. E. Busch, J. Appl. Phys. 57, 827-829 (1985).

[61] A. B. Bullock, P. R. Bolton, and F. J. Mayer, J. Appl. Phys. 82, 1828-1831 (1997).

[62] A. B. Bullock and P. R. Bolton, J. Appl. Phys. 85, 460-465 (1999).

[63] Y. Nakata and T. Okada, Appl. Phys. A 69, S275-S78 (1999).

[64] S. S. Wellershoff, J. Hohlfeld, J. Güdde, and E. Matthias, Appl. Phys. A 69, S99-S107 (1999).

[65] P. A. Atanasov, N. N. Nedialkov, S. E. Imamova, A. Ruf, H. Hügel, F. Dausinger, and P. Berger, Appl. Surf. Sci. 186, 369-373 (2002).

Chapter 3

Femtosecond laser fabrication of microspike-arrays for micro field-emitter on tungsten surface

Microspike-arrays were fabricated by irradiating the femtosecond laser on the tungsten surface through the mask opening in air with the aim of fabricating the micro field emitter for the field emission display using only the femtosecond laser. Natural logarithm of the calculated intensity distributions diffracted at the edge of the mask opening was qualitatively consistent with the experimental results of the shape and arrays of microspikes. The ability of the field emission of microspike arrays was evaluated. This method can be powerful tool to fabricate the field emitter.

3.1 Introduction

3.1.1 Laser induced surface microstructure

Laser Induced Periodic Surface Structure (LIPSS) was first discovered by Emmony *et al.* in 1973 [1]. The mechanism of this phenomena was suggested due to the interference of the scattered light with the cavity radiation because the damage of the Ge output mirror of TEA CO_2 laser showed the periodicity of 10.6 μm as the same as the laser wavelength. After that, the LIPSS for metals (Ni_xP_{1-x} [3], Al [6,9,11], Fe [14]), semiconductors (Si [4,5,7,11,15], GaAs [7], Ge [8,9,12]), polymers (acrylic resin [2], polyethersulfone film [13]), SiO_2 [2], glass [11], and Diamond [16] were investigated using different kind of lasers such as CO_2 laser [2,3], Nd:YAG laser [4,8,11,12,14], second harmonic Nd:YAG laser [9,11], high poser picosecond Nd:YAG laser [7], XeCl excimer laser [13,15], and femtosecond laser [16]. Theoretical work was also performed [10]. The LIPSS was considered to be developed as a result of the interaction between the incident laser front and the surface scattered light which grows exponentially. For the linear polarization of the laser, the LIPSS is formed perpendicular to the electric field vector. The spacing of the LIPSS is nearly equal to $\lambda/(1 \pm \sin \theta)$ where θ is the incident angle and λ is the laser wavelength.

Larger surface structure than the LIPSS can also be fabricated as a result of the laser irradiation on the solid surface. Kawakami *et al.* discovered the self-assembled microcones with the size of about 150 nm around the laser irradiated surface irradiating the nanoseconds Nd:YAG laser on the single crystalline tungsten [17-21]. The cones are arrayed hexagonally or square, which can not be explained by the LIPSS formation theory. Tungsten microcones with the aspect ratio of more than 6 were fabricated by the laser irradiation in an inert gas atmosphere. Radius of curvature of less than 100 nm was achieved by the chemical etching of the microcone with the radius of curvature of about 750 nm. Pedraza *et al.* fabricated the array of Si microcolumns irradiating the KrF excimer laser on the Si surface in mainly SF_6 atmosphere [22-32]. These microcolumns grow rapidly by a number of pulses, and the growth slows down after the number. Her *et al.* reported the development of the array of sharp conical microspikes when the femtosecond laser (100 fs, 1 J/cm^2) was irradiated on the Si surface in SF_6 or Cl_2 of 500 Torr [33,34]. Chemical reactions were suggested to be necessary to this formation because the microspikes were not formed in N_2 and Ne atmospheres and vacuum. Shen *et al.* of the same group fabricated the regular array of Si microspikes irradiating the femtosecond laser on the Si surface covered with the periodic mask [35]. This regulation was considered to be caused by the capillary wave of molten Si formed by the Fresnel diffraction of the laser through the mask aperture because the microspikes were arrayed irregularly without the mask. Fabrication of

surface microstructure for polyimide [36], $YBa_2Cu_3O_{7-x}$ [37], Si [38,40], and Co [39] were also reported.

3.1.2 Field emission display

Field emission display (FED) is considered to have many advantages as a thin display, and is expected to replace by CRT, LCD, and PDP as a future display.

FED is the device which displays the light emitted from the phosphor which is irradiated by the accelerated electron. The structure of FED is shown in FIG. 3.1 [41]. The spacing between the cathode and the anode substrates is from 200 μm to millimeters. Gate lines and the orthogonal emitter lines are formed on the cathode substrate, and the cold cathodes are formed at the intersection. FED is enable to display the two-dimensional image on the fluorescent screen using this matrix cathodes.
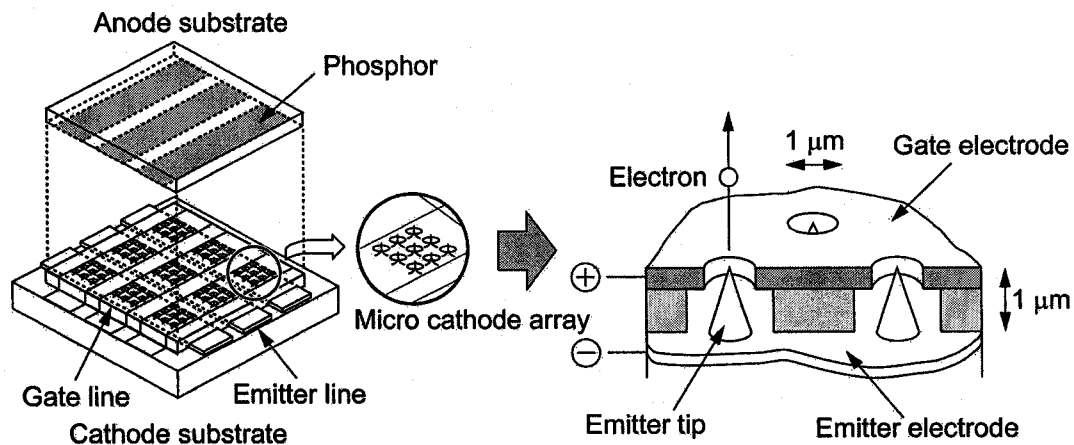
FIG. 3.1.   Schematic illustration of FED [41].

Field emission cathode is usually used as a cold cathode. The field emission cathode consists of a conical emitter tip with submicron size and a surrounding gate electrode to impress the voltage to take electrons out. Positive and negative potentials are impressed to the gate and emitter, respectively, to make electrons emit from the emitter tip. The electric fields are focused strongly to the tip because of the extremely small radius of curvature of the tip of 5 nm. As a result, electrons in the tip break the work functional barrier of the surface and are emitted into the vacuum.

Fabrication process of the cathode is shown in FIG. 3.2 [41]. Conventional Spindt type of the fabrication process [42] is improved. The process is as follows: 1. Formation of emitter lines, 2. Deposition of dielectric layer, 3. Formation of gate opening, 4. Deposition of gate

electrode, 5. Formation of release layer, 6. Deposition of emitter material, 7. Etch off of release
layer and formation of gate lines.

1. Formation of emitter line

2. Deposition of dielectric layer

3. Formation of gate opening

4. Deposition of gate electrode

5. Deposition of release layer

6. Deposition of emitter material

7. Etch off of release layer and formation of gate line
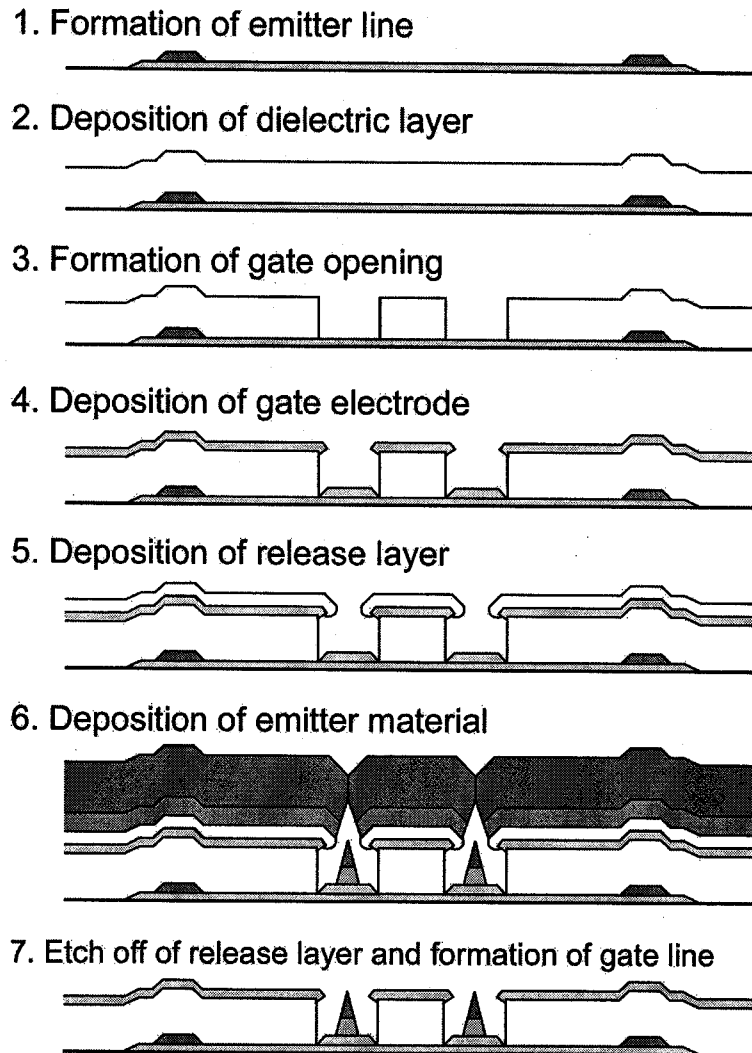
FIG. 3.2.   Field emission cathode fabrication [41].

3.1.3 Purpose

Multiple processes are required to fabricate the emitter tip as above mentioned. It is not eco-friendly because organic solvents for etching are used in the processes. The purpose of this chapter is to fabricate the field emitter for the emitter tip of the field emission display by using the eco-friendly dry process of the femtosecond laser ablation. Microspike arrays are fabricated in the opened region irradiating the femtosecond laser on the metal surface through the mask opening which is on the metal surface. Advantages of this method compared to the conventional method are follows; 1. complete dry process without using any organic solvents, 2. clean process without using and generating poisonous gases, and 3. single process of the laser ablation. Therefore, this method is eco-friendly and can save energy.

Optimum condition to achieve the sharp microspike is investigated by varying experimental conditions such as the number of pulses, the laser wavelength, the length of the mask opening, and the distance between the metal surface and the mask opening. Main factor to fabricate and array microspikes is also investigated. Intensity distributions diffracted at the edge of the mask opening are calculated and compared with the experimental results. The field emission current is measured to evaluate the ability of the microspike arrays fabricated for the field emitter.

3.2 Experiments

Polycrystalline tungsten (purity: 99.9 %, 10×10×t1 mm^3) is used as the target. The work function of tungsten is 4.55 eV. Femtosecond laser system described in Sec. 1.4 is used. Tungsten surface is polished after embedding in resin. Cu meshy mask is contacted with the polished tungsten surface in two ways; directly and via a carbon tape (about 100 μm thickness). The lengths of the mask opening sides d are 30, 45, and 85 μm in square and 30 and 45 μm in hexagon. The number of pulses at a point N is varied by scanning the laser pulses on the meshy mask. The laser polarization is linear, which is perpendicular to the laser scanning direction. The laser pulse energy E is fixed at 0.5 mJ/pulse. Two kinds of the laser wavelength λ, 800 and 400 nm, are used. The laser beam is focused by the single lens with the focal length of 1000 mm and irradiated on the surface through the mask opening in air at room temperature. Experimental conditions are listed in TABLE 3.1, and schematic illustration of sample preparation and the laser scanning method are shown in FIG. 3.3.

TABLE 3.1.   List of experimental conditions. Carbon tape "0" and "1" mean that the mesh is attached with the tungsten surface directly and by a carbon tape, respectively.

Wave length λ (nm)	Mask opening	Carbon tape	d (μm)	Number of pulses N	#
400	Square	0	30	20 – 180 (each 20 steps)	1
			45	20 – 180 (each 10 steps)	2
			30	100, 500, 1000	3
			45	100, 500, 1000	4
			85	100, 500, 1000	5
		1	30	100, 500, 1000	6
			45	100, 500, 1000	7
			85	100, 500, 1000	8
	Hexagon	0	30	100, 500, 1000	9
			45	100, 500, 1000	10
		1	30	100, 500, 1000	11
			45	100, 500, 1000	12
800	Square	1	30	100, 500, 1000	13
			45	100, 500, 1000	14
			85	100, 500, 1000	15
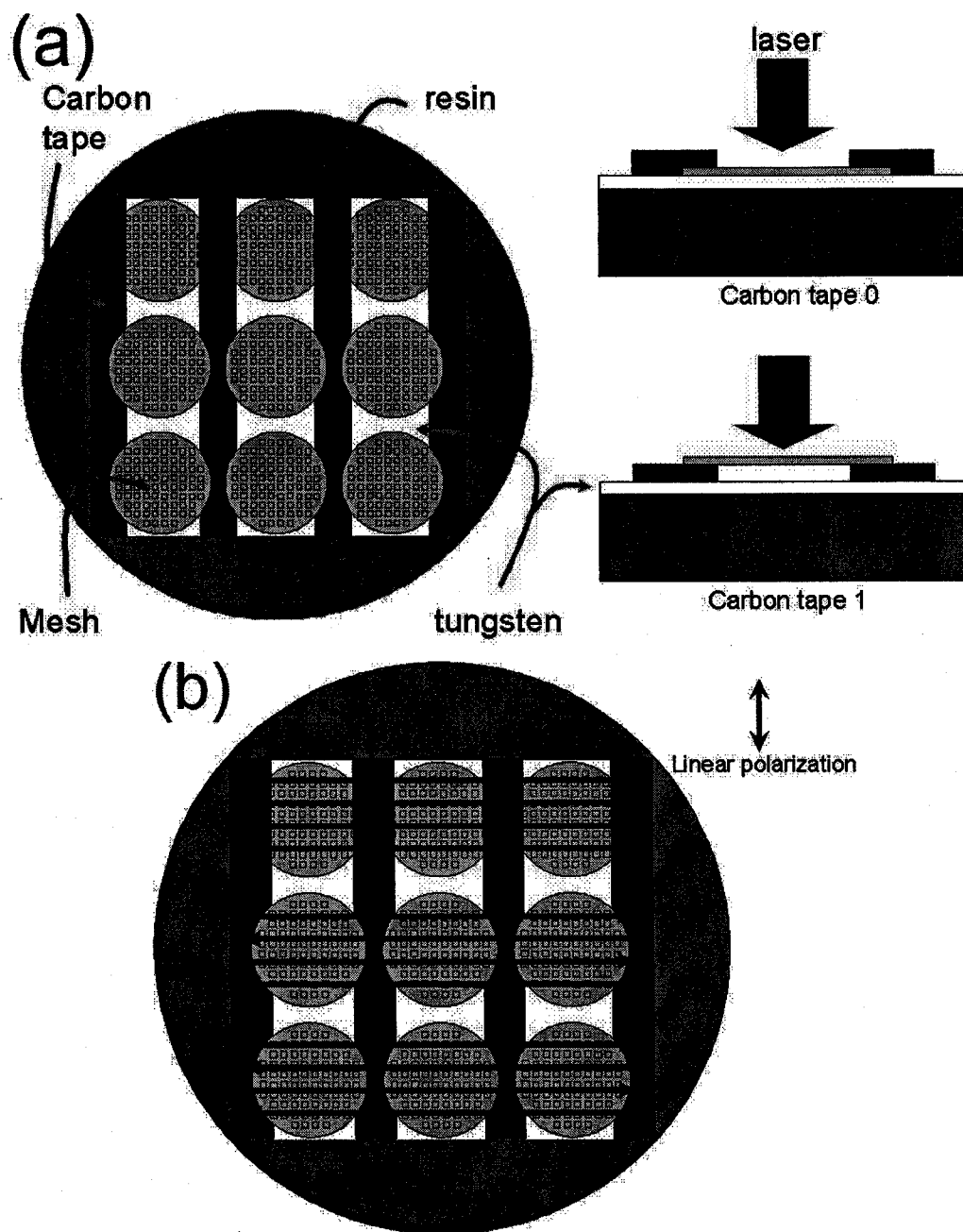
FIG. 3.3. Schematic illustrations of (a) sample preparation and (b) the direction of the laser scanning and the laser polarization.

3.3 Experimental results

Typical images of microspikes fabricated are shown in FIG. 3.4. Experimental condition is # 2 (λ = 400 nm, Carbon tape 0, Square mesh, d = 45 μm, N = 150). Multiple microspikes are fabricated and arrayed in a mask opening region. Main factor to fabricate and array microspikes is considered below.
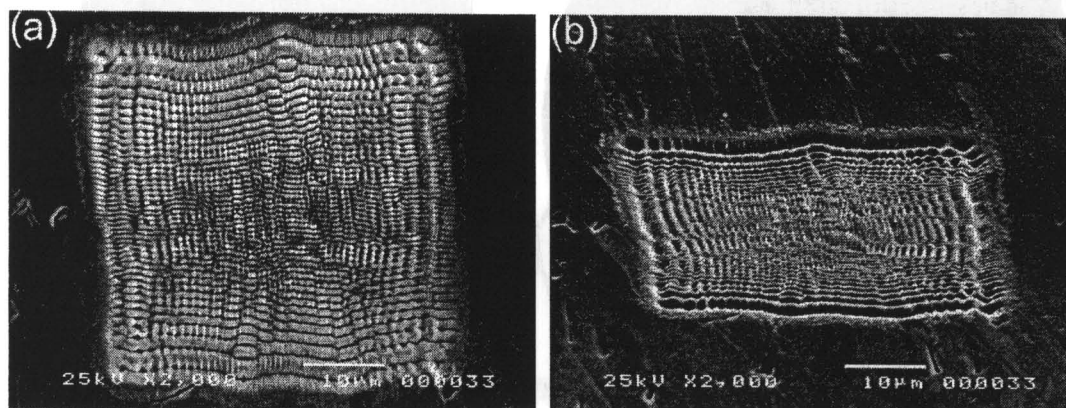
FIG. 3.4. (a) Typical top surface image and (b) its bird's eye view of microspike arrays. Experimental condition: #2, λ = 400 nm, Carbon tape 0, Square mesh, d = 45 μm, N = 150.

3.3.1 Influence of the number of pulses

SEM images of microspike-arrays fabricated at experimental conditions # 3, 4, and 5 (λ = 800 nm, carbon tape 1, N = 100, 500, 1000, d = 30, 45, 85 µm) are shown in FIG. 3.5. At an early stage, ripples are formed on the surface at each condition. Ripples remaining on the surface, surroundings of microspikes become deeper with increasing the number of pulses. Microspikes are formed by the ablation of the surroundings of microspikes because the top of the microspike is below the initial surface. The number in a unit square and size in the surface plane of microspikes formed depend on the length of the mask opening side.

N	d (µm)		
	30	45	85
100	(a)	(d)	(g)
500	(b)	(e)	(h)
1000	(c)	(f)	(i)
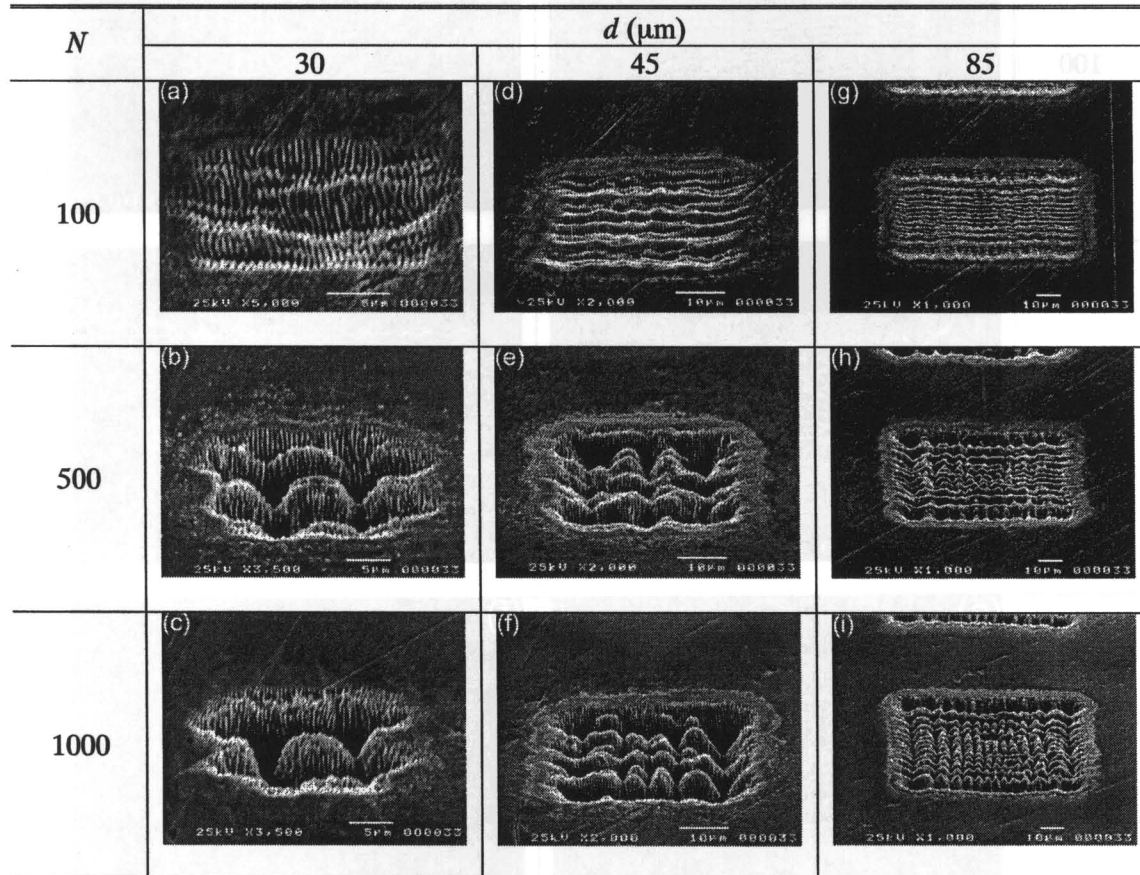
FIG. 3.5. Influence of the number of pulses. (Experimental conditions #3, 4, and 5, Laser wavelength λ = 800 nm, pulse energy E_p = 0.05 mJ/pulse, carbon tape 1).

3.3.2 Influence of the laser wavelength

Microspikes formed for the laser wavelength of 800 and 400 nm are shown in FIG. 3.6 (experimental conditions # 8 and 15; carbon tape 1, d = 85 μm). The number in a unit square and size in the surface plane of microspikes depends on the laser wavelength. The number is larger and the size is smaller for 400 nm compared to the case of 800 nm.
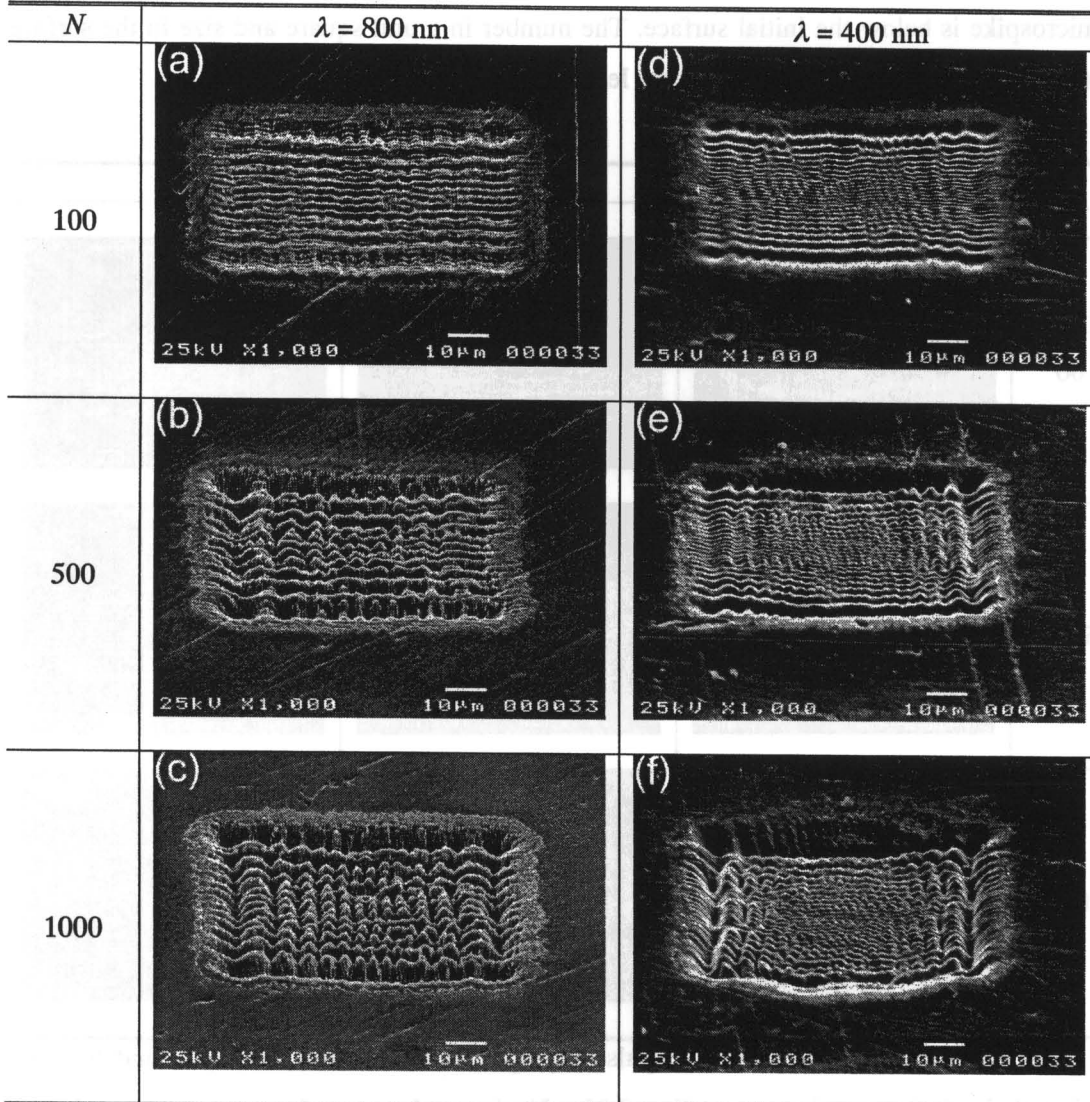
FIG. 3.6. Microspike arrays at λ = (a)-(c) 800 and (d)-(e) 400 nm. Experimental conditions #8 and 15, pulse energy E_p = 0.05 mJ/pulse, carbon tape 1, d = 85 μm.

3.3.3 Influence of the distance between the tungsten surface and the mask

Microspikes fabricated with and without a carbon tape of about 100 μm thickness between the tungsten surface and the mask are compared in FIG. 3.7. Experimental conditions are # 3 − 8 (λ = 400 nm, N = 100). The distance between the tungsten surface and the mask influences the fabrication of microspike arrays.

d (μm)	Carbon tape 0	Carbon tape 1
30	(a)	(d)
45	(b)	(e)
85	(c)	(f)
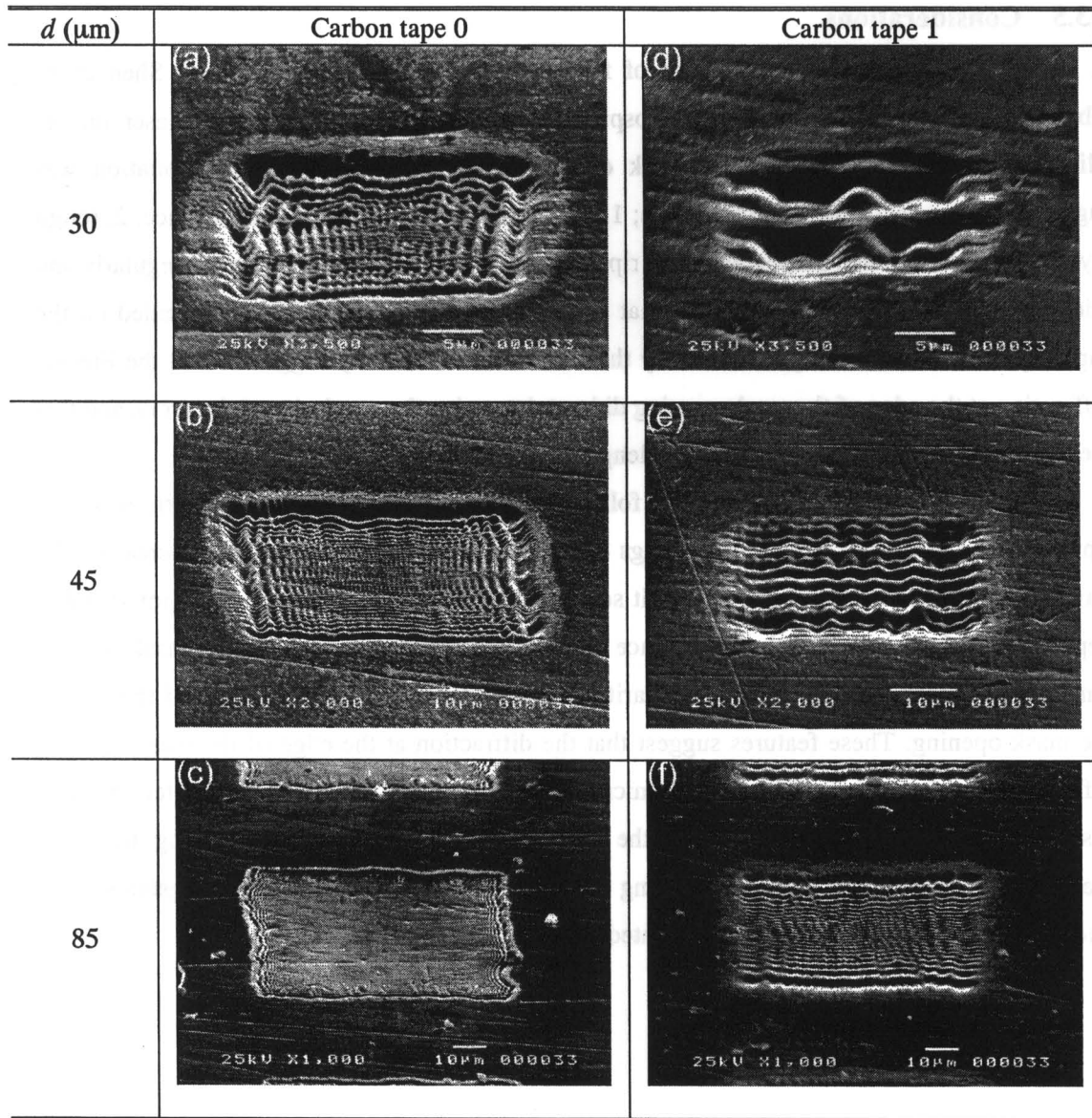
FIG. 3.7. Influence of the distance between the tungsten surface and the mesh. Experimental conditions: #3 − 8, λ = 400 nm, N = 100.

3.3.4 Influence of the shape of the mask opening

Microspikes fabricated using the mask opening in hexagon are shown in FIG. 3.8. Experimental conditions are # 9 – 12 (λ = 400 nm, N = 100). Ripples remain on the fabricated microspikes. The order of arrays depends on the side of the mask opening. This tendency is consistent with the case using the mask opening in square.

3.3.5 Considerations

In this section, the main factor of fabrication and array of microspikes. Shen *et al.* fabricated regular array of silicon microspikes by irradiating the femtosecond laser on the silicon surface through the meshy mask opening in SF_6 [35]. Microspike formation was suggested to consist of three steps follows; 1. ripples are formed on the silicon surface, 2. rough layers are formed on and perpendicular to ripples, and 3. rough layers are removed regularly and microspikes are formed. They showed that the distance of each rough layer depended on the capillary wave of molten layer formed by the laser irradiation. They suggested that the Fresnel diffraction at the edge of the mask opening did not determine the regularity of the array, and that the regularity was influenced by the wavelength of the capillary wave.

In this chapter, on the other hand, following features of microspike-arrays are shown; 1. ripples are on microspikes, 2. surroundings of microspikes become deeper with increasing the number of pulses, 3. the number in a unit square and size in the surface plane of microspikes depend on the laser wavelength, the distance between the tungsten surface and the mask, and the length of the mask opening side, 4. regularity of arrays depends on the direction of the side of the mask opening. These features suggest that the diffraction at the edge of the mask opening influences the formation and array of microspikes. Therefore, in the next chapter intensity distribution diffracted at the edge of the mask opening are calculated varying the laser wavelength, the length of the mask opening side, and the distance between the tungsten surface and the mask when a plane wave is irradiated into the mask opening.

d (µm)	Carbon tape 0	Carbon tape 1
30		
45		
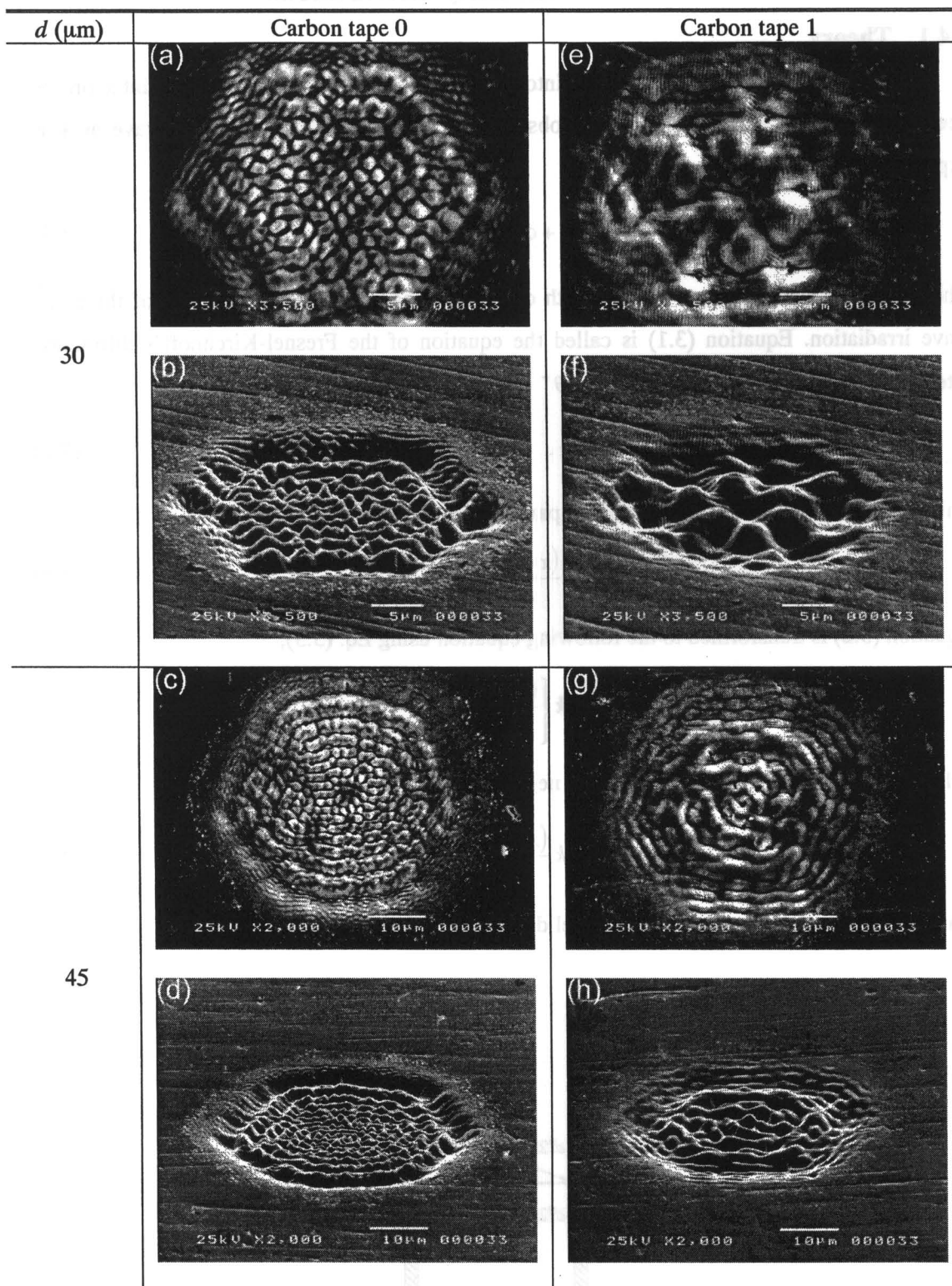
FIG. 3.8.   Microspikes formed using the hexagonal mesh. Experimental conditions: # 9 – 12, λ = 400 nm, N = 100.

3.4 Calculations of diffracted intensity distributions

3.4.1 Theory

When a plane wave is irradiated into an opening and a light wave at a point x on the opening propagates to a point X on an observation plane (FIG. 3.9), the light wave at X is expressed as follows;

$$U = \frac{A}{2}\sqrt{\frac{i}{\lambda}}\int_{-d/2}^{d/2}\frac{\exp[-ikr]}{\sqrt{r}}(1+\cos\theta)dx ,$$
(3.1)

where λ is the wavelength, d is the length of the opening, and z is the direction of the plane wave irradiation. Equation (3.1) is called the equation of the Fresnel-Kirchhoff's diffraction integration. When z is large enough, then $\theta \sim 0$ and Eq. (3.1) is transformed to

$$U = A\sqrt{\frac{i}{\lambda}}\int_{-d/2}^{d/2}\frac{\exp[-ikr]}{r}dx .$$
(3.2)

This equation is called the equation of the paraxial approximation. Then,

$$\frac{1}{r} \approx \frac{1}{z}, \quad r = z + \frac{(x-X)^2}{2z} - \frac{(x-X)^4}{8z^3} + \cdots .$$
(3.3)

Equation (3.2) is transformed to the following equation using Eq. (3.3);

$$U = Ae^{-ikz}\sqrt{\frac{i}{\lambda z}}\int_{-d/2}^{d/2}\exp\left[-ik\left\{\frac{(x-X)^2}{2z} - \frac{(x-X)^4}{8z^3}\right\}\right]dx .$$
(3.4)

When $(x-X)^4/8z^3$ is small enough and negligible, Eq. (3.4) is transformed to

$$U = Ae^{-ikz}\sqrt{\frac{i}{\lambda z}}\int_{-d/2}^{d/2}\exp\left[-ik\frac{(x-X)^2}{2z}\right]dx .$$
(3.5)

This equation is the equation of the Fresnel diffraction.
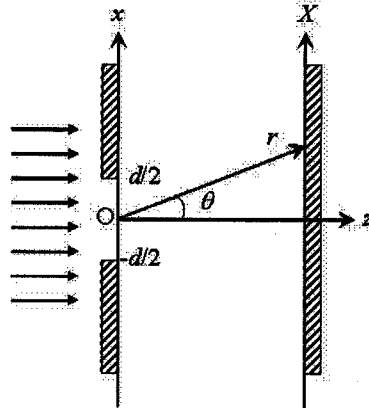
FIG. 3.9. Schematic of the irradiation of the planar optical wave.

Equations of the Fresnel-Kirchhoff's diffraction integration (Eq. (3.1)) for $z < d$, the paraxial approximation (Eq. (3.2)) for $z \sim d$, and the Fresnel diffraction (Eq. (3.5)) for $z > d$ are used.

3.4.2 Calculated results

Calculated results for $z = 10, 100, 1000$ μm, $d = 30, 45, 85$ μm are shown in FIG. 3.10 for $\lambda = 400$ nm and FIG. 3.11 for $\lambda = 800$ nm. The number of peaks of a diffracted intensity distribution becomes smaller with increasing z at the same λ and d. The number becomes larger with increasing d at the same λ and z. The number for $\lambda = 400$ nm is larger than that for $\lambda = 800$ nm at the same d and z. These tendencies show qualitatively good agreement with the experimental results.
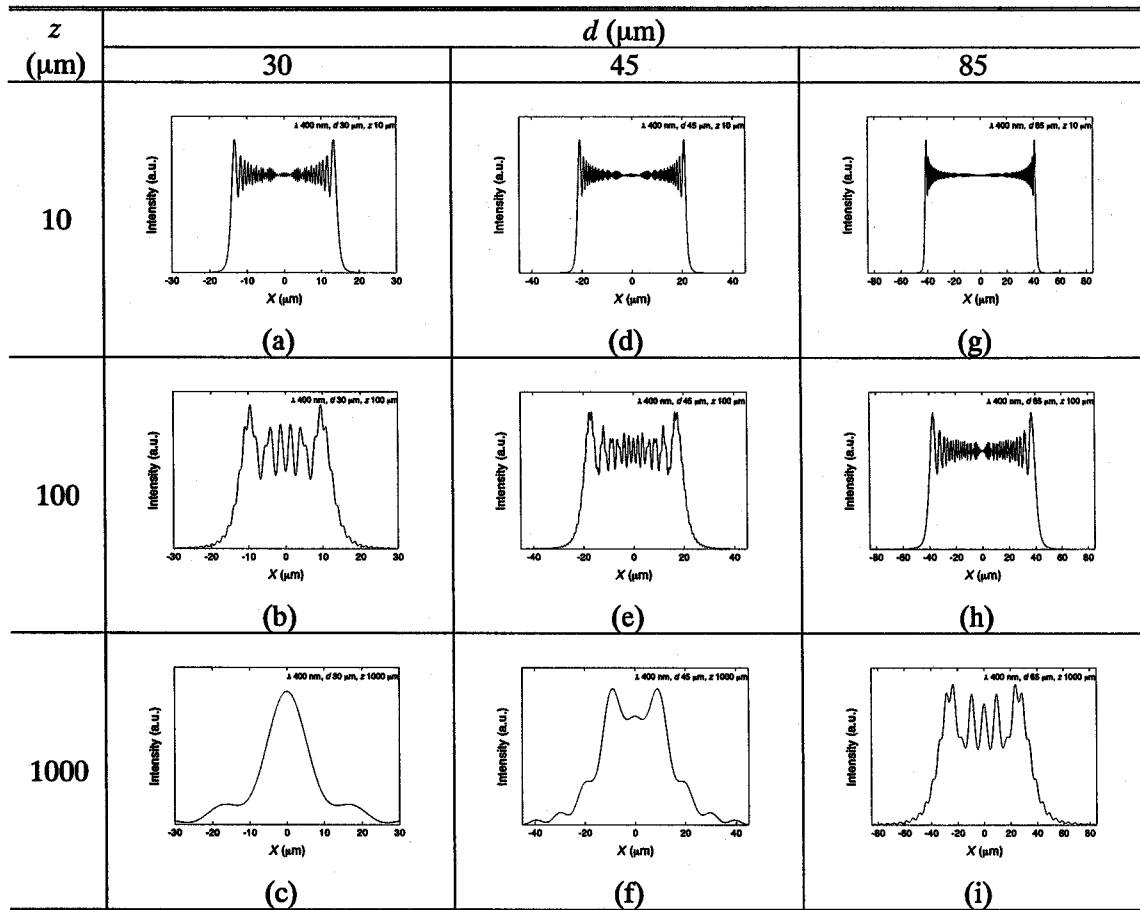
FIG. 3.10.   Calculated diffracted intensity distributions for $\lambda = 400$ nm.

z (μm)	d (μm)		
	30	45	85
10	(a)	(d)	(g)
100	(b)	(e)	(h)
1000	(c)	(f)	(i)
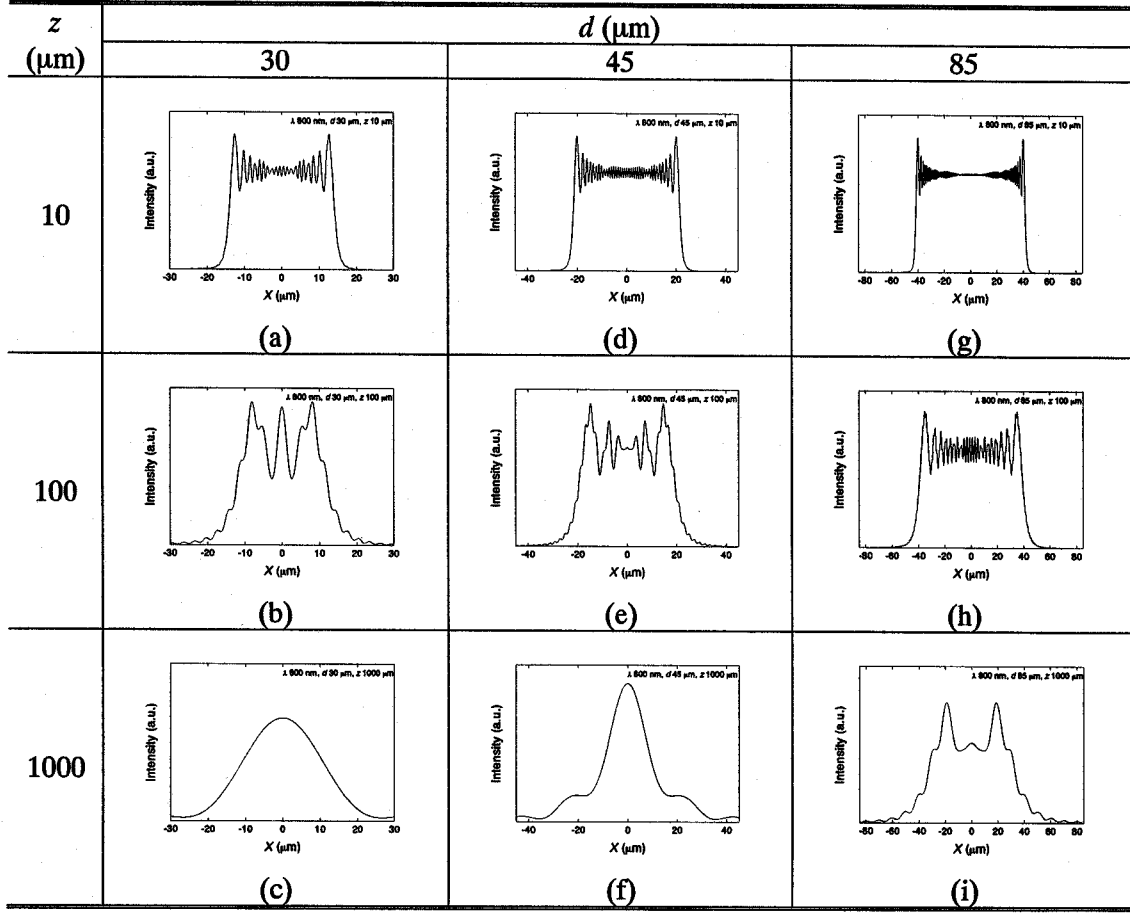
FIG. 3.11.   Calculated diffracted intensity distributions for λ = 800 nm.

Relationship between the diffracted intensity distributions and the form of microspikes is considered. Ablation depth per pulse L is expressed as

$$L \sim \frac{1}{\alpha} \ln \frac{I}{I_{th}}, \tag{3.6}$$

where α is the absorption coefficient, I is the laser intensity, and I_{th} is the ablation threshold fluence. Thus, the ablation depth per pulse is proportional to the natural logarithm of the laser intensity. Natural logarithm of the calculated result for λ = 800 nm, d = 85 μm, and z = 100 μm is shown in FIG. 3.12(a) and the corresponding experimental result at the same condition is shown in FIG. 3.12(b). Axis of ordinates in FIG. 3.12(a) indicates the relative removal depth. These results show qualitatively good agreement. The differences between the experimental and calculated results are resulted from the difference of the incidence intensity distribution, Gaussian for experiments and plane wave for calculation. One dimensional calculation is also another reason for the difference.
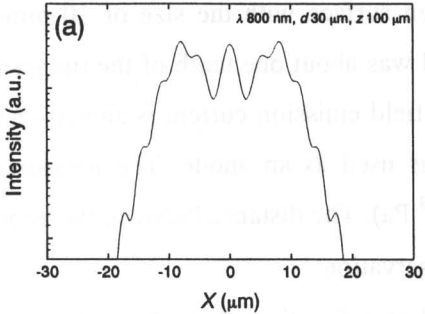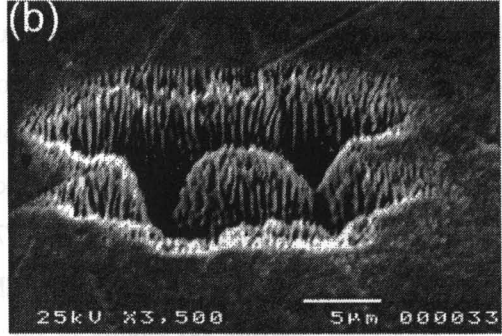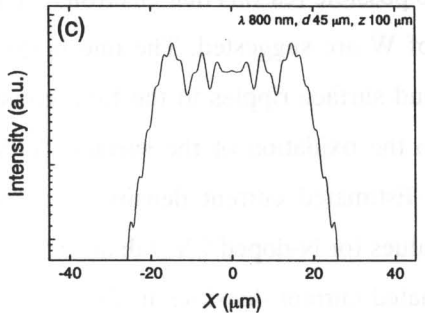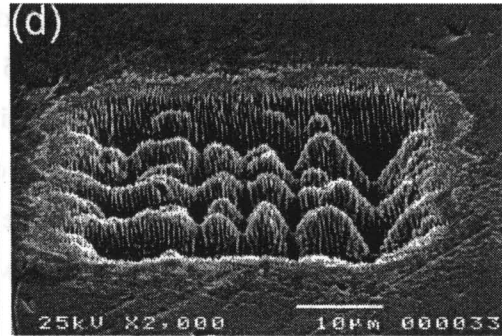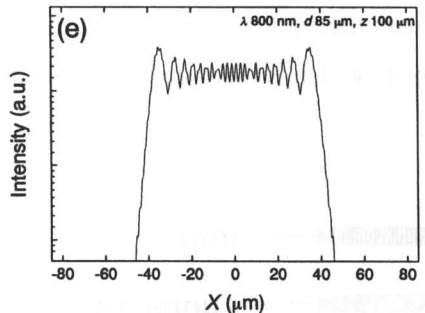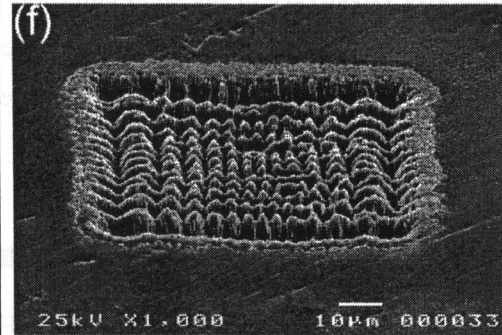
d (μm)	Calculated results	Experimental results
30		
45		
85		

FIG. 3.12. (a) Calculated results of the natural logarithm of the diffracted optical intensity for λ = 800 nm and z = 100 μm, and (b) the corresponding experimental results for N = 1000.

3.5 Measurement of the field emission current

Field emission current was measured to evaluate the ability of microspike-arrays for the field emitter. Fabrication condition was λ = 400 nm, d = 45 μm, N = 300, carbon tape 0. Microspike arrays were fabricated on the tungsten surface with the size of 10 mm x 5 mm. Actual area where microspike arrays were formed was about one tenth of the tungsten surface. Schematic illustration of the measurement of the field emission current is shown in FIG. 3.13. Iron (purity: 99.99 %) with polished surface was used as an anode. The measurement was performed in the vacuum chamber of SEM (7×10^{-3} Pa). The distance between the anode and the cathode was about 5 μm as a result of the SEM observation.

Measured currents are shown in FIG. 3.14 as a function of the time. Dotted and solid lines indicate the voltage and the current, respectively. Average currents of about 5×10^{-9} A for 10 V and about 2×10^{-10} A for 4 V were measured. Two possible reasons that electrons are emitted at 4 V which is below the work function 4.55 eV of W are suggested. The one is the effective contributions of the sharp shape of microspikes and surface ripples to the field emission. The other is the decrease of the work function due to the oxidation of the surface. XPS analysis showed oxidation of the laser irradiated region. Estimated current density as a function of electric field is shown in FIG. 3.15 together with values for N-doped CVD diamond [43], carbon nanotube [44], and graphite nanofiber [45]. Estimated current densities in this study are more than 2 orders lower than values for other materials. The reasons seem that a part of microspikes contributes effectively to the field emission because there are many microspikes of which tips are not sharp. Current density which is several orders higher than the present one is expected improving this problem. This means the current density which is the same or more order of CNT is obtained at the low voltage.
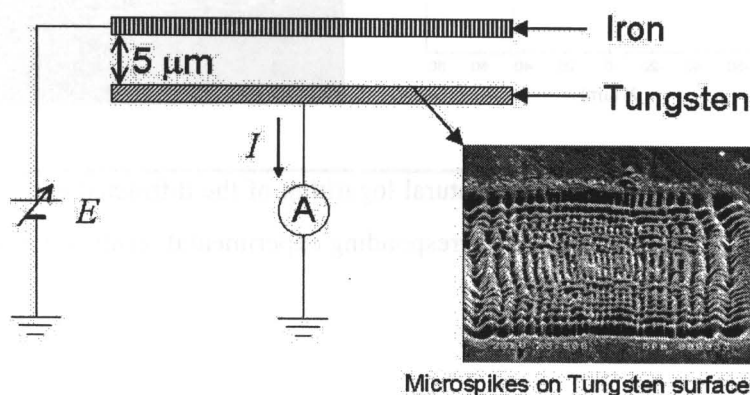
FIG. 3.13.   Schematic illustration of the measurement of the field emission current.
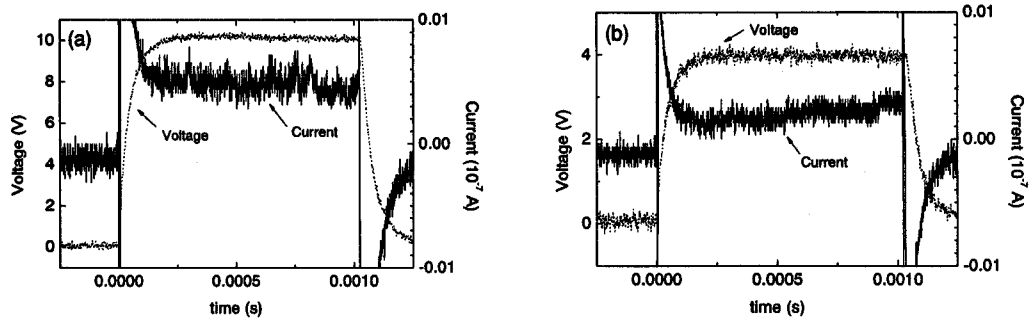
FIG. 3.14. Measured values of filed emission current for the voltage of (a) 10 V and (b) 4 V as a function of the time. Solid and dotted lines indicate the values of the current and the voltage, respectively.
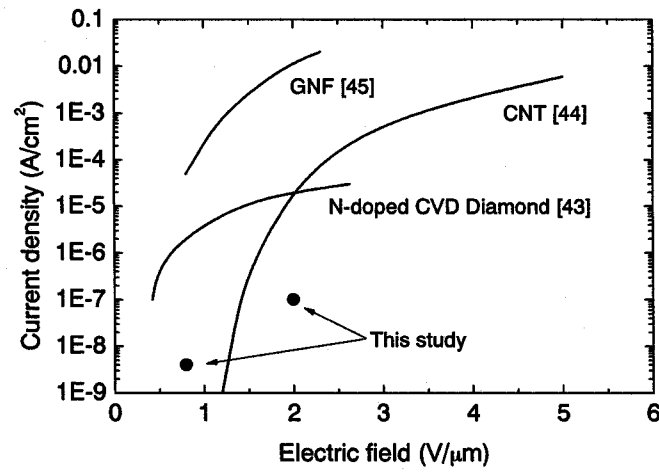
FIG. 3.15. Field-emission current density as a function of the electric field. Dots indicate measured values in this study.

3.6 Conclusions

In this study, microspike arrays were fabricated by irradiating the femtosecond laser on the tungsten surface through the mask opening in air with the aim of fabricating the micro field emitter for the field emission display using only the femtosecond laser. Natural logarithm of the calculated intensity distributions diffracted at the edge of the mask opening was qualitatively consistent with the experimental results of the shape and arrays of microspikes. The ability of the field emission of microspike arrays was evaluated. This method can be powerful tool to fabricate the field emitter.

References in Chapter 3

[1] D. C. Emmony, R. P. Howson, and L. J. Willis, "Laser mirror damage in germanium at 10.6 μm," Appl. Phys. Lett. 23, 598-560 (1973).

[2] C. T. Walters, "Surface scattering at LSD-wave initiation sites on nonmetallic materials," Appl. Phys. Lett. 25, 696-698 (1974).

[3] N. R. Isenor, "CO_2 laser-produced ripple patterns on Ni_xP_{1-x} surfaces," Appl. Phys. Lett. 31, 148-150 (1977).

[4] H. J. Leamy, G. A. Rozgonyi, T. T. Sheng, and G. K. Celler, "Periodic regrowth phenomena produced by laser annealing of ion-implanted silicon," Appl. Phys. Lett. 32, 535-537 (1978).

[5] M. Oron and G. Sørensen, "New experimental evidence of the periodic surface structure in laser annealing," Appl. Phys. Lett. 35, 782-784 (1979).

[6] A. K. Jain, V. N. Kulkarni, D. K. Sood, and J. S. Uppal, "Periodic surface ripples in laser-treated aluminum and their use to determine absorbed power," J. Appl. Phys. 52, 4882-4884 (1981).

[7] P. M. Fauchet and A. E. Siegman, "Surface rippiles on silicon and gallium arsenide under picosecond laser illumination," Appl. Phys. Lett. 40, 824-826 (1982).

[8] J. F. Young, J. E. Sipe, J. S. Preston, and H. M. van Driel, "Laser-induced periodic surface damage and radiation remnants," Appl. Phys. Lett. 41, 261-264 (1982).

[9] H. M. van Driel, J. E. Sipe, and J. F. Young, "Laser-induced periodic surface structure on solids: A universal phenomena," Phys. Rev. Lett. 49, 1955-1958 (1982).

[10] J. E. Sipe, J. F. Young, J S. Preston, and H. M. van Driel, "Laser-induced periodic surface structure. I. Theory," Phys. Rev. B 27, 1141-1154 (1983).

[11] J. F. Young, J. S. Preston, H. M. van Driel, and J. E. Sipe, "Laser-induced periodic surface structure. II. Experiments on Ge, Si, Al, and grass," Phys. Rev. B 27, 1155-1172 (1983).

[12] J. F. Young, J. E. Sipe, and H. M. van Driel, "Laser-induced periodic surface structure. III. Fluence regimes, the role of feedback, and details of the induced topography in germanium," Phys. Rev. B 30, 2000-2015 (1984).

[13] H. Niino, M. Shimoyama, and A. Yabe, "XeCl excimer laser ablation of a polyethersulfone film: Dependence of periodic microstructures on a polarized beam," Appl. Phys. Lett. 57, 2368-2370 (1990).

[14] A. Dauscher, V. Feregotto, P. Cordier, and A. Thomy, "Laser induced periodic surface structures on iron," Appl. Surf. Sci. 96-98, 410-414 (1996).

[15] G. K. Giust and T. W. Sigmon, "New ripple patterns obserbed in excimer-laser irradiated SiO$_2$/polycrystalline silicon/SiO$_2$ structures," Appl. Phys. Lett. 70, 3552-3554 (1997).

[16] A. M. Ozkan, A. P. Malshe, T. A. Railkar, W. D. Brown, M. D. Shirk, and P. A. Molian, "Femtosecond laser-induced periodic structure writing of diamond crystals and microclusters," Appl. Phys. Lett. 75, 3716-3718 (1999).

[17] Y. Kawakami, E. Ozawa, and S. Sasaki, "Coherent array of tungsten ultrafine particles by laser irradiation," Appl. Phys. Lett. 74, 3954-3956 (1999).

[18] Y. Kawakami, S. Sasaki, and E. Ozawa, "Effect of Nd-YAG laser irradiation on surface microstructure of single crystal tungsten," Surf. Eng. 16, 218-220 (2000).

[19] Y. Kawakami and E. Ozawa, "Self-assembled coherent array of ultra-fine particles on single-crystal tungsten substrate using SHG Nd:YAG laser," Appl. Phys. A 71, 453-456 (2000).

[20] Y. Kawakami and E. Ozawa, "Tungsten microcone arrays grown using nanosecond pulsed-Nd:YAG laser in a low-pressure He-gas atmosphere," Appl. Phys. A 74, 59-61 (2002).

[21] Y. Kawakami and E. Ozawa, "Tungsten microcone growth by laser irradiation," Appl. Surf. Sci. 218, 175-187 (2003).

[22] A. J. Pedraza, J. D. Fowlkes, and D. H. Lowndes, "Silicon microcolumn arrays grown by nanosecond pulsed-excimer laser irradiation," Appl. Phys. Lett. 74, 2322-2334 (1999).

[23] A. J. Pedraza, J. D. Fowlkes, and D. H. Lowndes, "Self-organized silicon microcolumn arrays generated by pulsed laser irradiation," Appl. Phys. A 69, 731-734 (1999).

[24] J. D. Fowlkes, A. J. Pedraza, and D. H. Lowndes, "Microstructural evolution of laser-exposed silicon targets in SF$_6$ atmosphere," Appl. Phys. Lett. 77, 1629-1631 (2000).

[25] A. J. Pedraza, J. D. Fowlkes, and D. H. Lowndes, "Laser ablation and column formation in silicon under oxygen-rich atmosphere," Appl. Phys. Lett. 77, 3018-3020 (2000).

[26] D. H. Lowndes, J. D. Fowlkes, and A. J. Pedraza, "Early stages of pulsed-laser growth of silicon microcolumns and microcones in air and SF$_6$," Appl. Surf. Sci. 154-155, 647-658 (2000).

[27] A. J. Pedraza, J. D. Fowlkes, S. Jesse, C. Mao, and D. H. Lowndes, "Surface micro-structuring of silicon by excimer-laser irradiation in reactive atmosphere," Appl. Surf. Sci. 168, 251-257 (2000).

[28] A. J. Pedraza, S. Jesse, Y. F. Guan, and J. D. Fowlkes, "Laser-induced surface pertubations in silicon," J. Mater. Res. 16, 3599-3608 (2001).

[29] J. D. Fowlkes, A. J. Pedraza, D. A. Blom, and H. M. Meyer III, "Surface microstructuring

and long-range ordering of silicon nanoparticles," Appl. Phys. Lett. 80, 3799-3801 (2002).

[30] S. Jesse, A. J. Pedraza, J. D. Fowlkes, and J. D. Budai, "Etching-enhanced ablation and the formation of a microstructure in silicon by laser irradiation in an SF_6 atmosphere," J. Mater. Res. 17, 1002-1013 (2002).

[31] A. J. Pedraza, J. D. Fowlkes, D. A. Blom, and H. M. Meyer, III, "Laser-induced nanoparticle ordering," J. Mater. Res. 17, 2815-2822 (2002).

[32] A. J. Pedraza, J. D. Fowlkes, and Y.-F. Guan, "Surface nanostructuring of silicon," Appl. Phys. A 77, 277-284 (2003).

[33] T.-H. Her, R. J. Finlay, C. Wu, S. Deliwala, and E. Mazur "Microstructuring of silicon with femtosecond laser pulses," Appl. Phys. Lett. 73, 1673-1675 (1998).

[34] T.-H. Her, R. J. Finlay, C. Wu, and E. Mazur, "Femtosecond laser-induced formation of spikes on silicon," Appl. Phys. A 70, 383-385 (2000).

[35] M. Y. Shen, C. H. Crouch, J. E. Carey, R. Youkin, E. Mazur, M. Sheehy, and C.M. Friend, "Formation of regular arrays of silicon microspikes by femtosecond laser irradiation through a mask," Appl. Phys. Lett. 82, 1715-1717 (2003).

[36] P. E. Dyer, S. D. Jenkins, and J. Sidhu, "Development and origin of conical structures on XeCl laser ablated polyimide," Appl. Phys. Lett. 49, 453-455 (1986).

[37] S. R. Foltyn, R. C. Dye, K. C. Ott, E. Peterson, K. M. Hubbard, W. Hutchinson, R. E. Muenchausen, R. C. Estler, and X. D. Wu, "Target modification in the excimer laser deposition of YBa2Cu3O7-x thn films," Appl. Phys. Lett. 59, 594-596 (1991).

[38] F. Sánchez, J. L. Morenza, and V. Trtik, "Characterization of the progressive growth of columns by excimer laser irradiation of silicon," Appl. Phys. Lett. 75, 3303-3305 (1999).

[39] A. Usoskin, H. C. Freyhardt, H. U. Krebs, "Influence of ligh scattering on the development of laser-induced ridge-cone structures on target surfaces," Appl. Phys. A 69, 823-826 (1999).

[40] S. I. Dolgaev, S. V. Lavrishev, A. A. Lyalin, A. V. Simakin, V. V. Voronov, and G. A. Shafeev, "Formation of conical microstructures upon laser evaporation of solids," Appl. Phys. A 73, 177-181 (2001).

[41] K. Betsui and T. Nakatani, "Field emission display," FUJITSU 49, 230-234 (1998). (in Japanese)

[42] C. A. Spindt, I. Brodie, L. Humphrey, and E. R. Westerberg, "Physical properties of thin-film emission cathodes with molybdenum cones," J. Appl. Phys. 47, 5248-5263 (1976).

[43] K. Okano, S. Koizumi, S. Ravi P. Silva, and G. A. J. Amaratunga, "Low-threshold cold cathodes made of nitrogen-doped chemical-vapour-deposited diamond," Nature 381, 140-141 (1996).

[44] H. Murakami, M, Hirakawa, C. Tanaka, and H. Yamakawa, "Field emission from well-aligned, patterned, carbon nanotube emitters," Appl. Phys. Lett. 76, 1776-1778 (2000).

[45] H. Murakami, "Development of carbon nanomaterials for field emission displays," J. Vac. Soc. Jpn. 45, 70-74 (2002). (in Japanese)

Chapter 4

Femtosecond laser quenching of the high-pressure phase of iron

The femtosecond laser driven shock quenching of the high pressure phase (ε phase) of iron is described in this chapter. In Sec. 4.1, properties of iron, the shock induced phase transition in iron, and the laser induced phase transition in iron are introduced. Experimental methods and results are described in Secs. 4.2 and 4.3, respectively. In Sec. 4.4, thermal properties of iron under the shock compression state are calculated theoretically. In Sec. 4.5, temperatures behind and inside the steady-plane shock wave fronts are calculated using the results obtained in Sec. 4.5. The femtosecond laser driven shock quenching of the ε phase in iron is explained in detail based on the experimental and calculated results obtained in the previous sections in Sec. 4.6.

4.1 Introduction

4.1.1 Iron

4.1.1.1 Properties of iron

Phase diagram and β phase dispute of iron

Iron is not only one of the most important materials for the life of the human being but interesting material in the fields of materials science and geophysics because it is the principal element in Earth's core that occupy approximately 30 % of all the Earth's mass [1,2]. The phase diagram of iron below 50.2 GPa and 2000 K is established as shown in FIG. 4.1 [3-7]: the α phase (ferromagnetic bcc) at low pressures and temperatures, the γ phase (nonmagnetic fcc) and the δ phase (nonmagnetic bcc) at low pressures and high pressures, and the ε phase (nonmagnetic hcp) at high pressures and temperatures. In FIG. 4.1, the author applies the data of Bundy [4] to the triple point of α-γ-ε phases, Anderson and Isaak [8] to the γ-ε-liquid triple point and melting curves, and Saxena and Dubrovinsky [9] and Brown [10] to the γ-ε-β and β-α'-liquid triple points, respectively, assuming that the β and α' phases exist (the β and α' phases will be introduced later). The phases at high pressures and temperatures that correspond to the region of the pressure and the temperature in Earth's core (300 – 400 GPa, 4000 – 8000 K) are not clear. Since Saxena *et al.* suggested the existence of the new β phase at the high pressure and temperature region in 1993 [11], the existence of the β phase has been disputed [12-42]. Experimental data reported by Andrault *et al.* [25] supports the existence of the β phase suggested by Saxena et al. [9,11-22]. If the β phase is verified, the β phase is displaced from the ε phase at the pressure and the temperature of Earth's inner core. Thus, the structure of the inner core is changed, a new theoretical stand on the function of Earth's core is required, and fields such as geophysics, space science, seismology, and the first-principle calculation are affected.

The Diamond Anvil Cell (DAC) was developed as the device for the high pressure generation at the end of the 1960s. It was improved and extended to above 2000 K at the beginning of the 1990s. The melting point T_m of iron above 50 GPa can be determined in this temperature range. Measurements of T_m were performed by detecting the jump of the physical properties such as the electrical resistance and the optical reflectance. The melting curve as a function of the pressure p was measured by Boehler *et al.* of Max Planck Institute for Chemistry to 43 GPa [43], 100 GPa [44], and finally 197 GPa at 3900 K [42]. $T_m(p)$ in higher pressure region was formed by Berkeley group (Ahrens *et al.*) [45], and the temperature in inner core was disputed for 10 years. Applying the Synchrotron Radiation (SR) to the DAC, in situ diffraction patterns of iron with high quality at high pressures could be obtained. As a result, the

liquid structure of iron found to be lower than the melting curve of Berkeley's group and higher than the Boehler *et al.*, and the dispute on $T_m(p)$ supported Boehler *et al.* and was solved [23].
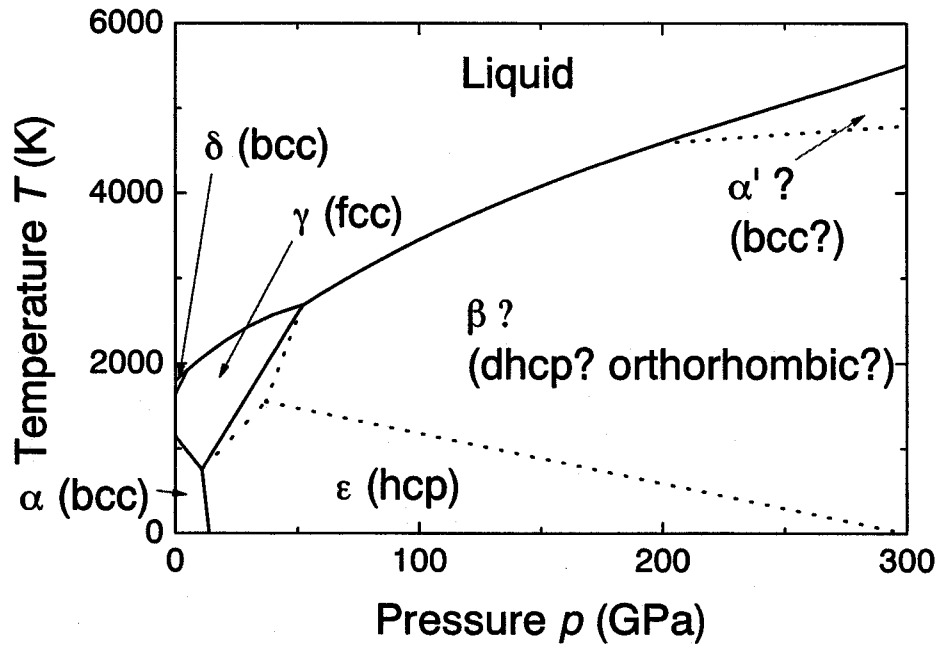
FIG. 4.1. Phase diagram of iron.

SR has become the tool for search the detail phase diagram of iron. Saxena *et al.* (Uppsala group) insisted to discover the structure of the β phase using this tool and reported that it had double hexagonal close-packed (dhcp) structure [11]. At the nearly same time as the report of the dhcp by Uppsala group, Yoo *et al.* reported that the structure of iron in the interesting region of pressure and temperature is hcp, not dhcp [23]. The articles which describe in detail the experiments on the β phase can be seen in two Technical Comments in Science [16,24]. Livermore group and Geophysical Lab group (authors of Ref. [23]) opponent to Uppsala group argued that the X-ray diffraction patterns for the dhcp structure suggested by Uppsala group can be treated as the other structure. And they argued that the diffraction patterns obtained from the argued region were accepted as the hcp structure from their own experimental data. Uppsala group was criticized that they did not perform the enough experiments to verify their suggestion for the new phase. As a response, Uppsala group showed the dhcp lines from the remained iron after rapid cooling from high temperatures [11], discovered the dhcp lines from the in-situ experiments [14], and determined the reversible point enough to establish the

γ-ε phase boundary [46].

Experimental results of Uppsala group support strongly their suggestion. On the other hand, the conclusion of Geophysical Lab group that the hcp exists in the region where Uppsala group suggested that equilibrium dhcp was discovered can not be negligible because they are prestigious in this field. Dr. Mao of Geophysical Lab said that Geophysical Lab observed the additional diffraction patterns which was interpreted ones originated from the dhcp structure for the remained iron samples at high pressures after the laser heating and the rapid cooling and that dhcp was not observed from the in situ X-ray diffraction experiments at high pressures and temperatures, so that the dhcp was considered to be generated by rapid cooling. This problem is whether the dhcp exists as the equilibrium phase together with the fcc and the hcp. Diffraction patterns of the dhcp structure add two weak lines to all the patterns of the hcp. The answer possibly includes the resolution of the detection and depends on the detection and the interpretation of the weak diffraction patterns. The accuracy of the detection and the resolution are improved by the angle-dispersive method. The argument on the β phase will be solved using the intense SR. Andrault et al. (French group) performed experiments using the beamline of the European Synchrotron Radiation Facility and verified the existence of the β phase. They reported, however, that the structure is not the dhcp but the orthorhombic [25].

Mainly four groups of four countries (Uppsala, MPI, Livermore and Geophysical Lab, France) are included in the argument of the β phase (TABLE 4.1). Two groups insist the existence of the β phase, but suggested structures are different.

TABLE 4.1.   Research groups on the argument of the existence of β phase of iron.

Group	Researchers	β phase
Uppsala	Saxena, Dubrovinsky et al.	dhcp
MPI	Boehler et al.	No
Livermore and Geophysical Lab	Yoo, Mao et al.	No
France	Andrault et al.	orthorhombic

A new prospective dispute is the existence of the α' phase above 200 GPa on the Hugoniot [10]. This phase was discovered by the shock experiments [47]. The triple point exists on 200 GPa because there is the evidence of the solid-solid boundary. Dynamics of the sound velocity at 200 GPa [47] was reproduced by the molecular dynamics simulation, and the structure was suggested to be the bcc [48,49].

Mechanism of the bcc-hcp transition of iron

Since the bcc-hcp phase transition of iron at 13.0 GPa was discovered by Minshall *et al.* in 1955 [50,51], many researches have been investigated this transition and the hcp structure of iron [52-78]. The transition starts at 13.0 GPa but it is very sluggish. The bcc and hcp exist together over the pressure range of about 8.0 GPa. This transition has a large hysteresis. In a case, the reverse transformation is not completed till 5.0 GPa [64]. This transition is an athermal process and the quantity of the phase dose not vary as a function of time but pressure. It is concluded that this transition is based on a large hysteresis and an athermal property and martensitic transformation based on the non-regulated form [57] of the boundary which the bcc and hcp coexist.

Some aspects of this transition, however, are not understood well. Some groups reported different lattice constants for the hcp phase during the transition, but the results after the transition are consistent [54,64-66]. Mao *et al.* measured the same values of the *c/a* ratio during and after the transition [54], but Jephcoat *et al.* reported that the *c/a* ratio decreases during the transition [64]. Bassett and Huang [65] and Huang *et al.* [67] observed considerable large *c/a* ratio during the transition. In the latter work, the significantly large change of the *c/a* ratio during the transition at different temperatures was observed [66]. These experiments were performed at different time scales and under different static high pressure conditions. Pressure transmission medium was not described and a pressure was retained for several hours to relax the system after the change of the pressure in Ref. [54]. Argon and Neon were used as a pressure transmission media and the system was relaxed for 24 hours after the change of the pressure in Ref. [64]. Measurement were performed for 100 hours at each pressure in Refs. [54] and [64]. Pressure medium was not used and the measurements were performed at several minutes after the pressure change in Ref. [65]. Similar experiment was reported at different four temperatures in Ref. [66]. The measurements were within one hour in Refs. [65] and [66]. Wang *et al.* clarified the effect of the experimental conditions on the hcp structure observed during the transition and the different dynamics of the hcp phase and suggested the model of the pressure induced bcc-hcp phase transition of iron [73]. Previous studies used the X-ray diffraction technique, while they measured the lattice constant using the XAFS method. The structurally distorted hcp phase which had the anomalously large *c/a* ratio during the transition and the distorted bcc phase which had the anomalously large lattice constant were observed as reported in Refs. [65] and [66]. This anomaly results in the distortion of the interface between the hcp and the bcc.

The bcc-hcp transition of iron is martensitic transformation. A newly formed martensitic

phase (in this case, hcp) is derived from the parent phase (bcc) via the collective shear movement of the atomic planes in this transition. One of the important feature is that there is a specific crystallographic relationship between the martensitic phase and the parent phase. For example, the following relationship is know for the temperature driven bcc-fcc martensitic transformation of iron: $(111)_{fcc} \parallel (011)_{bcc}$, $[10\bar{1}]_{fcc} \parallel [\bar{1}1\bar{1}]_{bcc}$. This is so called the Kurdjumov-Sachs relation [79]. Parallel planes during the transition such as $(111)_{fcc}$ and $(011)_{bcc}$ are called the conjugate plane of the transition.

Discrimination and investigation of the interface of the transition under high pressure circumstances are extremely difficult due to the complex morphology of the martensitic transition. The martensitic phase generated by the rapid cooling has the shapes of planes, needles, or bamboo leaves depending on the chemical composition such as the content of carbon in the steel and the temperature cooling rate. The conjugate plane of the martensitic phase is very often observed to be the transition interface [79]. If we do not know the correct morphology of the bcc-hcp transition of iron, we shall mistake the conjugate plane of the transition for the possible interface between the bcc and the hcp phases.

Three possible models of the bcc-hcp transition of iron are shown below.

Model I: Two-step process from the bcc to the hcp.

This model was suggested in Refs. [54] and [65] (FIG. 4.2). Firstly, the bcc lattice is compressed along the [001] direction and stretched along the $[1\bar{1}0]$ direction so that the (110) plane of the bcc becomes the atomic plane arranged in a hexagon corresponds to the (0002) plane of the hcp. Secondly, every other (110) plane shifts to the $[1\bar{1}0]$ direction keeping the interplane distance $d(110)$ unchanged. In this model, three sets of conjugate planes exist during the transition: (A) $(002)_{bcc} \parallel (\bar{2}110)_{hcp}$; (B) $(1\bar{1}0)_{bcc} \parallel (0\bar{1}10)_{hcp}$; (C) $(110)_{bcc} \parallel (0002)_{hcp}$. (A) and (B) have the similar atomic arrangement in two structures and considered the possible interface planes. In set (A), two orthogonal base vectors $\mathbf{X}_{bcc}$ and $\mathbf{Y}_{bcc}$ for the $(002)_{bcc}$ plane of the bcc are found, while the corresponding base vectors $\mathbf{X}_{hcp}$ and $\mathbf{Y}_{hcp}$ for the $(\bar{2}110)$ plane of the hcp are found. The direction and length of these base vectors are listed in TABLE 4.2. Base vectors $\mathbf{X}_{bcc}$ and $\mathbf{X}_{hcp}$ does not change because $d(110)$ does not change during the transition in this model. The evolution of $\mathbf{X}_{bcc}$ and $\mathbf{X}_{hcp}$ which was calculated in Ref. [73] are plotted in FIG. 4.3(a). The change of $\mathbf{X}_{bcc}$ and $\mathbf{X}_{hcp}$ are observed although $\mathbf{X}_{bcc}$ and $\mathbf{X}_{hcp}$ are predicted not to change during the transition. The magnitude of other sets of base vectors $\mathbf{Y}_{bcc}$ and $\mathbf{Y}_{hcp}$ is different. Evolution of these base vectors is shown in FIG. 4.3(b) as a function of pressure. Two hysteresis loops do not overlap. Thus, the evolution of both base vectors of the conjugate plane (A) does not give

the signature the distortion of the structure caused by the strain of the interface. The same is true for the conjugate plane (B). Therefore, the anomalous dynamics observed during the transition and the corresponding intermediate structural distortion can not be found in model I.
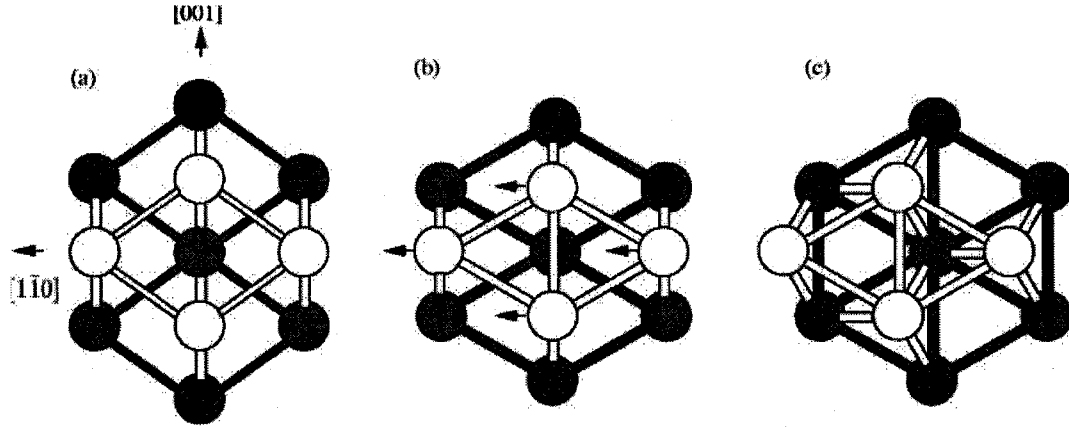
FIG. 4.2. Model I: two-step process. (a) → (b) → (c) during the bcc-hcp transition of iron. (a) and (c) are the projection from the [110]/[0001] directions of the bcc/hcp, respectively. (b) is the projected view of the intermediate structure obtained from the compression along the [001] direction and the expansion along [1$\bar{1}$0] direction of (a).

TABLE 4.2.   Base vectors of the conjugate plane $(002)_{bcc} \parallel (\bar{2}110)_{hcp}$.

	X_{bcc}	Y_{bcc}	X_{hcp}	Y_{hcp}
Direction	[110]	[1$\bar{1}$0]	[0001]/[110]	[0$\bar{1}$10]/[1$\bar{1}$0]
Length	$d(110)$	$2d(1\bar{1}0)$	$d(0002)$	$2d(0\bar{1}10)$
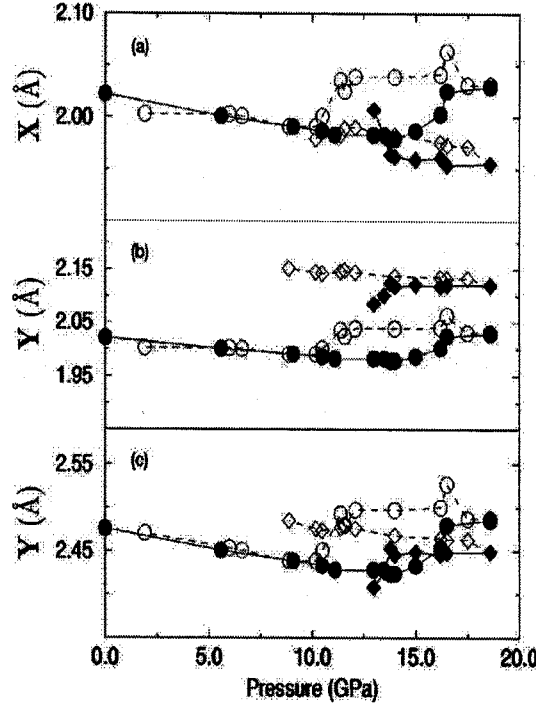
FIG. 4.3. Hysteresis loops calculated in Ref. [73]. (a) and (b) are hysteresis loops for the base vectors of the conjugate plane $(002)_{bcc} \parallel (\bar{2}110)_{hcp}$ in model I. (a) and (c) are hysteresis loops for the base vectors of the conjugate plane $[\bar{1}1\bar{1}]_{bcc} \parallel [11\bar{2}0]_{hcp}$ in model II. $\bigcirc$: bcc, $\Diamond$: hcp, $\bullet$ and $\blacklozenge$: forward transformation, $\bigcirc$ and $\Diamond$: reverse transformation.

Model II:

Model II is proposed by Burgers for the bcc-hcp transition of Zirconium on cooling from high temperatures [80]. Some other metals such as Li, Ti, Hf have this type of the bcc-hcp martensitic phase transition [79]. In this case, the following crystallographic relations between the bcc and the hcp were found: $(110)_{bcc} \parallel (0002)_{hcp}$, $[\bar{1}1\bar{1}]_{bcc} \parallel [11\bar{2}0]_{hcp}$. These planes are followed by the same two-step process proposed by Burgers [80] when they transforms from the bcc to the hcp (FIG. 4.4). At the first stage, (110) plane of the bcc changes to the atomic plane arranged in a hexagon corresponding to the (0002) plane of the hcp because of the shear to the $[\bar{1}1\bar{1}]$ direction along the $(\bar{1}12)$ plane. At the second stage, every other (110) plane shifts to the $[0\bar{1}10]$ direction while it keeps the plane interval constant. The result at the first stage of this model is the same one of model I that predicts the revolution of about 5 degree of the lattice. The shear process of model II is considered valid rather than the compression and expansion process of model I because the martensitic transition is usually driven by the collective shear movement of lattice planes. The second stage of model II is the same as model I except for the

shift direction for the bcc. Two sets of the conjugate planes are identified from model II: (A) $(\bar{1}12)_{bcc} \parallel (1\bar{1}00)_{hcp}$, (B) $(110)_{bcc} \parallel (0002)_{hcp}$. Only set (A) has the similar atomic arrangement of two phases, and is considered the candidate for the interface planes. Orthogonal base vectors X_{bcc} and Y_{bcc} in the $(\bar{1}12)_{bcc}$ plane of bcc phase and X_{hcp} and Y_{hcp} for the $(1\bar{1}00)_{hcp}$ plane of the hcp phase have to be considered. The direction and length of these vectors are listed in TABLE 4.3. The evolution of base vectors X_{bcc} and Y_{bcc} is the same one as shown in FIG. 4.3(a) because $d(110)_{bcc}$ keeps constant during the transition as model I. Therefore, the interfacial plane $(\bar{1}12)_{bcc} \parallel (1\bar{1}00)_{hcp}$ can not transform the structural anomaly observed in the X_{bcc} and X_{hcp} directions to the interfacial strain driven structural distortion. In contrast, base vectors Y_{bcc} and Y_{hcp} for the pressure generate the completely desirable overlapped hysteresis loops as shown in FIG. 4.3(c). These discovery means that model II can not explain the anomalously large c at the beginning of the transition but can predict both the accurate decrement of a of the hcp structure at the beginning of the transition and the accurate increment of a of the bcc structure at the end of the transition. Therefore model II can identify the interface that corresponds to the anomalous dynamics of the lattice constant a of the bcc and the hcp phases through the interfacial strain and does not correspond to the lattice constant c of the hcp phase.

TABLE 4.3   Base vectors of the conjugate plane $(\bar{1}12)_{bcc} \parallel (1\bar{1}00)_{hcp}$.

	X_{bcc}	Y_{bcc}	X_{hcp}	Y_{hcp}
Direction	$[110]$	$[\bar{1}1\bar{1}]$	$[0001]/[110]$	$[11\bar{2}0]/[\bar{1}1\bar{1}]$
Length	$d(110)$	$\frac{\sqrt{3}}{2}a_{bcc}$	$d(0002)$	a_{hcp}
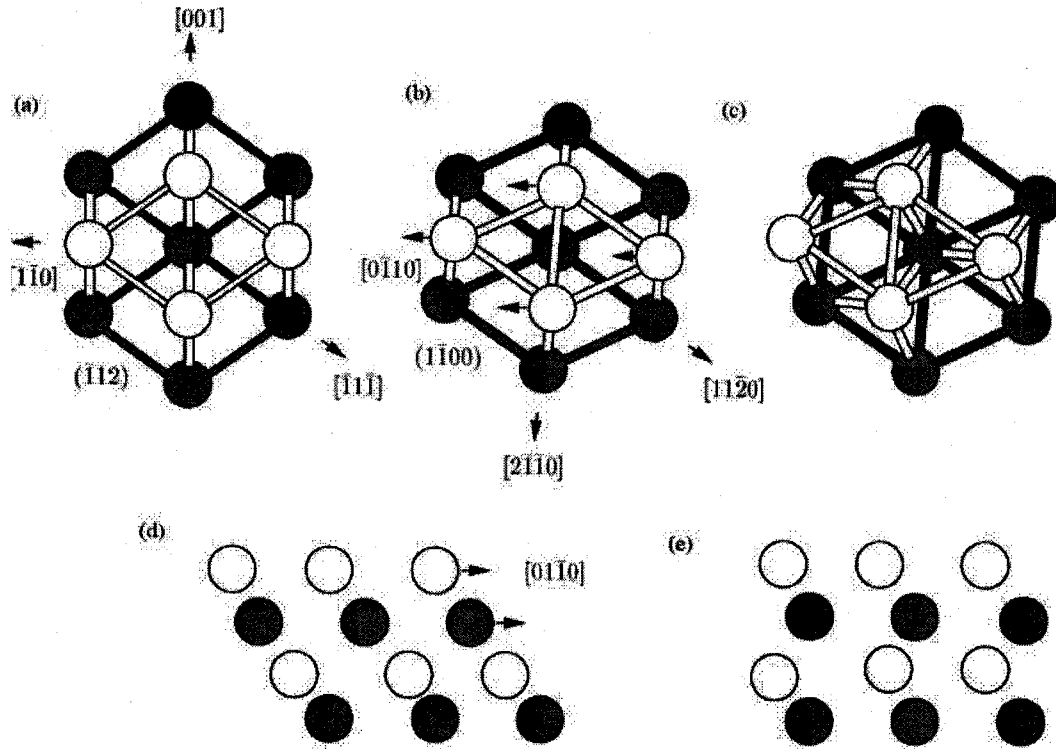
FIG. 4.4. Model II: Two-step process (a) → (b) → (c). Model III: Three-step process (a) → (b) → (d) → (e)/(c). (a) and (c) are the projected views from the [110]/[0001] directions of the bcc and hcp structures, respectively. (b) is the projected view of the intermediate structure during the bcc-hcp transition obtained from the shear of the ($\bar{1}$12) plane along the [$\bar{1}$1$\bar{1}$] direction. (d) and (e) are the projected views from the [2$\bar{1}$$\bar{1}$0] direction. (d) is the intermediate fcc phase obtained from (b) by the shear of (110)/(0001) along the [0$\bar{1}$10] direction. (e) is the hcp structure obtained from (d) by the slip of the (0001) and (0002) planes along the [01$\bar{1}$0] direction. (c) and (e) are the same hcp structure. Note that the angle between the [001] and [2$\bar{1}$$\bar{1}$] directions is not 180 but 185 degree.

Model III: Three-step process.

Model III is the three-step process proposed by Burgers [80] as an alternative plan for the bcc-hcp transition of Zirconium (FIG. 4.4). The first step is the same as model II. But for the second step, the intermediate fcc structure is obtained by the shear to the [0$\bar{1}$10]$_{hcp}$ direction along the (110)$_{bcc}$ plane. The third step that the fcc structure transforms to the hcp structure as a result of the shear of the (110) plane to the [01$\bar{1}$0] direction follows. Instead of the direct transition from the bcc to the hcp, the bcc transforms to the hcp via the fcc in this model. Although this model has an extra structure and a step, it consists of only shearing and slipping.

108

These processes are usual in the martensitic transformation compared to the shift of every other plane which is not suitable for the energetics in model I and II. Thus, model III is considered favorable from the view point of the physics.

In model III, there is a possibility that the fcc becomes metastable due to the lattice matching of the bcc and fcc structures after the little amount of the bcc-fcc transition. Therefore, the next step of the transition does not proceed without the additional pressure or a long waiting time. If this system is measured and interpreted as the bcc + hcp structures, the large lattice constant c can be detected because the fcc structure has the same c/a ratio of 1.633 as the ideal hcp structure, while the usual c/a ratio of the pure iron is 1.604. The c/a ratio reported in Ref. [65] and measured in Ref. [73] was 1.633 at the beginning of the transition. This value supports the possibility of the metastable fcc structure. In conclusion, model III can not only generate the energetically favorable pass from the bcc to the hcp but explain the large value of c and small value of a observed in Refs. [65] and [73],

Anomalously large c/a ratio was observed in Refs. [65] and [73] which reported the different dynamics of the lattice constant of the hcp structure during the transition under different experimental conditions. The structural anomaly reported in Refs. [65] and [73] possibly resulted in the metastable structure such as the intermediate fcc structure which disappears after a long waiting time and the structurally distorted interface. This anomalous was not observed in the experiment using a long waiting time [54].

The anomalous large c/a ratio decreases with the increment of the temperature as reported in Ref. [66]. The c/a ratio goes back to the normal value at 300 degrees Celsius. Due to the high thermal energy, the system can overcome the energy barrier between the metastable fcc structure and the stable hcp structure or can escape from the structurally distorted interface. Thus, the metastable structure is not observed. It is interesting that the c/a ratio become higher anomalously even at the high temperature (350 degree Celsius) in Ref. [66]. This supports the existence of the metastable fcc structure during the bcc-hcp transition. Since fcc iron itself become stable above 500 degree Celsius at the transition pressure, the metastable fcc phase becomes more stable as the temperature approaches 500 degree Celsius and the energy barrier for the stable hcp structure becomes higher. This effect makes the metastable fcc structure observable again near 450 degree Celsius, which is very close to the stable temperature of the fcc phase. Therefore, the reverse of the decreasing tendency of the c/a ratio with the temperature increment observed in Ref. [66] can be explained by the existence of the metastable fcc structure during the transition. Normal value of c and large value of a, which form the small c/a

ratio, was reported in Ref. [64]. The volume of the nucleus of the hcp decreases after the transition from the bcc. This effect can be explained by the discussion given in Ref. [65]. Voids generated by this transition can not be filled effectively by surrounding crystalline grains of the bcc due to the dome effect under isotropic stresses. Therefore, the final volume of this nucleus of the hcp tends to be a little bit larger than the normal volume under the standard pressure. The lattice constant c of the hcp nucleus is fixed by the matching with the bcc. Finally it resulted in larger value than the normal lattice constant a.

4.1.1.2 Shock induced phase transitions in iron

Shock wave propagates in the metal after the irradiation of the intense femtosecond laser on the metal surface as described in Chapter 1. Duvall and Graham reviewed widely on the shock wave dynamics in solids and the shock induced phase transition [81].

Features of shock compression of solids

Features of the shock compression of solids are as follows:

1. Adiabatic temperature increment with the increment of the entropy,

2. Realization of the ultra-high pressure state which is approximated by the static compression due to the loading of high stress above the elastic limit of the material in a ultrashort time,

3. For the planar shock wave, the shock wave is analyzed as one-dimensional flow, conservation laws of mass, momentum, and energy are formed before and behind the discontinuous shock front, and the pressure and the density under the compressed state are determined.

Propagation of the planar shock wave and the Hugoniot function

For one-dimensional compression by the planar shock wave propagating in solids at supersonic velocity, the shock front proceeds at the velocity of U_S and accelerates the material particle to the velocity of U_P. Conservation laws of mass, momentum, and energy are formed before and behind the shock front, so that the following equations are derived:

$$\rho_0 U_S = \rho_H (U_S - U_P),$$ (4.1)

$$p_H - p_0 = \rho_0 U_S U_P,$$ (4.2)

$$E_H - E_0 = \frac{1}{2}(V_0 - V_H)(p_H + p_0).$$ (4.3)

where p is the pressure, ρ is the density, E is the energy, V is the constant volume (= $1/\rho$), and

110

subscript 0 and H indicate states before and after shock compression, respectively. Eq. (4.3) is called the Rankin-Hugoniot equation of state.

When the change of the state such as the phase transition is not occurred, it is known empirically that the shock velocity and the particle velocity have the linear relation:

$$U_S = c + sU_P,$$ (4.4)

where it is suggested that c corresponds to the bulk sound velocity $\sqrt{K_0/\rho_0}$, and s corresponds to $(K_0' + 1)/4$ using the pressure derivatives K_0' of the bulk modulus K_0.

Shock induced phase transition of solids and generation of multi-structured shock wave

When the shock pressure is sufficiently large compared to the yielding stress of the material and the phase transition which causes the discontinuous decrement of the volume due to the shock compression occurs, the incident single shock wave becomes unstable and changes to the multi-structured shock wave (FIG. 4.5). This is interpreted as the stress relaxation due to the decrement of the volume. When the phase transition occurs and the material transforms to the high density state, the inflection corresponding to the phase transition is formed in the Hugoniot curve. The intersection point of the Hugoniot curve with the Rayleigh line which is expanded from the origin O to the transition point A makes the point C. When the shock pressure is between A and C, double-structured shock wave is generated. For the shock pressure above C, the shock wave remains single.
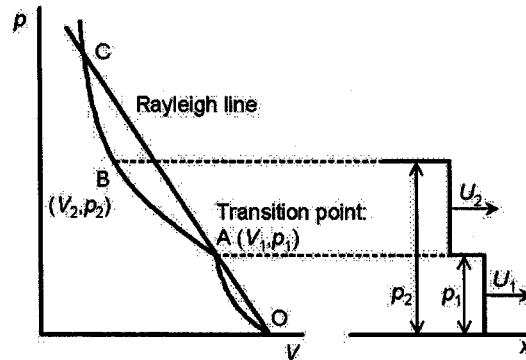
FIG. 4.5.   Generation of double-shock waves resulted from a phase transition.

p

R_1 C

R_2: Elastic

D

S_3: Plastic II

B: Transition point

R_3: Plastic

S_2: Plastic I

A: HEL

p_{HEL} S_1: Elastic precursor

E   O x
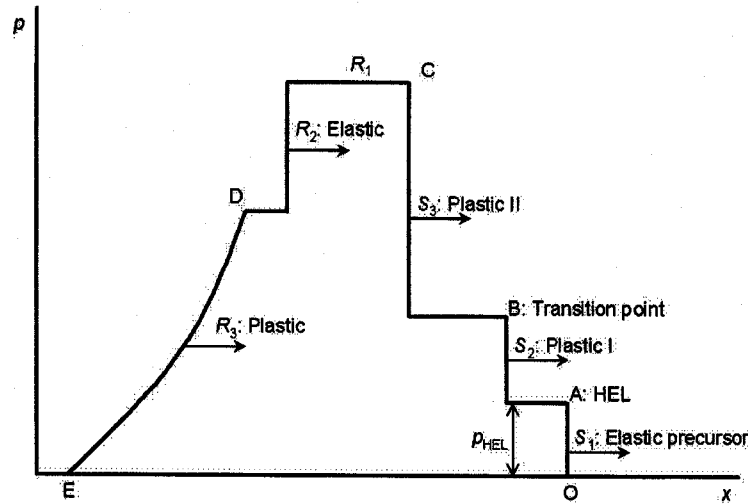
FIG. 4.6. Pressure distribution in a pulse propagating through a material undergoing a phase transition.

When the shock pressure is close to the yielding stress of the material, the strength effect of the material has to be considered. This case is well described as the elastic-plastic model shown in FIG. 4.6. Instantaneous compression on the solid surface and the following stress pulse formed by the pressure unloading have the beginning, the middle, and the final stages. The beginning stage is the shock front, nearly discontinuous compression. The middle stage is the region where the pressure, the density, and the temperature keep constant or vary slowly. The final stage is the rarefaction which returns the material to the beginning state. S_1 proceeds at the velocity of the compression wave, which is the elastic shock limited to the pressure below the shear strength of the material. The material is brought to the plastic deformation point by S_1. The deformation does not occur before S_2 reaches. The second shock S_2 is the plastic deformation wave, which is often called the plastic I wave. The pressure of S_2 is limited to the transition point. S_2 compresses the material to the boundary of the mixture region in the reversible transition. The transition does not occur till the plastic II wave S_3 arrives. The transition occurs inside the shock front S_3, and the transformation is completed if the driving pressure is sufficiently large. The magnitude of S_3 is determined by the driving pressure. S_3 propagates slower than S_2, which is slower than S_1. The material is relaxed to the equilibrium state in regions which are divided by S_1, S_2, and S_3. R_1 is the rarefaction relaxation wave, which just follows S_3. R_2 is the rarefaction elastic shock wave, which is related to the phase transition which is separated by S_2 and S_3. Finally, the rarefaction plastic wave R_3 follows. In FIG. 4.6, the point A is called the Hugoniot Elastic Limit (HEL), and OA, ABC, CD, and DE show the elastic

compression process, the plastic compression process, the elastic pressure unloading process, and the plastic pressure unloading process, respectively.

Shock induced phase transition in iron

A shock induced $\alpha \leftrightarrow \varepsilon$ phase transition in iron is one of the most famous transitions under high pressure. It was first reported by Minshall [50], and the Hugoniots in these two phases were measured first by Bancroft *et al.* [51]. The thermodynamically equilibrium Hugoniot was calculated by Andrews [58], and it was found different greatly from the experimental results. Forbes observed the decay of S_2 wave and estimated the relaxation time τ of $\alpha \rightarrow \varepsilon$ transition at $\tau = 50$ ns [60]. Barker and Hollenbach performed the high resolution VISAR measurement of the shock profile in iron [59]. They obtained the correct Hugoniot data from the experiments and estimated $\tau = 180$ ns. These Hugoniot data are shown in FIG. 4.7. Static compression curve measured by Mao *et al.* [54] and Giles *et al.* [57] is also shown. Boettger and Wallace reported the metastability and the dynamics of the $\alpha \rightarrow \varepsilon$ transition of iron [72]. They reported that the relaxation time τ of the $\alpha \rightarrow \varepsilon$ transition depends on the shock intensity and that τ is $60 \rightarrow 12$ ns for shocks of $17 \rightarrow 30$ GPa. Although τ represents the linear irreversible thermodynamic relaxation, it was shown that some nonlinear relaxations should exist in the shock process of iron. The shock induced $\alpha \leftrightarrow \varepsilon$ phase transition is considered complete reversible. No ε phase remains in the recovered iron because the $\varepsilon \rightarrow \alpha$ phase transition is induced by the unloading wave after the $\alpha \rightarrow \varepsilon$ phase transition is induced by the shock wave. On the other hand, for an irreversible type of phase transition, a high pressure phase can be quenched as a metastable state after unloading. For instance, diamond is synthesized from graphite using the shock compression and rapid quenching method [132-141]. High-pressure phases of Si_3N_4 [142-145], SiC [146,147], BN [148,149], and so on are also synthesized using conventional shock compression methods.

The extended line from the point where $V/V_0 = 1$ to the transition point intersects with the Hugoniot at about 40 GPa. Therefore, shock wave in iron has double structure and single structure for shocks 13 GPa $< p_H < 40$ GPa and $p_H > 40$ GPa, respectively.

The yielding stress of α-iron is 0.3 GPa. The shock pressure p and the normal stress σ in the shock compressed solid have the following relation:

$$\sigma = p + \tfrac{4}{3} y . \tag{4.5}$$

For iron,

$$\sigma = p + 0.4 \text{ GPa}. \tag{4.6}$$

113

Therefore, $\sigma \approx p$ for the overdriven shock of $p_H > 40$ GPa.
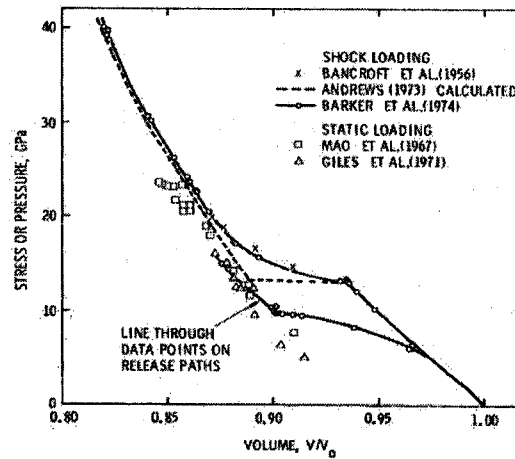
FIG. 4.7. Hugoniot and quasi-static $p(V)$ data of iron obtained by shock loading and static loading, respectively.

4.1.1.3 Laser induced phase transitions in iron

Laser induced phase transition in iron using nanoseconds high power laser and low power laser were studied. Laser driven shock and high temperature induced phase transitions are indicated for high and low power lasers, respectively. Femtosecond laser induced phase transition has never been investigated.

When the low power laser is irradiated on the iron surface, intense shock wave does not generated. Only temperature wave propagates into the iron sample, and this induces the high temperature phase transition. Teodorescu *et al.* investigated the α to γ phase transition using the high resolution TEM when KrF excimer laser was irradiated on the thin iron film in air [82,83]. If the laser pulse is absorbed only in the thin film and the pulse is over during the film attaches to the substrate, the cold substrate acts as a thermal sink. The thin films is rapidly heated and cooled. As a result of the laser heating, the structure is annealed. In this case, the heating rate is 10^{10} K/s, and the cooling rate is considered equally rapid. C (5 nm)/Fe (40 nm)/C (5 nm) was deposited on the KCl monocrystalline substrate. C was deposited for the prevention of oxidation. KrF excimer laser used had the pulse width of 20 ns and the fluence of $50 - 100$ mJ/cm^2. As a result of the observation using the high resolution TEM, the existence of γ phase was verified and the relation with α phase is close to the Kurdjmov-Sachs relation. The feature of this laser induced α to γ phase transition is the appearance of the microscopic mixed state of α phase and γ phase which shows the incomplete transition in the same crystalline block. This is different from the classical martensitic transformation because this is induced by the temperature rise and

114

the surface diffusion and the crystal growth process are followed.

The shock wave propagates in the metal and the intensity approaches to hundreds of GPa depending on the laser intensity when the high power laser is irradiated on the metal surface as described in Sec. 1.3. High power laser driven shock induced $\alpha \leftrightarrow \varepsilon$ phase transition in iron was first reported by Romain $et\ al.$ in 1987 [84]. Lasers with the pulse width of 2.5 and 25 ns and with the laser intensity of 7×10^{13} and 5.4×10^{14} W/cm^2 generated the shock wave with the intensity of 60 and 240 GPa. These shocks were applied to the monocrystalline and polycrystalline irons. As a result of the observation of the recovered samples after laser irradiations, high density deformation with the needle-like microstructure which is characterized by the appearance of the $\alpha \leftrightarrow \varepsilon$ phase transition was shown. The $\alpha \leftrightarrow \varepsilon$ phase transition was suggested from the existence of the needle-like structure. Existence of ε phase in the recovered sample was not reported. The similar experiments were performed later [85-87]. High density of twins and the needle-like structure existed in the recovered sample and suggested the $\alpha \leftrightarrow \varepsilon$ phase transition. Existence of the ε phase in the recovered sample was not also mentioned.

4.1.3   Purposes

Femtosecond laser is absorbed, and thermal conduction occurs into the sample at supersonic velocities before mass has time to ablate. Eventually ablation occurs and drives a mechanical shock into the material [112-114]. Eventually the thermal front cools and its velocity drops below that of the following ablation shock. The shock front passes the thermal front and the shock then traverses unheated material. The amplitude of the shock pressure decreases continuously to zero with increasing propagation distance. However, the region behind the shock front remains in thermal equilibrium [115,116]. Thus, ε-iron is made by such a conventional shock wave.

The pulse width of the laser used in the present study is 120 fs. The author would like to illustrate how short the laser pulse is by relating the 120 fs time width to the vibrational period of a phonon at the Debye temperature. The Debye temperature of ε-iron at high pressures is approximately 700 K [22].The vibrational period of this phonon is 7×10^{-14} s, which means that 120 fs is the time it takes for only two phonon vibrations. This is not expected to be long enough to drive a phase transition, which is evidence that the femtosecond laser pulse itself does not synthesize ε-iron. As described above, on the other hand, this implies that the α to ε transition is driven by the conventional shock wave that forms.

Even though high pressure and/or high temperature states are anticipated to occur in a region which is influenced by the femtosecond laser irradiation, phase transitions induced by the

irradiation have never been investigated.

The purposes of this chapter are, first, to observe the femtosecond laser induced phase transition in a recovered iron sample and, second, to determine the high pressure and/or high temperature phases crystallographically. The electron backscatter diffraction pattern (EBSP) [88], TEM, and synchrotron X-ray diffraction methods were used to determine the crystalline structure in a recovered sample (Secs. 4.2 and 4.3). Thermodynamic states inside the shock wave front are required to know because the transition occurs inside the wave front. Thus, temperatures inside the shock wave fronts are calculated using the equilibrium thermodynamic theory in Sec. 4.4. Correct thermal properties of iron under shock compressed states are required to calculate the inside temperature correctly. Thus, the thermal properties of iron are determined up to 400 GPa using Hugoniot functions in Sec. 4.3. The derail of the femtosecond laser driven shock quenching of the ε phase in iron is explained in Sec. 4.6.

4.2 Experiments

Polycrystalline iron (purity: 99.99%) was used as a target and annealed at 1200 K under a low pressure of 10^{-3} Pa for 72 hours to increase the size of the crystalline grains. The obtained grain sizes were on the order of a millimeter. The laser pulses can be irradiated on the single crystalline grain surface because the spot diameter of the laser beam of ~ 50 μm is small enough compared to the grain sizes. The femtosecond laser described in Sec. 1.4 (Spectra-Physics Inc., Spitfire; wavelength: 800 nm, pulse width: 120 fs) was irradiated on the iron surface polished.

4.3 Experimental results

4.3.1 Determination of the crystalline structures using the electron backscatter diffraction pattern system

FE-SEMs with minimum spatial resolution of 10 nm (Japan Electron Optics Laboratory Co., Ltd., JSM-6500F) equipped with EBSP systems (Oxford Instruments plc and TexSEM Laboratories Inc.) were used to determine the crystalline structure in a recovered iron sample. The electron beam was focused on a relevant part of the polished surface, and the orientations of the backscattered diffracted channeling patterns were determined using the EBSP system. The schematic illustration of the EBSP system is shown in FIG. 4.8. EBSP is the diffracted pattern of the backscattered electrons from the area where a focused electron beam is irradiated. The diffracted pattern depends on the crystalline structure. Crystalline structure where the electron beam is irradiated can be determined by analyzing the patterns [88].

A groove (~ 50 μm width and ~ 100 μm depth) was formed on the surface by scanning the laser beam with a Gaussian profile of the intensity of 8.0×10^{13} W/cm^2, of which 2000 pulses were directed to a point on the groove surface. This laser intensity is intense enough to induce the solid – plasma direct transition. A cross section of the sample perpendicular to the groove was polished after having been embedded in resin (FIG. 4.9). The crystalline structures of the iron solid which was influenced by the femtosecond laser irradiation were analyzed using the EBSP system.

Focused Electron Beam

Detector

Backscattered electrons
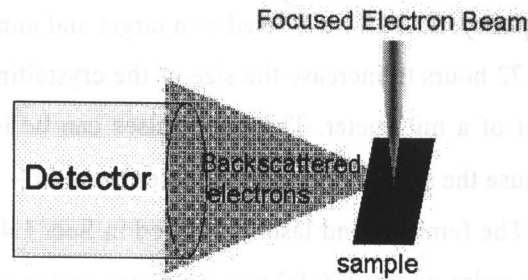
sample

FIG. 4.8.   Schematic illustration of EBSP.

Resin   Laser

Iron   10 μm

JSM-6500F   SEI   20.0kV   X3.000   1 μm   WD 19.2mm
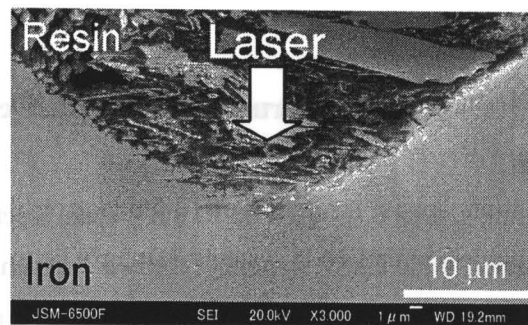
FIG. 4.9.   Cross section of the iron sample perpendicular to groove formed using femtosecond laser pulses. The laser was irradiated from up to down in the figure.

The results of the EBSP analysis are shown in FIG. 4.10. FIG. 4.10 (a), (c), (e) indicate the EBSPs at the position of several μm deeper from the bottom surface, and FIG. 4.10 (b), (d), (f) indicate the corresponding determined crystalline orientations, where red-, purple-, and yellow-colored lines indicate patterns originated from the α, ε, and γ phases, respectively. Patterns originated from not only the ε phase but a bit of the γ phase are confirmed in the figures. EBSPs which originated from the hcp and fcc structures are not observed in the area below 10 μm deeper from the bottom surface. The hcp and a little bit of the fcc structures are found to appear down to microns deeper from the bottom surface. These results contribute to the quenching of the hcp and a little bit of the fcc structures.

118

FIG. 4.10. (a), (c), and (e) EBSPs detected from the area several μm deeper from the bottom surface of the groove. (b), (d), and (f) Crystallographic orientations determined using EBSP system corresponding to (a), (c), and (e), respectively, where red-, purple-, and yellow-colored lines indicate orientations resulted from bcc (α phase), hcp (ε phase), and fcc (γ phase) structures, respectively.

119

FIGURE 4.11 illustrates the EBSP phase mapping data, where red, yellow, and green colors indicate α, ε, and γ phase, respectively. The black area indicates the resin or the area where any patterns were not detected. Crystalline grains of the ε phase with the typical size of several nanometers are scattered around 4 µm deeper than the bottom surface of the groove. Crystalline grains of the γ phase exist along the interface of the α grains. These results also contribute to the quenching of the hcp and a little bit of the fcc structures.

3.60 µm = 90 steps
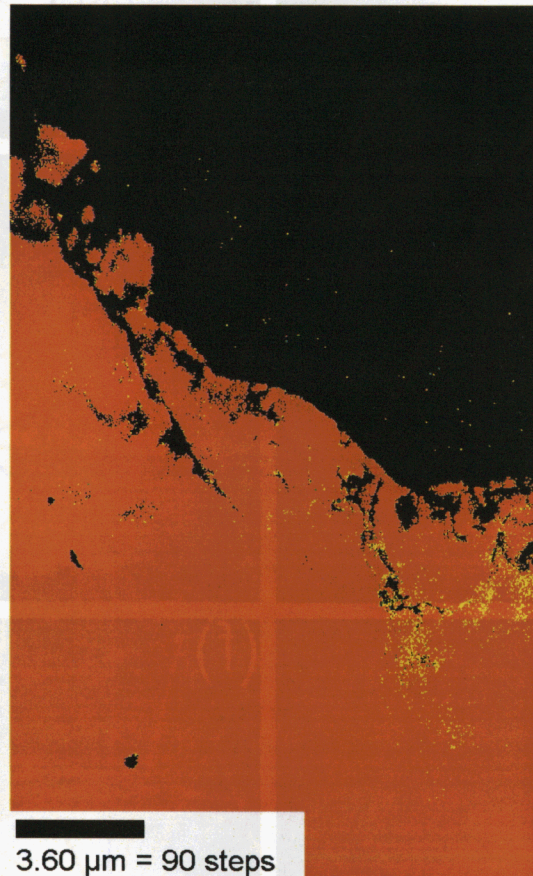
FIG. 4.11.   An EBSP mapping result. Red, yellow, and green indicate bcc (α phase), hcp (ε phase), and fcc (γ phase), respectively. Both hcp and fcc structured crystals are scattered as nanocrystals down to approximately 4 µm deeper from the bottom surface of the groove.

4.3.2 TEM observation

Microstructures in the laser irradiated region were observed using TEM and the structures in the region were determined by the selected area diffraction patterns. Laser irradiated sample was the same annealed polycrystalline iron (purity: 99.99 %, $10 \times 10 \times t1$ mm^3) as that used in the EBSP analysis. The femtosecond laser (wavelength: 800 nm, pulse width: 120 fs, intensity: 10^{14} W/cm^2, linear polarization) was focused by the single lens with the focal length of 70 mm and irradiated on the polished iron surface in air. Only single pulse was irradiated at a point each 100 μm steps, which is different from the case of the EBSP analysis. Multiple pulses were not irradiated at a point because the focused spot size of the laser was about 50 μm. The laser irradiated region which is parallel to the surface plane was made thin by polishing and observed by TEM. TEM observation results are shown in FIGs. 4.12-4.15 ((a) for a TEM image, (b) for a diffraction pattern, and (c) and (d) for key diagrams). Each figure shows results at different place irradiated under the same condition. Moiré fringes are observed in FIG. 4.12(a). But the crystalline structure determined is only α phase. Diffraction pattern at the interface of grains is shown in FIG. 4.13(b). ε and γ phases are determined in the region, which is agreement with the EBSP result. Analyzed results in other regions are shown in FIG. 4.14(c) and 4.15(c). Two diffraction patterns originated from two different crystalline structures are analyzed. The one is determined as α phase, but the other is not determined as any iron phases such as α, ε, γ phases, iron oxides, and iron carbides. Other analytical methods such as X ray diffraction are required to determine these unidentified patterns.

121

Beam // α-Fe (bcc) [-1 1 1]
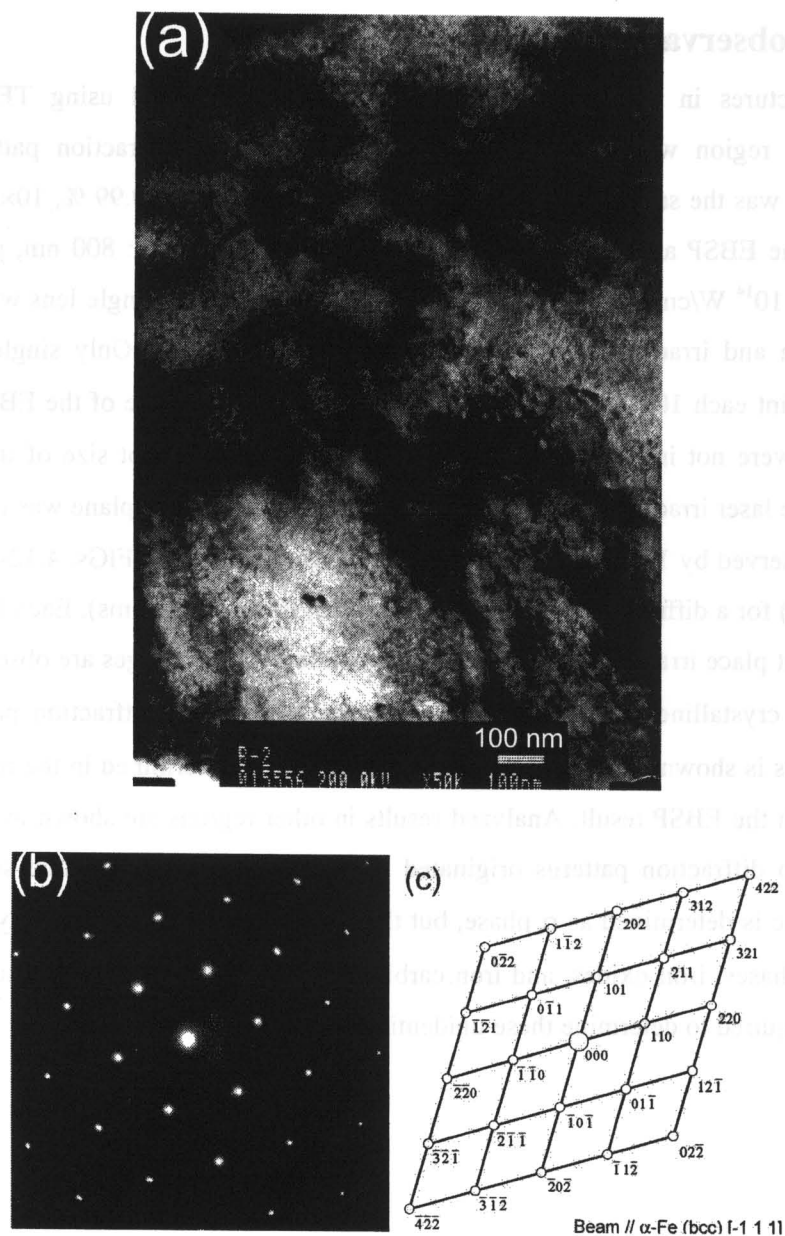
FIG. 4.12. (a) TEM image, (b) SAD pattern, and (c) key diagram of the laser irradiated iron.
Only α-Fe exists in this sample.
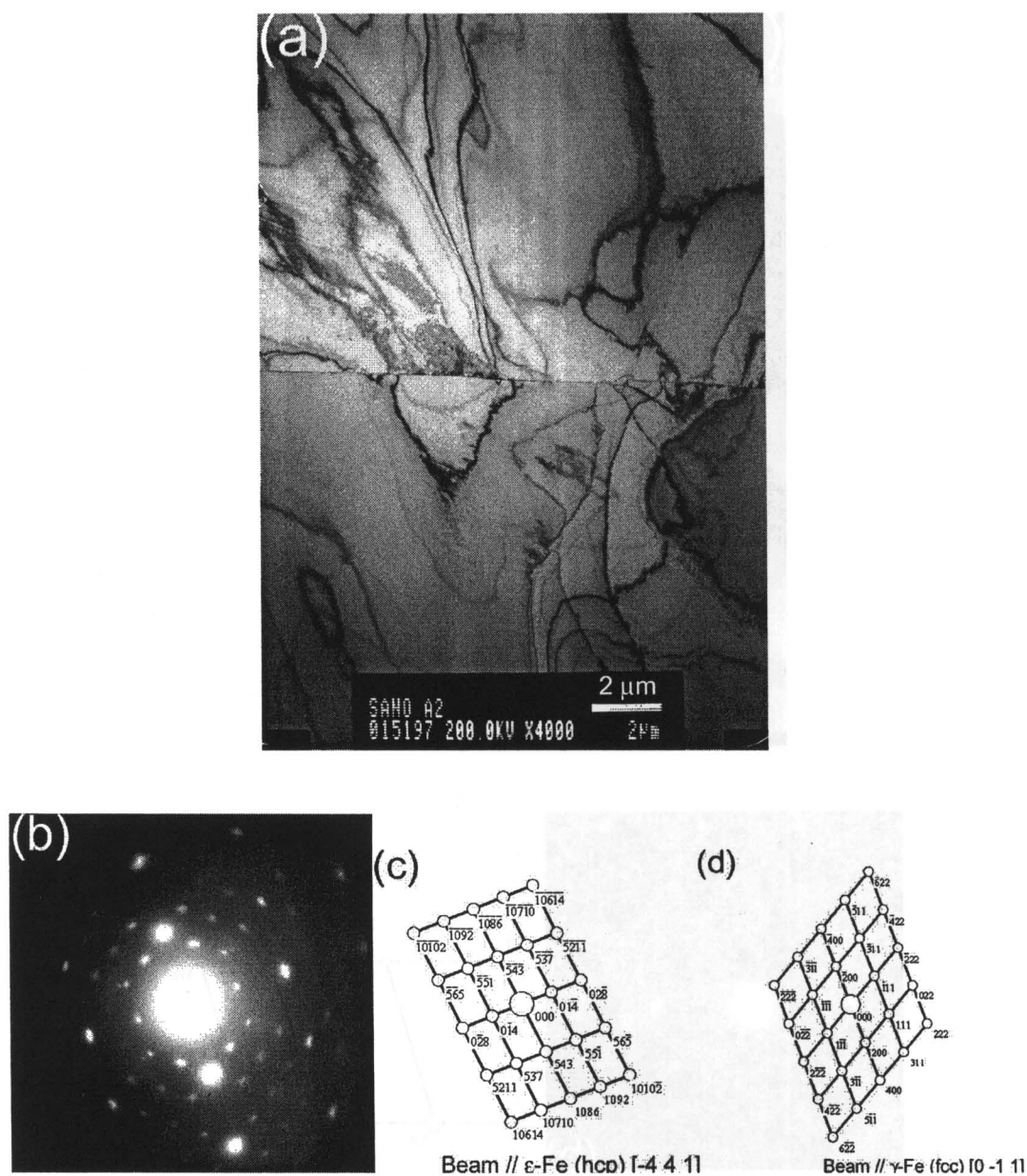
FIG. 4.13. (a) TEM image, (b) SAD pattern, and (c) key diagram at the interface of grains of the laser irradiated iron. ε-Fe and γ-Fe exist at the interface. This result corresponds to the EBSP analysis.
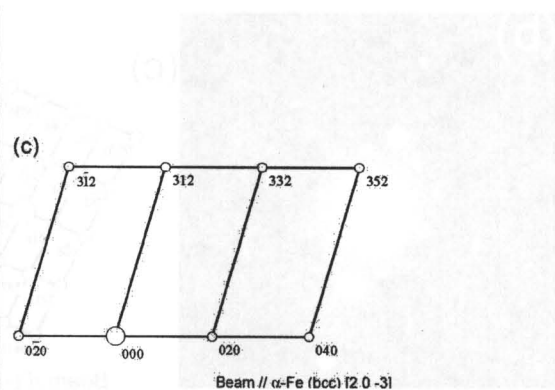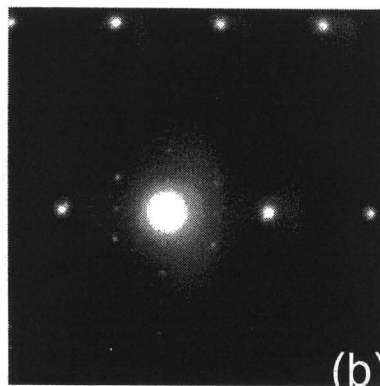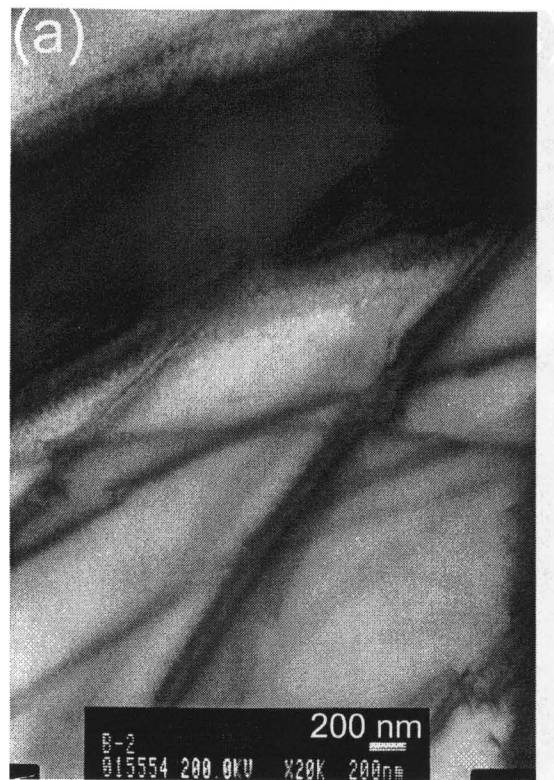
FIG. 4.14. (a) TEM image, (b) SAD pattern, and (c) key diagram of the laser irradiated iron. Two SAD patterns originated from two different structures are observed. The one is determined as α-Fe, but the other is not identified.
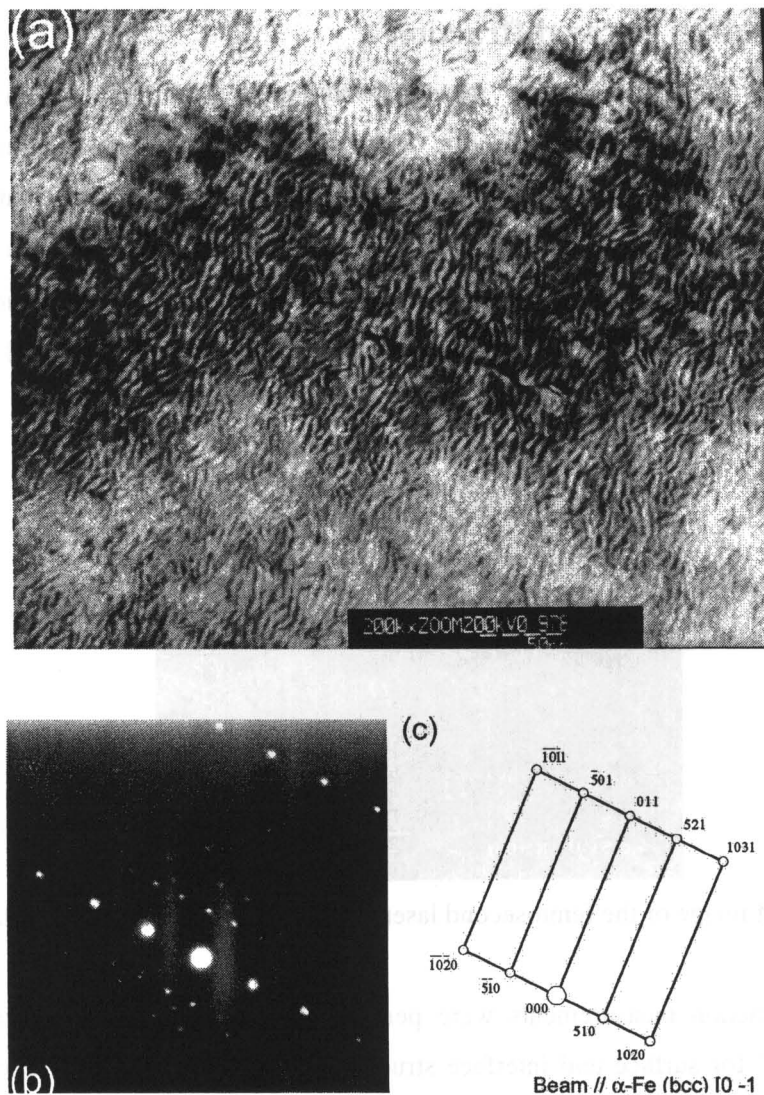
FIG. 4.15. (a) TEM image, (b) SAD pattern, and (c) key diagram of the laser irradiated iron. Two SAD patterns originated from two different structures are observed. The one is determined as α-Fe, but the other is not identified.

4.3.3 Synchrotron X-ray diffraction

Synchrotron X-ray diffraction measurements were performed to determine the crystalline structures in the recovered iron target after the femtosecond laser irradiation. Annealed polycrystalline iron (purity: 99.99 %) was used as a target. A femtosecond laser pulse (wavelength: 800 nm, pulse width: 120 fs, spot size: approximately 50 μm, pulse energy: 0.60 mJ/pulse, average intensity: 6.4×10^{13} W/cm^2, average fluence: 7.6 J/cm^2) was irradiated on the polished iron surface in the Ar atmosphere. The laser pulse was irradiated each 50 μm steps on the surface. SEM image of the irradiated surface is shown in FIG. 4.16.
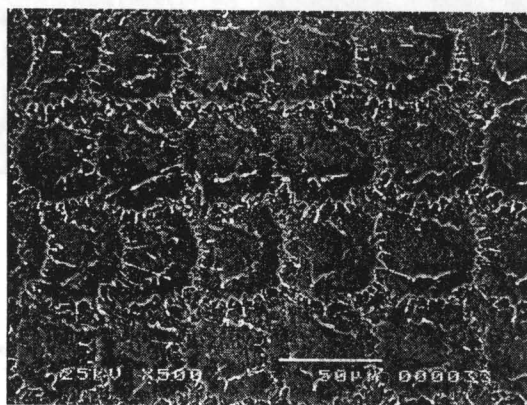
FIG. 4.16.   SEM image of the femtosecond laser irradiated surface of a polycrystalline iron.

X-ray diffraction measurements were performed using a six-circle diffractometer at beamline BL13XU for surface and interface structures, SPring-8. The layout and the photon flux as a function of the incident photon energy are shown in FIG. 4.17(a) and (b), respectively [129]. Photon energy 12.4 keV, wavelength 1 Å was used in this measurement. The incident angle was fixed and the detector angle was varied.

Spectrum measured at the incident angle of 0.5 deg, 0.05 deg/step, 2 s/step is shown in FIG. 4.18. The α-Fe (110), (200), (211), and (220) peaks were found. As described earlier, the quenched ε and γ phases exist at several μm deeper from the surface and their quantities are small. Therefore, the incident angle was fixed at 1.0 deg in order to the incident X-ray can penetrate into the sample deeper and measurements were performed at 0.05 deg/step and 100 s/step out of the peak angles of α-Fe. Spectra for the detector angle of 30 − 34, 45 − 49, and 52 − 58 are shown in FIGs. 4.19, 4.20, and 4.21, respectively. (a) shows the raw data measured and (b) shows the data from which the background is subtracted. In FIG. 4.19, two peaks of ε-Fe (101) are found. In FIGs. 4.20 and 4.21, peaks of ε-Fe (110) and ε-Fe (103) are found,

respectively. Two Gaussian curves are fitted to peaks of ε-Fe (110) and ε-Fe (103) because two peaks of ε-Fe (101) are found. Fitted peak angles, the corresponding crystalline structures and d-spacings, and previously reported d-spacings are listed in TABLE 4.4. The reason for two peaks of the same plane will be considered in Sec. 4.6.
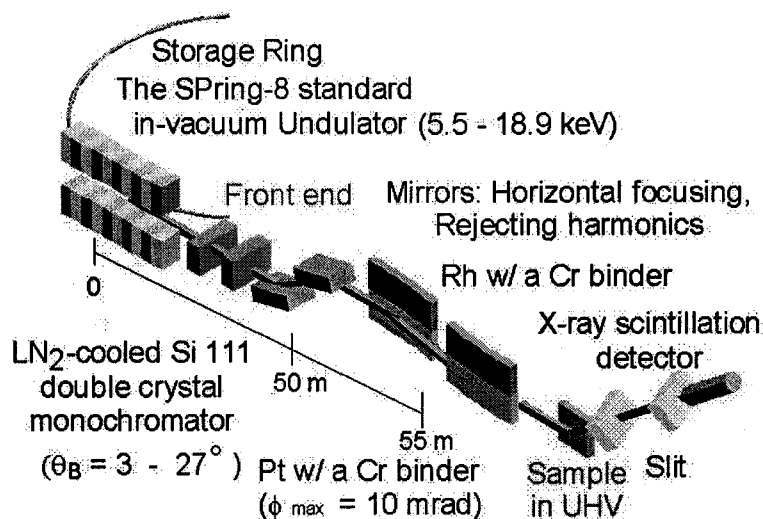
FIG. 4.17.   (a) Layout of BL13XU at Spring-8 [129].
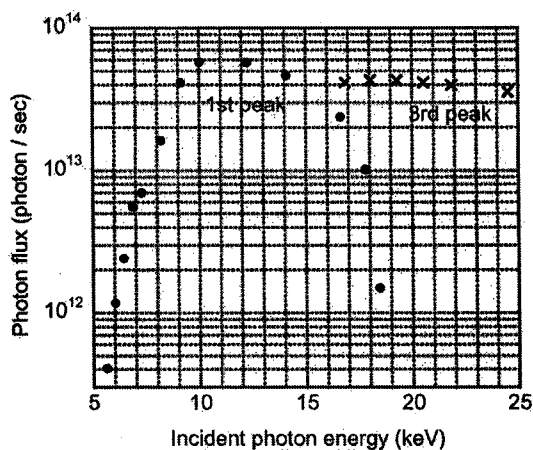
FIG. 4.17.   (b) Absolute X-ray photon flux densities measured [129]. 12.4 keV was used in this measurement.
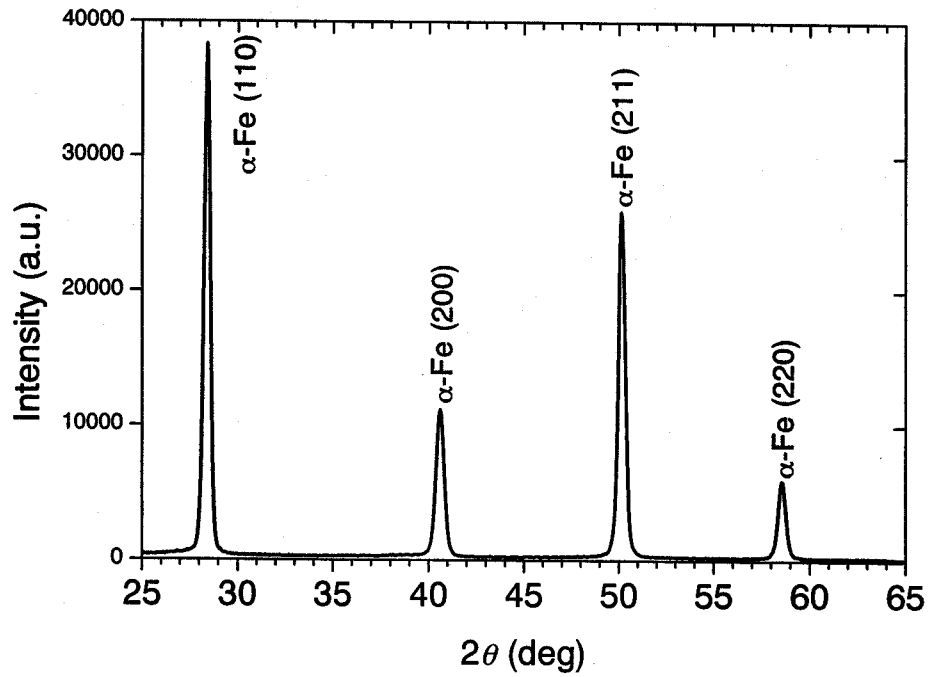
FIG. 4.18. X-ray diffraction spectrum as a function of 2θ (deg) for the femtosecond laser irradiated polycrystalline iron.

TABLE 4.4. List of peaks detected.

	Peak position (deg)	Estimated d-spacings (Å)	Previously reported d-spacings (Å)
ε-Fe (101)	31.29	1.853	1.864 at 31.76GPa, 1300 K [130]
	31.82	1.823	1.840 at 19.2 GPa, 300 K [131]
ε-Fe (110)	47.38	1.243	1.234 at 19.2 GPa, 300 K [131]
	47.88	1.232	1.220 at 31.76GPa, 1300 K [130]
ε-Fe (103)	53.66	0.8615	1.119 at 31.76GPa, 1300 K [130]
	53.97	0.8569	1.113 at 19.2 GPa, 300 K [131]
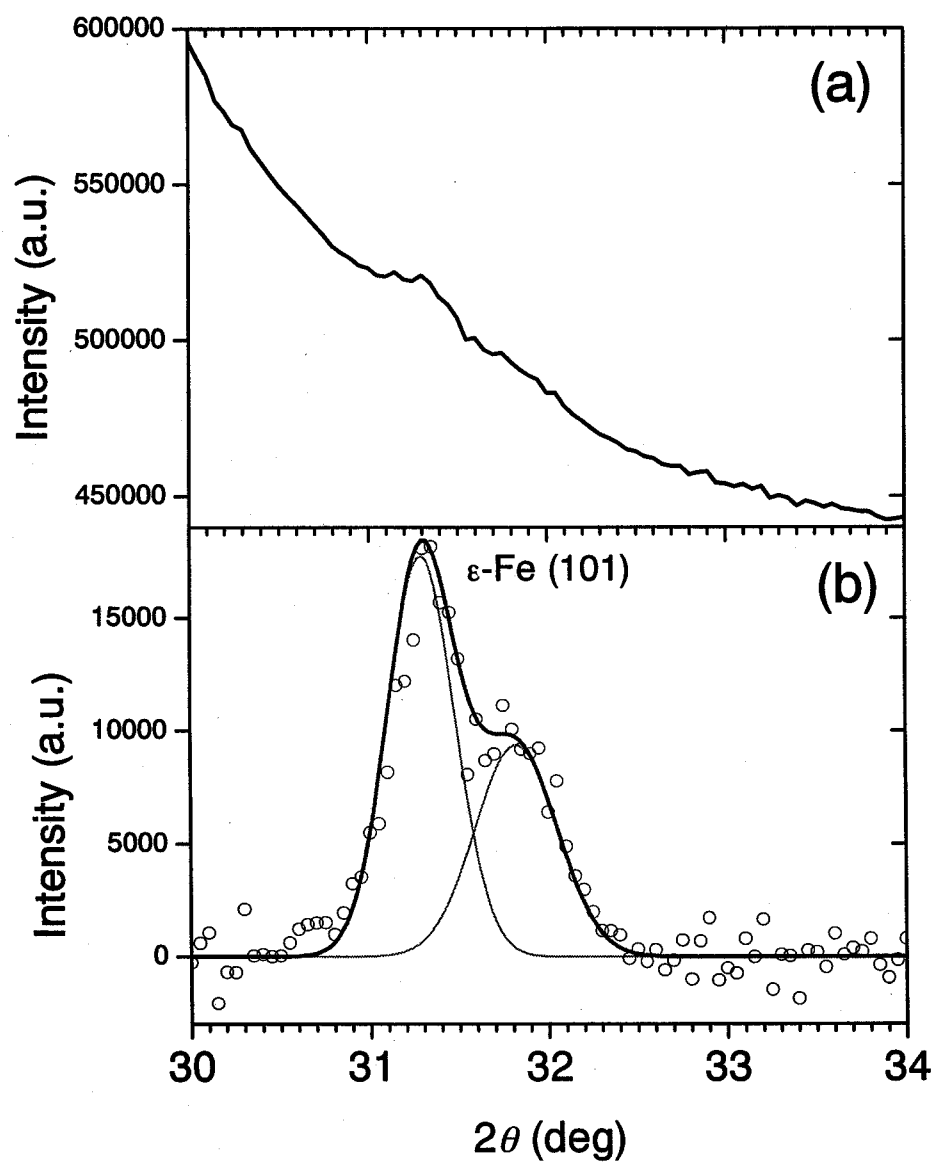
FIG. 4.19. SR-XRD spectrum from 30 to 34 deg for 2θ. (a) raw data and (b) Background is subtracted from the raw data and two Gaussian curves are fitted.
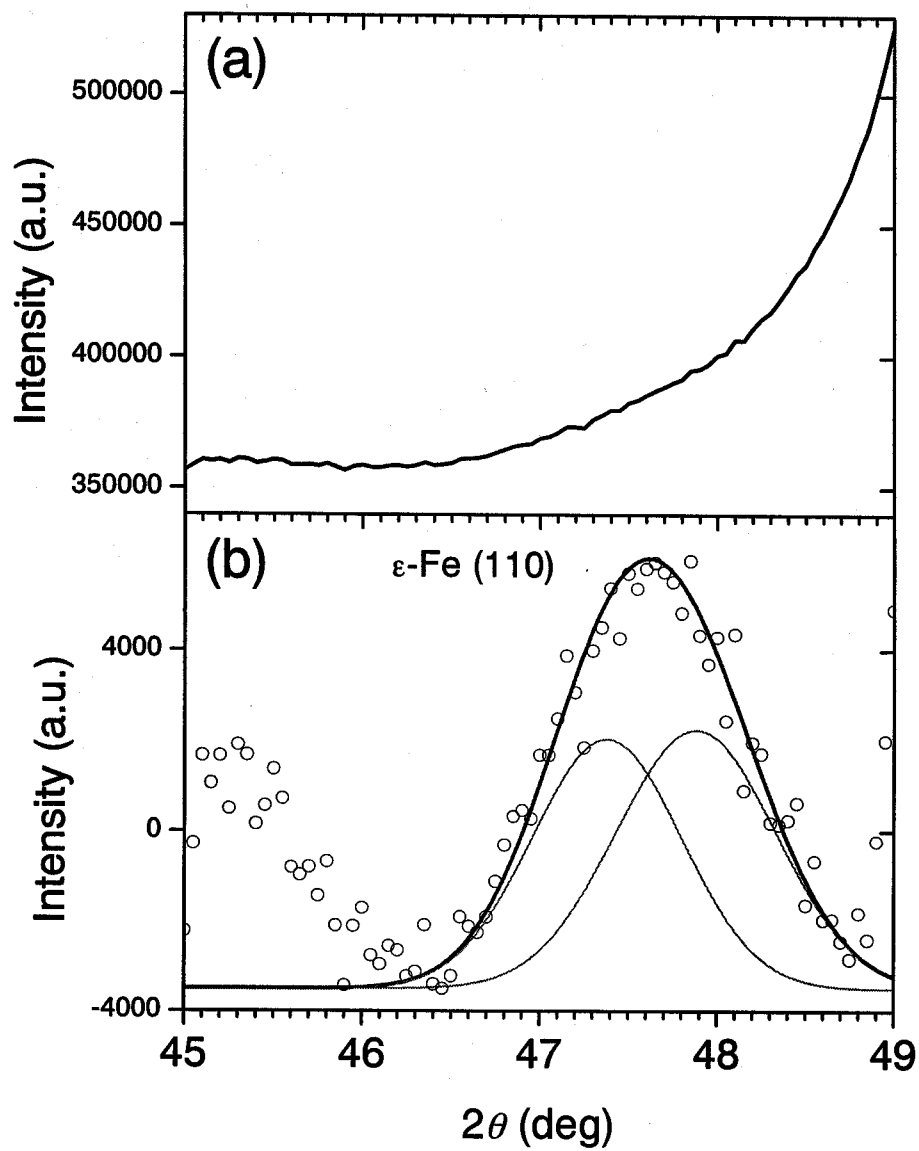
FIG. 4.20. SR-XRD spectrum from 45 to 49 deg for 2θ. (a) raw data and (b) Background is subtracted from the raw data and two Gaussian curves are fitted.
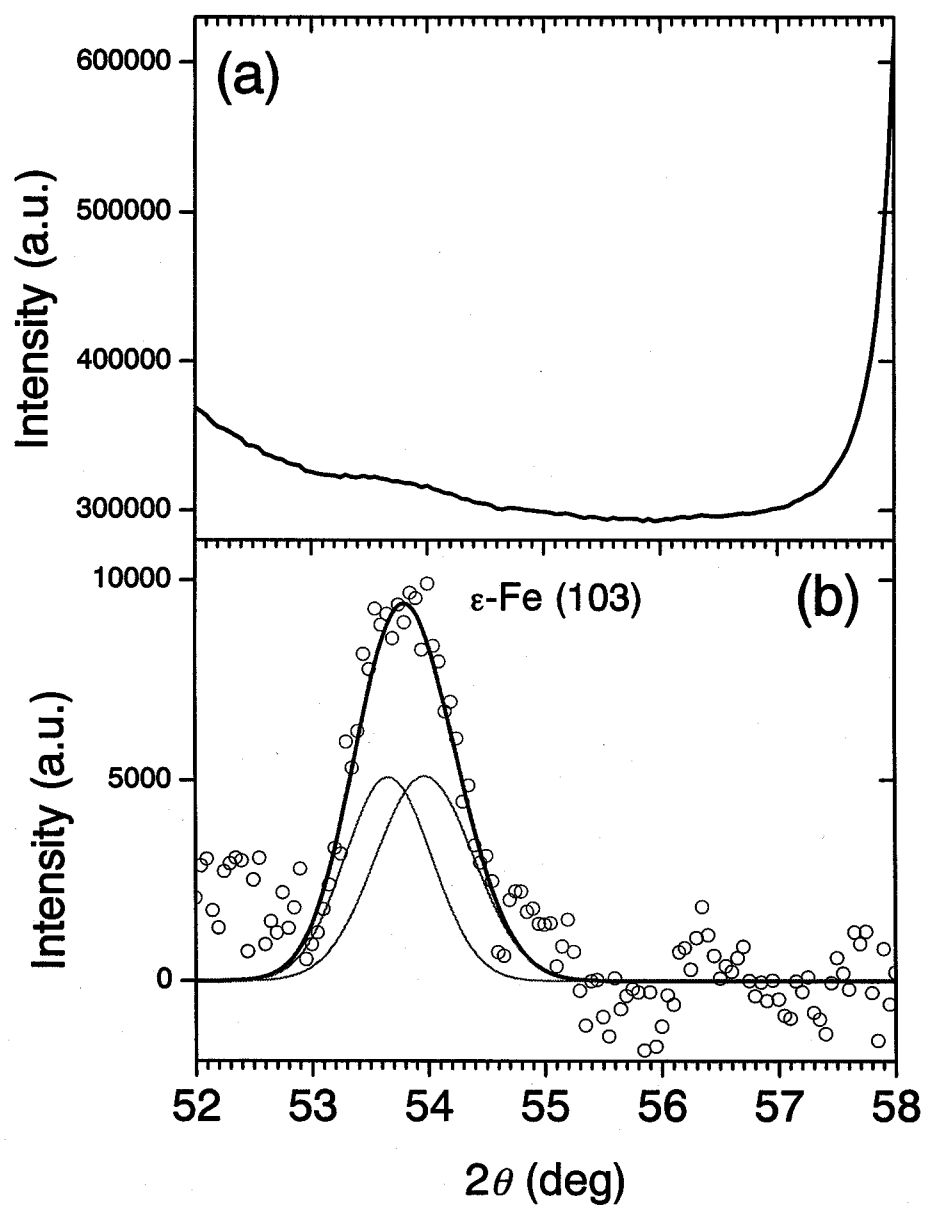
FIG. 4.21.   SR-XRD spectrum from 52 to 58 deg for 2θ. (a) raw data and (b) Background is subtracted from the raw data and two Gaussian curves are fitted.

131

4.4 Thermal properties of close-packed iron up to 400 GPa determined using Hugoniot functions

A quadratic equation for the temperature-independent Grüneisen parameter γ was derived by a method in which the Walsh-Christian and Mie-Grüneisen equations are combined. The inefficacy of some existing *ab initio* temperature Hugoniots for hexagonal close-packed solid iron was found by revealing the abnormality of the constant-volume specific heats on the Hugoniots C_{VH}, which are related uniquely to γ. A normal C_{VH} distribution in the solid phase range was demonstrated to agree approximately with a previous *ab initio* distribution. In contrast, the corresponding γ distribution was significantly different from the *ab initio* distribution in the lower pressure region, and the γ distribution in the liquid phase range had a considerably larger gradient than the *ab initio* distribution. The causes of these disagreements are clarified.

4.4.1 Introduction

The thermoelastic properties of hexagonal close-packed (hcp) iron at pressures up to 400 GPa were recently investigated using the *ab initio* approach. Wasserman, Stixrude, and Cohen [37] used a tight-binding total-energy method and the cell model of the vibrational partition function, while the calculations of Alfè, Price, and Gillan [34] were based on density-function theory (DFT) using a generalized-gradient approximation. The Hugoniot pressures calculated by Cohen *et al.* [37] agreed almost perfectly with the experimental data of Brown and McQueen [47] in the region of 150 to 240 GPa, as did the different statistical-mechanical calculations of Alfè *et al.* [34]. The temperature Hugoniots calculated by Cohen *et al.* [37] and Alfè *et al.* [34] approximate that of Brown and McQueen [47].

The constant-volume specific heats on the isotherms calculated by Cohen *et al.* [37], however, are significantly smaller than those of Alfè *et al.* [34]. The main reason for this seems to be the anharmonic corrections included by Alfè *et al.* [34]. Moreover, there is a crucial difference between the Grüneisen parameters on isotherms in the lower pressure region in the solid phase range predicted by both groups. The distributions of Cohen *et al.* increase rapidly with a decrease in pressure in the lower pressure region, whereas those of Alfè *et al.* vary only slightly in the solid phase range. It is important that we clarify the cause of this enigmatic difference between these distributions in the lower pressure region, because assumptions or estimates of the values of the Grüneisen parameter have a key role in constructing parameterized equations of state for iron [35]. We attempted to investigate the cause of the

difference by predicting the thermal properties of iron using classical thermodynamics, and without relying on the *ab initio* method.

In this study, we derive a quadratic equation for the Grüneisen parameter using a method that combines the Walsh-Christian and Mie-Grüneisen equations [89,90]. The assumptions used were that the constant-volume specific heat is a linear function of temperature and that the Grüneisen parameter is a function of specific volume alone. For solid iron, the validity of these two assumptions was verified. We obtained the Hugoniot pressures included in the solution of the quadratic equation from the experimental Hugoniot for iron of Brown *et al.* [47,91] and the quasi-static pressures at an ambient temperature from the experimental equation of state for iron of Mao *et al.* [92]. Unfortunately, there is no existing effective experimental temperature Hugoniot for iron. Therefore, for the Hugoniot temperatures included in the solution, we adopted the theoretical temperature Hugoniots for solid iron of Cohen *et al.* [37], Alfè *et al.* [34], Brown and McQueen [47], and Alfè *et al.* [35]; for liquid iron, we relied on the theoretical work of Alfè *et al.* [35] and Belonoshko, Ahuja, and Johansson [93]. Based on the experimental pressure Hugoniot and equation of state, we can examine the inefficacy of temperature Hugoniots. The inadequacy of some of the above-mentioned four temperature Hugoniots for solid iron was found by revealing the abnormality of the constant-volume specific heats on the Hugoniots corresponding to the solution of the quadratic equation. The cause of the enigmatic difference described above was also found. In addition, our Grüneisen parameter for the effective temperature Hugoniot calculated using a normal constant-volume specific heat on Hugoniot is compared with the *ab initio* result [34] and with the result calculated by another thermodynamic formalism [8].

4.4.2 Thermodynamic theory

4.4.2.1 Quadratic equation for the Grüneisen parameter

The Walsh-Christian equilibrium thermodynamic equation was expressed using the Hugoniot specific volume V_H as an independent variable by [89,90]

$$C_{VH}\frac{dT_H}{dV_H} + \frac{\gamma_H}{V_H}C_{VH}T_H = F_H,$$
(4.5)

where

$$F_H = \frac{1}{2}\frac{dp_H}{dV_H}(V_0 - V_H) + \frac{1}{2}p_H,$$
(4.6)

where p is the pressure, T is the temperature, V is the specific volume, C_V is the constant-volume specific heat, and γ is the Grüneisen parameter. The subscript 0 refers to an ambient

state and the subscript H to a shocked state, as in the example, $C_{VH} \equiv C_V(V_H,T_H) = C_{VH}(V_H)$, $\gamma_H \equiv \gamma(V_H,T_H) = \gamma_H(V_H)$. The following Mie-Grüneisen equation is derived by integrating,

$$dp = \frac{\gamma(V,T)}{V}C_V(V,T)dT,$$

along V = constant from an ambient state to a Hugoniot state:

$$p_H(V) - p_{T_0}(V) = \int_{T_0}^{T_H} \frac{\gamma(V,T)}{V}C_V(V,T)dT, \tag{4.7}$$

where p_{T_0} is the quasi-static pressure at an ambient temperature T_0. Note that $C_V = C_{Vharm} + C_{Vanharm} + C_{Vel}$, where the harmonic contribution to the constant-volume specific heat C_{Vharm} is equal to $3Nk_B$ to a good approximation (N being the number of atoms per unit mass and k_B the Boltzmann constant), and where the anharmonic contribution $C_{Vanharm}$ is proportional to T [34]. First, we assume that in the region of T_0 to T_H as defined in Eq. (4.7), the electronic contribution C_{Vel} is proportional to T. Then, because $C_{Vanharm} + C_{Vel} = \Gamma T$, where $\Gamma = \Gamma_{anharm} + \Gamma_{el}$, it follows that $C_V(V,T) = 3Nk_B + \Gamma(V)T$ in Eq. (4.7) and $C_{VH} = 3Nk_B + \Gamma(V_H)T_H$ in Eq. (4.5). Second, we assume that γ depends only on V, irrespective of T, in the region of T_0 to T_H. It then follows that $\gamma_H = \gamma(V_H)$ in Eq. (4.5) and $\gamma(V,T) = \gamma(V)$ in Eq. (4.7). For solid iron, Sections 4.4.3.1 and 4.4.3.4 verify the validities of the assumptions of linear $C_{Vel}(T)$ and temperature-independent γ, respectively. Equation (4.7) is integrated under the two assumptions described above to become

$$p_H - p_{T_0} = \frac{1}{2}\frac{\gamma}{V}(T_H - T_0)[6Nk_B + \Gamma(T_H + T_0)], \tag{4.8}$$

where $\Gamma = \Gamma(V)$ and $\gamma = \gamma(V)$. The Hugoniot pressure $p_H(V_H)$ and hence dp_H/dV_H and the Hugoniot temperature $T_H(p_H)$ and hence dT_H/dV_H are assumed to be known. Two unknown functions C_{VH} or $\Gamma(V_H)$ and $\gamma(V_H)$ are then included in Eq. (4.5). If $p_{T_0}(V)$ is also assumed to be known, then in Eq. (4.8), $\Gamma(V)$ and $\gamma(V)$ appear as unknowns.

We transform Eq. (4.5) to the following equation for $\Gamma(V_H)$:

$$\Gamma = \frac{1}{T_H}\left[\frac{F_H}{\dfrac{dT_H}{dV_H} + \dfrac{\gamma}{V_H}T_H} - 3Nk_B\right]. \tag{4.9}$$

We also obtain an equation for $\Gamma(V_H)$ from Eq. (4.8):

$$\Gamma = \frac{2(p_H - p_{T_0})}{T_H{}^2 - T_0{}^2}\left(\frac{\gamma}{V_H}\right)^{-1} - \frac{6Nk_B}{T_H + T_0}, \tag{4.10}$$

where $p_H = p_H(V_H)$, $p_{T_0} = p_{T_0}(V_H)$, and $\gamma = \gamma(V_H)$. We derive a quadratic equation for γ/V_H by

equating Eqs. (4.9) and (4.10):

$$a\left(\frac{\gamma}{V_H}\right)^2 + b\left(\frac{\gamma}{V_H}\right) + c = 0,\qquad(4.11)$$

where

$$a = 3Nk_B\left(T_H - T_0\right)^2,$$

$$b = \frac{T_H^2 - T_0^2}{T_H}F_H + 3Nk_B\frac{\left(T_H - T_0\right)^2}{T_H}\frac{dT_H}{dV_H} - 2\left(p_H - p_{T_0}\right)T_H,\qquad(4.12)$$

$$c = -2\left(p_H - p_{T_0}\right)\frac{dT_H}{dV_H},$$

where $b < 0$, $c > 0$ because $a > 0$ and $F_H < 0$, and $dT_H/dV_H < 0$ for iron in the pressure region of interest. For iron, therefore, a nontrivial solution of Eq. (4.11) is given by

$$\frac{\gamma}{V_H} = \frac{-b - \sqrt{b^2 - 4ac}}{2a},\qquad(4.13)$$

Three quantities p_H, p_{T_0}, and T_H included in coefficients a, b, and c are obtained, respectively, from the experimental pressure Hugoniot of Brown et al. [47,91], the experimental equation of state of Mao et al. [92], and several ab initio temperature Hugoniots [34,35, 37,93] presented by many authors.

4.4.2.2 Experimental pressure Hugoniot and equation of state for iron

Brown, Fritz, and Hixson [47] refined the $U_S(U_P)$ measurements for iron of Brown and McQueen [91] and gave $U_S = 3.691 + 1.788U_P - 0.038U_P^2$ for a quadratic fit to the refined data, where U_S and U_P are in km/s. Brown [10] transformed the measured data into pressure-specific volume data up to 400 GPa using the Rankine-Hugoniot jump conditions (FIG. 4.22). Mao et al. [92] reported the results of X ray diffraction experiments with the diamond anvil cell (DAC) to pressures above 300 GPa at room temperatures on hcp iron and gave the Birch-Murnaghan equation of state parameters of $V_{02} = 6.73$ cm^3/mol, $K_{02} = 165$ GPa, $K'_{02} = 5.33$. The Birch-Murnaghan equation of state $p_{T_0}(V)$ is shown in FIG. 4.22.
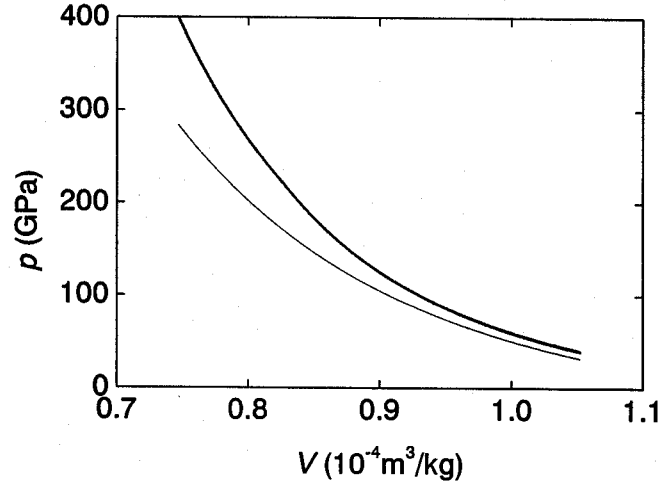
FIG. 4.22. $p_H(V_H)$ Hugoniot obtained using the quadratic $U_S(U_P)$ relation of Brown et al. [91] (heavy solid curve) and the static pressure-volume distribution $p_{T_0}(V)$ of Mao et al. [92] (solid curve).

4.4.2.3 $T_H(p_H)$ solid Hugoniots for iron

The ab initio $T_H(p_H)$ Hugoniot for hcp solid iron of Cohen et al. [37] in the region from 40 to 400 GPa is approximated by a quadratic equation for $40 = p_H = 100$ GPa and by a linear equation for $100 < p_H = 400$ GPa. The $T_H(p_H)$ Hugoniot for $40 = p_H = 400$ GPa of Alfè et al. [34] also is approximated by a quadratic equation. The solid Hugoniots of both groups are shown in FIG. 4.23(a). From 40 to 200 GPa, the Hugoniot of Alfè et al. [34] is in good agreement with that of Cohen et al. [37].

We can find a $T_H(p_H)$ solid Hugoniot which agrees well with the ab initio Hugoniot of Alfè et al. [35] up to 243 GPa from Eq. (4.5) using the following linear $\Gamma(p_H)$ and the corresponding γ/V_H:

$$\Gamma(p_H) = a_\Gamma p_H + b_\Gamma, \tag{4.14}$$

where $a_\Gamma = -8.4904 \times 10^{-5}$ J/kgK^2 GPa and $b_\Gamma = 0.080145$ J/kgK^2. The equation for γ/V_H, which is related to Γ, is obtained from Eq. (4.8):

$$\frac{\gamma}{V_H} = \frac{2(p_H - p_{T_0})}{(T_H - T_0)[6Nk_B + \Gamma(T_H + T_0)]}. \tag{4.15}$$

The $T_H(p_H)$ Hugoniot calculated using Eqs. (4.5), (4.14), and (4.15) under the initial condition of $T_H = 670$ K at $p_H = 40$ GPa [72] is shown in FIG. 4.23(a).

136

4.4.2.4 $T_H(p_H)$ solid Hugoniots, melting curves, and $T_H(p_H)$ liquid Hugoniots for iron

Because the material in question is a mixture of a solid and a liquid on a melting curve [$T_m(p)$], all the results obtained for C_{VH} and γ are meaningless, even if T_m is used instead of T_H. Our calculations apply only to single-phase solids and liquids but nevertheless, the melting curve plays an important role in determining the melting incipience and completion states. Several independent attempts to obtain *ab initio* melting curves were recently reported [35,93]. Belonoshko *et al.* [93] presented a melting curve that is in agreement with DAC experimental melting data [7] at low pressures and is in excellent agreement with the shock melting result of 5500 K at 243 GPa [47]. Using Eqs. (4.5) and (4.15), and the equation $C_{VH} = 3Nk_B + \Gamma T_H$ [$\Gamma = \beta_e (V_H/V_0)^{\gamma^e}$] of Brown and McQueen [47], where $\beta_e = 0.0612$ J/kgK^2 and $\gamma^e = 1.34$, we calculate a $T_H(p_H)$ solid Hugoniot that intersects the melting curve of Belonoshko *et al.* [93] at 221 GPa; we approximate the *ab initio* $T_H(p_H)$ liquid Hugoniot of Belonoshko *et al.* [93] by a linear equation in the region above 260 GPa. Our value for $\beta_e = 0.0612$ J/kgK^2 is smaller than that of 0.091 J/kgK^2 used by Brown and McQueen [47], and our value of $\gamma^e = 1.34$ is the same as that used by Brown and McQueen [47]. The solid Hugoniot, melting curve, and liquid Hugoniot are shown in FIG. 4.23(b).

Alfè *et al.* [35] constructed an improved DFT, which corrected the free energy F in their previous DFT [34]; in addition they presented a melting curve with an F correction, which is in quite good agreement with the measurement of Shen *et al.* [94] and with the shock melting result of 5500 K at 243 GPa [47]. Finally, Alfè *et al.* [35] introduced a $T_H(p_H)$ solid Hugoniot up to 243 GPa and a $T_H(p_H)$ liquid Hugoniot from 298 GPa that corrected F for consistency. The solid Hugoniot with the F correction is very close to our solid Hugoniot that was calculated using Eq. (4.14) and illustrated in FIG. 4.23(a). Therefore, we use our Hugoniot up to 243 GPa, where it intersects the melting curve of Alfè *et al.* [35] The liquid Hugoniot is approximated by a linear equation. The solid Hugoniot, melting curve, and liquid Hugoniot of Alfè *et al.* [35] are shown in FIG. 4.23(b).

Laio *et al.* [95] also calculated a melting curve for iron using their *ab initio* method. Boehler *et al.* [96] compared the melting curves of Belonoshko *et al.* [93], Laio *et al.* [95], and Alfè *et al.* [30] with the DAC data of Boehler [7,97] and demonstrated that only the results of Laio *et al.* [95], which are considerably lower than the others, are comparable with the DAC data. On the other hand, the experimental melting curve of Yoo *et al.* [98] is considerably higher than those of Belonoshko *et al.* [93] and Alfè *et al.* [30,35] in the pressure region of interest. Burakovsky *et al.* [99] presented a theory of the melting of elements as a dislocation-mediated

phase transition. Burakovsky *et al.* [100] derived an equation for the pressure dependence of the melting temperatures of the elements, calculated the melting curves for 24 elements, and obtained good agreement with existing experimental data. For iron, however, the curve is a little higher than that of Yoo *et al.* [98]. We chose the melting curves of Belonoshko *et al.* [93] and Alfè *et al.* [35] because they are in good agreement with the DAC data at low pressures and with the estimate based on the shock data at 243 GPa.
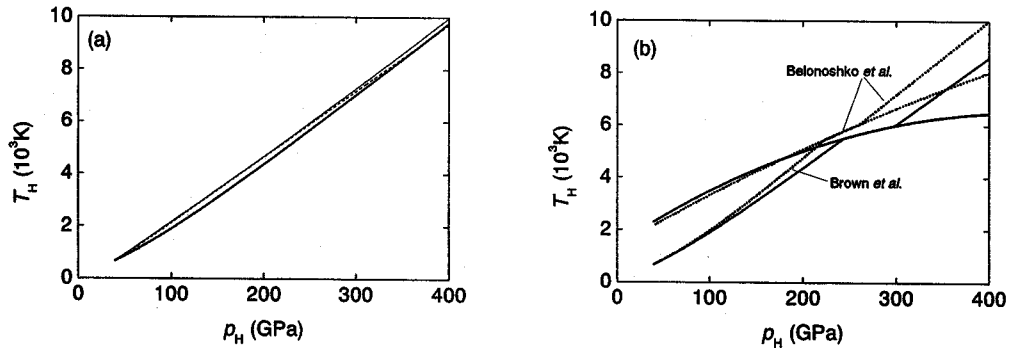
FIG. 4.23. (a) Solid Hugoniots of Cohen *et al.* [37] (dashed curve), Alfè *et al.* [34] (solid curve), and that calculated using Γ given by Eq. (10) (heavy solid curve). (b) Solid Hugoniot of Brown and McQueen [47], melting curve, and liquid Hugoniot of Belonoshko *et al.* [93] (heavy dotted curves) and solid Hugoniot, melting curve, and liquid Hugoniot of Alfè *et al.* [35] (heavy solid curves). All solid Hugoniots shown in (a) and (b) start from the point (40 GPa, 670 K) [72].

4.4.3 Thermal properties

4.4.3.1 Validity of linear C_{Vel} assumption

Alfè *et al.* [34] calculated the electronic specific heat $C_{perf}(T)$ [$= C_{Vel}$] of the rigid perfect lattice for hcp solid iron in the region of 0 to 6000 K using the *ab initio* method and plotted the resulting values for atomic volumes of 7.0 Å^3 ($V_H = 0.7548 \times 10^{-4}$ m^3/kg and $p_H = 377.1$ GPa), 8.0 Å^3 ($V_H = 0.8627 \times 10^{-4}$ m^3/kg, $p_H = 166.8$ GPa, and $T_H = 3546$ K), 9.0 Å^3 ($V_H = 0.9705 \times 10^{-4}$ m^3/kg, $p_H = 73.75$ GPa, and $T_H = 1318$ K), 10.0 Å^3. In these equations, p_H was calculated from V_H using the $p_H(V_H)$ Hugoniot of Brown *et al.* [47,91] and T_H was then calculated from p_H using the $T_H(p_H)$ solid Hugoniot of Alfè *et al.* [35]. The $C_{perf}(T)$ distribution for 7.0 Å^3 is the closest to a straight line. When the volume is large, the deviation of the distribution from a straight line is also large in the whole region of 0 to 6000 K, but it does not become large in a portion of T_0 to T_H, defined in Eq. (4.7), because T_H is low. The deviations over the regions of T_0 to T_H for any

volumes of interest are not great, so we consider that our assumption regarding the constant-volume heat in the region of T_0 to T_H, expressed by $C_{Vel} = \Gamma_{el}T$ or $C_V = 3Nk_B + \Gamma T$, is valid.

To substantiate the validity of $C_{Vel} = \Gamma_{el}T$ for hcp solid iron, we evaluate

$$\Gamma(p_H)T_H - ab\ initio\ C_{V\mathrm{Hanharm}},$$

where $\Gamma(p_H)$ is given by Eq. (4.14), and the *ab initio* $C_{V\mathrm{Hel}}$ of Alfè *et al.* [34]. We obtained

$$ab\ initio\ C_{V\mathrm{Hanharm}} = \frac{1}{6000}\left[0.28 + 0.25\frac{V_A - V_H}{V_A - V_B}\right]T_H N k_B,$$

where $V_A = 7$ and $V_B = 10$ Å^3, using the *ab initio* specific heat data of Alfè *et al.* [34]. The calculated $[\Gamma(p_H)T_H - ab\ initio\ C_{V\mathrm{Hanharm}}]/Nk_B$ distribution as a function of the Hugoniot temperature T_H is shown in FIG. 4.24. The calculated distribution (solid curve) is close to the values (circles) of the *ab initio* $C_{V\mathrm{Hel}}$ of Alfè *et al.* [34] at $T_H = 3546$ K for 8 Å^3 and $T_H = 1318$ K for 9 Å^3, indicating that

$$[\Gamma(p_H)T_H - ab\ initio\ C_{V\mathrm{Hanharm}}] \cong ab\ initio\ C_{V\mathrm{Hel}}.$$

This approximate equation can be transformed to

$$ab\ initio\ C_{V\mathrm{Hel}} \cong [\Gamma(p_H) - ab\ initio\ \Gamma_{\mathrm{anharm}}(V_H)]T_H,$$

that is,

$$ab\ initio\ C_{V\mathrm{Hel}} \cong \Gamma_{el}(V_H)T_H.$$

This means that the electronic specific heats at temperatures T within the regions of 0 to T_H for the specific volumes of interest V, $C_{Vel}(V,T)$, is expressed approximately by $\Gamma_{el}(V)T$. The validity of our linear $C_{Vel}(T)$ assumption was thus verified.
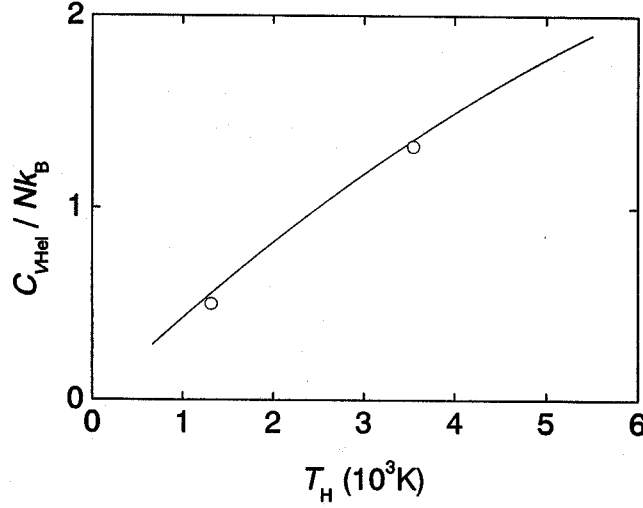
FIG. 4.24. Electronic specific heat $C_{V\text{Hel}}/Nk_B$ in the solid phase range calculated from $[\Gamma(p_H)T_H$ $- ab\ initio\ C_{V\text{Hanharm}}]/Nk_B$ using *ab initio* $C_{V\text{Hanharm}}$ formulated by incorporating the specific heat data of Alfè *et al.* [34] (solid curve) and *ab initio* $C_{V\text{Hel}}/Nk_B$ of Alfè *et al.* [34] at $T_H = 3546$ K for atomic volumes 8 Å^3 and $T_H =1318$ K for 9 Å^3 (circles).

4.4.3.2 Constant-volume specific heat

The distributions of $\Gamma(p_H)$ for the $T_H(p_H)$ solid Hugoniots of Cohen *et al.* [37] and Alfè *et al.* [34], which are obtained by substituting solution (4.13) into Eq. (4.10), are shown in FIG. 4.25. The difference between the two Γ distributions is due only to the difference between the $T_H(p_H)$ Hugoniots. The $T_H(p_H)$ Hugoniots of Cohen *et al.* [37] and Alfè *et al.* [34] are similar below 200 GPa, so that the $\Gamma(p_H)$ for both Hugoniots are also similar. The former and latter Hugoniots are not effective in the regions below 210 and 180 GPa, respectively, because the decrease in the $C_{V\text{H}}$ with decreasing p_H is abnormally great; that is, the two $C_{V\text{H}}$ become abnormal in those pressure regions due to Γ decreasing with a lowering of p_H. The $p_H(V_H)$ Hugoniots of both groups [34,37] greatly deviate from the experimental Hugoniot used in our calculations with a reduction in p_H from about 150 GPa; thus, the abnormality of the $C_{V\text{H}}$ might be caused by this deviation.

The distributions of $\Gamma(p_H)$ for the $T_H(p_H)$ liquid Hugoniots of Alfè *et al.* [35] and Belonoshko *et al.* [93] are shown in FIG. 4.25. The $\Gamma(p_H)$ distribution for the $T_H(p_H)$ liquid Hugoniot of Alfè *et al.* [35] is almost parallel to and is greatly above the linear $\Gamma(p_H)$ distribution (FIG. 4.25) in the solid phase range given by Eq. (4.14). The same is true of the

$\Gamma(p_H)$ distribution for the $T_H(p_H)$ liquid Hugoniot of Belonoshko *et al.* [93], although the $\Gamma(p_H)$ distribution (FIG. 4.25) of Brown and McQueen [47] with $\beta_e = 0.0612$ J/kgK^2 and $\gamma^r = 1.34$ is not linear.
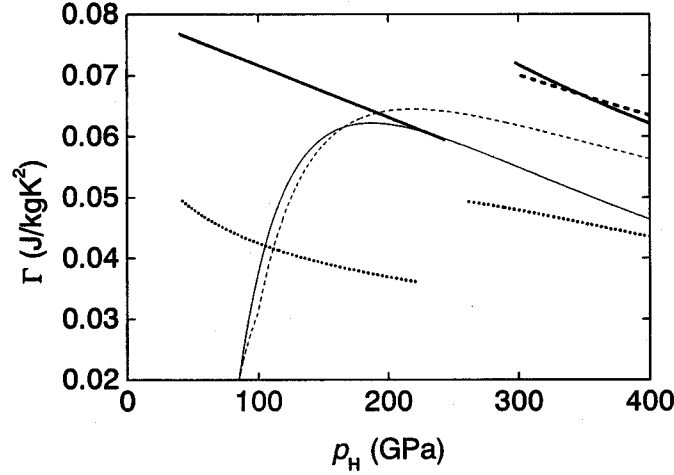
FIG. 4.25. Distributions of Γ for the solid Hugoniots of Cohen *et al.* [37] (dashed curve), Alfè *et al.* [34] (solid curve), Brown and McQueen [47] (heavy dotted curve), and Γ given by Eq. (10) (heavy solid curve) as a function of Hugoniot pressure p_H. Γ distributions for the liquid Hugoniots from 260 to 400 GPa of Belonoshko *et al.* [93] (heavy dotted curve), from 298 to 400 GPa of Alfè *et al.* [35] (heavy solid curve), and from 280 to 340 GPa of Alfè *et al.* [34] obtained using $\gamma = 1.51$ (heavy dashed curve) are also shown.

The $C_{VH}(p_H)/Nk_B$ distributions calculated using the $\Gamma(p_H)$ distributions described above are shown in FIG. 4.26. An abnormal portion of $C_{VH}(p_H)$ on the $T_H(p_H)$ Hugoniot of Cohen *et al.* [37] below 210 GPa was excluded, and the distribution of Brown and McQueen [47] with $\beta_e = 0.091$ J/kgK^2 and $\gamma^r = 1.34$ was added. The $C_{VH}(p_H)/Nk_B$ on the $T_H(p_H)$ Hugoniot of Alfè *et al.* [34] decreases greatly with a decrease in p_H from about 180 GPa, reaches 3 at about 70 GPa, and further lowers up to 40 GPa. The $C_{VH}(p_H)$ distribution of Brown and McQueen [47] with $\beta_e = 0.091$ J/kgK^2 and $\gamma^r = 1.34$ is normal, but it is lower than that on the $T_H(p_H)$ Hugoniot of Alfè *et al.* [35]. This difference can be explained by the anharmonic contribution neglected by Brown and McQueen [47]. In fact, in the solid phase range,

$$\beta_e (V_H/V_0)^{\gamma^r} T_H + ab\ initio\ C_{VHanharm}$$

coincides almost perfectly with the $\Gamma(p_H)T_H$, where $\Gamma(p_H)$ is given by Eq. (4.14). In the liquid

phase range, the $T_H(p_H)$ Hugoniots of Belonoshko *et al.* [93] and Brown and McQueen [47] with $\beta_e = 0.091$ J/kgK^2 and $\gamma^f = 1.34$ are close and both $C_{VH}(p_H)$ distributions are also similar, as shown in FIG. 4.26.

We here compare the normal constant-volume specific heat on the $T_H(p_H)$ solid Hugoniot of Alfè *et al.* [35] C_{VH} [= $3Nk_B + \Gamma(p_H)T_H$] with the *ab initio* C_{VH} of Alfè *et al.* [34]. We obtain *ab initio* $C_{VH} \cong 3Nk_B + \Gamma(p_H)T_H$ by substituting *ab initio* $C_{VHel} \cong [\Gamma(p_H)T_H - ab\ initio\ C_{VHanharm}]$ revealed above into *ab initio* $C_{VH} = 3Nk_B + ab\ initio\ C_{VHanharm} + ab\ initio\ C_{VHel}$. Therefore, $C_{VH} \cong$ *ab initio* C_{VH}.
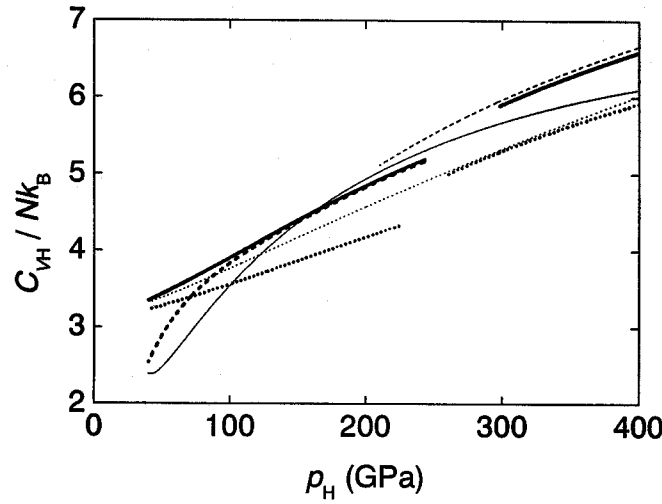
FIG. 4.26. Distributions of constant-volume specific heat C_{VH} per Nk_B obtained using Γ for the solid Hugoniots of Cohen *et al.* [37] (dashed curve), Alfè *et al.* [34] (solid curve), Brown and McQueen [47] with $\beta_e = 0.0612$ (heavy dotted curve) and 0.091 J/kgK^2 (dotted curve), Γ given by Eq. (10) (heavy solid curve), and Γ for the solid Hugoniot of Alfè *et al.* [35] obtained using estimated γ_H (heavy dashed curve) as a function of Hugoniot pressure p_H. Distributions of C_{VH} obtained using Γ for the liquid Hugoniots from 260 to 400 GPa of Belonoshko *et al.* [93] (heavy dotted curve) and from 298 to 400 GPa of Alfè *et al.* [35] (heavy solid curve) are also shown.

4.4.3.3 Temperature-independent Grüneisen parameter

The distributions of $\gamma(p_H)$ for the $T_H(p_H)$ solid Hugoniots of Alfè *et al.* [34] and Alfè *et al.* [35] calculated using Eq. (4.13) and Eq. (4.15), respectively, are shown in FIG. 4.27. As was the case with the γ distribution of Cohen *et al.* [37], both γ distributions increase rapidly with a decrease in p_H. An *ab initio ab initio* $\gamma_H(p_H)$ distribution estimated from the *ab initio* $\gamma_{isoth}(p)$

distributions of Alfè et al. [34] on isotherms at 2000 and 4000 K in the solid phase range below 243 GPa (heavy dashed curve) is shown in the FIG. 4.27. In the region of 170 to 243 GPa, the estimated γ_H distribution is just above the γ distribution for the $T_H(p_H)$ solid Hugoniot of Alfè et al. [35] As p_H decreases from about 170 GPa, γ increases rapidly up to 3.8 at 40 GPa; whereas γ_H increases only a little. $C_{VH} \approx$ ab initio C_{VH} in the solid phase range as demonstrated above, whereas the difference between both distributions is significantly large in this lower pressure region. Because the ab initio $p_H(V_H)$ Hugoniot of Alfè et al. [35] agrees well with the experimental data [47,91] in the region above about 80 GPa, the experimental Hugoniot used in our calculations could not have caused the difference from the γ_H distribution above 80 GPa. This means that in the lower pressure region, the significantly lower distribution of the Grüneisen parameter was predicted by the ab initio method.

We evaluate the C_{VH} corresponding to the estimated ab initio γ_H using our method, in which these two variables are related uniquely. Note that when γ is given, there is a C_{VH} that provides the same Hugoniot temperature as the T_H of Alfè et al. [35]. The C_{VH} distribution on the $T_H(p_H)$ solid Hugoniot of Alfè et al. [35] (heavy dashed curve), which is obtained by substituting the ab initio γ_H into γ in Eq. (4.10), is shown in FIG. 4.26. It consists of a normal portion, which is close to the C_{VH} distribution obtained from the linear Γ given by Eq. (4.14), in the region above 170 GPa and an abnormal portion, which is lower than the C_{VH} distribution obtained from the linear Γ, below 170 GPa. The abnormal portion of C_{VH} thus corresponds to the ab initio γ_H distribution in the region below 170 GPa, where it is significantly lower than the γ distribution. In the ab initio method, as mentioned above, the significantly smaller γ_H in the region below 170 GPa was obtained using the normal C_{VH}, which is close to the constant-volume specific heat obtained from the linear Γ given by Eq. (4.14). In contrast, the significantly smaller γ_H resulted from the abnormally small C_{VH} in our calculation.

A distribution of $\gamma(p_H)$ for the $T_H(p_H)$ liquid Hugoniot of Alfè et al. [35], calculated using Eq. (4.13), is shown in FIG. 4.27. γ is larger at the melting completion pressure of 298 GPa than at the melting incipience pressure of 243 GPa. Equation (4.15) indicates that this is due to the larger value of ($p_H - p_{T_0}$) at 298 GPa, in spite of the smaller value of V_H and the larger values of T_H and Γ (see FIG. 4.25) at 298 GPa. Note that the value of γ at 298 GPa varies with the gradient of the liquid Hugoniot, because Γ depends on dT_H/dV_H (see Eq. (4.9)). On the other hand, γ also decreases with an increase in p_H in the liquid phase range, as was the case in the solid phase range. This is due to the decrease in V_H and the increase in T_H in spite of the decrease in Γ with increasing p_H.

The *ab initio* $\gamma_H(p_H)$ distribution of Alfè *et al.* [34] in the liquid phase range from 280 to 340 GPa (heavy dashed curve, $\gamma_H \approx 1.51$) is shown in FIG. 4.27. The *ab initio* γ_H distribution approximates the γ distribution (heavy solid curve) for the liquid Hugoniot of Alfè *et al.* [35] although the difference in slope between both distributions is large. To investigate the cause of the large slope difference, we evaluate Γ for the liquid Hugoniot of Alfè *et al.* [35] by substituting $\gamma = 1.51$ into Eq. (4.10). The evaluated Γ distribution (heavy dashed curve) is shown in FIG. 4.25. Both Γ distributions (heavy dashed and solid curve) have a slope difference. Thus, the slope difference between both of the Γ (or C_{VH}) distributions caused the large slope difference between the γ_H and γ distributions.
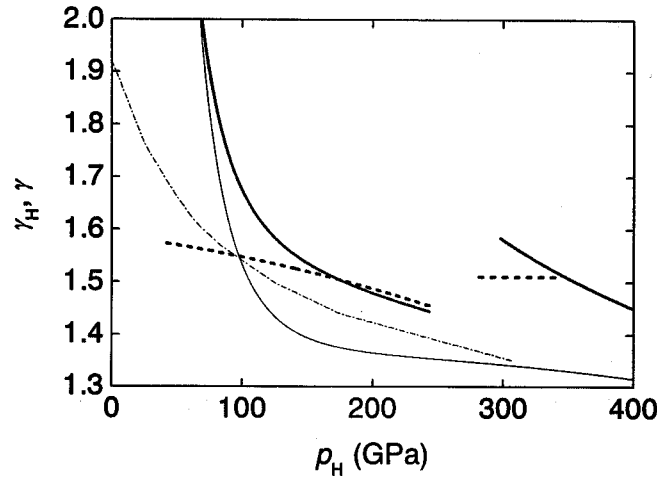
FIG. 4.27. Distributions of the Grüneisen parameter γ for the solid Hugoniots of Alfè *et al.* [34] (solid curve), γ for the solid and liquid Hugoniots of Alfè *et al.* [35] (heavy solid curve), γ_H estimated from the *ab initio* γ_{isoth} distributions on isotherms in the solid phase range and *ab initio* γ_H in the liquid phase range of Alfè *et al.* [34] (heavy dashed curve), and γ along the melting curve of Anderson and Isaak [8] (chain curve) as a function of Hugoniot pressure p_H.

Anderson and Isaak [8] found the Grüneisen parameter γ along the melting curve of hcp iron by a method combining the Lindemann melting equation with the Vinet equation of state. There are more thermal parameters in their calculation than in our calculation. FIGURE 4.27 shows their calculation result as a function of the Hugoniot pressure p_H, which was related to the Vinet equation of state pressure [8] using the $p_H(V_H)$ Hugoniot [91]. In the lower pressure region

144

in the solid phase range, their $\gamma(p_H)$ distribution also increases rapidly with a decrease in p_H, but the overall magnitude is considerably lower than the distributions for the $T_H(p_H)$ solid and liquid Hugoniots of Alfè et al. [35].

4.4.3.4 Temperature dependence of the Grüneisen parameter

We derived Eq. (4.11) from Eqs. (4.5) and (4.7) under the assumption that the Grüneisen parameter γ is temperature-independent. The *ab initio* parameters γ_{isoth} on isotherms at 2000, 4000, and 6000 K of Cohen et al. [37] and Alfè et al. [34], however, showed that γ is slightly temperature-dependent. Because the temperature-dependent $\gamma(V_H, T_H)$ can not be determined uniquely from Eqs. (4.5) and (4.7) alone, we here quantify γ_H in the solid phase range using the $T_H(p_H)$ solid Hugoniots shifted from that of Alfè et al. [35]. We express $\gamma(V, T)$ by the sum of a temperature-independent term, $\gamma_i(V)$, and a temperature-dependent term, $w(V)T$, that is, by $\gamma(V, T) = \gamma_i(V) + w(V)T$. It follows that $\gamma_H = \gamma_i(V_H) + w(V_H)T_H$ on a Hugoniot. We obtain the following equation for $w(p_H)$ by substituting $\gamma(V, T)$ into Eq. (4.7):

$$w = \frac{V_H(p_H - p_{T_0}) - \gamma_H d}{e - T_H d},$$

(4.16)

where

$$d = 3Nk_B(T_H - T_0) + \frac{1}{2}\Gamma(T_H^2 - T_0^2),$$

$$e = \frac{3}{2}Nk_B(T_H^2 - T_0^2) + \frac{1}{3}(T_H^3 - T_0^3),$$

where $\Gamma(p_H)$ is given by Eq. (4.14), but $T_H(p_H)$ and $\gamma_H(p_H)$ are unknown. Because γ_H is related to T_H through Eq. (4.5), however, $w(p_H)$ can be evaluated from Eq. (4.16) if T_H is given, $\gamma_i(p_H)$ is then obtained from $\gamma_i = \gamma_H - wT_H$, and finally $\gamma_{isoth}(p)$ is determined. Here, $\gamma_{isoth}(p) = \gamma_i(p) + w(p)T_{isoth}$, where $\gamma_i(p) = \gamma_i(p_H)$ and $w(p) = w(p_H)$.

We now verify the validity of our assumption concerning the Grüneisen parameter. We shifted the $T_H(p_H)$ solid Hugoniot of Alfè et al. [35] only slightly to estimate γ_H. In the case in which the shifted solid Hugoniot is lower by 12 K at 243 GPa (for the sake of simplicity, only the maximum difference between both Hugoniots is noted), w was clearly negative between 175 and 243 GPa. $w < 0$ appeared in the *ab initio* result [35] of Cohen et al. [37]. FIGURE 4.28(a) illustrates our γ_{isoth} distributions on isotherms at 2000 and 4000 K in the case in which the shifted solid Hugoniot is higher by 12 K at 243 GPa, together with the *ab initio* results of Alfè et al. [35]. Here, the shift of the solid Hugoniot was adjusted so that the following three conditions would be satisfied: (1) Our γ_{isoth} distribution on an isotherm at 2000 K is close to that of Alfè et

145

al. [35] at 243 GPa, (2) The same is true of our γ_{isoth} distribution on the isotherm at 4000 K, and (3) $w > 0$ and the form of both γ_{isoth} distributions on the isotherm at 2000 K (and 4000 K) does not differ greatly in the pressure region of interest. w is clearly positive between 130 and 243 GPa, and our γ_{isoth} distributions on the isotherms at 2000 K (and 4000 K) approximately satisfy the three conditions [FIG. 4.28(a)]. Our γ_{isoth} distribution on the isotherm at 2000 K is close to that of Alfè *et al.* [35] from 170 to 243 GPa, but both distributions rapidly part with a decrease in pressure from 170 GPa. A calculated γ_H distribution and the γ distribution depicted in FIG. 4.27 are shown in FIG. 4.28(b). The difference between these distributions is slight. The Grüneisen parameter is thus temperature-independent [101].

Dubrovinsky *et al.* [21] collected the experimental data of Mao *et al.* (300K) [92], Jephcoat *et al.* (300K) [64], Huang *et al.* (723K) [66], Funamori *et al.* (950-1050, 1150-1250 K) [71], and Saxena *et al.* (300, 650-750, 950-1050, 1150-1250 K) [13,18,20,46] and determined a thermal equation of state of hcp iron. Although the temperature dependence of the Grüneisen parameter was shown to be slight, if the thermal equation of state is incorporated into our theory, then the theory might give information about the form of the temperature dependence for the temperature-dependent Grüneisen parameter, a variable that we are attempting to calculate.
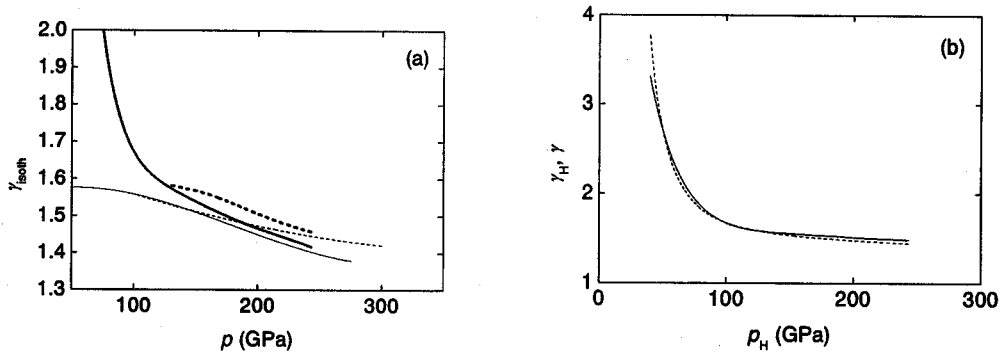
FIG. 4.28. (a) Distributions of the Grüneisen parameter γ_{isoth} on isotherms at 2000 (heavy solid curve) and 4000 K (heavy dashed curve) and *ab initio* γ_{isoth} on isotherms at 2000 (solid curve) and 4000 K (dashed curve) of Alfè *et al.* [34] as a function of pressure p. (b) Distributions of the temperature-dependent Grüneisen parameter γ_H (solid curve) in the solid phase range and temperature-independent γ for the solid Hugoniot of Alfè *et al.* [35] (dashed curve) as a function of Hugoniot pressure p_H.

4.4.3.5 Sound velocity

We calculate adiabatic sound velocities in the liquid phase range above 298 GPa using the equation:

$$C_S = \frac{V_H}{V_0} U_S \frac{1 + s\varepsilon_H - sV_0 \frac{\gamma}{V_H} \varepsilon_H^2}{1 - s\varepsilon_H},$$

where $c = 4089.0$ m/s, $s = 1.5470$, $\varepsilon_H = U_P/U_S$, and γ is the Grüneisen parameter for the $T_H(p_H)$ liquid Hugoniot of Alfè et al. [35]. The values of c and s were obtained by fitting $U_S = c + sU_P$ to the refined $U_S(U_P)$ data of Brown et al. [91] in the region above 260 GPa. In FIG. 4.29, our calculated C_S distribution is compared with the experimental sound velocity data in the liquid phase range above 260 GPa of Brown and McQuen [47] and Nguyen and Holmes [102]. Our sound velocity curve agrees well with the experimental data.
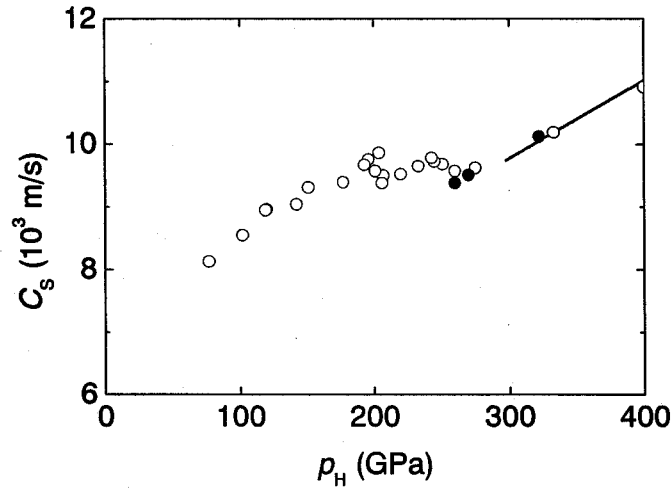
FIG. 4.29. Sound velocity distribution for the liquid Hugoniot from 298 to 400 GPa of Alfè et al. [4] (heavy solid curve) as a function of the Hugoniot pressure p_H and the experimental data for sound velocity of Brown and McQueen [47] (circles) and Nguyen and Holmes [102] (solid circles).

4.4.4 Conclusions

The constant-volume specific heats C_{VH} on Hugoniots and the Grüneisen parameters γ for iron were evaluated using a method that combines the Walsh-Christian and Mie-Grüneisen equations. The validities of our assumptions that the constant-volume specific heat is a linear function of temperature and that the Grüneisen parameter is a function of specific volume alone were verified in the solid phase range. In the lower pressure region, the *ab initio* γ_H distribution was significantly lower than our γ distribution. Because C_{VH} was related uniquely to γ through three known p_H, p_{T_0}, and T_H functions, our suggestion that the significantly smaller *ab initio* γ_H was caused by the abnormally small C_{VH} is considered to be appropriate. In the liquid phase range, the *ab initio* γ_H distribution had a smaller gradient than our γ distribution. The cause of this difference was also clarified. The sound velocities calculated using this γ distribution agreed well with the experimental data.

4.5 Temperatures inside and behind the overdriven steady-plane shock wave fronts in iron

Temperatures behind and inside the overdriven steady-plane shock wave fronts in iron for shocks up to 230 GPa are evaluated using the equilibrium thermodynamic theory. Equilibrium thermodynamics can be applied to these shocks and the assumption of heat transport is valid. Thus, the inside temperature distributions are evaluated correctly. Temperatures behind the overdriven steady shock wave fronts can be estimated correctly using the Walsh-Christian equation. Overestimations of the temperature distributions inside an inviscid solid iron mean that the viscous pressure influences greatly on the distributions. The underestimation of the constant-volume specific heat in a higher pressure region causes the overestimation of the inside temperature distributions.

4.5.1 Introduction

The inside temperature (IT_{IM}) method implicitly including heat transport was developed by Y. Sano and A. Abe to estimate temperature distributions inside steady wave fronts in solids [103]. In this method, it is assumed that the state of the solid in the wave front is close to thermodynamic equilibrium, and that both heat transport and the work performed by thermal pressure in the wave fronts can be neglected because they could cancel each other out. The latter assumption of heat transport is valid if the viscous component of the pressure is large enough compared to the thermal component. T. Sano and Y. Sano evaluated the temperature distributions in overdriven-steady wave fronts shocked up to 80 GPa in 2024 Al, 250 GPa in Pt, and 230 GPa in iron using the IT_{IM} method [90]. The evaluated temperatures behind shock fronts using the IT_{IM} method were sufficiently correct compared with the values calculated using Walsh-Christian theory [89]. The viscous components of the pressure were so large that the evaluated distributions were fairly correct. Therefore, two assumptions of thermodynamic equilibrium and heat transport were valid, and the IT_{IM} method was effective.

Strain rates in overdriven steady-plane wave fronts induced by shocks up to $200 - 300$ GPa might reach $10^{11} - 10^{12}$ s^{-1}. The deformations at any material point inside the shock wave fronts do not change greatly during the electron – phonon relaxation time of $10 - 100$ fs which is dominant up to $200 - 300$ GPa. The homogeneous volumetric component of the deformation is even small because heterogeneous plastic flow on an atomic scale is very large. Consequently, the electron – phonon system can maintain itself near thermodynamic equilibrium for shocks up to $200 - 300$ GPa, if the temporal rates of the change of inside temperatures are slower than the

characteristic relaxation times of temperature. The homogeneous component supports a great part of the pressure on the Rayleigh line, which is used in thermodynamics of irreversible processes. Therefore, irreversible thermodynamics can be applied to overdriven shocks up to $200 - 300$ GPa, if strain rates are less than 10^{12} s^{-1} and the states inside the shock wave fronts are regarded essentially as thermodynamic equilibrium.

It is known, however, whether irreversible thermodynamics is valid or not for overdriven shock waves because thermodynamic equilibrium of the states has not been determined. This question is still open because the macroscopic treatment of the material process is conceptually difficult without thermodynamics [104]. One method to answer this question is to verify that the system maintain itself near thermodynamic equilibrium through the shock process, *i.e.*, that the assumption of thermodynamic equilibrium is valid. This can be verified by first calculating the process from irreversible thermodynamics and then comparing the characteristic times mentioned above with the temporal rates of change.

T. Sano and Y. Sano calculated temperature distributions inside shock fronts in iron for shocks up to 230 GPa using the temperature-independent constant-volume specific heat C_V of Bass *et al.* [105] which is expressed by $C_V = 3Nk_B$, where N is the number of atoms per unit mass and k_B is the Boltzmann constant [90]. C_V is, however, essentially temperature-dependent. Brown and McQueen represented the temperature-dependent equation of C_V [47]. But this C_V of Brown and McQueen has a deviation from the ab initio results [34]. I obtained the equation of C_V which is consistent with the ab initio result of Alfè in Sec. 4.4.

The main purpose of the present study is to calculate the physically valid change of temperatures through shock fronts, applying the temperature-dependent constant-volume specific heat to the IT$_{IM}$ method. The validity of the assumption of thermodynamic equilibrium is investigated for shocks in iron up to 230 GPa which does not induce melting [105] by estimating the effective strain rates and temperature rise times. The validity of this method is investigated by comparing the viscous component of the pressure with the thermal component for this shock. In addition, temperature distributions inside overdriven steady wave fronts in inviscid iron for a 230 GPa shock are evaluated using the equation for temperatures derived from Mie-Grüneisen equation, and the effect of the viscous pressure is investigated by comparing the value in an inviscid iron with that in a viscous iron. The inviscid solid means the solid where viscous pressure is not induced during shock loading.

4.5.2 Equilibrium thermodynamic theory

First, three kinds of C_V are described. Second, the shock temperature method and the IT_{IM} method are described. These methods can treat adequately the temperature distributions behind and inside shock fronts, respectively. The derivation of the shock temperature method is described in Appendix A.1. Next, the method which estimates the effective temperature thickness is presented. Finally, the equation which correctly estimates the temperature distributions in an inviscid solid is derived.

4.5.2.1 Constant-volume specific heat

Bass *et al.* expressed the following temperature-independent C_V for iron [105]:

$$C_V = 3Nk_B. \tag{4.17}$$

C_V is, however, essentially temperature-dependent. Brown and McQueen represented the temperature-dependent equation of C_V as follows [47]:

$$\begin{aligned} C_V &= 3Nk_B + \Gamma T \\ &= 3Nk_B + \Gamma_0 \left(\frac{V}{V_0}\right)^g T, \end{aligned} \tag{4.18}$$

where $\Gamma_0 = 0.091$ J/kgK^2 and $g = 1.34$. On the other hand, I obtained the following equation of C_V which is consistent with the ab initio Hugoniot of Alfè *et al.* [35] in Sec. 4.4:

$$\begin{aligned} C_{VH} &= 3Nk_B + \Gamma(p_H)T_H \\ &= 3Nk_B + (a_\Gamma p_H + b_\Gamma)T_H, \end{aligned} \tag{4.19}$$

where $a_\Gamma = -8.4904\times10^{-5}$ J/kgK^2 GPa and $b_\Gamma = 0.080145$ J/kgK^2. In this section, temperatures behind and inside the overdriven steady-plane wave fronts are calculated using these three C_V.

4.5.2.2 Shock temperature method

Walsh and Christian derived the following thermodynamic equation (Walsh-Christian equation) [89]:

$$C_V \frac{dT}{dV} + \frac{\gamma}{V} C_V T = \frac{1}{2}\frac{dp}{dV}(V_0 - V) + \frac{1}{2}(p - p_0), \tag{4.20}$$

where thermodynamic variables are on the Hugoniot. Because the effect of heat transport is included implicitly, the temperatures behind the shocks can be accurately calculated by this equation.

4.5.2.3 Inside temperature method implicitly including heat transport

Y. Sano and A. Abe developed the IT_{IM} method which estimates the temperature inside steady shock wave fronts in a solid [103]. Pressure p inside the wave fronts is related to the specific volume V by the Rayleigh line equation:

$$dp = -\rho_0^2 U_s^2 dV, \tag{4.21}$$

where U_S is the constant shock velocity, $\rho = 1/V$ is the material density, and subscript 0 refers to an ambient state. The following approximate equation is derived by assuming that heat transport and the work performed by thermal pressure could cancel each other out:

$$TdS = -(p - p_E)dV, \tag{4.22}$$

where S is the entropy, and p_E is the thermoelastic component of the pressure p. This assumption is valid if the work performed by the viscous pressure is sufficiently large compared with the work performed by the thermal pressure and heat transport. The set of equations used in this method consists of the irreversible thermodynamics obtained by equating Eq. (4.22) with the thermodynamic identity, the equation for cold pressure p_C, and the equation for thermoelastic pressure p_E (FIG. 4.30). The thermodynamic equation is expressed by

$$C_V \frac{dT}{dV} + \frac{\gamma_0}{V_0} C_V T = -(p - p_E), \tag{4.23}$$

where γ is Grüneisen parameter, C_V is the constant-volume specific heat on the Rayleigh line, and $\gamma/V = \gamma_0/V_0$ is assumed. The equation for cold pressure p_C is given by

$$p_C = p_H - p_{T_H}, \tag{4.24}$$

where p_H is a known Hugoniot function which is represented as $p_H(V)$, p_{T_H} is the Hugoniot function $p_{T_H}(V)$ for thermal pressure, which is expressed by

$$p_{T_H} = \frac{\gamma_0}{V_0} \int_0^{T_H} C_V dT, \tag{4.25}$$

where T_H is the temperature behind shock fronts, i.e., the Hugoniot temperature. The Hugoniot temperature T_H is obtained using Walsh-Christian equation:

$$C_{VH} \frac{dT_H}{dV_H} + C_{VH} \frac{\gamma_0}{V_0} T_H = \frac{1}{2} \frac{dp_H}{dV_H} (V_0 - V_H) + \frac{1}{2}(p_H - p_0), \tag{4.20}$$

The equation for p_E is given by

$$p_E = p_C + p_T, \tag{4.26}$$

where p_T is thermal pressure expressed by

$$p_{\mathrm{T}} = \frac{\gamma_0}{V_0} \int_0^T C_V dT .$$ (4.27)

Calculations are performed using three kinds of C_V expressed by Eqs. (4.17)-(4.19). Eqs. (4.20)-(4.27) are analyzed using a known Hugoniot function $p_{\mathrm{H}}(V)$ and a known Rayleigh line – pressure function $p(V)$ to determine the temperature, cold pressure, thermoelastic pressure, and viscous pressure.
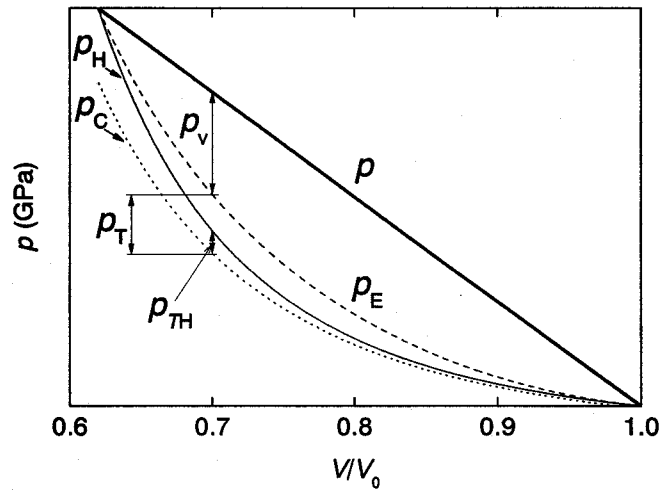
FIG. 4.30. Schematic of pressure-components as a function of V/V_0.

4.5.2.4 Effective temperature thickness

The effective thickness of the spatial profile of temperature (effective temperature thickness) is defined by [106-108]

$$\frac{\Delta T}{\Delta Z} = \left| \frac{dT}{dZ} \right|_{\max},$$ (4.28)

where Z is the Lagrangian coordinate moving with the same velocity as the constant velocity of overdriven steady shock fronts, which is of an infinite width [109], and $\Delta T = T_{\mathrm{H}} - T_0$. Therefore, it is assumed that the heat flux varies spatially slowly everywhere in the wave fronts. In general, the effective temperature thickness is larger than the effective specific volume thickness [106,107]. Derivative dT/dZ is related to the heat flux $J(Z)$ by the steady heat conduction equation:

$$J = -\frac{\kappa}{1-\varepsilon} \frac{dT}{dZ},$$ (4.29)

where κ is the heat conductivity, and $\varepsilon(Z) = 1 - V(Z)/V_0$ is the strain. Derivative $|dT/dZ|$ has its maximum when $(1 - \varepsilon)J$ is maximum, and this yields

$$\Delta Z = \frac{\kappa(T_H - T_0)}{[(1 - \varepsilon)J]_{max}}.$$ (4.30)

The continuity equation for heat transport is given by

$$\frac{dJ}{dZ} = \rho_0 U_S \frac{dQ}{dV} \frac{dV}{dZ},$$ (4.31)

where Q is the heat transferred to the material. The specific volume wave inside the steady wave front is assumed to expand from $Z = 0$ to $Z = \infty$. The following equation for the heat flux is obtained by integrating both sides of Eq. (4.29) from 0 to Z and using $J(0) = J_H = 0$:

$$J = U_S(\varepsilon_H - \varepsilon)\frac{dQ}{dV},$$ (4.32)

where $\varepsilon_H = 1 - V_H/V_0$.

The quantity $[(1 - \varepsilon)J]_{max}$ in Eq. (4.28) is determined by incorporating Eq. (4.30) into the IT_{IM} method. Here $dQ/dV = p_E - p_{S_0}$ is assumed, where p_{S_0} is the pressure which varies along the isentrope passing through the reference state. The effective temperature thickness is calculated, irrespective of the shape and the effective thickness of the specific volume wave.

4.5.2.5 Temperature in inviscid solids

The quadratic equation for the temperature T inside shock fronts is obtained by substituting the temperature-dependent constant-volume specific heat C_V expressed by Eqs. (4.18) and (4.19) into Eq. (4.27). The solution of this equation is given by

$$T = \frac{-3Nk_B + \sqrt{(3Nk_B)^2 + 2\Gamma(V_0/\gamma_0)p_T}}{\Gamma}.$$ (4.33)

where $p_T = p - p_C$ for an inviscid solid. The pressure p is given correctly by Eq. (4.21) and the cold pressure p_C is evaluated correctly using Eqs. (4.24)-(4.26). Thus, Eq. (4.33) estimates the temperature distribution inside shock wave fronts in inviscid solids correctly.

On the other hand, the following equation is obtained for the temperature-independent C_V (Eq. (4.17)):

$$T = \frac{1}{3Nk} \frac{V_0}{\gamma_0} p_T.$$ (4.34)

Equations (4.33) and (4.34) are used to investigate the effect of the viscous pressure on the temperature distributions for the temperature-dependent C_V (Eqs. (4.18) and (4.19)) and temperature-independent C_V (Eq. (4.17)), respectively.

154

4.5.3 Results

4.5.3.1 Thermodynamic equilibrium

I use the refined Hugoniot data of Brown *et al.* [91] as a known Hugoniot function $p_H(V)$. The Hugoniot is shown in FIG. 4.31. The data used for the calculation are listed in TABLE 4.5, where c and s are the constants expressed in the equation $U_S = c + sU_P$, which is estimated from the solid region of the data of Brown *et al.* [91], where U_P is the particle velocity. C_V/Nk_B distributions obtained from calculations using these values are shown in FIG. 4.32 as a function of the constant volume V and the Hugoniot pressure p_H. Solid and bold curves indicate the values of Brown and McQueen, and Sano, respectively. C_V of Brown and McQueen is found to be underestimated compared to C_V of Sano.
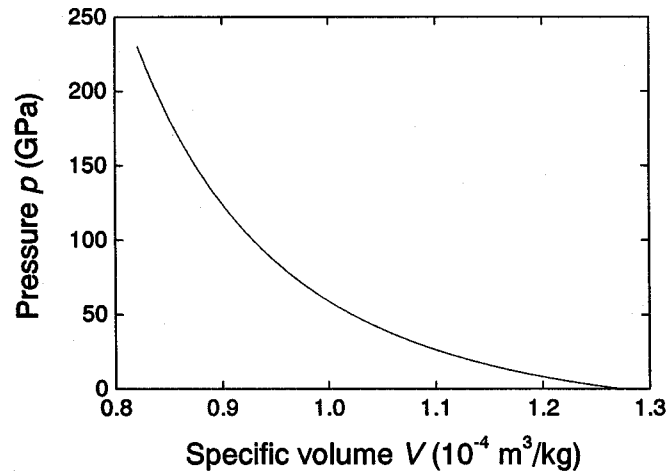
FIG. 4.31. Hugoniot obtained using the linear U_S-U_P relation of Brown *et al.* [91].
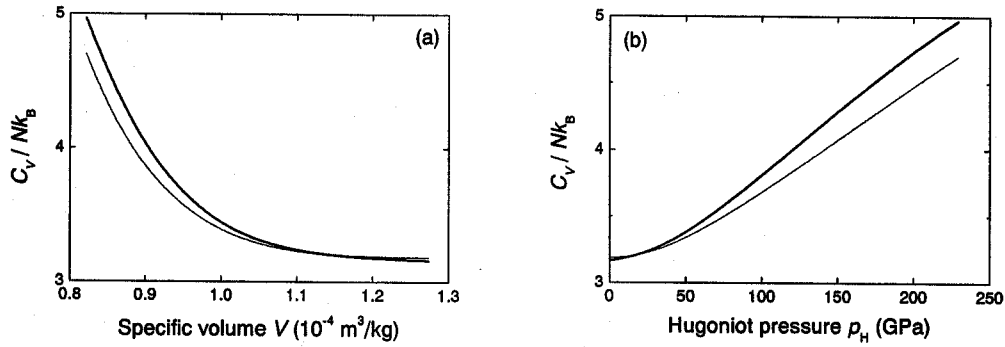
FIG. 4.32. Distribution of constant-volume specific heat C_V per Nk_B of Sano (heavy solid curve) Brown and McQueen (solid curve) [105] as a function of (a) constant-volume V and (b) Hugoniot pressure p_H..

TABLE 4.5. Input data for shock calculations in iron [111].

Ambient temperature T_0 (K)	300
Ambient density ρ_0 (g/cm^3)	7.85
c (km/s)	3.855
s	1.6196
Gruneisen parameter γ_0	1.69
Thermal conductivity κ (cal/cm s K)	0.10

The effective temperature thicknesses ΔZ and rise times Δt obtained using the IT$_{IM}$ method are listed in TABLE 4.5 for shocks up to 50, 100, 150, 200, 230 GPa, where $\Delta t \approx \Delta Z/U_S$. In spite of the assumption that the heat flux varies gradually everywhere, the effective temperature thicknesses of the order of tens of nm indicate that there is a region where the temperature varies rapidly inside each shock front. In this region heterogeneous plastic flow on an atomic scale is very large. The effective strain rates $\dot{\varepsilon}$ calculated using the Hugoniot strain ε_H and $\Delta t_S \approx \Delta t/3$ (see Ref. [106,107]) for shocks up to 50, 100, 150, 200, 230 GPa are also listed in TABLE 4.5. The effective strain rates of approximately 5.7×10^{11} s^{-1} which includes relatively large plastic flow deformation component is obtained for 230 GPa shock. Even this strain rate yields the increment of the strain of only 10^{-3} order during the electron – phonon relaxation time for metals (the order of 10 fs) which is dominant above the Debye temperature for shocks up to 200 – 300 GPa. In addition, the temperature rise time of approximately 1.8 ps for a 230 GPa shock is approximately 100 times longer compared with the relaxation time. Wallace discussed the equilibrium problem in solid metals in detail [110]. It is clear from Wallace's discussion that the electron – phonon system remains near thermodynamic

156

equilibrium even at the strain rate of the order of 10^{10} s^{-1}. The range of the strain rates is from 0.7×10^{11} s^{-1} to 5.7×10^{11} s^{-1} for shocks from 50 to 230 GPa, and this range is larger than 10^{11} s^{-1}. Thus, the assumption of thermodynamic equilibrium for shocks up to 230 GPa in iron is valid.

TABLE 4.5.   Effective temperature thickness ΔZ obtained using the equilibrium thermodynamic theory, shock wave velocities, and effective temperature rise times Δt, and Hugoniot strains ε_H and effective strain rates $\dot{\varepsilon}$ for 50, 100, 150, 200, 230 GPa shocks in iron.

Shock (GPa)	U_S (km/s)	ε_H	$C_V = 3Nk_B$ (Eq. (4.17))			$C_V = 3Nk_B + \Gamma_0(V/V_0)^g T$ (Eq. (4.18))			$C_V = 3Nk_B + (a_I p_H + b_\Gamma)T$ (Eq. (4.19))		
			ΔZ (nm)	Δt (ps)	$\dot{\varepsilon}$ (10^{11} s^{-1})	ΔZ (nm)	Δt (ps)	$\dot{\varepsilon}$ (10^{11} s^{-1})	ΔZ (nm)	Δt (ps)	$\dot{\varepsilon}$ (10^{11} s^{-1})
50	5.673	0.1979	50.3	8.9	0.67	47.3	8.3	0.71	46.9	8.3	0.72
100	6.862	0.2706	31.3	4.6	1.78	27.7	4.0	2.01	27.1	3.9	2.06
150	7.815	0.3129	25.8	3.3	2.84	21.6	2.8	3.39	20.8	2.7	3.53
200	8.634	0.3418	23.1	2.7	3.83	18.3	2.1	4.83	17.4	2.0	5.08
230	9.081	0.3553	22.1	2.4	4.39	16.9	1.9	5.72	16.0	1.8	6.04

4.5.3.2 Efficacy of the IT$_{IM}$ method

Thermoelastic pressure distributions (dashed curves) obtained using the IT$_{IM}$ method for shocks of 50, 150, 200, and 230 GPa in iron are shown in FIG. 4.33(a)-(d) together with the Rayleigh lines (heavy solid lines), the Hugoniots (solid curves), and the cold pressure distributions (dotted curves). It is verified in Ref. [103] that the assumption of heat transport is valid when the viscous pressure component $p_v = p - p_E$ is sufficiently large compared with the thermal pressure component $p_T = p_E - p_C$. FIG. 4.33(a)-(d) indicate the situation. Thus, the assumption of heat transport for shocks up to 230 GPa is valid. In addition, the validity of the fundamental assumption of thermodynamic equilibrium has been verified in the previous section. Therefore, the IT$_{IM}$ method is valid for shocks up to 230 GPa in iron, that is, temperature distributions inside shock fronts (inside temperature distributions) are predicted to a good approximation.
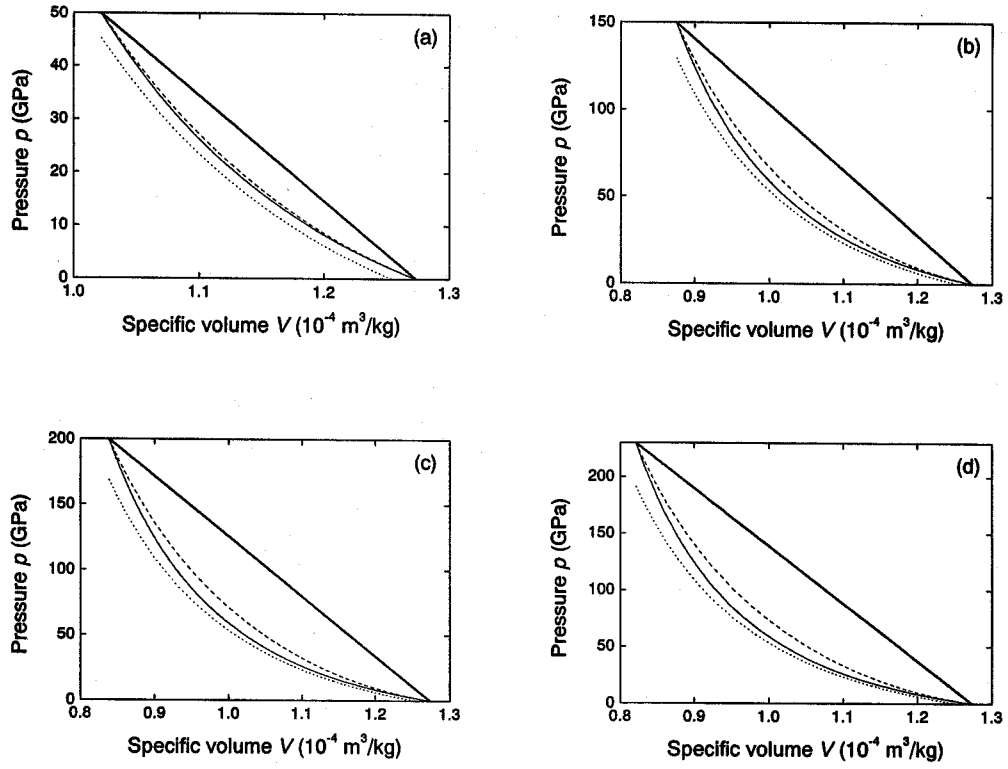
FIG. 4.33. Thermoelastic pressure distributions (dashed curves) obtained using the IT$_{IM}$ method, Hugoniots (solid curves), Rayleigh lines (heavy solid lines), and cold pressure distributions (dotted curves) for (a) 50, (b) 150, (c) 200, and (d) 230 GPa shocks in iron for $C_V = 3Nk_B$.

4.5.3.3 Influence of the viscous pressure

For three kinds of C_V, the inside temperature distribution (dashed curve) calculated using the IT_{IM} method and Eqs. (4.33) and (4.34) for a 230 GPa shock in an inviscid iron are shown in FIGs. 4.34-4.36 together with the inside temperature distribution (heavy solid curve) in a viscous iron and the temperature Hugoniot (solid curve). The inside temperature distributions in an inviscid iron are convex upward, because thermal pressure $(p_T)_{\text{IV}} = p - p_C$ increases and then decreases with a decrease in specific volume, where subscript IV refers to an inviscid solid. It is much higher than that in a viscous iron. The reason for this is accounted for using Eq. (4.33).

$(p_T)_{\text{IV}}$ is equal to $p - p_C$ as mentioned above because $p_E = p$ for an inviscid solid. On the other hand, p_T is equal to $p_{\text{EOS}} - p_C$ for a solid which is not inviscid because p_E is equal to p_{EOS}, where p_{EOS} is a pressure on the equation-of-state surface. The thermal pressures differ because p is not equal to p_{EOS}. It follows from $(p_T)_{\text{IV}} - p_T = p_v$ that $(p_T)_{\text{IV}} > p_T$. Eq. (4.33) indicates that the temperature is higher when the thermal pressure is larger. Therefore, the high temperature for an inviscid iron solid is due to the viscous pressure included in the temperature calculation. FIG. 4.33(a)-(d) indicates that the viscous pressure component is sufficiently large for any shock, and that the viscous pressure component increases with shock loading. As a result, the difference of the temperature distributions between an inviscid and a viscous solid increases with shock loading.

The underestimation of C_V is found to causes the overestimation of the temperature in FIGs. 4.34-4.36.
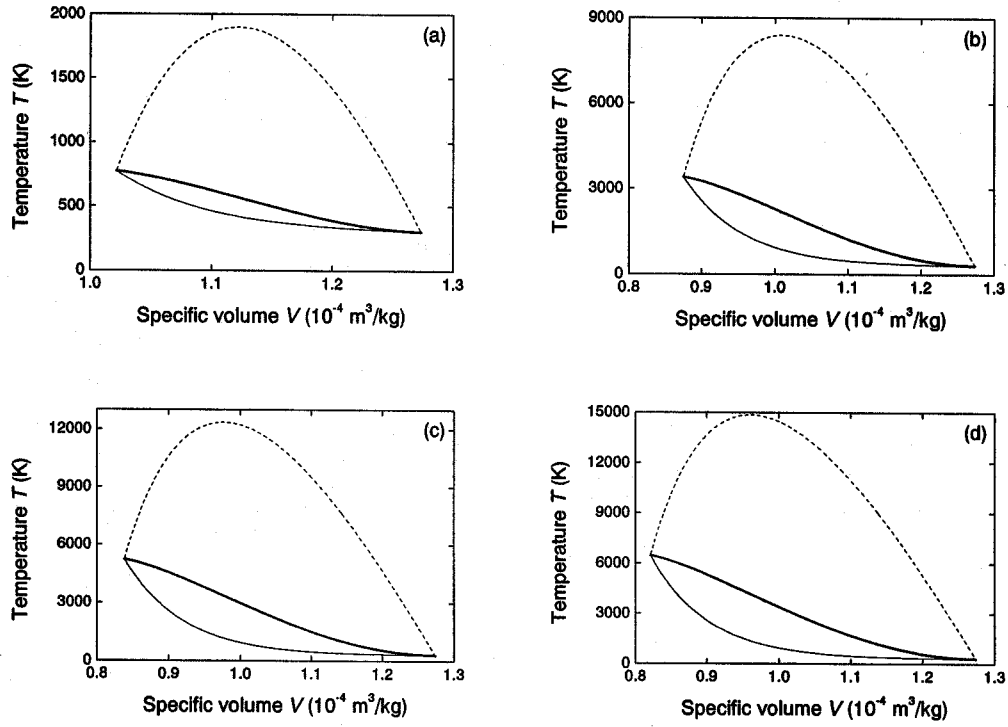
FIG. 4.34. Temperature distributions in a steady wave front for (a) 50, (b) 150, (c) 200, and (d) 230 GPa shock in iron obtained using IT_{IM} method (heavy solid curve) and in inviscid iron solid obtained using Eq. (4.34) (dashed curve), and temperature Hugoniot (solid curve) using temperature-independent C_V.

160
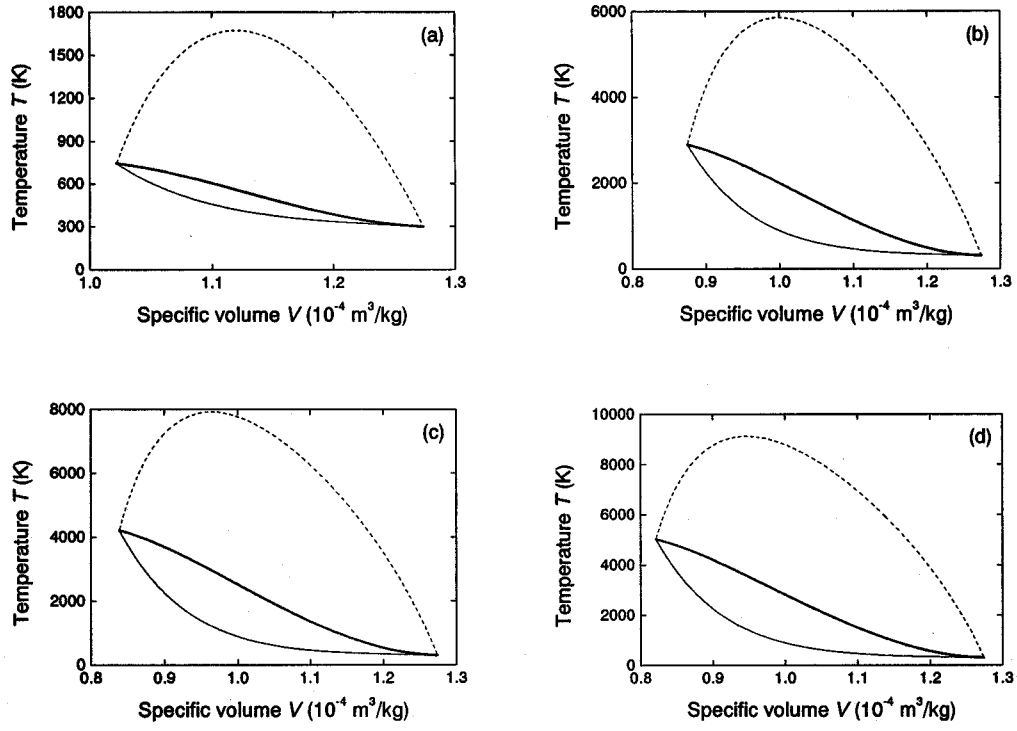
FIG. 4.35. Temperature distributions in a steady wave front for (a) 50, (b) 150, (c) 200, and (d) 230 GPa shock in iron obtained using IT_{IM} method (heavy solid curve) and in inviscid iron solid obtained using Eq. (4.33) (dashed curve), and temperature Hugoniot (solid curve) using temperature-dependent $C_V = 3Nk_B + \Gamma_0(V/V_0)^g T$ of Brown and McQueen [47].
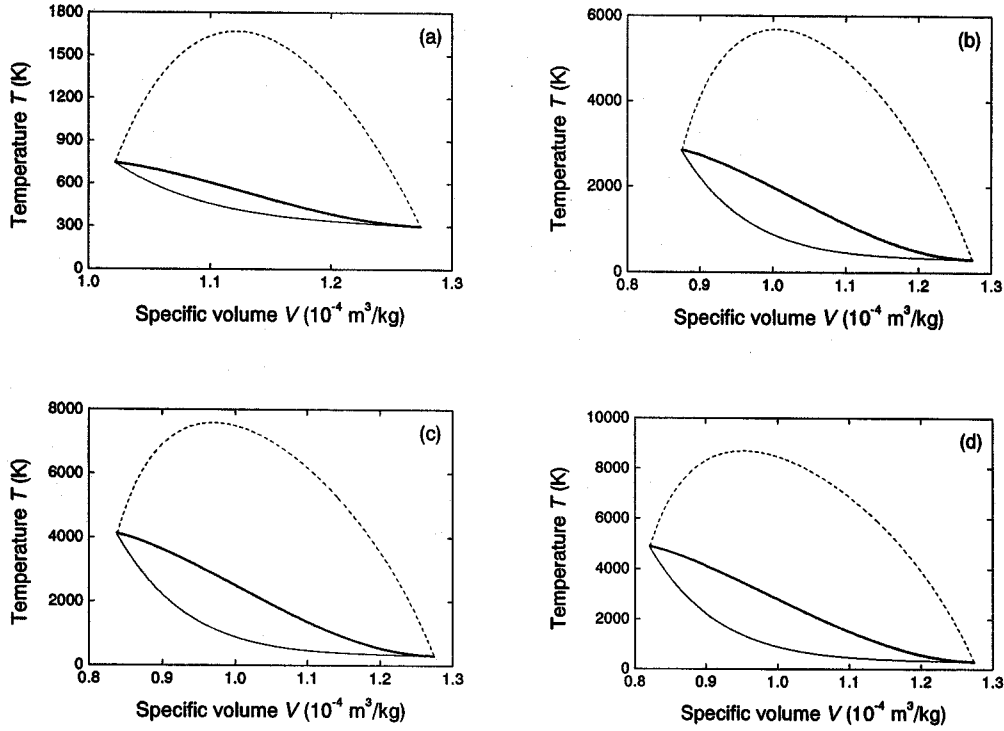
FIG. 4.36. Temperature distributions in a steady wave front for (a) 50, (b) 150, (c) 200, and (d) 230 GPa shock in iron obtained using IT_{IM} method (heavy solid curve) and in inviscid iron solid obtained using Eq. (4.33) (dashed curve), and temperature Hugoniot (solid curve) using temperature-dependent $C_V = 3Nk_B + (a_{\text{I}}p_{\text{H}} + b_{\Gamma})T_{\text{H}}$ of Sano.

4.5.4 Conclusions

Temperature distributions inside overdriven steady-plane wave fronts in solid iron shocked up to 230 GPa, where melting does not occur, were evaluated by applying the temperature-dependent constant-volume specific heat to the inside temperature method implicitly including heat transport which is based on the equilibrium thermodynamic theory. The inside temperature distributions are evaluated correctly because a fundamental assumption that the solid state inside the wave fronts is close to the thermodynamic equilibrium and another assumption on heat transport are valid. Overestimations of inside temperature distributions in an inviscid solid iron indicate that the viscous pressure influences the distributions. The underestimation of constant-volume specific heat in a higher pressure region causes the overestimation of the temperature distributions.

4.6   Detail explanation of the quenching of the ε phase of iron

Crystalline structures of the recovered iron sample after the femtosecond laser irradiation of a polycrystalline α-Fe were determined using EBSP, electron diffraction, and X-ray diffraction methods in Sec. 4.3. EBSP analysis shows the existence of the high pressure ε phase around the interface between crystalline grains and 4 μm deeper from the surface after the laser irradiation. Smaller quantity of the γ phase is also found to exist. Selected area electron diffraction measurements indicate the existence of both ε and γ phases. The existence of the ε phase and two d-spacings for a plane are indicated as a result of the synchrotron X-ray diffraction measurements. These experimental results are summarized that the ε phase and smaller quantity of the γ phase are formed around the interface between crystalline grains and that two d-spacings are found for a plane of the ε phase. The ε phase which is stable at high pressures is induced by the conventional shock compression and returns back to the original phase after the shock release, and the ε phase is not quenched. The reasons of the inducing and the quenching of the ε phase and smaller quantity of the γ phase after the femtosecond laser irradiation on the α-Fe will be considered below.

Firstly, the femtosecond laser ablation of iron will be described. The incident femtosecond laser pulse is absorbed by the free electrons in an iron sample as explained in Sec. 1.2. The electron relaxation is determined by the electron − electron collision and the heat propagation velocity v_T is independent of the time for the intense incident energy like this study [112]. This velocity decreases $v_T \propto 1/F$ as the increment of the laser fluence F. Laser is absorbed, and thermal conduction occurs into the sample at supersonic velocities before mass has time to ablate. Eventually ablation occurs and drives a mechanical shock into the material. Eventually the thermal front cools and its velocity drops below that of the following ablation shock [113-115]. The shock front passes the thermal front and the shock then traverses unheated material. This physical state is the classical problem of the hydrodynamic phenomena [116]. The amplitude of the shock pressure decreases continuously to zero with increasing propagation distance. However, the region behind the shock front remains in thermal equilibrium [117].

The pulse width of the laser used in the present study is 120 fs. The author illustrates how short the laser pulse is by relating the 120 fs time width to the vibrational period of a phonon at the Debye temperature. The Debye temperature of ε-iron at high pressures is approximately 700 K [22]. The vibrational period of this phonon is 7×10^{-14} s, which means that 120 fs is the time it takes for only two phonon vibrations. This is not expected to be long enough to drive a phase transition, which is evidence that the femtosecond laser pulse itself does not

163

synthesize ε-iron. As described earlier, on the other hand, this implies that the α to ε transition is driven by the conventional shock wave that forms.

In Sec. 4.5, temperatures inside and behind the steady shock wave fronts were calculated using the constant-volume specific heat $C_V = 3Nk_B + (a_\Gamma p + b_\Gamma)T$, where $a_\Gamma = -8.4904 \times 10^{-5}$ J/kgK^2 GPa, $b_\Gamma = 0.080145$ J/kgK^2, which was estimated in Sec. 4.4 and valid for the high pressure range. These temperatures as a function of the pressure are shown in FIG. 4.37. This phase diagram is valid for the shock data because the transition pressure from the bcc to the hcp obtained from shock data is nearly equal to that from static data as shown in FIG. 4.7. The temperature inside the shock front affects the phase transition because the shock induced phase transition occurs inside the shock front. The inside temperature crosses the α – ε phase boundary and the ε – β and β – α' boundaries assuming the β and α' phases exist as shown in FIG. 4.37. Therefore, this shock compression can induce the ε, β, and α' phases. The inside temperature is always below the transition point to the γ phase. This means that the γ phase is not induced by the shock compression directly.
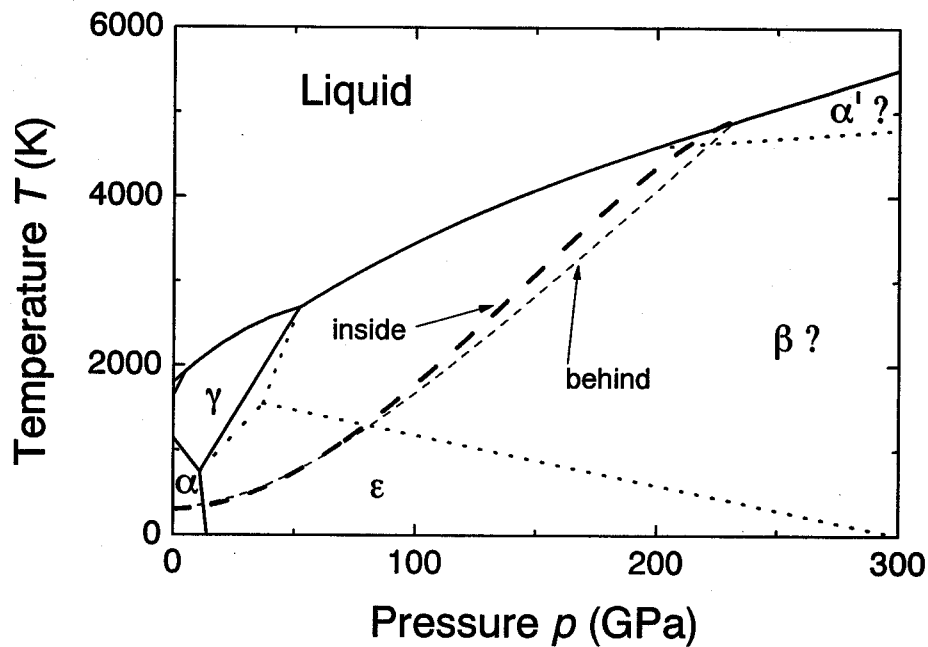
FIG. 4.37. Temperatures inside (bold dashed curve) and behind (dashed curve) the steady shock fronts as a function of the pressure. The valid constant-volume specific heat $C_V = 3Nk_B + (a_\Gamma p + b_\Gamma)T$, where $a_\Gamma = -8.4904 \times 10^{-5}$ J/kgK^2 GPa and $b_\Gamma = 0.080145$ J/kgK^2, which was estimated in Sec. 4.4 was used to calculate. The phase diagram is the same as FIG. 4.1.

164

The shock induced bcc to hcp transition of iron will be considered. As described in Sec. 4.1.1.2, it was first reported by Minshall [50], and the Hugoniots in these two phases were measured first by Bancroft *et al.* [51]. The thermodynamically equilibrium Hugoniot was calculated by Andrews [58], and it was found different greatly from the experimental results. Forbes observed the decay of S_2 wave and estimated the relaxation time τ of $\alpha \rightarrow \varepsilon$ transition at $\tau = 50$ ns [60]. Barker and Hollenbach performed the high resolution VISAR measurement of the shock profile in iron [59]. They obtained the correct Hugoniot data from the experiments and estimated $\tau = 180$ ns. These Hugoniot data are shown in FIG. 4.7. Static compression curve measured by Mao *et al.* [54] and Giles *et al.* [57] is also shown. Boettger and Wallace reported the metastability and the dynamics of the $\alpha \rightarrow \varepsilon$ transition of iron [72]. They reported that the relaxation time τ of the $\alpha \rightarrow \varepsilon$ transition depends on the shock intensity and that τ is $60 \rightarrow 12$ ns for shocks of $17 \rightarrow 30$ GPa. Although τ represents the linear irreversible thermodynamic relaxation, it was shown that some nonlinear relaxations should exist in the shock process of iron. In Sec. 4.5, the author showed that the effective temperature rise time is several picoseconds. Gahagan *et al.* measured the shock rise time and estimated it to be several picoseconds when the similar laser pulse (wavelength: 800 nm, pulse width: 130 fs, intensity: 10^{13} W/cm^2) to this study is irradiated on the thin metal films (Al and Ni) [115]. These values of the picoseconds rise time are valid because our calculated value is agreement with the experimental value. Overdriven shock wave profile in iron is shown in FIG. 4.38 taking account of picoseconds rise time and the nanoseconds relaxation time of the bcc to hcp transition. The time taken from the state O to the state M is the picoseconds rise time where the point M is the intersection point of the Rayleigh line with the extended curve of the Hugoniot OA, and the time taken from the state M to the final state B is the nanoseconds relaxation time.
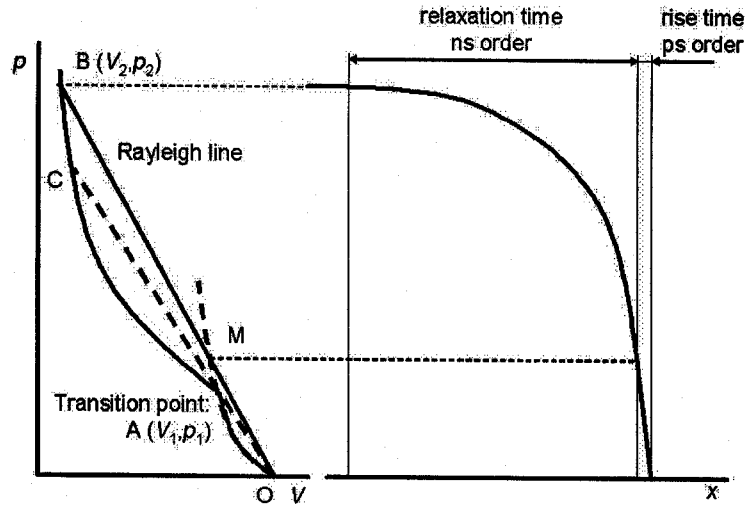
FIG. 4.38.　Pressure profile for an overdriven shock wave including a phase transition.

The model of the bcc to hcp transition of iron will be considered. As described in Sec. 4.1.1.1, the bcc – hcp transition of iron is martensitic. Three steps process of bcc – fcc – hcp including the interfacial fcc structure is thought to be valid as the transition model [73]. At the first step, (110) plane of the bcc shifts to the hexagonal plane which corresponds to (0002) plane of the hcp including the shear of the $[\bar{1}1\bar{1}]$ direction along the $(\bar{1}12)$ plane. At the second step, the interfacial fcc structure is formed shearing to the $[0\bar{1}10]_{hcp}$ direction along the $(110)_{bcc}$ plane. At the third step, the fcc transforms to the hcp structure shearing to the $[01\bar{1}0]$ direction along the (110) plane. There is a possibility that the fcc becomes metastable due to the lattice matching of the bcc and fcc structures after the little amount of the bcc – fcc transition. Therefore, the next step of the transition does not proceed without the additional pressure or a long waiting time. A shortage of the additional pressure or an insufficient waiting time can cause the incomplete γ to ε phase transition and the following remain of the γ phase.

Two d-spacings are detected for ε-Fe (101) as shown in FIG. 4.19. The one is thought to be originated from the ε phase which is induced by the shock wave propagating in the non-disturbed α-iron. The shock wave propagating into the laser-heated iron behind the heat front may induce the different ε phase from the above mentioned ε phase.

The reason for the quenching of the ε and γ phases may the incomplete hcp to bcc and fcc to bcc transitions due to the short rise time of the shock release wave which is similar to that of the shock compression wave.

166

4.7 Conclusions

4.7.1 Progress made in the present study

Results obtained in this chapter are summarized as follows;

1. It was found that the high pressure ε phase of iron, which is induced but not quenched using the conventional shock and static compression methods, is quenched by irradiating the femtosecond laser on the polycrystalline iron as a result of the determination of crystalline structures of the recovered iron using the EBSP, electron diffraction, and synchrotron X-ray diffraction methods. The γ phase of iron was also confirmed to exist.

2. Thermodynamic state in the shock front has to be known to investigate the mechanism of the shock induced phase transition because the transition occurs inside the shock front. Therefore, temperatures inside and behind the shock front were calculated using the thermodynamic theory. It was found that the ε phase is induced by the femtosecond laser driven shock compression as a result of calculations. On the other hand, it was suggested that the γ phase was not induced by the shock compression but induced as an intermediate phase between the bcc – hcp transition.

3. Correct values of the constant-volume specific heat C_{VH} and the Grüneisen parameter γ on the Hugoniot are required to calculate the temperatures inside and behind the shock front correctly. Therefore, these values were evaluated combining the Walsh-Christian equation with the Mie-Grüneisen equation. The validity of assumptions that the constant-volume specific heat is proportional to the temperature and that the Grüneisen parameter is the function of only the constant volume is verified in the solid range.

4. The reason for the quenching of the ε and γ phases may be due to the incomplete hcp – bcc and fcc – bcc transitions because the rise time of the shock release wave may be as short as that of the shock compression wave.

The high pressure phase of iron was quenched using the shock wave driven by the femtosecond laser ablation of iron. Though the mechanism of the quenching is not clear, this mechanism can be applied to other materials. Therefore, high pressure phases which are impossible to quench using conventional methods can be quenched using this method. This method is a powerful tool to pioneer new scientific and industrial fields which produce new materials of high pressure phase.

4.7.2 Subjects left in the future

In this study, mechanism of the quenching of the ε and γ phases is not clear though it was considered. We have to do many things to make it clear; *e.g.*, investigation of the quantity and the position in the sample of the ε and γ phases using synchrotron X-ray diffraction method varying the laser intensity and the surface plane of the single crystalline iron, confirmation that the ε and γ phases are not quenched after the conventional shock compression, measurements of the amplitude and the profile of the femtosecond laser driven shock wave using the frequency-domain interferometer [113,114,117-121].

Possibility of the quenching of the β and α' phases, which have been argued on the existence and crystalline structures in this decade, using this method is high. More intense laser will make it possible to complete the dispute. This is extremely significant in the fields of materials physics and geophysics.

We have to try to quench high pressure phases of other materials, *e.g.*, Si [122], Ge [123,124], GaAs [125], GaP [126], CdS [127], KCl [128], which are impossible to quench using the conventional shock compression method. This trial has great significance for verification of the originality of this method.

References in Chapter 4

[1]   F. Birch, "Elasticity and constitution of the Earth's interior," J. Geophys. Res. 57, 227-286 (1952).

[2]   O. L. Anderson, "Ramsey silicate core revisited," Nature 314, 407-408 (1985).

[3]   H. M. Strong, J. Geophys. Res. 64, 653 (1959).

[4]   F. P. Bundy, "Pressure-temperature phase diagram of iron to 200 kbar, 900 °C," J. Appl. Phys. 36, 616-620 (1965).

[5]   H. M. Strong, R. E. Tuft, and R. E. Hanneman, Metall. Trans. 4, 2657 (1973).

[6]   A. F. Guillermet and P. Gustafson, High Temp. High Press. 16, 591 (1984).

[7]   R. Boehler, "The phase diagram of iron to 430 kbar," Geophys. Res. Lett. 13, 1153-1156 (1986).

[8]   O. L. Anderson and D. G. Isaak, "Calculated melting curves for phases of iron," Am. Mineral. 85, 376-385 (2000).

[9]   S. K. Saxena and L. S. Dubrovinsky, "Iron phases at high pressures and temperatures: Phase transition and melting," Am. Mineral. 85, 372-375 (2000).

[10]   J. M. Brown, "The equation of state of iron to 450 GPa: Another high pressure solid phase?" Geophys. Res. Lett. 28, 4339-4342 (2001).

[11]   S. K. Saxena, G. Shen, and P. Lazor, "Experimental evidence for a new iron phase and implications for Earth's core," Science 260, 1312-1314 (1993).

[12]   S. K. Saxena, G. Shen, and P. Lazor, "Temperature in Earth's core based on melting and phase transformation experiments on iron," Science 264, 405-407 (1994).

[13]   S. K. Saxena, L. S. Dubrovinsky, P. Häggkvist, Y. Cerenius, G. Shen, and H. K. Mao, "Synchrotron x-ray study of iron at high pressure and temperature," Science 269, 1703-1704 (1995).

[14]   S. K. Saxena, L. S. Dubrovinsky, and P. Häggkvist, "X-ray evidence for the new phase β-iron at high temperature and high pressure," Geophys. Res. Lett. 23, 2441-2444 (1996).

[15]   S. K. Saxena, L. S. Dubrovinsky, P. Häggkvist, Y. Cerenius, G. Shen, and H. K. Mao, "Synchrotron x-ray study of iron at high pressure and temperature," Science 269, 1703-1704 (1995).

[16]   S. K. Saxena and L. S. Dubrovinsky, "Detecting phases of iron," Science 275, 94-96 (1997).

[17]   N. A. Dubrovinskaya, L. S. Dubrovinsky, and S. K. Saxena, "Systematics of thermodynamic data on solids: Thermochemical and pressure-volume-temperature

properties of some minerals," Geochim. Cosmochim. Ac. 61, 4151-4158 (1997).

[18] L. S. Dubrovinsky, S. K. Saxena, and P. Lazor, "X-ray study of iron with in-situ heating at ultra high pressures," Geophys. Res. Lett. 24, 1835-1838 (1997).

[19] L. S. Dubrovinsky, S. K. Saxena, P. Lazor, and H.-P. Weber, "Structure of β-iron at high temperature and pressure," Science 281, 11a (1998).

[20] L. S. Dubrovinsky, S. K. Saxena, and P. Lazor, "High-pressure and high-temperature in situ X-ray diffraction study of iron and corundum to 68 GPa using an internally heated diamond anvil cell," Phys. Chem. Miner. 25, 434-441 (1998).

[21] L. S. Dubrovinsky, S. K. Saxena, F. Tutti, and S. Rekhi, "In situ x-ray study of thermal expansion and phase transition of iron at multimegabar pressure," Phys. Rev. Lett. 84, 1720-1723 (2000).

[22] L. S. Dubrovinsky, S. K. Saxena, N. A. Dubrovinskaia, and T. L. Bihan, "Grüneisen parameter of β-iron up to 300 GPa from in-situ x-ray study," Am. Mineral. 85, 386-389 (2000).

[23] C. S. Yoo, J. Akella, A. J. Campbell, H. K. Mao, and R. J. Hemley, "Phase diagram of iron by in-situ x-ray diffraction: Implications for earth's core," Science 270, 1473 (1995).

[24] C. S. Yoo, J. Akella, A. J. Campbell, H. K. Mao, and R. J. Hemley, "Response to Detecting phases of iron," Science 275, 96 (1997).

[25] D. Andrault, G. Fiquet, M. Kunz, F. Visocekas, and D. Häusermann, "The orthorhombic structure of iron: An in situ study at high-temperature and high-pressure," Science 278, 831-834 (1997).

[26] D. Andrault, G. Fiquet, M. Kunz, F. Visocekas, and D. Häusermann, "Response to Structure of β-iron at high temperature and pressure," Science 281, 11a (1998).

[27] D. Andrault, G. Fiquet, T. Chrpin, and T. L. Bihan, "Structure analysis and stability field of β-iron at high P and T," Am. Mineral. 85, 364-371 (2000).

[28] O. L. Anderson, "Iron: Beta phase frays," Science 278, 821-822 (1997).

[29] G. A. de Wijs, G. Kresse, L. Vocadlo, D. Dobson, D. Alfè, M.J. Gillan, and G. D. Price, "The viscosity of liquid iron at the physical conditions of the Earth's core," Nature 392, 805-807 (1998).

[30] D. Alfè, M. J. Gillan, and G. D. Price, "The melting curve of iron at the pressures of the Earth's core from ab initio calculations," Nature 401, 462-464 (1999).

[31] L. Vocadlo, J. Brodholt, D. Alfè, and G. D. Price, "The structure of iron under the conditions of the Earth's inner core," Geophys. Res. Lett., 26, 1231-1234 (1999).

[32] D. Alfè, G. Kresse, and M. J. Gillan, "Structure and dynamics of liquid iron under Earth's

core conditions," Phys. Rev. B 61, 132-142 (2000).

[33] L. Vocadlo, J. P. Poirer, and G. D. Price, "Grüneisen parameters and isothermal equations of state," Am. Mineral. 85, 390-395 (2000).

[34] D. Alfè, G. D. Price, and M. J. Gillan, "Thermodynamics of hexagonal-close-packed iron under Earth's core conditions," Phys. Rev. B 64, 45123 (2001).

[35] D. Alfè, G. D. Price, and M. J. Gillan, "Iron under Earth's core conditions: Liquid-state thermodynamics and high-pressure melting curve from ab initio calculations," Phys. Rev. B 65, 165118 (2002).

[36] L. Stixrude, R. E. Cohen, and D. J. Singh, "Iron at high pressure: Linearized-augmented-plane-wave computations in the generalized-gradient approximation," Phys. Rev. B 50, 6442-6445 (1994).

[37] E. Wasserman, L. Stixrude, and R. E. Cohen, "Thermal properties of iron at high pressures and temperature," Phys. Rev. B 53, 8296-8309 (1996).

[38] L. Stixrude, E. Wasserman, and R. E. Cohen, "Composition and temperature of Earth's inner core," J. Geophys. Res. 50, 24729-24739 (1997).

[39] G. Steinle-Neumann and L. Stixrude, and R. E. Cohen, "First-principles elastic constants for the hcp transition metals Fe, Co, and Re at high pressure," Phys. Rev. B 60, 791-799 (1999).

[40] P. Söderlind, J. A. Moriarty, and J. M. Wills, "First-principles theory of iron up to earth-core pressures: Structural, vibrational, and elastic properties," Phys. Rev. B 53, 14063-14072 (1996).

[41] R. S. Rao, P. Modak, B. K. Godwal, and S. K. Sikka, "Stability of the pressure-induced orthorhombic phase of iron," Phys. Rev. B 59, 13498-13500 (1999).

[42] R. Boehler, "Temperatures in the Earth's core from melting-point measurements of iron at high static pressures," Nature 363, 534-536 (1993).

[43] R. Boehler, "The phase diagram of iron to 430 kbar," Geophys. Res. Lett. 13, 1153-1156 (1986).

[44] R. Boehler, N. von Bargen, and A. Chopelas, "Melting, thermal expansion, and phase traisitions of iron at high pressures," J. Geophys. Res. 95, 21731-31736 (1990).

[45] Q. Williams, R. Jeanloz, J. Bass, B. Svendsen, and T. J. Ahrens, "The melting curve of iron to 250 GPa: A constraint on the temperature at Earth's center," Science 236, 181-182 (1987).

[46] L. S. Dubrovinsky, S. K. Saxena, and P. Lazor, "Stability of beta-iron: A new synchrotron X-ray study of heated iron at high pressure," Eur. J. Mineral. 10, 43-47 (1998).

[47] J. M. Brown and R. G. McQueen, "Phase transitions, Grüneisen parameter, and elasticity for shocked iron between 77 GPa and 400 GPa," J. Geophys. Res. 91, 7485-7494 (1986).

[48] M. Matsui and O. L. Anderson, "The case for a body-centered cubic phase (α') for iron at inner core conditions," Phys. Earth Planet. In. 103, 55-62 (1997).

[49] O. L. Anderson and A. Duba, "Experimental melting curve of iron revisited," J. Geophys. Res. 102, 22659-22669 (1997).

[50] S. Minshall, "Investigation of a polymorphic transition in iron at 130 k.b.," Phys. Rev. 98, 271 (1955).

[51] D. Bancroft, E. L. Peterson, and S. Minshall, "Polymorphism of iron at high pressure," J. Appl. Phys. 27, 291-298 (1956).

[52] P. C. Johnson, B. A. Stein, and R. S. Davis, "Temperature dependence of shock-induced phase transformations in iron," J. Appl. Phys. 33, 557-561 (1962).

[53] L. Kaufman, E. V. Clougherty, and R. J. Weiss, Acta Metall. 11, 323-335 (1963).

[54] H. K. Mao, W. A. Bassett, and T. Takahashi, "Effect of pressure on crystal structure and lattice parameters of iron up to 300 kbar," J. Appl. Phys. 38, 272-276 (1967).

[55] H. G. Bowden and P. M. Kelly, "The crystallography of the pressure induced phase transformations in iron alloys," Acta Metall. 15, 1489-1500 (1967).

[56] S. N. Vaidya and G. C. Kennedy, "Compressibility of 18 metals to 45 kbar," J. Phys. Chem. Solids 31, 2329-2345 (1970).

[57] P. M. Giles, M. H. Longenbach, and A. R. Marder, J. Appl. Phys. 42, 4290 (1971).

[58] D. J. Andrews, "Equation of state of the alpha and epsilon phases of iron," J. Phys. Chem. Solids 34, 825-840 (1973).

[59] L. M. Barker and R. E. Hollenbach, "Shock wave study of the $\alpha \leftrightarrow \varepsilon$ phase transition in iron," J. Appl. Phys. 45, 4872-4887 (1974).

[60] J. W. Forbes and G. E. Duvall, "Experimental investigation of the kinetics of the shock induced alpha to epsilon phase transformation in Armco iron," Rev. Phys. Chem. Jpn., 480-481 (1975).

[61] T. J. Ahrens, "Dynamic compression of Earth materials," Science 207, 1035-1041 (1980).

[62] G. Cort, R. D. Taylor, and J. O. Willis, "Search for magnetism in hcp ε-Fe," J. Appl. Phys. 53, 2064-2065 (1982).

[63] H. Hasegawa and D. G. Pettifor, "Microscopic theory of the temperature-pressure phase diagram of iron," Phys. Rev. Lett. 50, 130-133 (1983).

[64] A. P. Jephcoat, H. K. Mao, and P. M. Bell, "Static compression of iron to 78 GPa with rare gas solids as pressure-transmitting media," J. Geophys. Res. 91, 4677-4684 (1986).

[65] W. A. Bassett and E. Huang, "Mechanism of the body-centered cubic hexagonal close-packed phase-transition in iron," Science 238, 780-783 (1987).

[66] E. Huang, W. A. Bassett, and P. Tao, "Pressure-temperature-volume relationship for hexagonal close packed iron determined by synchrotron radiation," J. Geophys. Res. 92, 8129-8135 (1987).

[67] G. L. Krasko and G. B. Olson, "Energetics of bcc-fcc lattice deformation in iron," Phys. Rev. B 40, 11536-11545 (1989).

[68] V. P. Dmitriev, Yu. M. Gufan, and P. Tolédano, "Theory of the phase diagram of iron and thallium: The Burgers and Bain deformation mechanisms revised," Phys. Rev. B 44, 7248-7255 (1991).

[69] R. D. Taylor, M. P. Pasternak, and R. Jeanloz, "Hysteresis in the high pressure transformation of bcc- to hcp-iron," J. Appl. Phys. 69, 6126-6128 (1991).

[70] K. S. Cheung, R. J. Harrison, and S. Yip, "Stress induced martensitic transition in a molecular dynamics model of α-iron," J. Appl. Phys. 71, 4009-4014 (1992).

[71] N. Funamori, T. Yagi, and T. Uchida, "High-pressure and high-temperature in situ x-ray diffraction study of iron to above 30 GPa using MA8-type apparatus," Geophys. Res. Lett. 23, 953-956 (1996).

[72] J. C. Boettger and D. C. Wallace, "Metastability and dynamics of the shock-induced phase transition in iron," Phys. Rev. B 55, 2840-2849 (1997).

[73] F. M. Wang and R. Ingalls, "Iron bcc-hcp transition: Local structure from x-ray-absorption fine structure," Phys. Rev. B 57, 5647-5654 (1998).

[74] M. Ekman, B. Sadigh, and K. Einarsodotter, "Ab initio study of the martensitic bcc-hcp transformation in iron," Phys. Rev. B 58, 5296-5304 (1998).

[75] H. C. Herper, E. Hoffmann, and P. Entel, "Ab initio full-potential study of the structural and magnetic phase stability of iron," Phys. Rev. B 60, 3839-3848 (1999).

[76] J. P. Rueff, M. Krisch, Y. Q. Cai, A. Kaprolat, M. Hanfland, M. Lorenzen, C. Masciovecchio, R. Verbeni, and F. Sette, "Magnetic and structural α-ϵ phase transition in Fe monitored by x-ray emission spectroscopy," Phys. Rev. B 60, 14510-14512 (1999).

[77] J. Jiang, J. S. Olson, and L. Gerward, "Grain-size and alloying effects on the pressure-induced bcc-to-hcp transition in nanocrystalline iron," Mater. Trans. 42, 1571-1574 (2001).

[78] S. S. Saxena and P. B. Littlewood, "Iron cast in exotic role," Nature 412, 290-291 (2001).

[79] Z. Nishiyama, Martensitic Transformation (Academic, New York, 1978).

[80] W. G. Burgers, "On the process of transition of the cubic-body-centered modification into

the hexagonal-close-packed modification of zirconium," Physica 1, 561-586 (1934).

[81]   G. E. Duvall and R. A. Graham, "Phase transitions under shock-wave loading," Rev. Mod. Phys. 49, 523-579 (1977).

[82]   V. S. Teodorescu, L. C. Nistor, J. Van Landuyt, and M. Dinescu, "TEM study of laser induced phase transition in iron thin films," Mat. Res. Bull. 29, 63-71 (1994).

[83]   V. S. Teodorescu, I. M. Mihailescu, M. Dinescu, N. Chitica, L. C. Nistor, J. Van Landuyt, and A. Barborica, "Laser induced phase transition in iron thin films," J. de Physique IV, C4-127 (1994).

[84]   J. P. Romain, M. Hallouin, M. Gerland, F. Cottet, and L. Marty, "$\alpha \rightarrow \varepsilon$ phase transition in iron induced by laser generated shock waves," in *Shock Waves in Condensed Matter 1987*, edited by S.C. Schmidt and N.C. Holmes (Elsevier Science Publishers B.V., Amsterdam, 1988), p. 787-790.

[85]   B. I. Gromov, M. V. Erofeev, A. A. Kalin, and V. A. Moiseev, "Evolution of nanosecond shock waves and the phase transition time in Armco-iron," Sov. Tech. Phys. Lett. 16, 391-392 (1990).

[86]   I. V. Erofeev, V. V. Silberschmidt, A. A. Kalin, V. A. Moiseev, and I. V. Solomatin, "Evolution of a laser-generated shock wave in iron and its interaction with martensitic transformation and twinning," Shock Waves 8, 177-181 (1998).

[87]   T. de Rességuier and M. Hallouin, "Interaction of two laser shocks inside iron samples," J. Appl. Phys. 90, 4377-4384 (2001).

[88]   B. L. Adams, S. I. Wright, and K. Kunze, Metall. Trans. A 24, 819 (1993).

[89]   J. M. Walsh and R. H. Christian, "Equation of state of metals from shock wave measurements," Phys. Rev. 97, 1544-1556 (1955).

[90]   T. Sano and Y. Sano, "Equilibrium thermodynamic theory for the evaluation of temperature distributions in overdriven steady-plane wave fronts," J. Appl. Phys. 90, 3754-3761 (2001).

[91]   J. M. Brown, J. N. Fritz, and R. S. Hixon, "Hugoniot data for iron," J. Appl. Phys. 88, 5496-5498 (2000).

[92]   H. K. Mao, Y. Wu, L. C. Chen, and J. F. Shu, "Static compression of iron to 400 GPa and Fe0.8Ni0.2 alloy to 260 GPa: Implications for compression of the core," J. Geophys. Res. 95, 21737-21742 (1990).

[93]   A. B. Belonoshko, R. Ahuja, and B. Johansson, "Quasi-ab initio molecular dynamic study of Fe melting," Phys. Rev. Lett. 84, 3638-3641 (2000).

[94]   G. Shen, H. K. Mao, R. J. Hemley, T. S. Duffy, and M. L. Rivers, "Melting and crystal

structure of iron at high pressure and temperatures," Geophys. Res. Lett. 25, 373-376 (1998).

[95] A. Laio, S. Bernard, G. L. Chiarotti, S. Scandolo, and E. Tosatti, "Physics of iron at Earth's core conditions," Science 287, 1027-1030 (2000).

[96] D. Erradonea, B. Schwager, R. Ditz, C. Gessmann, R. Boehler, and M. Ross, "Systematics of transition-metal melting," Phys. Rev. B 63, 132104 (2001).

[97] R. Boehler, "High-pressure experiments and the phase diagram of lower mantle and core materials," Rev. Geophys. 38, 221-245 (2000).

[98] C. S. Yoo, N. C. Holmes, M. Ross, D. J. Webb, and C. Pike, "Shock temperatures and melting of iron at earth core conditions," Phys. Rev. Lett. 70, 3931-3934 (1993).

[99] L. Burakovsky, D. L. Preston, and R. R. Silbar, "Melting as a dislocation-mediated phase transition," Phys. Rev. B 61, 15011-15018 (2000).

[100] L. Burakovsky, D. L. Preston, and R. R. Silbar, "Analysis of dislocation mechanism for melting of elements: Pressure dependence," J. Appl. Phys. 88, 6294-6301 (2000).

[101] The reasons why we adopted $w(V)T$ into the temperature-dependent part are as follows: The Grüneisen parameter at zero pressure and temperature T can be shown to be a linear function of temperature in the region below 2000 K to a good approximation by calculating a thermodynamic relationship $\gamma_{T,0} = (\alpha_{T,0} K_{T,0} V_{T,0})/(C_V)_{T,0}$ using the constant-volume specific heat $(C_V)_{T,0} = 3Nk_B + \Gamma_1 T$, the bulk modulus $K_{T,0} = (b_0 + b_1 T + b_2 T^2)^{-1}$, the thermal expansivity $\alpha_{T,0} = a_0 + a_1 T + a_2 T^2$, and the specific volume $V_{T,0} = V_0 \exp\left[\int \alpha_{T,0} dT\right]$ at zero pressure and temperature T (see Refs.[13,18,20,21,46,64,66,71] for the constants in these thermodynamic parameters); In addition, our γ_{isoth} distributions on isotherms at 2000 and 4000 K calculated using $w(V)T^2$ (and $w(V)T^3$) for the temperature-dependent part did not satisfy the three conditions discussed in Sec. IIID as did the γ_{isoth} distributions for $w(V)T$.

[102] J. H. Nguyen and N. C. Holmes, "Iron sound velocities in shock wave experiments," in *Shock Compression of Condensed Matter – 1999*, edited by M. D. Furnish, L. C. Chhabildas, and R. S. Hixon (AIP Conf. Proc. 505, New York, 2000), p. 81-84.

[103] Y. Sano and A. Abe, "Estimate of temperature distributions in steady-plane wave fronts using a Hugoniot function," J. Appl. Phys. 89, 105-114 (2001).

[104] D. C. Wallace, in *Shock Compression of Condensed Matter – 1985*, edited by Y.M. Gupta (Elsevier, New York, 1986), p. 37.

[105] J. D. Bass, B. Svendsen, and T. J. Ahrens, in *High-Pressure Research in Mineral Physics*, edited by M. H. Manghnani and Y. Syono (Terra Scientific, Tokyo, 1987), p. 393.

[106] D. C. Wallace, "Irreversible thermodynamics of overdriven shocks in solids," Phys. Rev. B 24, 5597-5606 (1981).

[107] D. C. Wallace, "Nature of the process of overdriven shocks in metals," Phys. Rev. B 24, 5607-5615 (1981).

[108] Ya. B. Zel'dovich and Yu. P. Raizer, in *Physics of Shock Waves and High Temperature Hydrodynamic Phenomena*, edited by W. D. Hayes and R. F. Probstein (Dover Publications, New York, 2002).

[109] L. Davison, "Shock-wave structure in porous solids," J. Appl. Phys. 42, 5503 (1971).

[110] D. C. Wallace, "Irreversible thermodynamics of flow in solids," Phys. Rev. B 22, 1477-1486 (1980).

[111] R. G. McQueen, S. P. Marsh, J. W. Taylor, J. N. Fritz, and W. J. Crater, in *High Velocity Impact Phenomena*, edited by R. Kinslow (Academic, New York, 1970), p. 293.

[112] A. Ng, A. Forsman, and P. Celliers, "Heat front propagation in femtosecond-laser-heated solids," Phys. Rev. E 51, 5208-5211 (1995).

[113] R. Evans, A.D. Badger, F. Falliès, M. Mahdieh, T.A. Hall, P. Audebert, J.-P. Geindre, J.-C. Gautheier, A. Mysyrowicz, G. Grillon, and A. Antonetti, "Time- and space-resolved optical probing of femtosecond-laser-driven shock waves in aluminum," Phys. Rev. Lett. 77, 3359-3362 (1996).

[114] K.T. Gahagan, D.S. Moore, D.J. Funk, R.L. Rabie, S.J. Buelow, and J.W. Nicholson, "Measurement of shock wave rise times in metal thin films," Phys. Rev. Lett. 85, 3205-3208 (2000).

[115] R. J. Trainor and Y. T. Lee, "Analytic models for design of laser-generated shock-wave experiments," Phys. Fluids 25, 1898-1907 (1982).

[116] R. Pakula and R. Sigel, "Self-similar expansion of dense matter due to heat transfer by nonlinear conduction," Phys. Fluids 28, 232-244 (1985).

[117] E. Tokunaga, A. Terasaki, and T. Kobayashi, "Frequency-domain interferometer for femtosecond time-resolved phase spectroscopy," Opt. Lett. 17, 1131-1133 (1992).

[118] E. Tokunaga, A. Terasaki, and T. Kobayashi, "Induced phase modulation of chirped continuum pulses studied with a femtosecond frequency-domain interferometer," Opt. Lett. 18, 370-372 (1993).

[119] J. P. Geindre, P. Audebert, A. Rousse, F. Falliès, J. C. Gauthier, A. Mysyrowicz, A. Dos Santos, G. Hamoniaux, and A. Antonetti, "Frequency-domain interferometer for measuring the phase and amplitude of a femtosecond pulse probing a laser-produced plasma," Opt. Lett. 19, 1997-1999 (1994).

[120] E. Tokunaga, A. Terasaki, and T. Kobayashi, "Femtosecond phase spectroscopy by use of frequency-domain interference," J. Opt. Soc. Am. B 12, 753-771 (1995).

[121] D. J. Funk, D. S. Moore, K. T. Gahagan, S. J. Buelow, J. H. Reho, G. L. Fisher, and R. L. Rabie, "Ultrafast measurement of the optical properties of aluminum during shock-wave breakout," Phys. Rev. B 115114 (2001).

[122] T. Goto, T. Sato, and Y. Syono, "Reduction of shear-strength and phase transition in shock-loaded silicon," Jpn. J. Appl. Phys. Part 2, 21, L369-L371 (1982).

[123] R. A. Graham, O. E. Jones, and J. R. Holland, "Shock-wave compression of germanium from 20 to 140 kbar," J. Appl. Phys. 36, 3955 (1965).

[124] R. A. Graham, O. E. Jones, and J. R. Holland, "Physical behavior of germanium under shock wave compression," J. Phys. Chem. Solids 27, 1519 (1966).

[125] T. Goto, Y. Syono, J. Nakai, and Y. Nakagawa, "Pressure-induced phase-transition in GaAs under shock compression," Solid State Commun. 18, 1607-1609 (1976).

[126] T. Goto and Y. Syono, "Shock-induced phase-transition in GaP," AIP Conference Proceedings 78, 320-324 (1982).

[127] J. D. Kennedy and W. B. Benedick, "Shock-induced phase transition in single crystal CdS," J. Phys. Chem. Solids 27, 125 (1966).

[128] D. B. Hayes, "Polymorphic phase-transformation rates in shock-loaded potassium-chloride," J. Appl. Phys. 45, 1208-1217 (1974).

[129] O. Sakata, Y. Furukawa, S. Goto, T. Mochizuki, T. Uruga, K. Takeshita, H. Ohashi, T. Ohata, T. Matsushita, S. Takahashi, H. Tajiri, T. Ishikawa, M. Nakamura, M. Ito, K. Sumitani, T. Takahashi, T. Shimura, A. Saito, and M. Takahashi, "Beamline for surface and interface structures at SPring-8," Surf. Rev. Lett. 10, 543-547 (2003).

[130] N. Funamori, T. Yagi, and T. Uchida, "High-pressure and high-temperature in situ x-ray diffraction study of iron to above 30 GPa using MA8-type apparatus," Geophys. Res. Lett. 23, 953-956 (1996).

[131] T. Takahashi and W. A. Bassett, "High-pressure polymorph of iron," Science 145, 483-486 (1964).

[132] C. S. Yoo, W. J. Nellis, M. L. Sattler, and R. G. Muskett, "Diamondlike metastable carbon phases from shock-compressed C_{60} films," Appl. Phys. Lett. 61, 273-275 (1992).

[133] H. Hirai and K. Kondo, "Modified phases of diamond formed under shock compression and rapid quenching," Science 253, 772-774 (1991).

[134] H. Hirai, K. Kondo, and H. Sugiura, "Possible structural models of n-diamond: A modified form of diamond," Appl. Phys. Lett. 61, 414-416 (1992).

[135] H. Hirai, K. Kondo, N. Yoshizawa, and M. Shiraishi, "Amorphous diamond from C_{60} fullerene," Appl. Phys. Lett. 64, 1797-1799 (1994).

[136] H. Hirai, T. Ohwada, and K. Kondo, "Shock compression of graphite materials bearing different microstructures and their relations to diamond transition," J. Mater. Res. 10, 175-182 (1995).

[137] H. Hirai, S. Kukino, and K. Kondo, "Predominant parameters in the shock-induced transition from graphite to diamond," J. Appl. Phys. 78, 3052-3059 (1995).

[138] H. Hirai and K. Kondo, "Changes in structure and electronic state from C_{60} fullerene to amorphous diamond," Phys. Rev. B 51, 15555-15558 (1995).

[139] H. Hirai, Y. Tabira, K. Kondo, T. Oikawa, and N. Ishizawa, "Radial distribution function of a new form of amorphous diamond shock induced from C_{60} fullerene," Phys. Rev. B 52, 6162-6165 (1995).

[140] H. Hirai, K. Kondo, M. Kim, H. Koinuma, K. Kurashima, and Y. Bando, "Transparent nanocrystalline diamond ceramics fabricated from C_{60} fullerene by shock compression," Appl. Phys. Lett. 71, 3016-3018 (1997).

[141] H. Hirai, M. Terauchi, M. Tanaka, and K. Kondo, "Band gap of essentially fourfold-coordinated amorphous diamond synthesized from C_{60} fullerene," Phys. Rev. B 60, 6357-6361 (1999).

[142] T. Sekine, H. He, T. Kobayashi, M. Zhang, and F. Xu, "Shock-induced transformation of β-Si_3N_4 to a high-pressure cubic-spinel phase," Appl. Phys. Lett. 76, 3706-3708 (2000).

[143] M. Zhang, H. He, F. F. Xu, T. Sekine, T. Kobayashi, and Y. Bando, "High-resolution transmission electron microscopy of cubic Si_3N_4," J. Appl. Phys. 88, 3070-3072 (2000).

[144] H. He, T. Sekine, T. Kobayashi, and H. Hirosaki, "Shock-induced phase transition of β-Si_3N_4 to c-Si_3N_4," Phys. Rev. B 62, 11412-11417 (2000).

[145] R. G. Egdell, V. E. Henrich, R. Bowdler, T. Sekine, "On the difference in valence electron plasmon energy and density of states between beta- and cubic-Si_3N_4," J. Appl. Phys. 94, 6611-6615 (2003).

[146] T. Sekine and T. Kobayashi, "Shock compression of 6H polytype SiC to 160 GPa," Phys. Rev. B 55, 8034-8037 (1997).

[147] T. Kobayashi, T. Sekine, and H. He, "Effect of inelastic deformation on crystallite size in post-shock 6H polytype SiC," Phys. Rev. Lett. 85, 2969-2972 (2000).

[148] T. Sekine and T. Sato, "Shock-induced mechanisms of phase transformation from rhombohedral BN to cubic BN," J. Appl. Phys. 74, 2440-2444 (1993).

[149] T. Sekine, T. Kobayashi, and H. Nameki, "Effects of deviatoric stress and radial strain on

the shock-induced diffusionless transformation in boron nitride," J. Appl. Phys. 81, 527-529 (1997).

Chapter 5

Conclusions

In this study, the femtosecond laser ablation of metals is applied to three kinds of microprocessing; laser direct writing of micro metal patterns in Chapter 2, formation of microspike arrays for micro field emitter utilizing the optical diffraction in Chapter 3, and the quenching of the high pressure phase using the femtosecond laser driven shock wave in Chapter 4. In Chapter 2, advantage of the femtosecond laser induced forward transfer of thin metal films was shown compared to the excimer laser. In Chapter 3, micro removal processing which can not be achieved without using the femtosecond laser was realized. In Chapter 4, a new method that the femtosecond laser is used as the shock wave driver was tried and the quenching of the high pressure phase of iron, which is impossible using the conventional shock compression method, was succeeded.

Results described in this dissertation are summarized follows.

In Chapter 2, laser induced forward transfers of thin metal films using a single pulse of excimer laser (wavelength: 248 nm, pulse width: 30 ns) with the flat-top profile of the laser intensity (Excimer-LIFT) and femtosecond laser (wavelength: 800 nm, pulse width: 120 fs) with the Gaussian profile (Fs-LIFT) were described. The purpose was to achieve the high-resolution deposition of micropatterns. The different point between the Excimer-LIFT and the Fs-LIFT processes is the absorption of the laser energy from the laser induced plume. For the Excimer-LIFT, the ablation occurs during the laser pulse and the laser induced plume is generated. The plume is heated by absorbing the latter part of the laser pulse. The scatter of microparticles expands as a result of the growth of the plume due to the evaporation of the deposited pattern. For the Fs-LIFT, on the other hand, the growth of the plume depends only on the fluence because the ablation occurs after the whole laser pulse and the laser energy is not absorbed by the plume. Therefore, the scatter of microparticles is prevented. Scatter of droplets depends on the melted area outside the laser irradiated region in the thin film for the Excimer-LIFT and the difference of the laser intensity in the laser beam for the Fs-LIFT. The Fs-LIFT is a powerful tool to achieve the high-resolution micropatterning of metals when the thin film does not contact with the acceptor substrate.

In Chapter 3, microspike arrays were fabricated by irradiating the femtosecond laser on the tungsten surface through the mask opening in air with the aim of fabricating the micro field emitter for the field emission display using only the femtosecond laser. Natural logarithm of the calculated intensity distributions diffracted at the edge of the mask opening was qualitatively consistent with the experimental results of the shape and arrays of microspikes. The ability of

the field emission of microspike arrays was evaluated. This method can be powerful tool to fabricate the field emitter.

In Chapter 4, the high pressure phase of iron was quenched using the shock wave driven by the femtosecond laser ablation of iron. Though the mechanism of the quenching is not clear yet, this mechanism can be applied to other materials. Therefore, high pressure phases which are impossible to quench using conventional methods can be quenched using this method. This method is a powerful tool to pioneer new scientific and industrial fields which produce new materials of high pressure phase.

As described above, advantages and originalities of applications of the femtosecond laser ablation of metals to microprocessing, which have not been investigated actively, were represented in this dissertation. The author hopes that this dissertation will be a trigger to diffuse the femtosecond laser ablation of metals into the industrial market and to stimulate scientific researchers of the related fields.

Appendix A

Derivation of Walsh-Christian equation

In Sec. 4.4, a quadratic equation for the temperature-independent Grüneisen parameter γ is derived by a method in which the Walsh-Christian and Mie-Grüneisen equations are combined. In Sec. 4.5, the temperature behind the shock front is calculated using the Walsh-Christian equation. In this chapter, the Walsh-Christian equation is derived.

Walsh and Christian derived the following thermodynamic equation (Walsh-Christian equation) assuming that C_V and $(dp/dT)_V$ are constant.

$$C_{V\mathrm{H}}\frac{dT_\mathrm{H}}{dV_\mathrm{H}} + \frac{\gamma_0}{V_0}C_{V\mathrm{H}}T_\mathrm{H} = \frac{1}{2}\frac{dp_\mathrm{H}}{dV_\mathrm{H}}(V_0 - V_\mathrm{H}) + \frac{1}{2}(p_\mathrm{H} - p_0). \tag{A.1}$$

This equation is obtained by integrating the thermodynamic equation along the Hugoniot. Therefore, the temperature behind the shock front is calculated correctly without depending on the structure in the steady wave front because the entropy generation due to the heat transport in the wave front is included implicitly.

Symbols used in this chapter are follows; p: pressure, V: specific volume, T: temperature, C_V: constant-volume specific heat, γ: Grüneisen parameter, E: specific internal energy, S: specific entropy, U_S: shock velocity, U_P: particle velocity, c, s: $U_\mathrm{S} = c + sU_\mathrm{P}$, ρ: specific density, ε: strain, N: the number of atoms per unit mass, k_B: Boltzmann constant, subscript 0: an ambient state, and subscript H: a shocked state.

Firstly, the Walsh-Christian equation:

$$C_{V\mathrm{H}}\frac{dT_\mathrm{H}}{dV_\mathrm{H}} + \frac{\gamma_0}{V_0}C_{V\mathrm{H}}T_\mathrm{H} = \frac{1}{2}\frac{dp_\mathrm{H}}{dV_\mathrm{H}}(V_0 - V_\mathrm{H}) + \frac{1}{2}(p_\mathrm{H} - p_0), \tag{A.1}$$

is derived. Equations (A.2) and (A.3) will be derived after the derivation of Eq. (A.1).

The following thermodynamic equation is derived from the first law of thermodynamics.

$$TdS = dE + pdV. \tag{A.2}$$

Eq. (23) in Ref. [1] is

$$TdS = C_V dT + \left(\frac{\partial p}{\partial T}\right)_V TdV. \tag{A.3}$$

The following equation is obtained by integrating Eq. (A.2) from 0 to H along the Hugoniot;

185

$$\int_{S_0}^{S_{\mathrm{H}}} TdS = \int_{E_0}^{E_{\mathrm{H}}} dE + \int_{V_0}^{V_{\mathrm{H}}} p_{\mathrm{H}} dV . \qquad (A.4)$$

Hugoniot shock jump equation derived from the conservation law of energy is expressed as follows;

$$E_{\mathrm{H}} - E_0 = \frac{1}{2}(p_{\mathrm{H}} + p_0)(V_0 - V_{\mathrm{H}}) . \qquad (A.5)$$

The following equation is obtained by substituting Eq. (A.5) into Eq. (A.4);

$$\int_{S_0}^{S_{\mathrm{H}}} TdS = \frac{1}{2}(p_{\mathrm{H}} + p_0)(V_0 - V_{\mathrm{H}}) + \int_{V_0}^{V_{\mathrm{H}}} p_{\mathrm{H}} dV . \qquad (A.6)$$

The definition of the constant-volume specific heat is

$$C_V = \left(\frac{\partial E}{\partial T}\right)_V . \qquad (A.7)$$

Mie-Grüneisen equation is expressed as follows;

$$\frac{\gamma}{V} = \left(\frac{\partial p}{\partial E}\right)_V . \qquad (A.8)$$

The following equation is obtained by combining Eq. (A.7) with Eq. (A.8);

$$\frac{\gamma}{V} C_V = \left(\frac{\partial p}{\partial T}\right)_V . \qquad (A.9)$$

The following equation is obtained by substituting Eq. (A.9) into Eq. (A.3);

$$TdS = C_V dT + \frac{\gamma}{V} C_V T dV . \qquad (A.10)$$

The following equation is obtained by by integrating Eq. (A.10) from 0 to H along the Hugoniot assuming $\gamma/V = \gamma_0/V_0$;

$$\int_{S_0}^{S_{\mathrm{H}}} TdS = \int_{T_0}^{T_{\mathrm{H}}} C_{V\mathrm{H}} dT + \int_{V_0}^{V_{\mathrm{H}}} \frac{\gamma_0}{V_0} C_{V\mathrm{H}} T_{\mathrm{H}} dV , \qquad (A.11)$$

Combining Eq. (A.6) with Eq. (A.11) results in the following equation;

$$\frac{1}{2}(p_{\mathrm{H}} + p_0)(V_0 - V_{\mathrm{H}}) + \int_{V_0}^{V_{\mathrm{H}}} p_{\mathrm{H}} dV = \int_{T_0}^{T_{\mathrm{H}}} C_{V\mathrm{H}} dT + \int_{V_0}^{V_{\mathrm{H}}} \frac{\gamma_0}{V_0} C_V T_{\mathrm{H}} dV . \qquad (A.12)$$

Differentiating Eq. (A.12) by V_{H};

$$\frac{1}{2}\frac{dp_{\mathrm{H}}}{dV_{\mathrm{H}}}(V_0 - V_{\mathrm{H}}) - \frac{1}{2}(p_{\mathrm{H}} + p_0) + p_{\mathrm{H}} = C_{V\mathrm{H}}\frac{dT_{\mathrm{H}}}{dV_{\mathrm{H}}} + \frac{\gamma_0}{V_0}C_{V\mathrm{H}}T_{\mathrm{H}} , \qquad (A.13)$$

$$\Leftrightarrow C_{V\mathrm{H}}\frac{dT_{\mathrm{H}}}{dV_{\mathrm{H}}} + \frac{\gamma_0}{V_0}C_{V\mathrm{H}}T_{\mathrm{H}} = \frac{1}{2}\frac{dp_{\mathrm{H}}}{dV_{\mathrm{H}}}(V_0 - V_{\mathrm{H}}) + \frac{1}{2}(p_{\mathrm{H}} - p_0) . \qquad (A.1)$$

Walsh-Christian equation (Eq. (A.1) is obtained.

Secondly, Eq. (A.2) obtained from the first law of thermodynamics;

$$TdS = dE + pdV ,$$
<div align="right">(A.2)</div>

is derived. The definition of the entropy by the first law of thermodynamics is

$$dS = \frac{dQ}{T} .$$
<div align="right">(A.14)</div>

$$dQ = dE - dW ,$$
<div align="right">(A.15)</div>

is obtained from the first law of thermodynamics

$$Q = E - W .$$
<div align="right">(A.16)</div>

Substituting Eq. (A.16) into the first law of thermodynamics

$$dW = -pdV ,$$
<div align="right">(A.17)</div>

results in

$$dQ = dE + pdV .$$
<div align="right">(A.18)</div>

Eq. (A.2);

$$TdS = dE + pdV ,$$
<div align="right">(A.2)</div>

is obtained by substituting Eq. (A.18) into Eq. (A.14).

Finally, Eq. (23) in Ref. [1];

$$TdS = C_V dT + \left(\frac{\partial p}{\partial T} \right)_V TdV .$$
<div align="right">(A.3)</div>

is derived.

$$dS = \left(\frac{\partial S}{\partial T} \right)_V dT + \left(\frac{\partial S}{\partial V} \right)_T dV ,$$
<div align="right">(A.19)</div>

is obtained from $S = S(V,T)$.

Substituting $dW = -pdV$ and $dQ = TdS$ into Eq. (A.19) results in

$$dE = TdS - pdV .$$
<div align="right">(A.20)</div>

The following equation is obtained by dividing Eq. (A.20) by dT fixing V

$$\left(\frac{\partial E}{\partial T} \right)_V = T \left(\frac{\partial S}{\partial T} \right)_V .$$
<div align="right">(A.21)</div>

Substituting Eq. (A.21) into Eq. (A.7) results in

$$C_V = T \left(\frac{\partial S}{\partial T} \right)_V .$$
<div align="right">(A.22)</div>

The Helmholtz free energy F is defined as

$$F = E - TS .$$
<div align="right">(A.23)</div>

This equation is transformed to

$$dF = dE - TdS - SdT .$$
<div align="right">(A.24)</div>

Substituting Eq. (A.20) into Eq. (A.24) results in

$$dF = -pdV - SdT .$$ (A.25)

$$dF = \left(\frac{\partial F}{\partial V}\right)_T dV + \left(\frac{\partial F}{\partial T}\right)_V dT ,$$ (A.26)

is obtained from $F = F(V,T)$.

$$p = -\left(\frac{\partial F}{\partial V}\right)_T ,$$ (A.27)

$$S = -\left(\frac{\partial F}{\partial T}\right)_V ,$$ (A.28)

are obtained from Eqs. (A.25) and (A.26), respectively. Differentiating Eq. (A.27) by T fixing V results in

$$\left(\frac{\partial p}{\partial T}\right)_V = -\frac{\partial}{\partial T}\left(\frac{\partial F}{\partial V}\right)_T$$

$$= -\frac{\partial}{\partial V}\left(\frac{\partial F}{\partial T}\right)_V$$ (A.29)

The following equation is obtained by combining Eq. (A.29) with Eq. (A.28);

$$\left(\frac{\partial p}{\partial T}\right)_V = \left(\frac{\partial S}{\partial V}\right)_T .$$ (A.30)

Multiplying Eq. (A.19) by T results in

$$TdS = T\left(\frac{\partial S}{\partial T}\right)_V dT + T\left(\frac{\partial S}{\partial V}\right)_T dV .$$ (A.31)

Substituting Eqs. (A.22) and (A.30) into Eq. (A.31) results in Eq. (A.3);

$$TdS = C_V dT + \left(\frac{\partial p}{\partial T}\right)_V TdV .$$ (A.3)

Reference in Appendix A

[1]   J. M. Walsh and R. H. Christian, "Equation of state of metals from shock wave measurements," Phys. Rev. 97, 1544-1556 (1955).

List of Publications

Regular journals

1. T. Sano, H. Mori, E. Ohmura, and I. Miyamoto, "Femtosecond laser quenching of the ε phase of iron," Appl. Phys. Lett. 83, 3498-3500 (2003). [Chapter 4]

2. H. Yamada, T. Sano, T. Nakayama, and I. Miyamoto, "Optimization of laser-induced forward transfer process of metal thin films," Appl. Surf. Sci. 197-198, 411-415 (2002). [Chapter 2]

3. T. Sano, T. Nakayama, H. Yamada, and I. Miyamoto, "Experimental investigation of laser induced forward transfer process of metal thin films," Appl. Surf. Sci. 186, 221-226 (2002). [Chapter 2]

4. T. Sano and Y. Sano, "Equilibrium thermodynamic theory explicitly including heat transport for evaluation of temperature distributions in steady plane-wave fronts," J. Appl. Phys. 90, 5576-5584 (2001). [Chapter 4]

5. T. Sano and Y. Sano, "Equilibrium thermodynamic theory for the evaluation of temperature distributions in overdriven steady-plane wave fronts," J. Appl. Phys. 90, 3754-3761 (2001). [Chapter 4]

6. Y. Sano and T. Sano, "Thermal properties of close-packed Fe up to 400 GPa determined using Hugoniot functions," Phys. Rev. B (accepted). [Chapter 4]

7. T. Sano, "Temperature distributions inside overdriven steady-plane wave fronts in iron," Sci. Technol. Adv. Mater. (accepted). [Chapter 4]

8. T. Okamoto, Y. Morishige, E. Ohmura, T. Sano, and I. Miyamoto, "Analytical study on metal microstructures using femtosecond laser," Appl. Phys. A (submitted).

9. Y. Sano and T. Sano, "Thermal properties of close-packed Fe at high pressures (First report: Classical thermodynamic theory)," Transactions of the Japan Society of Mechanical Engineers A (submitted). (in Japanese) [Chapter 4]

10. Y. Sano and T. Sano, "Thermal properties of close-packed Fe at high pressures (Second report: Theoretical prediction)," Transactions of the Japan Society of Mechanical Engineers A (submitted). (in Japanese) [Chapter 4]

11. T. Sano, H. Mori, O. Sakata, E. Ohmura, and I. Miyamoto, "Synchrotron X-ray diffraction evidence for quenching of the high-pressure phase of iron," Phys. Rev. Lett. (to be submitted) [Chapter 4]

189

12. T. Sano, M. Yanai, E. Ohmura, Y. Nomura, Y. Hirata, and I. Miyamoto, "Femtosecond laser fabrication of microspike-arrays for micro field emitter on tungsten surface," Appl. Phys. Lett. (to be submitted) [Chapter 3]

13. T. Sano, H. Mori, O. Sakata, E. Ohmura, I. Miyamoto, and K. F. Kobayashi, "Femtosecond laser driven shock quenching of the high-pressure phase of iron," Appl. Surf. Sci. (to be submitted) [Chapter 4]

14. T. Sano, T. Nakayama, H. Yamada, E. Ohmura, and I. Miyamoto, "Laser direct writing of metal micro-patterns (First report: Fabrication using excimer laser)," Transactions of the Japan Society of Mechanical Engineers C (to be submitted). (in Japanese) [Chapter 2]

15. T. Sano, H. Yamada, E. Ohmura, and I. Miyamoto, "Laser direct writing of metal micro-patterns (Second report: Fabrication using femtosecond laser)," Transactions of the Japan Society of Mechanical Engineers C (to be submitted). (in Japanese) [Chapter 2]

Proceedings

1. T. Sano, H. Mori, E. Ohmura, and I. Miyamoto, "Femtosecond pulsed laser induced phase transition in iron," Proc. SPIE 4977, 136-141 (2003).
   Laser Applications in Mircoelectronics and Optoelectronic Manufacturing (LAMOM) VIII, LASE 2003, Photonics West 2003, 25-31 January 2003, San Jose, CA, USA. [Chapter 4]

2. H. Yamada, T. Sano, E. Ohmura, and I. Miyamoto, "Excimer and femtosecond pulsed laser induced forward transfer process of metal thin film," Proc. SPIE 4977, 426-433 (2003).
   Laser Applications in Mircoelectronics and Optoelectronic Manufacturing (LAMOM) VIII, LASE 2003, Photonics West 2003, 25-31 January 2003, San Jose, CA, USA. [Chapter 2]

3. M. Murai, T. Sano, E. Ohmura, and I. Miyamoto, "Electron emission at an early stage of femtosecond pulsed laser ablation," Proc. SPIE 4830, 467-470 (2003).
   International Congress on Laser Advanced Materials Processing (LAMP) 2002, Osaka University, Japan, May 27-31, 2002. [Chapter 3]

4. T. Okamoto, Y. Morishige, E. Ohmura, T. Sano, and I. Miyamoto, "Femtosecond laser ablation of Cr-SiO_2 binary mask," Proc. SPIE 4830, 510-514 (2003).
   International Congress on Laser Advanced Materials Processing (LAMP) 2002, Osaka University, Japan, May 27-31, 2002. [Chapter 3]

5. K. Komorita, T. Sano, H. Yamada, and I. Miyamoto, "Oxidation state control of micro metal oxide patterns produced by using laser-induced forward transfer technique," Proc. SPIE 4830, 20-24 (2003).

International Congress on Laser Advanced Materials Processing (LAMP) 2002, Osaka University, Japan, May 27-31, 2002. [Chapter 2]

6. T. Sano, H. Yamada, T. Nakayama, and I. Miyamoto, "Laser induced rear ablation of metal thin films," Proc. SPIE 4426, 70-73 (2001).

The 2nd Symposium on Laser Precision Microfabrication (LPM), Singapore, May 16-18, 2001. [Chapter 2]

7. T. Sano and I. Miyamoto, "Removal process of metal thin films during laser rear patterning," Proc. SPIE 4088, 401-404 (2000).

Laser Applications in Microelectronic and Optoelectronic Manufacturing (LAMOM) VI, San Jose, USA, Jan. 22-24, 2001. [Chapter 2]

8. S. Asada, T. Sano, and I. Miyamoto, "High efficient microdrilling of silicon wafer using excimer laser," Proc. SPIE 4088, 132-135 (2000).

Laser Applications in Microelectronic and Optoelectronic Manufacturing (LAMOM) VI, San Jose, USA, Jan. 22-24, 2001. [Chapter 3]

9. T. Sano, I. Miyamoto, H. Hayashi, and H. Ochi, "Analysis of excimer laser patterning process of Cu thin film," Proc. SPIE 3933, 356-364 (2000).

Laser Applications in Microelectronic and Optoelectronic Manufacturing (LAMOM) V, San Jose, USA, Jan. 20-24, 2000. [Chapter 2]

Other publications on microprocessing

1. A. M. Ektessabi and T. Sano, "Sputtering and thermal effect during ion microbeam patterning of polymeric films," Rev. Sci. Instrum. 71, 1012-1015 (2000).

2. A. M. Ektessabi and T. Sano, "Microfabrication of polymers using ion micro beam," Journal of the Japan Society for Precision Engineering, 65, 997-1001 (1999). (in Japanese)

3. T. Nakayama, T. Sano, I. Miyamoto, K. Tanaka, and Y. Uchida, "Study on CO_2 laser drilling of printed wiring boards and development of in-process monitoring system," Proc. SPIE 3933, 379-386 (2000).

Laser Applications in Microelectronic and Optoelectronic Manufacturing (LAMOM) V, San Jose, USA, Jan. 20-24, 2000.